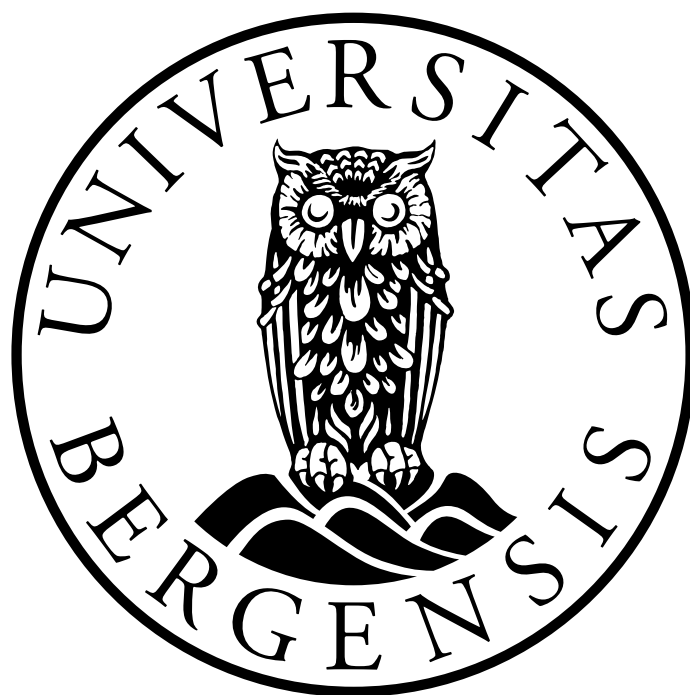


FUELING THE FUTURE WITH SUSTAINABLE CHEMISTRY

Furfural Synthesis from Xylose, Plums and Cherries in a Biphasic
Reaction System for Renewable Fuel and Chemicals Production



MASTER THESIS IN RENEWABLE ENERGY

Chemistry and Environment

AUTHOR: JOAKIM LINDGAARD MOLNES

SUPERVISOR: TANJA BARTH

CO-SUPERVISOR: MIKE KLEINERT

UNIVERSITY OF BERGEN

DEPARTMENT OF CHEMISTRY

JUNE 2021

ACKNOWLEDGEMENTS

First and foremost, I would like to express my deepest gratitude to my supervisor Tanja Barth for exceptional guidance, supervision, and encouragement throughout my past years as a student at the University of Bergen. You believed in me even before I was accepted to the master's program in Energy, and I would not be where I am today without your outstanding ability and genuine interest in helping others succeed. Secondly, a big thanks to my co-supervisor, Mike Kleinert, for repeatedly making room in your otherwise busy schedule to share your knowledge and expertise when I needed it the most.

Thanks to the staff at the Department of Chemistry, especially Jarl Underhaug and José Guerrero at the Norwegian NMR Platform (NNP), for magnificent help concerning sample acquisition and structural elucidations, Cecilie Dybsland for the excellent training and help with the GC-MS and HPLC instruments, Egil Nodland for helping me with multivariate data analysis, and Beate Halsvik for assisting me with reaction mechanisms over the past year.

I would also like to extend my heartfelt gratitude to Camilla Løhre, Solmaz Ghoreishi, and Stian Hegdahl for their exceptional help and guidance over the past year. Thank you for your endless patience, moral support, constructive feedback, and for continuously sharing your insight and experience to help me overcome the countless hurdles I have encountered over the course of this thesis. To the rest of the research group, thank you for welcoming me with open arms, and for wonderful lunch conversations. Additional thanks to Anja Molnes, Camilla Løhre, Maxime Grandin, and Sam Black for invaluable feedback when proofreading my thesis.

To my dearest family and friends, thank you for your unconditional love and support and for always believing in me wherever I have lived and whatever dream I have been pursuing over the past decade. You have made me the person I am today, something I will be forever grateful for. I will continue to work hard every single day to make you proud.

Lastly, I would like to dedicate this thesis to my grandpa, Tron Leidland, who was unable to see me finish my studies. Still, his insatiable curiosity and thirst for knowledge continues to inspire me every single day.

ABSTRACT

Furfural (FUR) is a furanic compound derived from the dehydration of pentoses found in abundance in biomass and various sugar-containing industrial waste streams. FUR could potentially serve as an essential biobased platform molecule as it can be upgraded into a plethora of different fuels and chemicals currently produced from petroleum-based resources. In this thesis, the production of FUR from D-xylose (XYL) and fruit and berry (F&B) rejects was investigated using a biphasic reaction system. Methyl isobutyl ketone (MIBK) was used as an *in-situ* extraction solvent to enhance the FUR yield by stabilizing the final product, thus minimizing by-product formation. The influence of substrate loading, catalyst loading, the volumetric ratio between the organic extraction phase and the aqueous reaction phase, residence time, and reaction temperature, and how each factor affected FUR yield, XYL conversion, and reaction selectivity were investigated. The best FUR yield obtained in this thesis was 42.9mol% from the dehydration of 0.83M XYL using 0.032M sulfamic acid as a catalyst with an organic-to-aqueous ratio of 1:4 at 200°C for 90 min. However, the reaction system still has potential for further optimization. When cherry rejects were used as feedstock under the same reaction conditions, a maximum FUR and HMF yield of 0.56wt% and 9.87wt% were obtained, respectively. For plums, the FUR and HMF yields were 0.45wt% and 11.93%, respectively. The work conducted in this thesis has also established reliable analytical procedures using qNMR for accurate and precise quantification of furanic derivatives generated in a biphasic solvent system. In addition, the results have demonstrated that F&B rejects could serve as a promising biobased feedstock for the production of value-added fuels, chemicals, and materials that have traditionally been produced from petroleum resources, which is highly desirable seen from a sustainable perspective.

LIST OF CONTENTS

ACKNOWLEDGEMENTS	II
ABSTRACT	III
ABBREVIATIONS	V
1. INTRODUCTION	1
2. BACKGROUND	3
2.1 THE CARBON CYCLE.....	3
2.2 THE ADVANCEMENT OF GREEN CHEMISTRY	5
2.3 BIOFEEDSTOCKS	6
2.3.1 First generation feedstocks	6
2.3.2 Second generation feedstocks	6
2.3.3 Third and fourth generation feedstocks	12
2.4 THE BIOREFINERY CONCEPT.....	12
2.4.1 Utilization of fruit and berry residues as a biorefinery feedstock	14
2.5 FURANS.....	15
2.6 FURFURAL.....	16
2.6.1 Mechanistic pathways to furfural.....	17
2.6.2 Degradation, side-reactions and by-product formation	19
2.6.3 Furfural derivatives and energy applications.....	21
2.6.4 Established industrial processes	23
2.6.5 State-of-the-art production of furfural	23
3. OBJECTIVES	31
4. MATERIALS, METHODS AND EXPERIMENTAL	33
4.1 ANALYTICAL METHODS	33
4.1.1 Chromatography	33
4.1.2 Nuclear Magnetic Resonance (NMR)	36
4.1.3 Experimental design.....	41
4.2 MATERIALS.....	45
4.3 EXPERIMENTAL.....	46
4.3.1 Experimental design.....	46
4.3.2 Dehydration of D-xylose to furfural.....	46
4.3.3 Dehydration of F&B rejects to furfural and 5-hydroxymethylfurfural.....	47
4.3.4 Experimental procedures - GC-MS.....	47
4.3.5 Experimental procedures – HPLC.....	50
4.3.6 Experimental procedures – NMR.....	52

4.3.7 Preparation of procedural blanks	54
4.3.8 Catalyst testing.....	55
4.4 EQUATIONS	56
5. RESULTS AND DISCUSSION	57
5.1 COMPARISON OF GC-MS, HPLC, AND QNMR AS QUANTIFICATION TOOLS	57
5.1.1 Interpretation of results from qNMR.....	64
5.1.2 Interpretation of results from HPLC.....	65
5.1.3 Interpretation of results from GC-MS.....	65
5.1.4 ¹ H-qNMR vs. ¹³ C-qNMR.....	66
5.2 REACTION SYSTEM SELECTION	72
5.2.1 Solvent selection.....	72
5.2.2 Catalyst selection	74
5.2.3 Substrate selection	78
5.3 EXPERIMENTAL DESIGNS	79
5.3.1 Results from the first experimental design.....	79
5.3.2 Results from the second experimental design	84
5.4 HYPOTHESIZED SIDE-REACTIONS	108
5.5 UTILIZATION OF F&B AS FEEDSTOCK FOR PRODUCTION OF FUR AND HMF	111
6. CONCLUSION	115
7. FURTHER WORK.....	118
8. BIBLIOGRAPHY.....	120
APPENDICES.....	128
APPENDIX A – STRUCTURAL ELUCIDATIONS	128
Appendix A1 – Structural elucidation of α and β -D-xylose	128
Appendix A2 – Structural elucidation of furfural	149
Appendix A3 – Structural elucidation of 5-hydroxymethylfurfural.....	156
Appendix A4 – Structural elucidation of gamma-valerolactone (GVL).....	163
Appendix A5 - Additional standard spectra (NMR).....	165
APPENDIX B – RAW DATA FROM THE SECOND EXPERIMENTAL DESIGN	166
APPENDIX C – RAW DATA FROM THE FIRST EXPERIMENTAL DESIGN	183
APPENDIX D – RAW DATA – HPLC, GC-MS	190
APPENDIX E – PHYSICO-CHEMICAL PROPERTIES OF CENTRAL COMPOUNDS	195
APPENDIX F – SECOND PROCEDURAL BLANK GC-MS	198
APPENDIX G – STACKED NMR SPECTRA OF REPLICATES	203
APPENDIX H – NMR SPECTRA F&B REJECTS	207
APPENDIX I – CALCULATION OF THEORETICAL YIELD FROM D-XYLOSE AND HEMICELLULOSE.....	210
APPENDIX J – INFLUENCE OF EXTRACTION TIME ON CALCULATED FURFURAL YIELD	211
APPENDIX K – ADDITIONAL REACTION SCHEMES AND PICTURES	212

ABBREVIATIONS

ABBREVIATION	MEANING
ADC	Analog to Digital Converter
ARA	Arabinose
AX	Arabinoxylan
B	Counter magnetic field
B ₀	External magnetic field
BA	Brønsted acid
BP	Boiling Point
CH	Chlorohexane
CMF	Chloromethylfurfural
COSY	Homonuclear Correlation Spectroscopy
CP	Center point
CPME	Cyclopentyl methyl ether
CPON	Cyclopentanone
D ₂ O	Deuterium oxide
Da	Dalton
DAD	Diode Array Detector
DOE	Department of Energy
DMF	Dimethylfuran
DMSO	Dimethyl sulfoxide
DMSO ₂	Dimethylsulfone
DP	Degree of Polymerization
EA	Elemental Analysis
EFE	Ethyl furfuryl ether
EHS	Environment, Health and Safety
EMR	Electromagnetic Radiation
EP	Extraction Phase
EPA	Environmental Protection Agency
EtOAc	Ethyl acetate
F	Fluorine

F&B	Fruit and Berry
FA	Formic acid
FD	Factorial Design
FDCA	2,5-Furandicarboxylic acid
FE	Furfuryl ester
FFD	Fractional Factorial Design
FID	Free-induction decay
FOL	Furfuryl alcohol
FP	Flash Point
FT	Fourier Transformation
FUC	Fucose
FUR	Furfural
GAL	Galactose
GAM	Galactomannans
GAX	Glucuronoarabinoxylan
GC	Gas Chromatography
GC-MS	Gas Chromatography Mass Spectrometry
GGM	Galactoglucomannans
GHG	Greenhouse gas
GLC	Glucose
GLCA	Glucuronate anion
GM	Glucomannans
GtC/yr	Gigatons carbon per year
GVL	γ -valerolacetone
GX	Glucuronoxylan
H	Hydrogen
HD	Hexadecane
HMBC	Heteronuclear Multiple Bond Correlation
HMF	5-Hydroxymethylfurfural
HPLC	High performance liquid chromatography
HSQC	Heteronuclear single quantum coherence
HTL	Hydrothermal Liquefaction
IEA	International Energy Agency

IPCC	Intergovernmental Panel on Climate Change
IR	Infrared spectroscopy
k	Retention factor
kDa	Kilodalton
kTon	Kilotons
LA	Levulinic acid
LC	Liquid chromatography
LCB	Lignocellulosic biomass
LeA	Lewis acid
LHSV	Liquid Hourly Space Velocity
LoQ	Limit of Quantification
LtL	Lignin-to-Liquid
M	Miscible
MAN	Mannose
MeTHF	Methyltetrahydrofuran
MF	Methylfuran
MIBK	Methyl Isobutyl Ketone
MeP	Melting Point
MP	Mobile phase
MTHF	Methyltetrahydrofuran
NIBIO	The Norwegian Institute of Bioeconomy Research
NIST	National Institute of Standards and Technology
NMR	Nuclear Magnetic Resonance
NOK	Norwegian kroner
NOAA	National Oceanic and Atmospheric Administration
NP	Normal Phase
NR	Not relevant
NS	Not specified
OHE	One-step Hydrogenation Esterification
Org/aq	Organic/aqueous ratio
PA	Paris Agreement
PC	Principal component vector
PCA	Principal Component Analysis

PLS	Partial least square
qNMR	Quantitative Nuclear Magnetic Resonance
RF	Radio Frequency
RHA	Rhamnose
RP	Reverse Phase
Ru	Ruthenium
SA	Sulfamic acid
SD	Standard Deviation
SDGs	Sustainable Development Goals
SP	Stationary phase
T	Temperature
t	Time
T ₁	Relaxation time
THF	Tetrahydrofuran
TMS	Tetramethylsilane
TOL	Toluene
t _R	Retention time
TSP	Trimethylsilyl)-propionic-2,2,3,3-d ₄ acid)
U	Monomeric units
UN	United Nations
UNFCCC	United Nations Framework Convention on Climate Change
USD	United States Dollar
UV-vis	Ultraviolet-visible spectrophotometry
WCED	World Commission on Environment and Development
WEO	World Energy Outlook
XOS	Xylooligosaccharides
XYGs	Xyloglucans
XYL	D-xylose
γ	Gyromagnetic ratio
δ	Chemical shift
ε	Molar absorptivity
λ _{max}	Maximum absorbance wavelength

1. INTRODUCTION

Global primary energy consumption continues to rise due to a rapidly growing global population and increased energy demand per capita. Consequently, providing the world with clean, affordable, and renewable sources of energy is of paramount importance in order to cut greenhouse gas (GHG) emissions and mitigate climate change. Even though the feasibility of fossil exploitation is anticipated to decline due to its inevitable depletion, fossil-derived energy continues to dominate the global energy market in the twenty-first century, with an estimated market share of 81% in 2020 (Sundaram, 2015, IEA, 2020b). Numerous projections regarding the global “peak oil” production have been made ever since the concept was introduced in 1956 (Hubbert, 1956). How steep the downward facing slope of diminishing economic returns will be after peak oil has been reached, is still an ongoing debate and is highly dependent upon future policy frameworks and technological development (Kuhns and Shaw, 2018). In the World Energy Outlook (WEO), published by the International Energy Agency (IEA) in 2020, oil production and demand are expected to reach their peak around 2040 (106mb/d) based on existing policy frameworks and the outlined trajectory of global energy consumption, emission levels, and energy security (IEA, 2020b). In order to reduce this prolonged dependence on fossil feedstocks, deployment of renewable technologies capable of generating viable and energy-efficient fuels and chemicals is critical to ensure the future prosperity of the human enterprise (Cherubini, 2010).

Acknowledging sustainability as an integral part of societal, economic, and environmental well-being has led to numerous scientific publications and the introduction of several international policies and agreements concerning energy and climate over the past decades. The publication of the Twelve Principles of Green Chemistry in 1998 (Anastas and Warner, 1998) established a fundamental basis for state-of-the-art production of more environmentally friendly fuels and chemicals. The subsequent announcement of the 17 sustainable development goals (SDGs) by the United Nations (UN) in 2015 in combination with the signing of the Paris Agreement (PA) later the same year resulted in a revived surge in the development of greener alternatives to fossil-derived energy, chemicals and products (Acheampong et al., 2017).

In this context, it has become increasingly apparent that biomass can serve as a replacement for a considerable fraction of the fossil feedstocks currently being used as raw materials in the

energy- and production sectors. The recognition of biomass as an invaluable renewable resource has been a major driving force for the advancement of biorefineries, aiming for the efficient valorization of different biobased feedstocks. In fact, it is estimated that one-eighth of the biomass produced each year could accommodate the annual global energy demand if utilized to its full potential (Wertz and Bédoué, 2013, Cherubini, 2010). Hence, biorefineries must strive to identify the best universal platform molecules that can be upgraded to a plethora of different fuels and chemicals (Cherubini, 2010). Dehydration of carbohydrates into furanic compounds, like FUR and 5-hydroxymethylfurfural (HMF), derived from sustainable biomass sources can potentially serve as viable replacements for petroleum-based platform molecules due to their diverse applicability as renewable intermediates (Danon et al., 2014, Liu et al., 2020). Consequently, FUR and HMF, sometimes referred to as “the sleeping giants” of sustainable chemistry, could potentially play a key role in the ongoing sustainable revolution (Huber et al., 2006, Millan et al., 2019).

2. BACKGROUND

2.1 THE CARBON CYCLE

There is a general understanding that carbon-containing greenhouse gas (GHG) emissions affects Earth's climatic systems. Therefore, a basic understanding of the carbon cycle is fundamental in order to apprehend the concept of climate change and potential measures that can help shape a sustainable future.

Carbon constitutes the fourth most abundant element in the universe after hydrogen, helium, and oxygen. It is continuously cycled between the Earth's main components, namely the geosphere, hydrosphere, atmosphere, and Earth's interior in biogeochemical cycles. Carbon is stored and captured in these reservoirs by several short- and long-term processes referred to as the biological and geological carbon cycle, respectively. The latter includes long-term storage of inorganic carbon in the ocean, the atmosphere, and in geological formations, primarily in the form of carbonate rocks, minerals, and carbon dioxide (CO₂). The short-term biological carbon cycle includes carbon stored in biomass which has been defined as all “material produced by the growth of microorganisms, plants and animals” (IUPAC, 1997). Carbon in the form of CO₂ is sequestered by photosynthetic organisms, i.e., terrestrial plants and aquatic phytoplankton and converted into organic molecules through photosynthetic processes. The biologically fixed organic carbon is then distributed throughout the Earth's ecosystems before it is either re-emitted as CO₂ into the atmosphere by respiration and decomposition, or buried under terrestrial and/or marine sediments where it is slowly converted into fossil resources (Figure 2-1) (Wertz and Bédué, 2013).

Carbon stored as fossil fuels, i.e., coal, oil, and natural gas, constitute the third-largest carbon reservoir on the planet (Figure 2-1). Anthropogenic activities like exploitation and utilization of fossil resources and alteration of natural landscapes have resulted in a strong disequilibrium in the global carbon cycle. Carbon is efficiently moved from long-term storage reservoirs into the atmosphere at a much higher rate than is being stored through natural processes, resulting in increased atmospheric CO₂ levels (IPCC, 2018). As of October 2020, the National Oceanic and Atmospheric Administration (NOAA) reported that the average atmospheric CO₂ concentration had reached 415ppm. As a comparison, in the middle of the 18th century, i.e., during pre-industrial times, the atmospheric CO₂ concentration was in the 280ppm range

(NOAA, 2020). According to the Intergovernmental Panel on Climate Change (IPCC), the key to limiting the global-mean temperature to 1.5°C above pre-industrial levels is to limit the annual anthropogenic emissions of long-lived greenhouse gases like CO₂ by about 45% compared to 2010 levels (49±4,5 gigatons CO₂-equivalents per year) by 2030 (IPCC, 2018, Edenhofer et al., 2014). IPCC further highlighted in the Fifth Assessment Report (AR5) from 2014 that fossil fuels should be completely phased out by 2100 if the 2°C goal set by the Paris Agreement (PA) is to be reached. To achieve this, they further suggested that renewable energy should constitute 80% of the global primary energy consumption by 2050 (Acheampong et al., 2017). However, in a report from 2020, IEA concluded that the global energy system is currently not on course to meet the ambitious goals set by the UN through the implementation of the SDGs and the PA. To make matters even worse, the spread of the Covid-19 pandemic has resulted in a systematic decline in global investments in renewable technologies, drastically slowing the deployment of renewable energy solutions that are crucial for the clean energy transition (IEA, 2020a, IEA, 2020b). Based on the abovementioned facts, it seems reasonable to postulate that no single solution can solve the global climate- and energy dilemmas. Therefore, several measures must be taken to meet the increasing demand for primary energy, fuels, and products while simultaneously reducing carbon emissions.

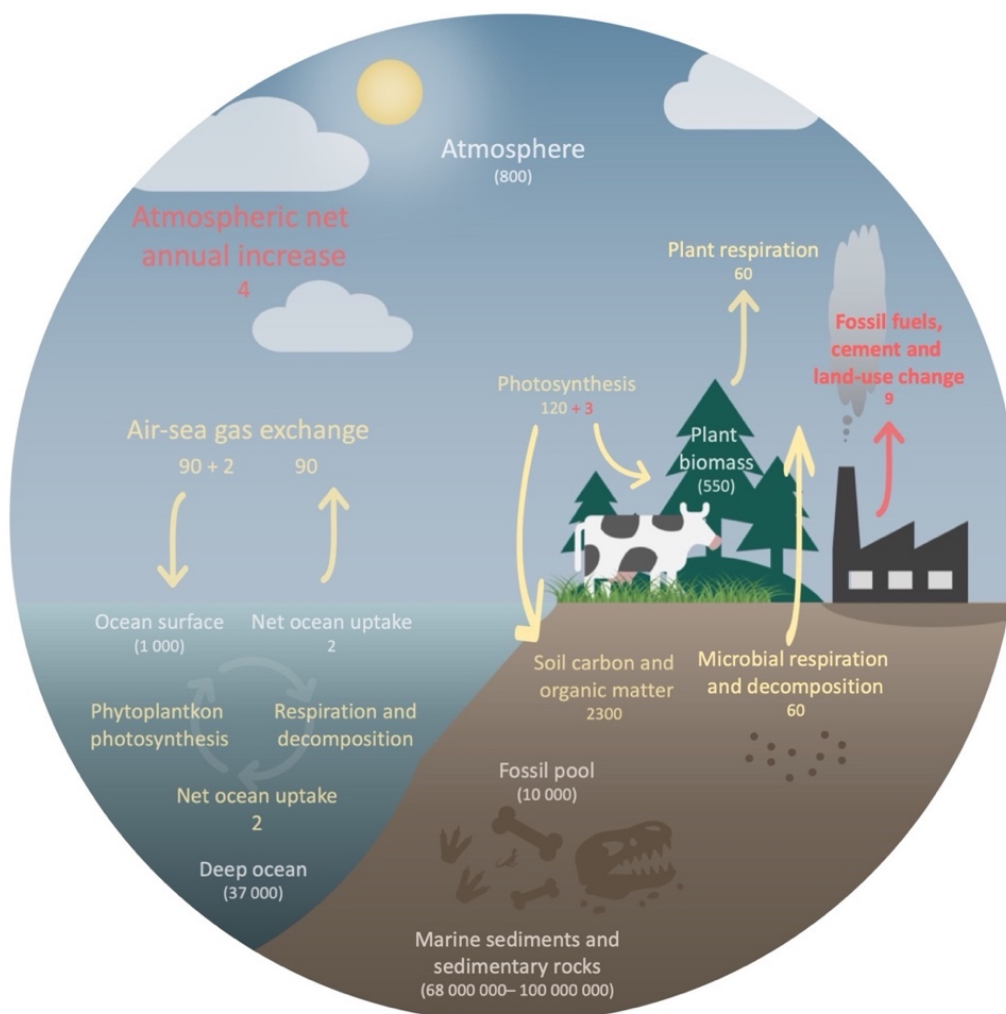


Figure 2-1: Simple schematic of the carbon cycle. The figure depicts how carbon is cycled between different reservoirs. Each number is in gigatons carbon per year (GtC/yr). Yellow and red numbers indicate natural carbon fluxes and anthropogenic carbon emissions, respectively. White numbers in brackets indicate organic and inorganic carbon pools. The figure was adapted from (DOE, 2015) by Anja Lindgaard Molnes.

2.2 THE ADVANCEMENT OF GREEN CHEMISTRY

A major challenge within the field of chemistry and engineering is the development and implementation of sustainable industrial processes and technologies. In the early 1990s, the US Environmental Protection Agency (EPA) defined the phrase green chemistry "to promote innovative chemical technologies that reduce or eliminate the use or generation of hazardous substances in the design, manufacture, and use of chemical products" (Lancaster and Chemistry, 2016). Later, a collaboration between John Warner and Paul Anastas resulted in the publication of the "Twelve Principles of Green Chemistry" (Anastas and Warner, 1998). The list was prepared to aid chemists and chemical engineers in developing industrial processes and

technology that were “benign by design” by making them more mass- and energy-efficient thus preventing the generation of pollutants instead of managing waste "end-of-pipe". Sheldon later formulated that the take-home message of green chemistry could be summarized as follows (Sheldon, 2014):

- Waste minimization through efficient use of feedstocks and raw materials.
- Minimize the risk for environmental, health, and safety (EHS) issues by avoiding toxic and/or hazardous chemicals and solvents.
- Replace conventional, non-renewable fossil-derived feedstocks with renewable feedstocks like biomass.

Principle number 7 of green chemistry states that "a raw material or feedstock should be renewable rather than depleting whenever technically and economically practical" (Anastas and Warner, 1998). As a result, both the scientific and industrial communities have put much effort into identifying potential bio-based feedstocks that could replace petroleum resources.

2.3 BIOFEEDSTOCKS

2.3.1 FIRST GENERATION FEEDSTOCKS

The utilization of first-generation feedstocks currently represents the majority of industrial scale processes aiming at utilizing biomass for higher-value applications. First-generation feedstocks primarily constitute the edible fractions of various food crops for fuel production, viz. bioethanol and biodiesel production. However, the "food versus fuel dilemma" has sparked a debate that has intensified over the past decade as first-generation fuel production diverts farmland previously devoted to food and feed production. As a result, scientists and politicians have advocated that our moral imperative is to explore alternative biobased sources for conversion into fuels and value-added products (Sundaram, 2015).

2.3.2 SECOND GENERATION FEEDSTOCKS

Second-generation feedstocks, comprising lignocellulosic biomass (LCB), represent the vast bulk of biologically derived matter on the planet and include inedible plant materials primarily consisting of cellulose (30 – 50wt%), hemicellulose (20 – 40wt%), and lignin (10 – 25wt%)

(Figure 2-2). Examples of potential feedstocks include agricultural wastes (e.g., straw, corn stover, corn cob, bagasse, molasses), forestry waste and energy-crops (e.g., switchgrass, poplar) (Sadhukhan et al., 2014, Wertz and Bédoué, 2013). Viable utilization of second-generation biomass has proven difficult due to the complex structural matrix formed by the principal structural components (*vide infra*). Consequently, development and deployment of technologies capable of maximizing valorization of this bountiful feedstock is highly sought after.

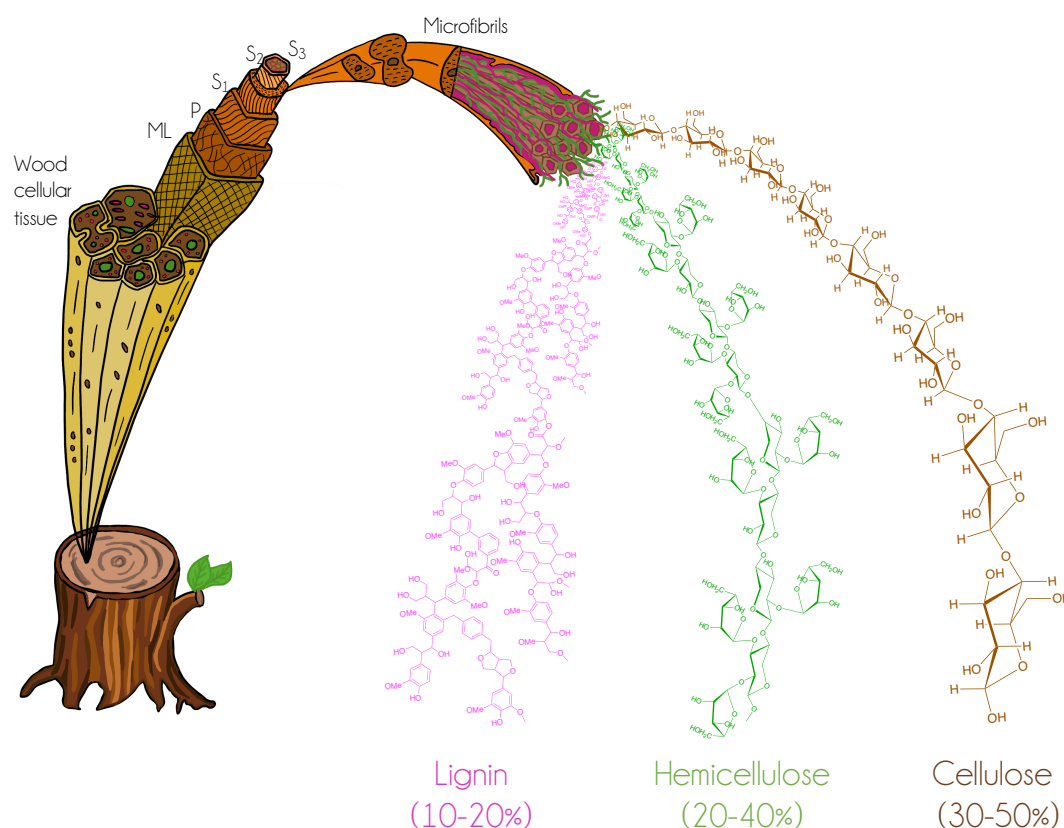


Figure 2-2: General structure of LCB. P = Primary cell wall, S₁, S₂, S₃ = Secondary cell wall layers, ML = Middle lamella. Redrawn and modified from (Hoffmann, 1989).

2.3.2.1 CELLULOSE

Cellulose is the most abundant organic compound on Earth. It is a linear, unbranched polymer composed of β -D-glucose units. Two distinct cyclic variants of D-Glucose occur naturally, specifically as a six-membered or a five-membered ring termed pyranose and furanose, respectively. Pyranose is the more stable cyclic form and involves the aldehydic function and the oxygen attached to C5 (Figure 2-3). The anomeric center (C1) generated as a result of the

hemiacetal ring formation results in the existence of two anomers, designated α and β . Cellulose consists of β -D-anhydroglucopyranose units ($(C_6H_{12}O_6)_n$) in the energetically favorable chair conformation, linked by β -1,4-glycosidic bonds (Figure 2-3) (Wertz and Bédudé, 2013). α -D-glucose constitute the monomeric building block of starch.

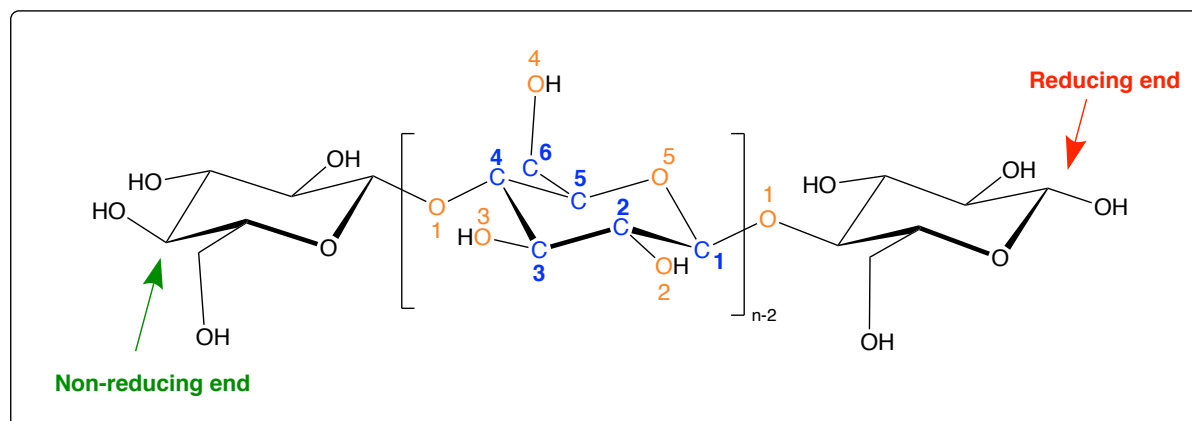


Figure 2-3: General structure of cellulose. The carbon and oxygen atom numbering are shown for the glucose monomer inside the brackets. The reducing end with a hemiacetal is marked in red, and the non-reducing end with a free hydroxyl group attached to C4 is marked in green. Adapted from (Wertz and Bédudé, 2013).

Glycosidic bonds are formed when the anomeric center (C1) of one β -D-glucose unit (glycone) is coupled to an oxygen atom on an alcohol (aglycone). For cellulose, the anomeric center is coupled to the alcoholic oxygen atom (O1) attached to C4 of another glucose monomer, thus generating an oxygen-ether bridge between C1 and C4 of adjacent glucose monomers, generating a disaccharide. O5 is the oxygen that is part of the pyranose ring. O2 and O3 are the oxygen atoms in the secondary alcohols, while O4 is the oxygen atom in the primary alcohol (Figure 2-3). Further chain propagation generates cellulose, which can contain up to 8000 monomeric units (U). The β -anomeric configuration of cellulose involves the formation of equatorial linkages. The two-fold helical conformation of the cellulose chain means that adjacent glucose units are oriented with their mean planes at 180° angles relative to each other. This forms a ribbon-like structure that enables intermolecular hydrogen bonding as the cellulose molecules align in a parallel fashion. Consequently, cellulose molecules organize into supramolecular crystals that form morphological structures known as microfibrils (Schobert, 2013). Cellulose is the chief constituent of lignocellulosic cell walls (Figure 2-2) and can constitute as much as 65% of the holocellulosic fraction present in lignocellulosic plants, that is, the total carbohydrate fraction consisting of cellulose and hemicellulose (Wertz and Bédudé, 2013).

2.3.2.2 HEMICELLULOSE

Hemicellulose differs from cellulose in several ways. Firstly, hemicellulose constitute a heterogeneous group of branched polymers with backbones consisting of D-pyranosyl residues linked by β -1,4-glycosidic bonds, where C1 and C4 exhibit equatorial configuration (Figure 2-4) (Wertz and Bédoué, 2013).

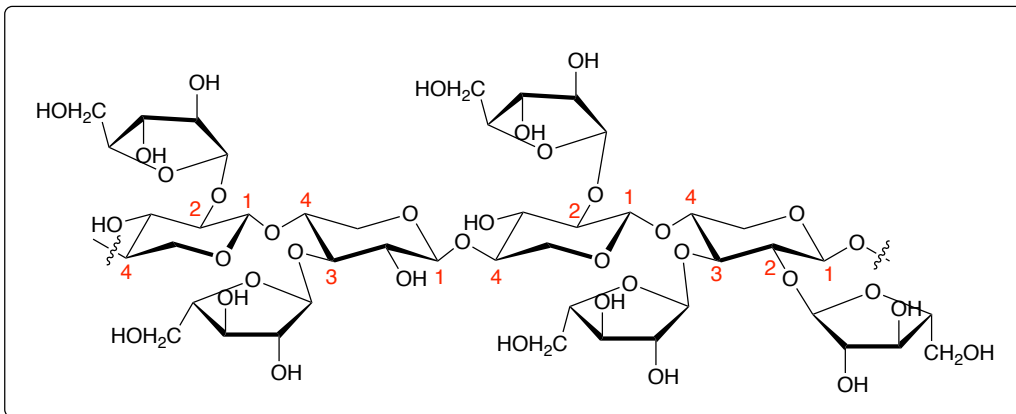


Figure 2-4: General structure of hemicellulose.

In other words, the backbone and branches can contain a variety of both pentose and hexose monomeric units (Figure 2-5), of which XYL is the most abundant molecule (Young, 1985). Hence, many different types of hemicellulose occur naturally. Hemicellulose can therefore be divided into four major groups with further subdivisions, depending on the molecular composition of the backbone and associated branches:

1. The first group, Xyloglucans (XyGs), have a glucose backbone with XYL branches. This is the dominant hemicellulose in primary cell walls of vascular plants.
2. Xylan, an aldopentose polymer, is the dominant hemicellulose present in the secondary cell wall in angiosperms (hardwood). The backbone is made up of XYL with both glucuronic acid and/or arabinose branches, giving rise to glucuronoxylan (GX), arabinoxylan (AX), and glucuronoarabinoxylan (GAX).
3. Mannans, the third group of hemicelluloses, can be subdivided into glucomannans (GM), galactomannans (GAM), and galactoglucomannans (GGM). GGM is the

predominant hemicellulose present in the secondary cell walls of gymnosperms (softwood) (Atalla et al., 1993).

- The last group of hemicelluloses are called mixed-linked glucans (β -1,3;1,4-glucans), and are most prominent in plants belonging to the grass family (Poaceae) (Wertz and Bédoué, 2013).

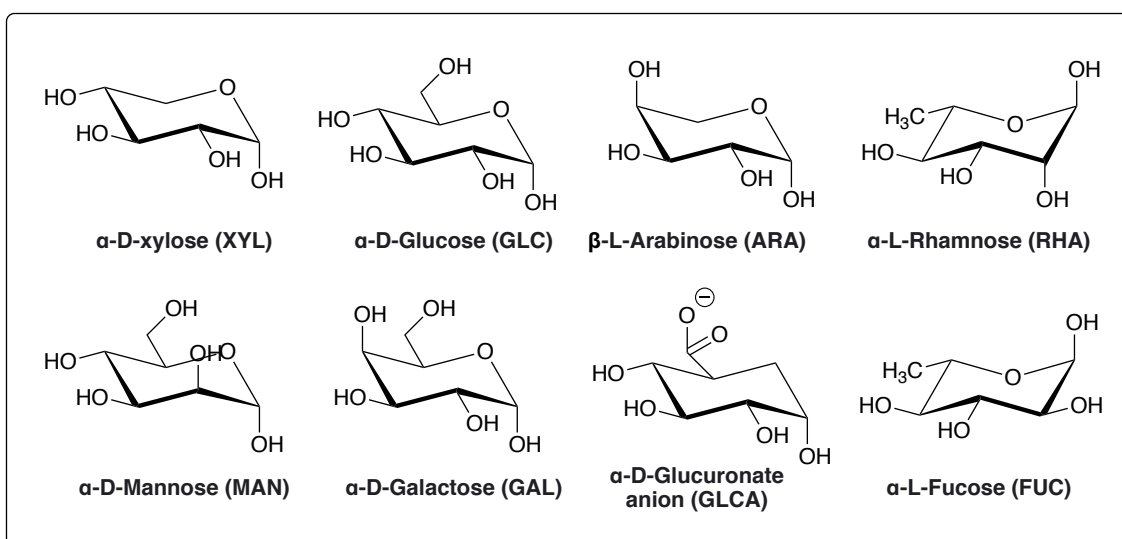


Figure 2-5: Common monomeric sugars of hemicellulose. Adapted from (Wertz and Bédoué, 2013).

Hemicellulose normally has a degree of polymerization (DP) ranging between 100-200 monomeric units (U), about 1/100 of the DP of cellulose (Pallardy and Kozłowski, 2008, Luo et al., 2019). Hemicelluloses are also referred to as cross-linking glycans, as they form hydrogen bonds and Van der Waal's interactions to cellulose microfibrils and other hemicellulose molecules. Consequently, it provides some of the structural rigidity and tensile strength of the primary and secondary cell walls in plants. In fact, the rigidity of the cell wall is proportional to the amount of hemicellulose present. The holocellulosic fraction of LCB normally contain between 35-50% hemicellulose. Hemicellulose is still an under-valorized resource making it a major field of investigation in both academia and industry. However, the structural complexity makes selective conversion of hemicellulose into specific platform molecules challenging.

2.3.2.3 LIGNIN

Lignin, a complex amorphous phenolic heteropolymer (600 – 15000 kDa), is the second most abundant organic compound found in nature and is the only naturally occurring polymer with an aromatic backbone. Consequently, lignin can be used as a feedstock to produce a wide spectrum of aromatic specialty chemicals, including vanillin, phenols, adhesives, and aromatic fuel components. Paracoumaryl (4-hydroxycinnamyl), coniferyl (4-hydroxy-3-methoxycinnamyl), and sinapyl (4-hydroxy-3,5-dimethoxycinnamyl) alcohol are the three most abundant monolignols (Figure 2-6). When incorporated into polymeric structures, they are referred to as *p*-hydroxyphenyl (H-lignin), guaiacyl (G-lignin) and syringyl (S-lignin) units, respectively, and are interlinked through different ether (C-O-C) and carbon (C-C) bonds (Wertz and Bédoué, 2013, Løhre et al., 2018).

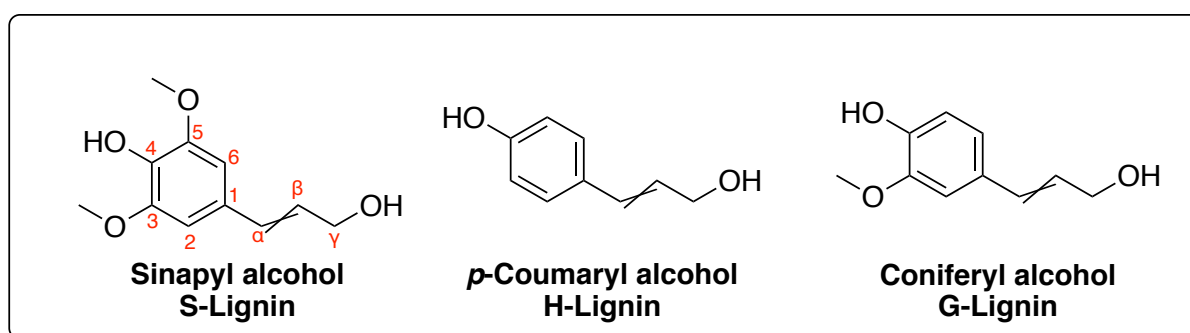


Figure 2-6: Structure of the most common monolignols.

The evolution of lignin played a crucial role in the terrestrial colonization by vascular plants, as it provided the necessary structural rigidity to grow large aerial structures. It is hydrophobic and highly resistant to both mechanical stress and enzymatic breakdown (Koupaie et al., 2019). In LCB, lignin forms covalent ether bridges to cellulose and covalent feruloyl ester-ether bridges to hemicellulose (Jin et al., 2006, Luo et al., 2019). In terrestrial plants, these cross-linking interactions contribute to the high structural rigidity of the three-dimensional structure of the secondary cell walls. Consequently, lignin is also the major obstacle impeding a rapid expansion of thermochemical conversion of LCB into fuels and value-added products, as it makes separation of the principal structural components complex and energy intensive (Zheng et al., 2014). Therefore, identification of potential solutions regarding the efficient utilization of lignin for higher-value applications has been a hot topic for several years.

For example, studies conducted by Barth and her research group deal with thermochemical conversion of different types of lignin extracted from LCB through different pretreatment methods, e.g., enzymatic hydrolysis, acid hydrolysis, organosolv, steam explosion, etc. The research group has achieved very promising results with respect to future implementation into full-scale biorefinery concepts. In their work, lignin-to-liquid solvolysis (LtL) and hydrothermal liquefaction (HTL) is being used to convert LCB and high purity lignin into bio-crudes (Kleinert and Barth, 2008, Løhre et al., 2018, Hita et al., 2021, Halleraker and Barth, 2020, Løhre et al., 2017)

2.3.3 THIRD AND FOURTH GENERATION FEEDSTOCKS

Third-generation biomass includes photosynthetic microbes like micro-and macroalgae. Algae are both morphologically and chemically distinct and offer many advantages when compared to first- and second-generation biomass. Consequently, algae serve as a promising feedstock for producing a wide variety of products, including secondary energy carriers and value-added products used in the pharmaceutical and cosmetic industries (Das, 2015, Anto et al., 2020). Fourth-generation feedstocks include genetically modified algal strains aiming to maximizing production by improving cellular composition and accelerating cellular growth rate (Arpia et al., 2021). Third- and fourth-generation feedstocks will not be discussed in any further detail in this thesis.

2.4 THE BIOREFINERY CONCEPT

Renewable energy sources like wind, hydropower, photovoltaics, geothermal etc. can, to a large extent, provide a substantial fraction of the primary energy required to accommodate anthropogenic activities in the ongoing sustainable transformation. However, considering the fact that the majority of chemicals produced today are derived from petrochemical industries means that a gradual suspension of fossil carbon and energy consumption will result in a global chemical deficiency in the long run. This is where the concept of biorefineries emerges as a promising solution as we move toward a global circular economy. The biorefinery concept has been developed by analogy to a conventional crude oil refinery (Figure 2-7), as it aims for complete utilization of various sources of biomass, including food crops, LCB, animal-, forestry-, and food-waste, sewage sludge, algae, as well as various sugar-containing industrial

waste streams. In the Task 42 report published by the IEA in 2012, the term “Biorefining” was defined as “the sustainable processing of biomass into a spectrum of bio-based products (food, feed, chemicals, materials) and bioenergy (biofuels, power and/or heat)” (de Jong et al., 2012). Borregaard AS, a Norwegian lignocellulosic biorefinery, is considered the oldest biorefinery in the world with a history dating back to the 1600s century. Today, Borregaard produces and sells biopolymers and biovanillin from lignin, specialty cellulose for the production of cellulose ethers, fine chemicals for the pharmaceutical industries and second-generation bioethanol (Borregaard, 2021).

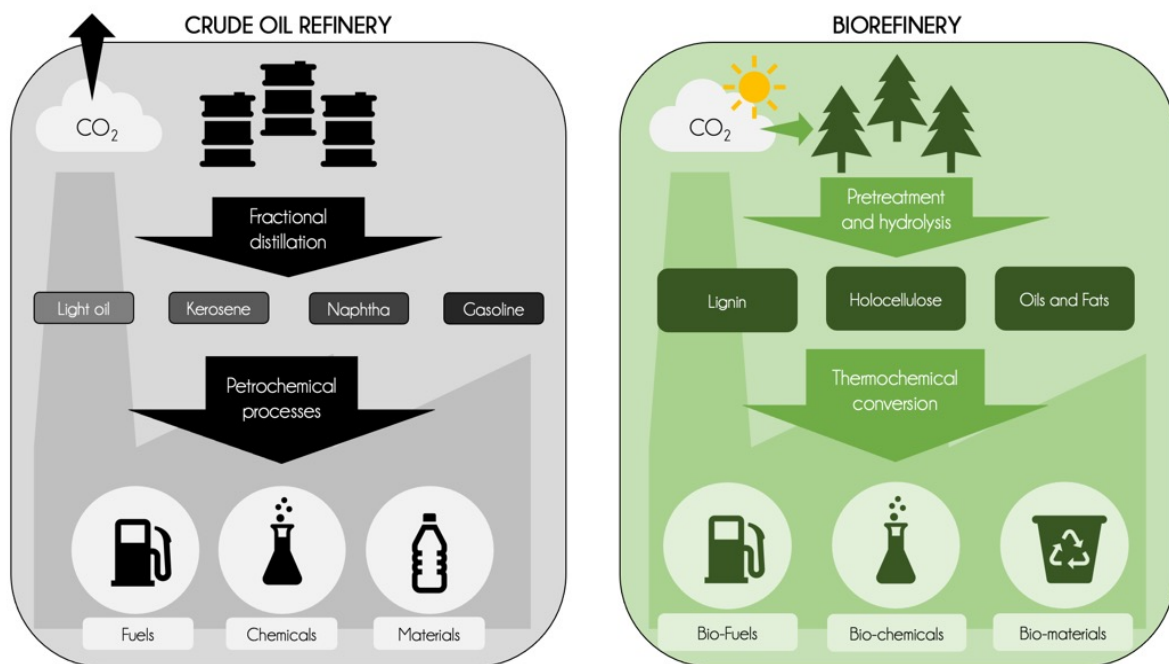


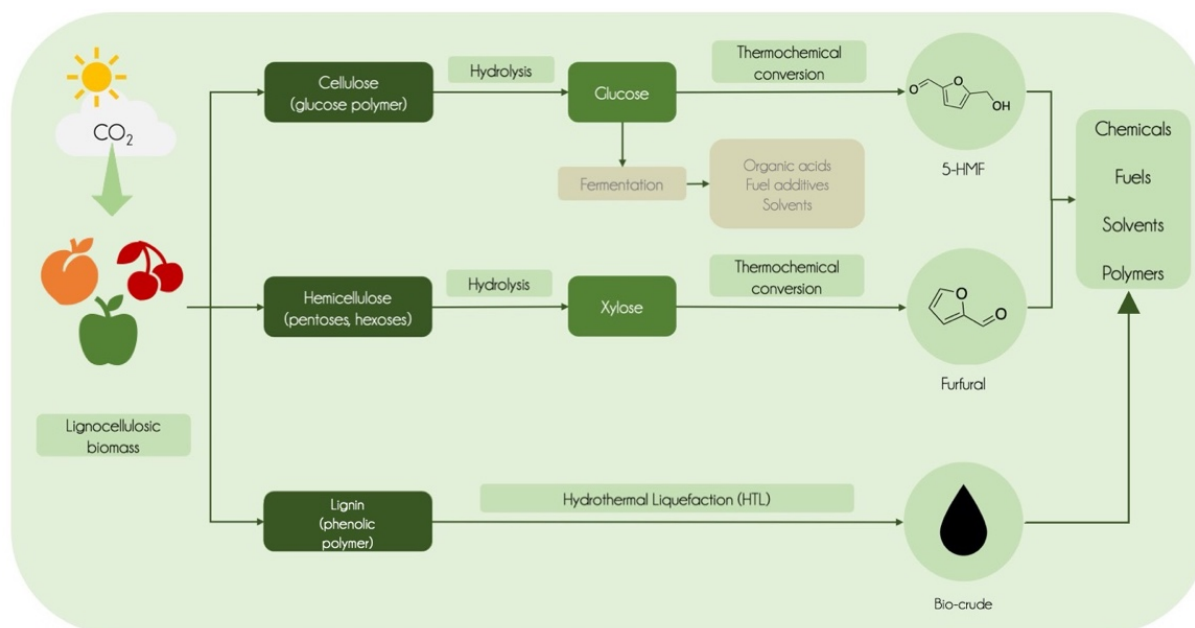
Figure 2-7: Conventional crude oil refinery vs biorefinery. Adapted from (Hülsey, 2018).

Utilizing biobased waste streams as raw materials in biorefineries has additional benefits apart from producing much-needed products and chemicals. It will for example help alleviate many of the negative environmental impacts that are associated with environmental waste deposition. In addition, valorization of locally produced biowastes will also contribute towards circular value creation, which is in line with the Norwegian Government's aspiration of becoming a world-leading bioeconomy (The Norwegian Government, 2016). Consequently, the identification of universal platform molecules capable of maximizing economic outputs while simultaneously minimizing environmental impacts is highly desirable (Cherubini, 2010, Kumar and Verma, 2021).

2.4.1 UTILIZATION OF FRUIT AND BERRY RESIDUES AS A BIOREFINERY FEEDSTOCK

Sugar-containing industrial waste streams generated by the agricultural sector are currently under-valorized resources. Industrial processing of fruit and berry (F&B) generates significant amounts of waste and by-products (20 – 60 wt%) that have traditionally been used as fertilizers, converted into low-value animal feed, or deposited in municipal landfills (Fava et al., 2015). In addition to the high volumes of residues generated from the processing of F&B, a substantial fraction of the annual F&B production never reaches the market due to minor visual imperfections that do not meet the demand of modern consumers. In Norway, most F&B residues originate from processing of drupe (stone fruits) for juice and cider production. In fact, many of the largest manufacturers and storage facilities in Norway, e.g., Lerum AS, Synnøve Finden AS, Hardanger Fjordfrukt BA, and Ullensvang Fruktlager SA, have expressed a desire for better utilization of F&B rejects and residuals (personal communication, Dr. Camilla Løhre, Postdoctoral Fellow at the University of Bergen) (Løhre, 2021).

The by-product remaining after processing of F&B is called pomace, which is primarily composed of dietary fibers, cellulose, hemicellulose, lignin, and free sugars (Szymanska-Chargot et al., 2017). The low digestibility (due to a high lignin/cellulose ratio) and high free sugar content makes pomace undesirable as ruminant feed, as the free sugars can undergo fermentation in the rumen, causing alcoholemia without the addition of silage additives (Villas-Boas et al., 2003). However, the high free sugar and carbohydrate content of pomace derived from F&B processing means that it could serve as a promising feedstock for biorefineries to produce furanic platform chemicals. The Norwegian Institute of Bioeconomy Research (NIBIO) estimated in a report from 2016 that bioeconomic outputs from industrial waste streams generated by the Norwegian agricultural- and food sectors could reach 5 – 6 billion NOK within 2050 if exploited to its full potential (Bardalen, 2016). Successful implementation of F&B residues for large-scale production of furanic derivatives could in other words be an important step towards the goal of Norway becoming a biobased circular economy, as it would drastically improve resource efficiency and reduce waste generation while simultaneously providing jobs to local communities (The Norwegian Government, 2016). Scheme 2-8 illustrates a hypothetical biorefinery concept utilizing F&B residues as feedstock.



Scheme 2-8: Biorefinery concept using F&B residues as feedstock.

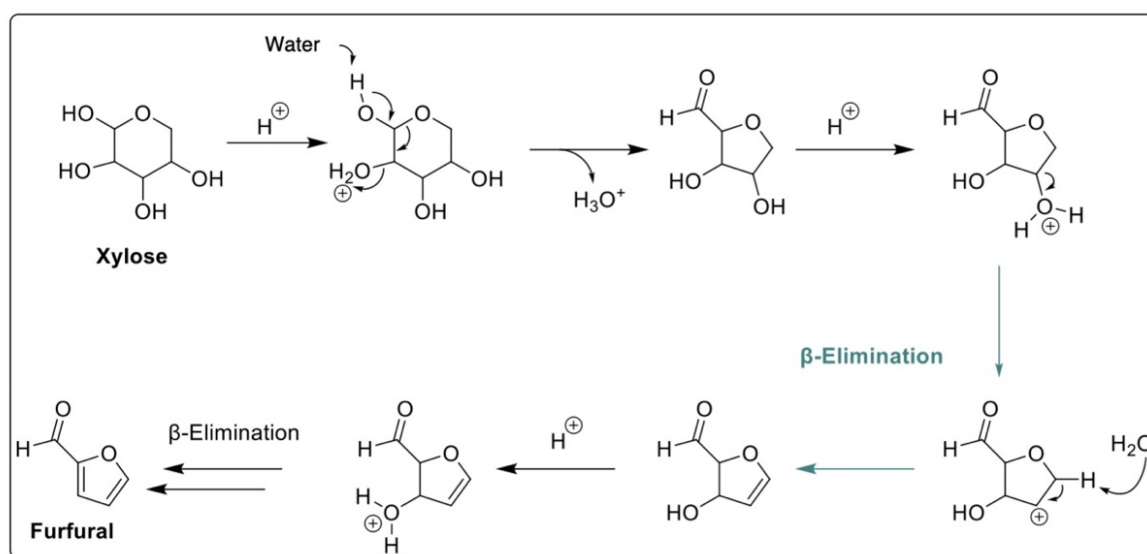
2.5 FURANS

In recent years, production of value-added, furan-based monomeric and polymeric compounds have received considerable attention for different industrial applications due to their potential for providing a wide range of biobased chemicals, fuels and materials. Structurally, furans are heterocyclic organic compounds. All furanic compounds contain a five-membered ring with a pronounced dienic character. The principal furanic ring contains one oxygen atom and four carbon atoms, to which a variety of functional groups may attach (Iroegbu et al., 2020). Furanic compounds derived from sustainable and renewable sources can play a key role as we move towards becoming a sustainable, biobased global economy (Danon et al., 2014, Liu et al., 2020) as they can potentially replace conventional, petroleum-derived platform molecules. Because of this, FUR and HMF are both included in Bozell's "Top 10 Chemicals from Biomass" list, which is an updated version of the original list released by the U. S. Department of Energy (DOE) in 2004 ("Top value-added chemicals from biomass") (Werpy et al., 2004). However, the main hurdle slowing the widespread use of FUR, HMF, and other furanic platform molecules is the lack of efficient and competitive synthetic routes from different bio-based feedstocks. The high oxygen content and various functional groups of these compounds also make transformational routes complex and nonselective (Huber et al., 2006). This thesis will

primarily focus on production of FUR, however, production of HMF from F&B will be discussed in chapter 5.5.

2.6 FURFURAL

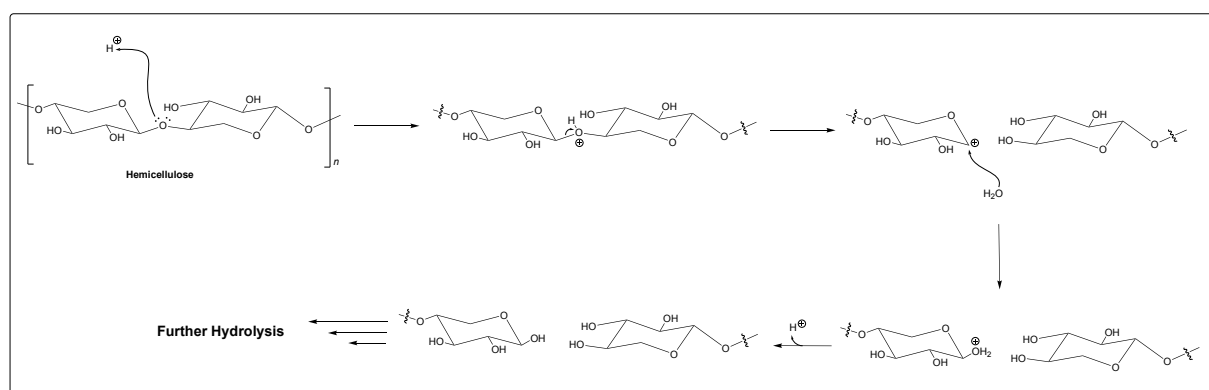
Furfural (FUR) or furan-2-carbaldehyde is a furanic aldehyde that can be derived from the dehydration of pentoses (primarily XYL), predominantly found in the hemicellulosic fraction of LCB, or in xylooligosaccharides (XOS) found in fruits, vegetables, bamboo shoots and honey (Mitmesser and Combs, 2017). At ambient conditions, FUR appears as a clear, viscous fluid, with a light brown tint. Table E-1 in Appendix E summarizes physical and chemical properties of FUR. The established production of FUR is achieved through acid-catalyzed depolymerization (hydrolysis) of pentosans to XYL followed by triple dehydration into FUR (Scheme 2-9). The triple dehydration reaction resulting in FUR formation from XYL includes a 1,4-elimination reaction followed by two consecutive 1,2-eliminations (β -eliminations). Initiation of the 1,4-elimination occurs when water abstracts a proton from a hydroxyl group. This results in an electron transfer chain that leads to ring reduction and elimination of a hydronium ion (H_3O^+). The second protonation produces a carbocation intermediate that is stabilized by a β -elimination, generating a C=C bond. A second β -elimination takes place during the third protonation step, which ultimately leads to the formation of FUR (Xu et al., 2020b).



Scheme 2-9: General reaction mechanism showing the triple dehydration of XYL to FUR. Mechanism by Beate Halsvik, PhD. candidate at UiB.

Hemicelluloses are, as previously described, primarily made up of pentoses linked by β -1,4-glycosidic bonds. The hydrolysis of these ether linkages connecting the monomeric units has traditionally been carried out using dilute acid pretreatments or by using steam in the presence of concentrated sulfuric acid (H_2SO_4), e.g., the QUAKER OATS process developed in 1921 (Liu et al., 2014a). The reaction mechanism involves four steps (Scheme 2-10) (Agirrezabal-Telleria et al., 2014, Xu et al., 2020a):

1. Protonation of the oxygen bridging the etheric bond leading to the formation of a trivalent bond.
2. Scission of the etheric bond results in the formation of a carbocation (carbonium ion) on one side and a hydroxyl group on the other side.
3. The carbocation will subsequently react with water.
4. Finally, a hydroxyl group will form as a result of deprotonation (liberation of H^+).

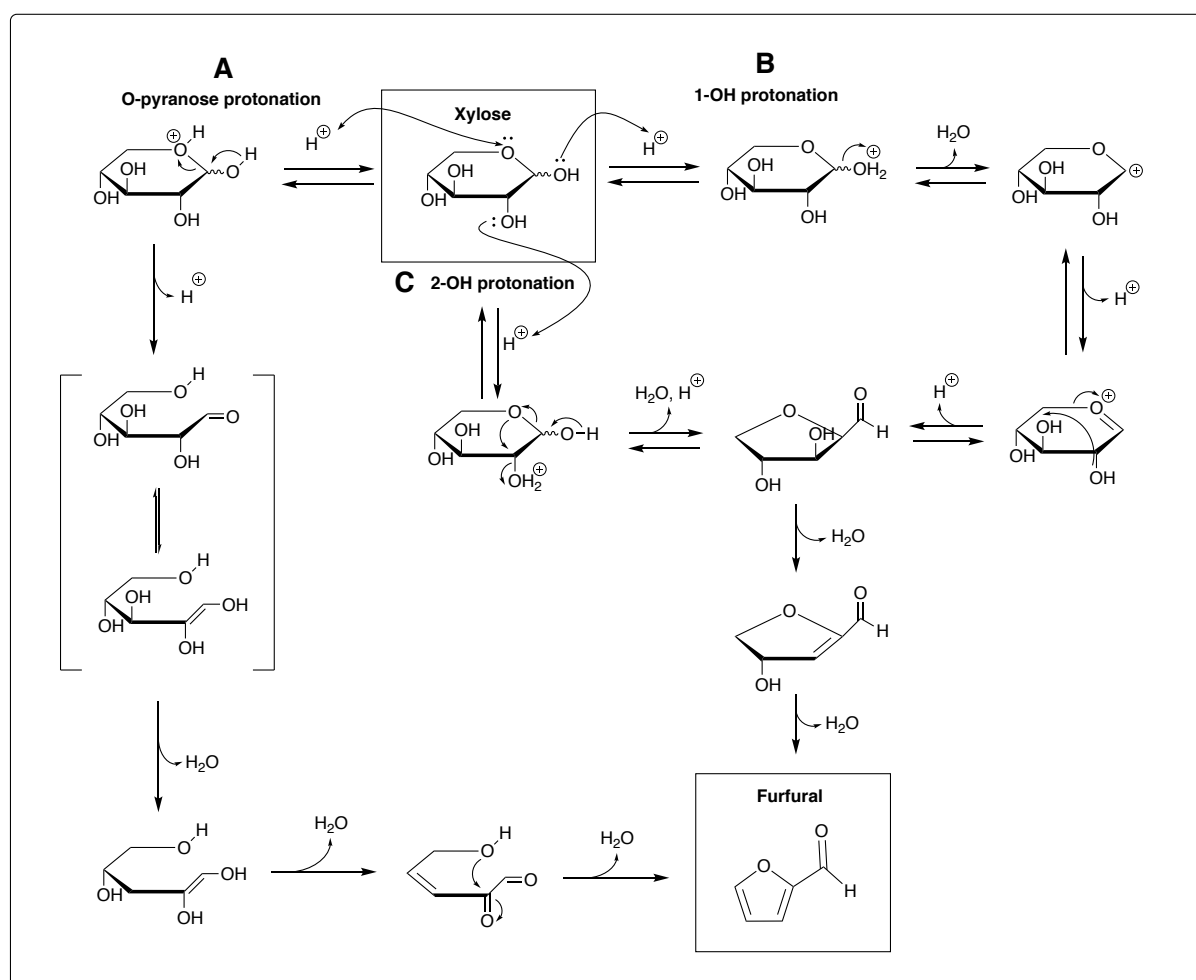


Scheme 2-10: Acid-catalyzed hydrolysis of glycosidic bonds in hemicellulose. Thanks to Beate Halsvik, PhD. candidate at the University of Bergen for the assistance with this reaction mechanism.

2.6.1 MECHANISTIC PATHWAYS TO FURFURAL

In 2014, Rasmussen et al. described that both acyclic and cyclic mechanisms resulting in the formation of FUR are supported by experimental findings, indicating that thermochemical degradation of XYL to FUR is a complex process (Rasmussen et al., 2014). Molecular simulations have suggested that the rate-limiting step during XYL dehydration is the initial protonation step, which also determines the subsequent transformational pathway. However, according to ab initio molecular dynamics simulations and quantum mechanics models used to predict the plausible degradation pathways for XYL, protonation of the pyranose oxygen (**A**,

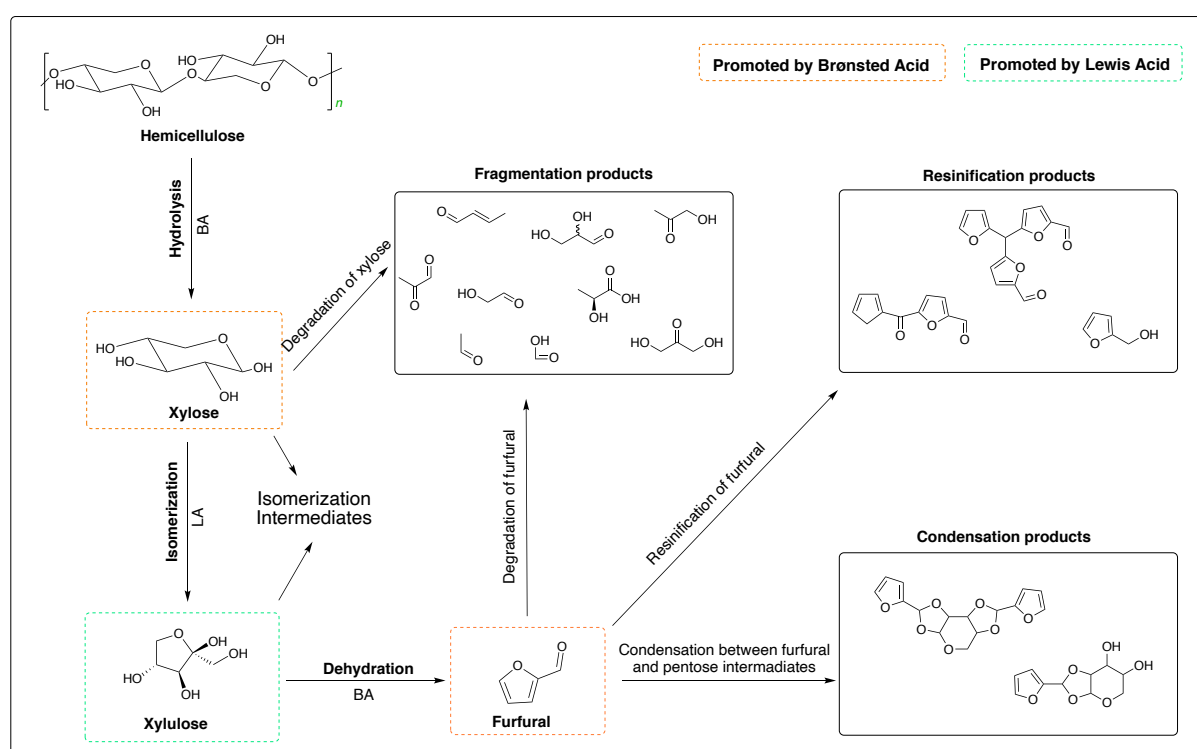
Scheme 2-11) does not generate FUR. The models predict that protonation of the pyranose oxygen (O5) inducing ring scission only produces an equilibrium between pyranose and aldose without further reaction to FUR. In addition, the cyclic degradation mechanism resulting from the protonation of 1-OH (**B**, Scheme 2-11) does not result in any observable reaction according to the models. In other words, simulations contradict experimental findings, as they predict that FUR is derived solely from the cyclic 2-OH protonation pathway (**C**, Scheme 2-11). Rasmussen further described that the intermolecular interactions formed between water and substrate are crucial for the initial protonation step as water molecules compete for protons and thus form hydrogen bonds to the hydroxyl groups. Additionally, reaction parameters like type of organic solvent, pH, temperature, the addition of modifiers like inorganic salts, etc. can also drastically alter the properties of the aqueous phase, affecting the initial site of protonation and thus the subsequent degradation pathway (Rasmussen et al., 2014).



Scheme 2-11: Suggested acyclic (**A**) and cyclic (**B** and **C**) synthetic routes for the synthesis of FUR from XYL. As shown, the XYL pyranose ring can either undergo protonation at the O-pyranose (**A**), 1-OH (**B**) or 2-OH (**C**). The reaction mechanism is redrawn from (Rasmussen et al., 2014).

2.6.2 DEGRADATION, SIDE-REACTIONS AND BY-PRODUCT FORMATION

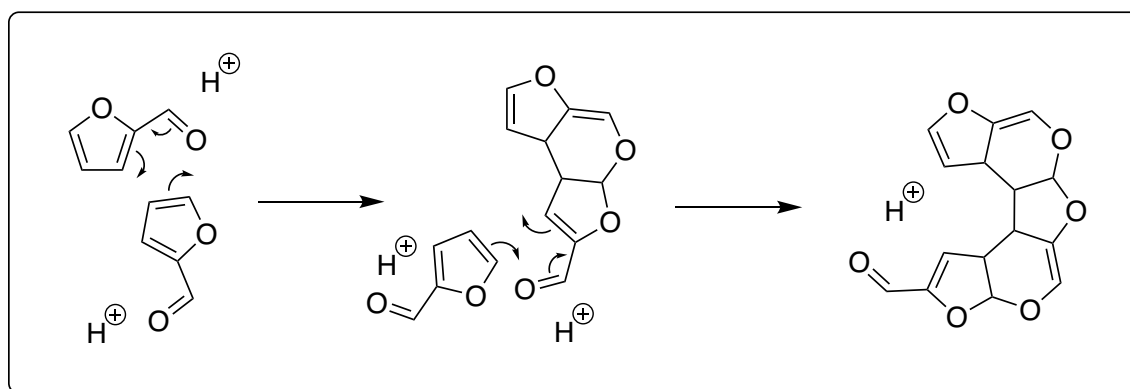
Thermochemical conversion of carbohydrates is often accompanied by co-generation of undesired by-products, resulting in yield loss. Side-reactions that can take place can be divided into two main categories, namely FUR degradation and FUR condensation. FUR degradation includes self-polymerization (resinification), ring opening, and decomposition reactions, while FUR condensation includes polymerization reactions between FUR and intermediates (Lamminpaa et al., 2014). Scheme 2-12 contains potential degradation pathways of both XYL and FUR.



Scheme 2-12: Degradation pathways of FUR and XYL. Redrawn and adapted from (Vilonen et al., 2011).

During resinification, FUR will undergo self-polymerization generating various oligomeric by-products. Studies indicate that resinification is more likely to occur at moderate to severe reaction conditions when solid particles are present in the aqueous reaction medium. However, Zeitsch found that resinification most likely plays a lesser role when reaction temperatures exceed 200°C. At temperatures above 200°C, ring-opening and fragmentation reactions are thought to be the predominant degradation mechanisms. This claim was attributed to the “entropy effect”, which promotes molecular fragmentation instead of polymerization (Zeitsch,

2001). Fragmentation reactions, where sugars, intermediates, and FUR are cleaved to form compounds with molecular masses lower than FUR, e.g., carboxylic acids like formic (FA) and levulinic acid (LA), are also thought to occur in highly acidic environments ($\text{pH} < 0.9$). In fact, studies indicate that hydrolytic ring opening primarily occurs if the acid concentration in the aqueous phase is too high, resulting in the formation of an aliphatic, open-chain by-product that can undergo subsequent polymerization by reacting with other FUR molecules. The Diels-Alder reaction in Scheme 2-13 has been proposed to be a plausible mechanism explaining the formation of oligomeric by-products (Lamminpaa et al., 2014).



Scheme 2-13: Diels-Alder reaction mechanism resulting in formation of oligomeric by-products. Scheme proposed by Lamminpää et al. 2014 (Lamminpaa et al., 2014).

When considering FUR condensation, Luo et al. described that high lignin concentrations in the hydrolysates derived from LCB are reported to cause condensation reactions between lignin, unreacted sugars, intermediates, and FUR, drastically decreasing the product yield (Liu et al., 2014b, Luo et al., 2019). They also reported that prolonged reaction times associated with traditional heating methods tend to increase unwanted side reactions, thereby decreasing FUR selectivity. Microwave-assisted hydrothermal selective dissolution has been proposed as a potential solution to overcome the lignin-associated condensation problem as reaction times can be drastically reduced. Microwave-assisted heating (MWAH) has also proven to facilitate efficient dissolution of hemicellulose (>95%) while obtaining a residue consisting of mostly intact cellulose and lignin that can undergo further valorization to various products (Luo et al., 2019). Alternatively, Mazar et al. found that sulfonation of lignin prior to hydrolysis of LCB could render lignin less reactive, resulting in fewer condensation reactions and increased yields (Mazar et al., 2018).

The formation of solid polymeric by-products caused by resinification, fragmentation, and condensation reactions are collectively referred to as humins. Humins are dark, solid, amorphous resins generated under acidic conditions. Studies have shown that humins grow as spherical particles solely derived from furanic compounds and not from by-products like short-chain fatty acids, e.g., levulinic acid (LA) and formic acid (FA). The morphology and chemical composition of the precipitated particles will also change due to thermal decomposition, as they can go from amorphous furanic polymers to benzene-based frameworks under certain conditions. The elemental composition of humins have been reported to be 55 – 65% carbon, 4 – 5% hydrogen and 30 – 40% oxygen (Patil and Lund, 2011). Studies also indicate that particle diameter of humins will increase as a function of time due to particle agglomeration.

The formation of humins can have adverse implications on the overall reaction efficiency, conversion yield, and selectivity. The reactive nature of humins means that their formation can have adverse implications on the overall reaction efficiency if not controlled, as they can induce unwanted polymerization reactions between humins, FUR, and other reactive intermediates. Humins may also cause significant catalyst deactivation. IR-spectra of humins generated under various acidic and thermal conditions indicate that aldol condensation is a central mechanism involved in their formation. This claim is supported by the absence of aldehyde groups in recorded IR-spectra (Al Ghatta et al., 2021).

2.6.3 FURFURAL DERIVATIVES AND ENERGY APPLICATIONS

As stated earlier, FUR could become a key chemical platform in the continuously developing biorefinery industry due to its profitable physical and chemical properties. The highly reactive nature of the aromatic ring and the aldehydic function makes FUR an excellent platform for synthesizing various fuels, plastics, pharmaceuticals, cosmetics, flavors, fragrances, and agrochemicals (Mariscal et al., 2016). On a global scale, approximately 400 kilotons of FUR is produced annually, and according to MarketsandMarkets, the global annual production of FUR is projected to increase from 551 million USD in 2019 to over 700 million USD by 2024 (MarketsandMarkets, 2019). The number of potential pathways for converting FUR or chemicals obtained from FUR into fuels and secondary energy carriers is enormous. In fact, more than 80 chemicals have been produced either directly or indirectly from FUR. Figure 2-14 depicts some of the most important compounds that have been derived directly or indirectly from FUR (Mariscal et al., 2016).

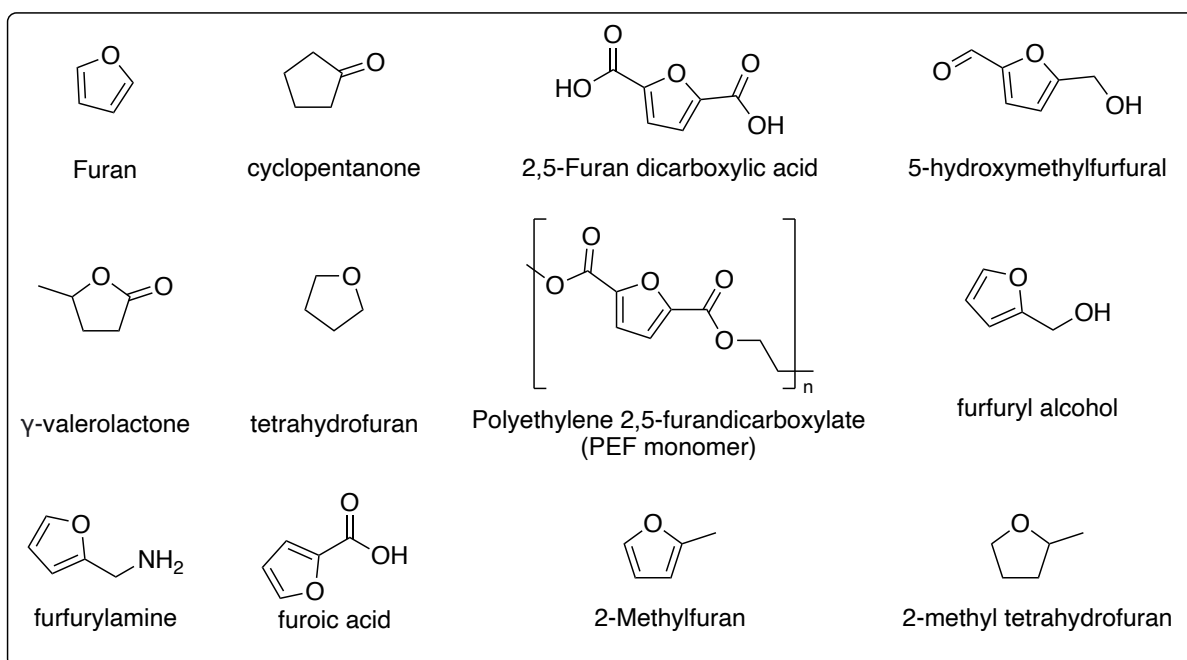


Figure 2-14: Furanic compounds derived from FUR.

Today, furfuryl alcohol (FOL) constitutes around 60% of the total FUR market and is currently the most important chemical derived from FUR. FOL can be used as a thermoset polymer matrix for various adhesives, coatings, composites, cements, and foundry resins. FOL can also be used as a fuel additive, or it can undergo further upgrading to produce fuel-range alkanes. In fact, recent scientific advances have resulted in a sparked interest in utilizing FUR and its derivatives as precursors to produce fuel-range alkanes and fuel additives (Xing et al., 2011, Xing et al., 2010, Climent et al., 2014). However, FUR and other short-chained oxygenates like HMF are not suitable for direct incorporation into conventional transportation fuels due to their high oxygen content, high reactivity, water-solubility, boiling point, and low energy densities. One of the key challenges associated with the conversion of furanic derivatives to fuel-range hydrocarbons is sufficient deoxygenation combined with adequate chain propagation. In a study from 2020, Pino and colleagues successfully synthesized fuel-range hydrocarbons that could be incorporated into naphtha ($C_5 - C_9$), gasoline ($C_5 - C_{10}$), and kerosene ($C_{10} - C_{15}$) fractions from FUR by utilizing a base-catalyzed aldol-condensation reaction between FUR and cyclopentanone (CPON) followed by hydrodeoxygenation. The aldol-condensation reaction generated $C_{10} - C_{14}$ oxygenates, which were further upgraded to linear alkanes and saturated cyclic hydrocarbons ($C_7 - C_{15}$) via hydrodeoxygenation using carbon-supported Ruthenium (Ru) and Palladium (Pd) nanoparticles (Pino et al., 2020). Production of a mixture of C-C

coupled oligomers derived from FOL followed by subsequent hydrogenation to produce a mixture of hydrocarbons in the C₉ – C₂₀ range have also been reported and patented. After separation by fractional distillation, the higher fractions can undergo catalytic cracking or hydrocracking to produce gasoline-range hydrocarbons (Climent et al., 2014).

Production of fuel additives either directly or indirectly from FUR has also received much attention. For example, FUR can be converted into γ -valerolactone (GVL) via hydrolysis of FOL (Timokhin et al., 1999). GVL exhibits attractive physicochemical properties (table E-4, Appendix E) as it can be used both as a green solvent and as a fuel additive to improve combustion characteristics (Paniagua et al., 2020, Xu et al., 2020a). Scheme K-4 in appendix K summarizes noteworthy synthetic transformational pathways of FUR and HMF into various fuel additives and liquid alkanes.

2.6.4 ESTABLISHED INDUSTRIAL PROCESSES

Most of the established processes producing FUR on an industrial scale have traditionally used mineral acids like hydrochloric acid (HCl) and sulfuric acid (H₂SO₄) as catalysts for the hydrolysis and subsequent dehydration into FUR. However, mineral acids suffer from several drawbacks, including problems with product separation, corrosion of equipment, poor recyclability, and the need for downstream treatment of effluents (Huang and Fu, 2013). According to Mittal *et al.*, the highest FUR yield obtained on an industrial scale is currently 55% (Mittal et al., 2017).

2.6.5 STATE-OF-THE-ART PRODUCTION OF FURFURAL

Numerous studies have over the past decade sought to identify efficient and economically viable reaction systems that adhere to the principles of green chemistry for producing furanic derivatives like FUR and HMF from biobased feedstocks (Xing et al., 2011, Yang et al., 2012b, Mariscal et al., 2012, Wang et al., 2019, Hua et al., 2016, Liu et al., 2014a, Pholjaroen et al., 2014, Zhang et al., 2019, Zhang et al., 2013, Abou-Yousef and Hassan, 2014, Danon et al., 2014, Marcotullio and De Jong, 2010, Mazar et al., 2017, Mittal et al., 2017, Mittal et al., 2020, Morais et al., 2016, Romo et al., 2018, Vilonen et al., 2011, Xing et al., 2010, Zang et al., 2020, García-Sancho et al., 2013, Pawar, 2020, Sener et al., 2014, Weingarten et al., 2010a). Even

though several reported reaction systems have shown outstanding performance in terms of conversion rate and selectivity towards FUR, few fulfill the required specifications for converting lab-scale experiments to full-scale biorefinery concepts. Recurring problems that usually inhibit viable industrialization include the use of solvents, catalysts, and modifiers with significant EHS- and/or price-related concerns. In addition, the lack of adequate, industrial-scale equipment necessary to reproduce the high yields obtained in the laboratory has also impeded potential scale-up. The following section covers scientific developments related to the production of FUR over the past decade, some of which could potentially become industrialized in the future with the deployment of adequate biotechnological equipment.

2.6.5.1 MONOPHASIC VS BIPHASIC REACTION SYSTEMS

Both monophasic (Gürbüz et al., 2013, Motagamwala et al., 2018) and biphasic reaction systems (Weingarten et al., 2010b, Gómez Millán et al., 2020, Le Guenic et al., 2015, Mittal et al., 2017, Wang et al., 2019, Yang et al., 2017) employing either homogenous acid catalysts (Xing et al., 2010, Yang et al., 2012a, Delbecq et al., 2016) or heterogeneous solid acid catalysts (García-Sancho et al., 2013, Agirrezabal-Telleria et al., 2014, Arias et al., 2020, Gómez Millán et al., 2019, Gürbüz et al., 2013, Li et al., 2017) have been rigorously tested in the production of FUR. The main challenge concerning monophasic reaction systems employing water as the sole reaction medium is that FUR will undergo several unwanted side-reactions in the prolonged presence of water. To solve this problem, biphasic systems have been proposed as a potential solution (Figure 2-15).

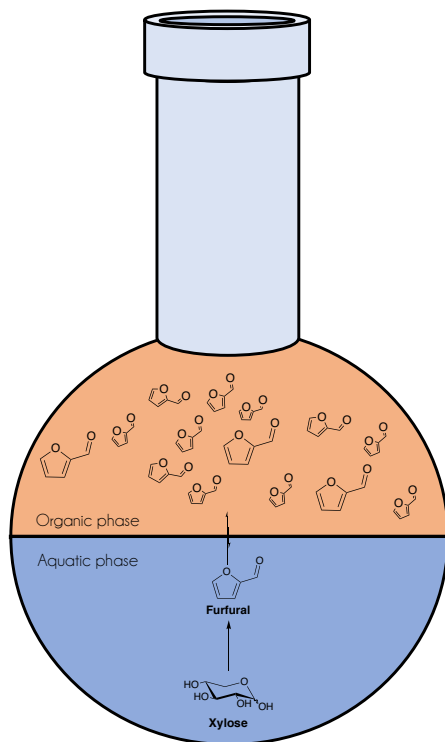


Figure 2-15: General concept of a biphasic reaction system.

Research has shown that biphasic reaction systems exhibit far better dehydration performance in terms of yield when compared to monophasic reaction systems. A kinetic study conducted by Weingarten et al. (Weingarten et al., 2010a) demonstrated the superior performance of a biphasic reaction system compared to a monophasic reaction system. Using MIBK/H₂O as a biphasic solvent system, the authors achieved a FUR yield of 85% from pure XYL. An identical monophasic system operating at the same reaction conditions without the addition of MIBK achieved a maximum yield of 30%. The fundamental reaction kinetics of the biphasic system remains unaltered compared to the analogous monophasic system. The primary role of the organic phase is the *in-situ* extraction of FUR to prevent degradation and formation of undesired by-products (Wang et al., 2019, Weingarten et al., 2010a). Not only does the extraction of FUR into the organic phase suppress the formation of undesirable side-products, but it also helps shift the equilibrium of the reaction towards FUR formation (Le Chatelier's principle), thereby improving the overall yield of formation (Luo et al., 2019, Weingarten et al., 2010a). However, it is important to note that the type of solvent used for the *in-situ* extraction of FUR can drastically complicate the downstream processing of FUR, mainly due to the carry-over of water into the organic phase. In addition, the azeotrope formed between FUR and water

drastically increases the energy and equipment requirements associated with downstream purification steps.

Currently, MIBK (Table E-3, Appendix E) is one of the most researched solvents used for the *in-situ* extraction of FUR and HMF as it has several advantages compared to other frequently used solvents. For example, MIBK is considered a green solvent as it can be generated from LCB. It is almost completely immiscible in water (0.28wt% at 25°C) and is more efficient in extracting both FUR and HMF from the aqueous reaction phase than other frequently used solvents like 2-methylfuran, 2-butanone, ethyl acetate (EtOAc), tetrahydrofuran (THF) and toluene (TOL) (Matsagar et al., 2015, Romo et al., 2018). GVL has also received much attention in the literature. GVL can as previously discussed, be produced from both FUR and HMF, making it very appealing in terms of biomass conversion economics. In addition, GVL is biodegradable, has low toxicity, and does not form an azeotrope with water. It also has a low vapor pressure (boiling point of 207 – 208°C) and does not form harmful peroxides in the air (Bollar et al., 2018, Paniagua et al., 2020, Qi et al., 2014). Work conducted by Mellmer et al. found that using GVL as an organic phase leads to a significant increase in both reaction rate and product selectivity compared to conversion in aqueous media only. They also found that GVL lowers the activation energy for the dehydration of XYL into FUR from 145KJ/mol to 114KJ/mol, while simultaneously increasing the activation energy for FUR degradation from 85KJ/mol to 105KJ/mol, compared to aqueous-only reaction media, thereby stabilizing the desired product (Mellmer et al., 2014). Table 2-1 and Table 2-2 contains a selection of reported biphasic reaction systems that have attained promising results with regards to FUR and HMF production over the past two decades.

Table 2-1: Reported biphasic reaction systems for FUR production over the past decade ordered in chronological order.

Feedstock	Catalyst	Solvent System(s)	Org:Aq (v/v)	Modifier	T [°C]	t [min]	FUR Yield [%]	Reference
D-Xylose	HCl (0,1M)	MIBK//H ₂ O	1:1	-	170	70	85.0	(Weingarten et al., 2010a) ^c
Pentose hydrolysate	HCl (0,44M)	THF/H ₂ O	2:1	NaCl	110-200	1.12/h ^b	90.0	(Xing et al., 2011) ^a
Maple wood chips (5 wt%)	H ₂ SO ₄ (0,1M)	MIBK//H ₂ O	1:1	-	170	50	85.0	(Zhang et al., 2013)
D-xylose (0.001M)	Formic acid	CPME//H ₂ O	3:1	NaCl/KC 1	170	60	80.0	(Delbecq et al., 2016)
Glucose (0.15 g)	Amberlyst-38 (0,21mg) + CrCl ₃ (10 mol%)	GVL/H ₂ O	2:1	KBr	160	3	74.0	(Wrigstedt et al., 2016) ^c
D-Xylose (0.75 g)	SO ₃ H-SBA-15	Ethyl butyrate/H ₂ O	2.33:1.00	-	200	180	75.0	(Hua et al., 2016).
Corn stover hydrolysate (8 wt%)	H ₂ SO ₄ (0,05M)	MIBK//H ₂ O TOL/H ₂ O	2:1	-	170	20	80.0 77.0	(Mittal et al., 2017)
Raw corn stover (150 mg)	SC-CaC-700 (45 mg)	GVL	nr ^e	-	200	100	93.0	(Li et al., 2017)
Xylan (2mmol)	(Al ₂ (SO ₄) ₃) (20 mol%)	GVL/H ₂ O MIBK//H ₂ O THF/H ₂ O 2-MTHF/H ₂ O	4:1	-	130	30	87.8 68.5 51.2 32.5	(Yang et al., 2017) ^c
Corncoobs	HCl	MIBK//H ₂ O	10:1	-	170	20	72.5	(Peleteiro et al., 2018) ^c
Bagasse	H-USY	MIBK//H ₂ O	1:1	-	170	6 h	55.0	(Romo et al., 2018)
D-Xylose (2 wt%)	NH ₂ SO ₃ H (10 mol%)	GVL//H ₂ O	9:1	-	190	15	70.2	(Zhang et al., 2019) ^c
D-Xylose (1,0 mmol)	MMCSA (0,1 g)	MIBK//H ₂ O GVL//H ₂ O	4:1	-	190	10	79.0 80.5	(Qi et al., 2020) ^c
Corn stalk	(Al(NO ₃) ₃) (0,1M)	MIBK//H ₂ O	ns ^d	-	160	60	52.0	(Li et al., 2020)

^aEmployed continuous two-zone biphasic reactor, ^boptimal liquid hourly space velocity (LHSV), ^cmicrowave-assisted heating, ^dnot specified, ^enot relevant

Table 2-2: Reported biphasic reaction systems for the simultaneous production of FUR/HMF ordered in chronological order.

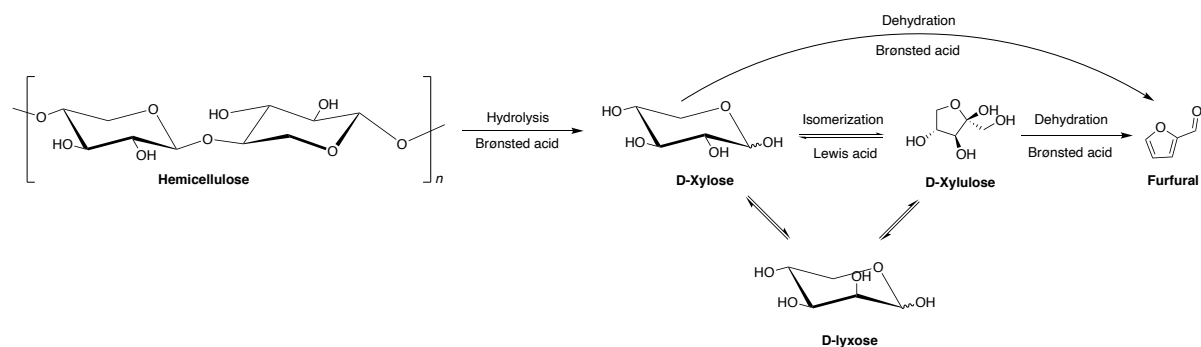
Feedstock	Catalyst	Solvent System	Org/Aq (v/v)	Modifier	Temp [°C]	time [min]	Yield FUR/HMF [%]	Reference
D-Xylose Glucose Fructose (10-30 wt%)	HCl H ₂ SO ₄	MIBK:2-butanol/ Water:DMSO	1:1	-	170	-	ns ^a	(Chheda et al., 2007)
Aqueous phase bio-oil sugars	Formic acid (0,5M) Formic acid (1,5M)	MIBK/H ₂ O MIBK/H ₂ O:DMSO	3:1	-	190 170	60 45	13.5/39.2 22.6/29.6	(Abou-Yousef and Hassan, 2014)
LCB (11.1 wt%) Eucalyptus Pinewood Sawdust (0.4 g) Straw	NaHSO ₄ (3.3 wt%) Levulinic acid (0.1 g) Sulfanilic acid	THF/Water MTHF Toluene/Water MIBK/Water	10:1 1:1 2:1	-	190 180 150	90 15 60	50.0-60.0 ns ^a 41.0/50.0	(Shi et al., 2015) (Seemala et al., 2016) (Mirzaei and Karimi, 2016)
Wheat straw (1g) Corn stover Switchgrass Loblolly pine Pure Cellulose Bamboo leaf (0.05g)	CrPO ₄ (0.15 g) HCl (33 mM) + AlCl ₃ (8mM) HCl (0.13M)	THF//H ₂ O Dioxane/H ₂ O MIBK/Water	3:1 4:1 19:1	NaCl - -	180 200 177	90 5 60	67.0/32.0 88.0-91.0/ 60.0-69.0 34.0/37.0	(Xu et al., 2018) (Mittal et al., 2020) (Sweygers et al., 2020) ^b

^aNot specified, ^bMicrowave assisted heating.

2.6.5.2 UNIFUNCTIONAL VS BIFUNCTIONAL CATALYSIS

Delbecq et al. (Delbecq et al., 2018) identified in a recent review different catalytic processes applicable for the conversion of bio-based feedstocks into furanic platforms. They found that when utilizing conventional homogeneous Brønsted acids as catalysts, several challenges exist. A major challenge is getting over the high activation barrier associated with dehydration of XYL into FUR. A promising solution to this problem is to combine a Brønsted acid (BA) catalysts with a Lewis acid (LeA) salt or use bifunctional acid catalysts. The introduction of a LeA catalyst will promote isomerization of aldoses like XYL and glucose into their highly reactive keto intermediates, i.e., xylulose and fructose, respectively. In fact, thermodynamic and kinetic studies have proposed that formation of xylulose and fructose can drastically improve FUR and HMF yields as the process requires less energy input as well as being more

selective towards FUR and HMF formation compared to the conventional stepwise dehydration obtained when only using a BA (Delbecq et al., 2018). However, it is important to note that the epimerization products mannose and lyxose, both of which are aldoses, also are plausible isomerization products, which are far less reactive than their ketose counterparts.



Scheme 2-16: Stepwise dehydration vs. isomerization dehydration for the conversion of hemicellulose into FUR.

To exemplify, Yang and co-workers used aluminum sulfate ($\text{Al}_2(\text{SO}_4)_3$), a highly efficient, low-cost, low-toxicity, bifunctional catalyst in a GVL/ H_2O biphasic solvent system for the production of FUR. The study utilized microwave-assisted heating at 130°C , attaining a FUR yield of 87.8%. By combining LeA and BA species, the reaction pathway is shifted from a stepwise dehydration to isomerization-dehydration, increasing both yield and selectivity of FUR (Scheme 2-16). The bifunctional catalyst was thought to be a major factor for the high degree of conversion (Yang et al., 2017). In a similar study, Zhang et al. attained FUR yields over 70% from six different types of biomass using sulfamic acid ($\text{NH}_2\text{SO}_3\text{H}$) as a bifunctional catalyst in a GVL/ H_2O solvent system (Zhang et al., 2019). Sulfamic acid is a readily available, inexpensive, non-hygroscopic, non-volatile, non-corrosive, crystalline organic acid with highly desirable physical and chemical properties. It is moderately soluble in water and insoluble in most organic solvents, enabling easy recycling. When dissolved in water, sulfamic acid is ionized, forming strongly acidic solutions. Sulfamic acid is a promising, bifunctional organic acid catalyst for many synthetic reactions as it acts as both a proton donor and an electron acceptor (Veera Swamy Konkala Pramod Kumar, 2017). Studies also indicate that sulfamic acid forms zwitterionic species ($\text{H}_3\text{N}^+\text{SO}_3^-$) when dissolved in water, which is thought to promote isomerization and dehydration reactions due to its electron-rich sulfonate group and high acidity (Zhang et al., 2019). Kinetic measurements have suggested that the catalytic efficiency of sulfamic acid increases up to $\sim 0.2\text{ M}$. For concentrations exceeding 0.2 M , the rate constant remains independent of acidity (Williams, 2004).

In 2020, Mittal and colleagues obtained simultaneous FUR and HMF yields of 88 – 91% and 60 – 69%, respectively, from four different types of untreated biomass. In previous work, they had found that a single LeA catalyst like AlCl_3 was sufficient for achieving efficient dehydration of monomeric sugars to FUR/HMF. However, when dealing with untreated biomass, using AlCl_3 as a sole LeA catalyst resulted in poor FUR and HMF yields. The authors theorized that insufficient carbohydrate hydrolysis was the main factor contributing to the low yields and found that the addition of a BA catalyst like HCl or H_2SO_4 drastically increased the yield due to increased hydrolysis of the glycosidic bonds (Mittal et al., 2020). However, Guo et al. also found that chloride concentrations exceeding 1 M may cause a substitution reaction in which the hydroxyl group attached to HMF is replaced by chloride, thus forming 5-chloromethylfurfural (CMF) (Guo et al., 2020).

Heterogeneous catalysis has also received considerable attention over the past decade due to its massive potential of advancement beyond the current “state-of-the-art” catalytic conversion. Solid catalysts can be synthesized with a high degree of tunability regarding chemical and physical properties, including broad surface acidity and high product selectivity, by adjusting the porosity and hydrothermal stability. Additionally, their ease of separation and recovery by simple filtration also eliminates many EHS-related concerns associated with conventional homogeneous catalysis (Agirrezabal-Telleria et al., 2014). Hence, heterogeneous catalysis is an essential concept in green chemistry as it can reduce the environmental footprint of reaction systems used for the conversion of LCB to furanic derivatives. Although heterogeneous catalysis has several advantages compared to homogeneous catalysis, two main limitations have limited their broad industrial utilization. These drawbacks include their associated cost of preparation and deactivation tendency due to catalytic poisoning and sintering. (Lancaster and Chemistry, 2016). Heterogeneous catalysts will not be discussed in further detail in this thesis.

3. OBJECTIVES

The primary objective of this thesis is to find a biphasic reaction system that can be used for the efficient conversion of simple sugars and F&B rejects to furanic derivatives like FUR and HMF. In order to achieve this, the thesis has been divided into four main tasks:

1. In the first task, identification of reliable quantification procedures of both organic and aqueous reaction phases will be done by comparing the accuracy and precision of GC-MS, HPLC, and qNMR as analytical tools. This will be done by preparing a procedural blank containing a known amount of FUR. For GC-MS and HPLC, calibration curves will be used for the quantification. For qNMR, comprehensive structural elucidations of both substrate (XYL) and the desired products from F&B rejects (FUR and HMF) using $^1\text{H-NMR}$, $^{13}\text{C-NMR}$, COSY, HSQC, HMBC, H2BC will be performed to enable accurate identification and quantification of all compounds in both reaction phases.
2. In the second task, a selection of different solvents and catalysts will be evaluated in order to find a biphasic reaction system that coincide with the specifications of this thesis, that is, efficient production of FUR and/or HMF using environmentally benign solvents and catalysts that follow the concepts of green chemistry. To achieve this, the physical and chemical properties of each compound, the principles of green chemistry, and previously reported literature findings will be used as guidelines during the selection process.
3. The third task involves performing an experimental fractional factorial design (FFD) using the selected biphasic reaction system with XYL as a substrate. The FFD will be used to evaluate the effect of five main factors, namely substrate loading, catalyst loading, reaction temperature, residence time, and organic-to-aqueous ratio. Multivariate analysis (PCA and PLS) will be used to uncover how the chosen factors can be adjusted to approach optimal reaction conditions for the selected reaction system in terms of FUR yield, XYL conversion, and reaction selectivity.
4. In the final task, F&B residues, more specifically, plum- and cherry rejects, will replace XYL as a feedstock to produce FUR and HMF. This will be done to evaluate whether

F&B can be used as a potential biorefinery feedstock for the large-scale production of FUR and HMF. The experiments will be conducted by applying the best reaction conditions identified from the experimental screening process using FFD and multivariate analysis.

4. MATERIALS, METHODS AND EXPERIMENTAL

4.1 ANALYTICAL METHODS

4.1.1 CHROMATOGRAPHY

Chromatography is an analytical method used for separating chemical components in a sample matrix. The technique is based on two fundamental physical and chemical principles, namely diffusion and phase distribution. A chromatographic system is composed of a moving fluid (gas or liquid), known as the mobile phase (MP) which is passed over a fixed stationary phase (SP). When the MP containing the sample is passed over and through the SP, the structural components will continuously move between the MP and the SP, driven by diffusion, which causes separation of the sample components. The higher the affinity for the SP, the higher the retention factor, k , for a particular compound. The time it takes for a compound to elute from the column is referred to as the retention time (t_R). In other words, $k \propto t_R$. Although many different types of chromatographic techniques exist, gas-chromatography (GC) and liquid chromatography (LC) have become the leading methods in organic chemistry for separation and identification of compounds in a sample matrix. In general, a chromatographic system consists of four main parts: a module (pump) that is responsible for delivering the MP, an injector used for sample injection, a column used for separation of the sample matrix, and a detector that detects the different solutes (Figure 4-1). The information collected by the detector is processed by a computer and the concentration profiles of the different solutes are displayed as peaks in a chromatogram, where time and concentration are plotted on the x- and y-axis, respectively (Miller, 2005).

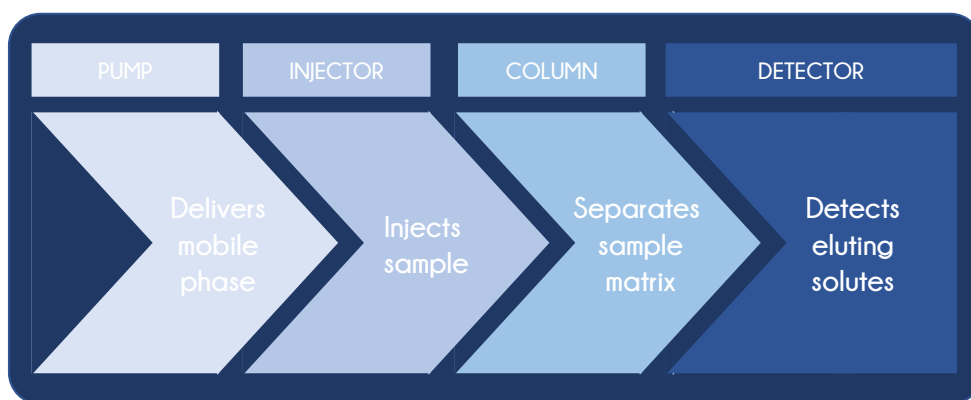


Figure 4-1: Four main parts of a chromatographic system.

4.1.1.1 GAS CHROMATOGRAPHY-MASS SPECTROMETRY (GC-MS)

Gas Chromatography-Mass Spectrometry (GC-MS) is a type of chromatography that is used for the separation and analysis of volatile compounds. It has become the “benchmark” for molecular identification as it compares the fragmentation pattern of sample compounds to an extensive library containing molecular fragmentation patterns for a huge number of chemical compounds (NIST database). Following injection and elution from the GC-column, the compounds are injected into an ionization chamber in the MS unit, where the molecules are ionized and fragmented. The molecular fragments are then separated based on a mass to charge ratio (m/z). The incident charges are then amplified by an electron multiplier that transforms the ionized fragments into electrical signals that can be detected in a mass spectrum. GC enables analysis up to 350°C but has an upper molecular weight limit of ~600Da. However, according to Miller, GC-MS is assumed to be best suited for qualitative analysis (Miller, 2005). Figure 4-2 illustrates a general instrumental setup for GC-MS.

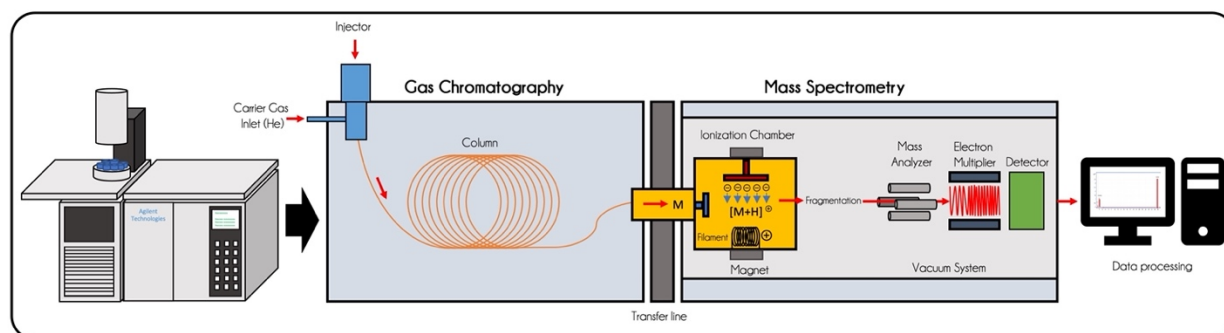


Figure 4-2: Simple flow chart showing sample acquisition and instrumental parts of a GC-MS setup.

4.1.1.2 HIGH-PERFORMANCE LIQUID CHROMATOGRAPHY (HPLC)

High-performance liquid chromatography (HPLC) has greater versatility than GC as it can be used for higher molecular compounds that are less volatile and more polar. In addition, both the SP and the MP can be tuned in order to optimize the separation of the sample matrix. In HPLC, the sample is first injected into the column where separation takes place. HPLC can be operated in two different separation modes, known as normal phase (NP) and reverse phase (RP), depending on the properties of the sample in question. In NP-HPLC, the stationary phase is more polar than the mobile phase. The NP-SP is typically composed of hygroscopic silica particles on which OH-groups can form. The t_R of a given analyte is positively correlated with

the relative affinity to the SP. The MP used during NP-HPLC is typically an organic solvent with low to medium polarity. The strength of the MP can be increased by increasing the polarity of the solvent. In NP-HPLC, apolar molecules like hydrocarbons have limited retention. In RP-HPLC, on the other hand, the MP is more polar than the SP. Consequently, apolar compounds have a higher t_R than polar compounds. The strength of the MP can be increased by decreasing the polarity of the solvent. Both NP- and RP-HPLC separate the sample matrix based on polarity. However, retention in NP chromatography is typically dependent on the properties of the functional groups, while in RP chromatography, separation typically depends on the properties of the molecules, which is better for separating individual components within a molecular class (Miller, 2005). HPLC is also compatible with several different detector types, including UV-vis detectors, refractive index detectors (RI), evaporative light scattering detectors (ELSD), etc. A UV-vis detector, more specifically, a diode array detector (DAD) was coupled to the HPLC instrument used in this thesis. As the analytes elute from the column, they enter the DAD, which enable simultaneous acquisition of multiple spectral profiles within the UV-vis spectrum as the sample matrix moves through the flow cell (Mizell, 2021). Figure 4-3 shows a simple flow chart of an HPLC-DAD setup.

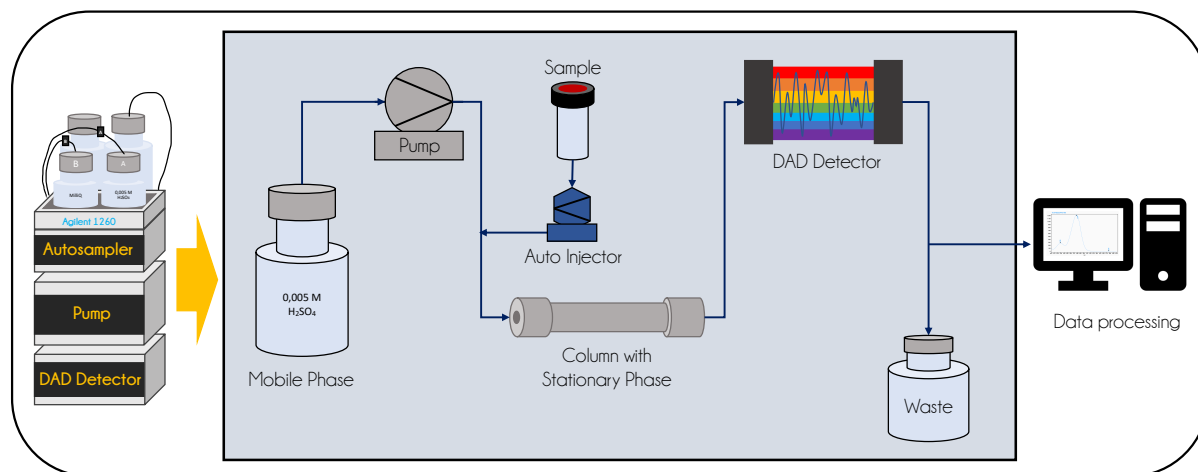


Figure 4-3: Simple flow chart of the HPLC setup.

4.1.2 NUCLEAR MAGNETIC RESONANCE (NMR)

Nuclear magnetic resonance (NMR) is a spectrometric technique that enables structural elucidation and accurate quantification of organic molecules based on a nucleus-dependent ratio between the spin angular moment and the magnetic moment (gyromagnetic ratio, γ) of nuclei with odd masses and/or odd atomic numbers. Nuclei commonly used for NMR-analysis include hydrogen-1 (^1H), carbon-13 (^{13}C), and phosphorus-31 (^{31}P). This thesis will mainly focus on ^1H -NMR, however ^{13}C -NMR will also be discussed in chapter 5.1.4, as both can be used as quantitative tools. Table 4-1 contains pros and cons associated with ^1H -NMR and ^{13}C -NMR.

Table 4-1: Pros and cons associated with ^1H -NMR and ^{13}C -NMR.

	Pros	Cons
^1H -NMR	<ul style="list-style-type: none">- Short T_1 relaxation time.- High natural abundance of ^1H (99.98%).- High gyromagnetic ratio.- Higher sensitivity than ^{13}C-NMR (Pavia, 2015).	<ul style="list-style-type: none">- Water suppression can affect quantitative accuracy of peaks located in close proximity to the chemical shift of water ($\sim 4,8\text{ppm}$).- Dynamic range problem.
^{13}C -NMR	<ul style="list-style-type: none">- Does not require water suppression, meaning that loss of signal intensity due to spillover from water is avoided.- ^{13}C has great potential for accurate quantification of complex mixtures due to its large chemical shift range and good peak separation.	<ul style="list-style-type: none">- Less sensitive than ^1H-NMR due to the low natural abundance of ^{13}C (1.08%), relative to ^1H, causing the resonances associated with ^{13}C to be about 6000 times weaker than the ^1H resonances.- Requires larger sample volumes than ^1H-NMR.- Low gyromagnetic ratio compared to the proton nucleus ($\gamma_{^{13}\text{C}} < \gamma_{^1\text{H}}$). This causes ^{13}C nuclei to have a lower resonance frequency than protons, which reduces the sensitivity of the NMR detection procedures even further (Pavia, 2015).- Much longer T_1 relaxation time compared to ^1H, which means that longer interscan delays are required, resulting in prolonged sample acquisition.

4.1.2.1 NMR – SAMPLE ACQUISITION

When an external magnetic field (B_0) is applied, atoms with nuclear spin will align with the external magnetic field and start to precess about their own axes of spin with an angular frequency, ω , called the Larmor or precessional frequency. The relative charge of a nucleus generates an oscillating electric field identical to the Larmor frequency. When a nucleus is exposed to a radio frequency (RF) pulse with a frequency identical to the Larmor frequency, resonance is achieved, leading to field coupling, which causes the nucleus to absorb energy from the incoming RF radiation. This will again result in a reorientation of the nuclear spin

states, which the instrument can detect as resonance peaks in the NMR spectrum. Resonance can, however, only be detected when there is a small excess of nuclei in the lower spin state relative to the upper spin state. When the number of nuclei in the upper and lower spin state is identical, the system becomes saturated, and no observable signal will be generated.

The resonance frequency of a given proton is dependent upon the surrounding electromagnetic environment. When a magnetic field (B_0) is applied, the valence electrons surrounding a proton will generate a local diamagnetic current that creates a counter magnetic field (B) that opposes B_0 . This effect is called diamagnetic anisotropy, which shields the protons from B_0 . Consequently, the degree of magnetic shielding for a given nucleus depends on the electron density of the diamagnetic current created by the surrounding chemical environment. In other words, the diamagnetic current determines the resonance frequency of a proton, which in turn determines the associated chemical shift (δ). This means that nuclei with low-density diamagnetic currents will appear downfield (left) in the spectrum, while nuclei with high-density diamagnetic currents will appear upfield (right), as a higher magnetic field strength (B_0) is required to achieve resonance for highly shielded protons. Since the differences in resonance frequencies between individual protons are very small, the resonance frequency is measured relative to the resonance frequency of a reference compound (Tetramethylsilane – TMS). In other words, the NMR instrument measures the frequency *difference* between a given proton and TMS ($\delta = 0$ ppm), which is converted to ppm values on the x-axis in an NMR spectrum (Pavia, 2015).

Spin-spin splitting, coupling constants, dihedral torsion angles, relative peak intensities are four additional phenomena that are necessary to understand in order to enable the efficient use of NMR as an analytical tool, as it can be used when performing structural elucidation of complex anomeric mixtures (see Appendix A1 for the structural elucidation of XYL). The concept of spin-spin splitting arises as protons coupled via three-bond vicinal couplings ($^3J_{HH}$) alter the diamagnetic shielding of each other depending on the nuclear spin direction of its neighboring proton. In Figure 4-4, the chemical shift (δ) of H_A will be shifted downfield when the spin of H_B is aligned with the applied magnetic field (scenario I). If, on the other hand, the nuclear spin of H_B opposes the applied magnetic field (B_0), the chemical shift of H_A will be shifted upfield due to a reduced diamagnetic shielding (scenario II). For a molecule containing only one proton, the chemical shift of the peak would be positioned at the dotted line. However, since scenarios I and II occur simultaneously in an NMR sample, the resonance peak of both H_A and H_B will

be displayed as doublets in the NMR spectrum as both protons affect each other to the same extent. The splitting pattern of a given signal can be explained by the $n + 1$ rule, where n describes the number of protons coupled via a three-bond vicinal coupling ($^3J_{HH}$).

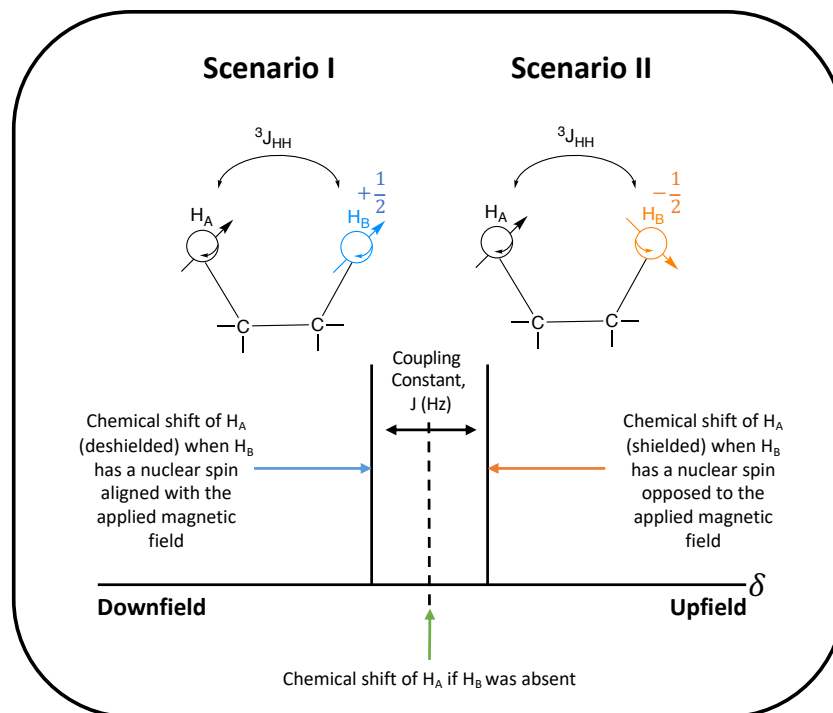


Figure 4-4: Doublet formation in NMR caused by spin-spin splitting. The figure is redrawn and modified from (Pavia, 2015).

The distance between the peak splitting is called the coupling constant (J), which is a measure of how strongly a proton is affected by the spin states of neighboring protons (Figure 4-4). The coupling constant is independent of the strength of the magnetic field and is measured in hertz (Hz). The integration value of a peak is proportional to the number of protons located in identical chemical environments, meaning that peak integration can be used to determine the number of hydrogens responsible for generating a certain peak, which makes NMR an effective tool for accurate quantification of different compounds (Pavia, 2015). Relative peak intensities can also give valuable information about the stability and relative abundance of different structural anomers in aqueous solutions, as it enables peak separation between anomers based on the relative integration values (Schmidt et al., 1996).

The Karplus equation describes the relationship between the 3J -coupling constants and the dihedral torsion angles in NMR spectroscopy. The dihedral torsion angle is the angle created by three consecutive molecular bonds and is defined by the angle formed between the two outer

bonds, e.g., the angle created between two protons with a vicinal coupling ($^3J_{HH}$). The closer the dihedral torsion angle is to 90° , the smaller the vicinal coupling constant between two adjacent protons ($^3J_{HH}$). The closer the torsion angle is to 0° and 180° , the larger the coupling constant (Pavia, 2015).

During sample acquisition, the NMR tube is placed in a spinner that is suspended in the gap between the two magnetic poles. The sample is then spun around its own axis to ensure that the sample experiences a uniform magnetic field. The magnetic gap also contains a coil attached to a synthesizer (RF generator), which supplies the electromagnetic energy required to reach resonance and consequently induce spin reorientation of the protons. The resonance signal is detected by a detector coil situated perpendicular to the RF coil. The detector will only detect a signal when the sample absorbs energy, i.e., during resonance.

Modern pulsed Fourier transformation (FT) NMR spectrometers use powerful superconducting solenoid magnets cooled by liquid helium (He) and nitrogen (N). The synthesizer generates RF waves that is phase shifted according to the pulse program. During a pulse period, the pulse gate closes, allowing the wave to pass along the RF transmitter to an amplifier. The high-energy RF pulse is then directed to the NMR-probe by the duplexer, which excites all the magnetic nuclei in the sample simultaneously. When the pulse is interrupted by opening the pulse gate, the excited nuclei return to their original spin states while emitting electromagnetic radiation (EMR). Since a molecule contains nuclei located in several different chemical environments, many different frequencies of EMR will be emitted during the relaxation period, thus generating a free-induction decay (FID) signal. The FID is a superimposed signal containing all frequencies emitted when the excited nuclei realign with B_0 during the relaxation period. The low-power FID is subsequently conveyed to the receiver which converts the signal to two audio frequency signals by subtracting a reference frequency. The signals will then be digitalized by the analog-to-digital converter (ADC) and sent to the computer. By applying a Fourier transformation (FT), the FID can be extracted into separate sine or cosine waves by mathematically converting the waves from the time domain to the frequency domain, thus displaying the signal as separate peaks in the NMR spectrum (Figure 4-5). The advantage with pulsed FT-NMR is that the signal-to-noise ratio improves as a function of the square root of the number of scans, meaning that it is especially suitable for examining nuclei that have limited natural occurrence like ^{13}C , or when analyzing very dilute samples (Pavia, 2015, Underhaug, 2004).

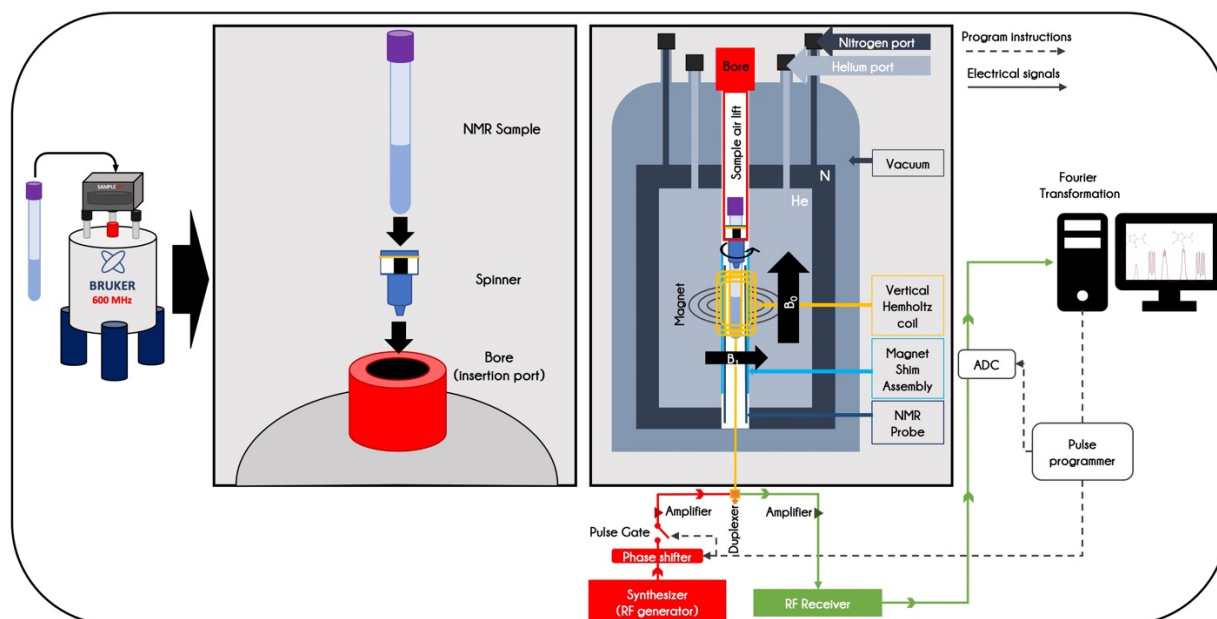


Figure 4-5: Schematic overview of an NMR-spectrometer. The flow chart in the bottom right of the figure is adapted from (Levitt, 2008).

4.1.2.2 ANALYTICAL METHODS – PROS AND CONS

Table 4-2 contains pros and cons associated with GC-MS, HPLC, and qNMR.

Table 4-2: Pros and cons associated with GC-MS, HPLC and qNMR.

Analytical Tool	Pros	Cons
GC-MS	<ul style="list-style-type: none"> - Allows for high-resolution separation of the sample matrix - Higher sensitivity than NMR - Facilitates analysis of volatile compounds unsuited for HPLC - NIST library enables fast and easy identification of sample constituents - Upper temperature limit of 350°C - Fully automated 	<ul style="list-style-type: none"> - Known to have relatively poor quantitative accuracy and precision (Miller, 2005) - Not suited for samples containing polar compounds - Upper molecular weight limit of 600Da - Not applicable for aqueous samples - MS detector fragments sample matrix
HPLC-UV	<ul style="list-style-type: none"> - Applicable to samples containing non-volatile, thermally labile compounds with high polarities - High sensitivity - Both MP and SP can be tuned to maximize chromatographic resolution - Fully automated - Can be used for accurate and precise quantification (Miller, 2005) 	<ul style="list-style-type: none"> - Generally longer analysis times than GC-MS and NMR - Requires deeper understanding of the physical and chemical properties of the sample constituents to get good chromatographic resolution - More work intensive than GC-MS and NMR - UV-detector cannot detect monomeric sugars
NMR	<ul style="list-style-type: none"> - Quick and easy sample preparation and analysis - Highly versatile - Fully automated - High reproducibility 	<ul style="list-style-type: none"> - Low sensitivity → Requires larger sample volumes than GC-MS and HPLC - Dynamic range problem - Accurate identification of specific compounds requires comprehensive structural elucidations, which is time consuming - Expensive

4.1.3 EXPERIMENTAL DESIGN

Experimental design and optimization are statistical tools applied to systematically examine and resolve challenges that arise within research, development, and production. Several experimental variables, termed factors/predictors, may influence the final results (responses) in an experimental procedure. This means that meticulous experimental planning and factor selection should be conducted to ensure that valuable information can be obtained from the experimental design.

In a factorial design (FD), the influences of all factors and factor interactions on one or more responses are investigated. If the combination of k variables is examined at two levels, a FD will consist of 2^k experiments. Each variable is divided into a high and a low value denoted (+) and (-), respectively. In a FD, at least two center point experiments (CP) using median values (0) of the high and low factor settings for each variable should also be conducted. This minimizes the risk of missing non-linear relationships in the middle of the intervals. CP also makes it possible to calculate confidence intervals and experimental error.

The span between the high and low level for all factors defines the experimental domain, i.e., the experimental area of investigation. The experimental domain should be defined according to what is assumed to be a reasonable variation to investigate. During initial experimental screenings, the experimental domain should span a wide enough area that a maximum of information can be extracted by performing a minimum number of experiments. All factors excluded from an experimental design should be kept at a constant level throughout the entire experimental series (Lundstedt et al., 1998). When planning FD, a Hadamard matrix is normally used for the experimental setup. A Hadamard matrix is a table where all columns are orthogonal (Carlson and Carlson, 2005). As the number of experimental variables increases, the number of experiments increases exponentially. Hence, in order to limit the number of experiments in a full FD, a fractional factorial design (FFD), with 2^{k-p} experiments, can be performed as third-order variable interactions usually are negligible, meaning that they usually can be excluded from the polynomial model. The p denotes the size of the fraction of a 2^k design (Gunst and Mason, 2009).

One of the key advantages of planning and conducting experimental designs is that they can help elucidate variables and variable interactions that have significant effects on the measured responses, both positively and negatively. When the most influential variables affecting the desired responses have been identified, further optimization can be done by following the slope of the acquired response surface for the explored domain. Examples of optimization methods include the method of steepest ascent, the simplex method, and response surface modeling (Carlson and Carlson, 2005).

4.1.3.1 PRINCIPAL COMPONENT ANALYSIS

The main goal of a principal component analysis (PCA) is to extract the most essential information from the accumulated responses in a data set. This is done by minimizing the size of the dataset by only keeping the most critical information, i.e., removing variables that do not give valuable information about the system. To accomplish this, a PCA computes latent variables known as principal component vectors (PC) plotted in a multidimensional descriptor space (Abdi and Williams, 2010).

The fundamentals behind a principal component analysis (PCA) can be explained by using a geometrical description of the method. The direction of the first PC is calculated by identifying the linear combination of the original data that shows the most significant variation in their spatial distribution, i.e., explain the largest part of the dataset. By anchoring PC1 to the average value of the original data points in the descriptor space, it is possible to make perpendicular projections of all the points in the space of this principal component vector. Consequently, a projected data point will then have a coordinate, measured from the average value along PC1, known as a score, t . If the dataset contains more systematic variation that is not described by PC1, a new PC (PC2) describing the second largest variation can be drawn by removing PC1. PC2 must be orthogonal to PC1 and must be anchored to the average value of the original data points. Every subsequent PC should be orthogonal to the preceding PC and follow the same constraints (Carlson and Carlson, 2005). Figure 4-6 illustrates the projection of a set of data points from the descriptor space to the plane spanned by PC1 and PC2.

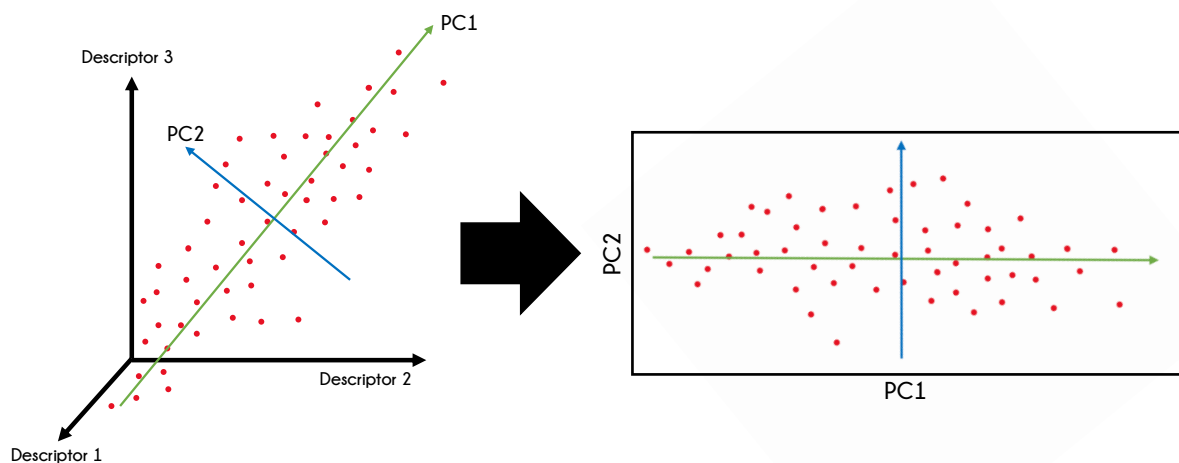


Figure 4-6: Projection of data points in PCA.

The principal component vectors can be used to generate two-dimensional plots known as biplots which combines the principal component scores for all objects (experiments), the variable loadings, and measured responses. The distance from the origin (normally denoted as an + in the plot) of a given variable is proportional to the relative weight of that variable on the PC. In other words, the most influential variables will be located the furthest away from the origin. In addition, the plot also displays how different objects correlate with each other, different variables, and the measured responses. If the angle between two points is $<90^\circ$, a positive correlation exists, while angles $>90^\circ$ indicates a negative correlation. An angle of exactly 90° means that no correlation is observed in the plane spanned by the two principal components. In addition, the more similar objects/variables/responses are, the more closely grouped they will be in the biplot.

4.1.3.2 PARTIAL LEAST SQUARES METHOD

Partial least squares (PLS) regression is a computational method in which quantitative relations between variables can be established and used for system optimization. The method can be used when dealing with two interdependent blocks of data, e.g., one matrix containing independent variables (descriptors or factors) for a given reaction system (X-block), and a matrix containing the dependent variables (responses) for the same reaction system (Y-block). PLS will create a linear regression model describing the relationship between the two matrices, i.e., data inputs in the X block can be used to predict the responses in the Y block. In other words, results from PLS analysis makes it possible to approach optimal factor settings in the X block in order to attain the best responses in the Y block. The advantage with PLS is that the results can be

graphically presented in various plots, where it is possible to extract the correlation coefficient (R) for the model. The closer the R is to 1, the better the model describes the system. PLS also enables identification of weighted correlation coefficients which describes the relative importance of each factor for a given response (Carlson and Carlson, 2005). The mathematical representation of a linear regression model including second order interactions can be expressed as:

$$y = b_0 + b_1x_1 + b_2x_2 + \dots + b_kx_k + b_{ij}x_ix_j$$

Where y is the dependent variable, e.g., FUR yield, b_0 is constant, b_1, b_2, \dots, b_k is the weighted regression coefficients for the main factors, b_{ij} is the cross-product coefficients, and x is the numerical value of each variable. The mathematical representation of the prediction model acquired in this thesis is given in chapter 5.3.2.

4.2 MATERIALS

All reagents, catalysts and solvents were purchased from Sigma-Aldrich and used without further purification. Fruit and Berry residues (F&B), more specifically, cherries and plums, were obtained from Hardanger Fjordfrukt BA. The F&B residues were grinded to a purée using a mortar and pestle and used without further pretreatment. All chemicals used in this thesis are listed in Table 4-3 below.

Table 4-3: List of reagents, solvents, and catalysts used in this thesis organized in alphabetical order.

Chemical	Abbreviation	Chemical Formula	Purity [%]
Aluminium Sulfate	ALS	$\text{Al}_2(\text{SO}_4)_3$	>97
1-Chlorohexane	CH	$\text{C}_6\text{H}_{13}\text{Cl}$	99
Deuterium oxide	D_2O	D_2O	99.9% D w/0.05 wt% TSP
Formic acid	FA	CH_2O_2	≥ 98
2,5-Furandicarboxylic acid	FDCA	$\text{C}_6\text{H}_4\text{O}_5$	97
Furfural	FUR	$\text{C}_5\text{H}_4\text{O}_2$	Analytical standard, ≥ 98
γ -valerolactone	GVL	$\text{C}_5\text{H}_8\text{O}_2$	≥ 99 , FCC, FG
Hexadecane	HD	$\text{C}_{16}\text{H}_{34}$	99%
Hydrochloric acid	HCl	HCl	≥ 37
5-Hydroxymethylfurfural	HMF	$\text{C}_6\text{H}_6\text{O}_3$	>99, FG)
Levulinic acid	LA	$\text{C}_5\text{H}_8\text{O}_3$	98
Methyl-isobutyl-ketone	MIBK	$\text{C}_6\text{H}_{12}\text{O}$	≥ 99.5
Sulfamic acid (H_3NSO_3 , $\geq 99\%$)	SA	H_3NSO_3	≥ 99
Sulfuric acid	H_2SO_4	H_2SO_4	95-97
D-xylose	XYL	$\text{C}_5\text{H}_{10}\text{O}_5$	≥ 98

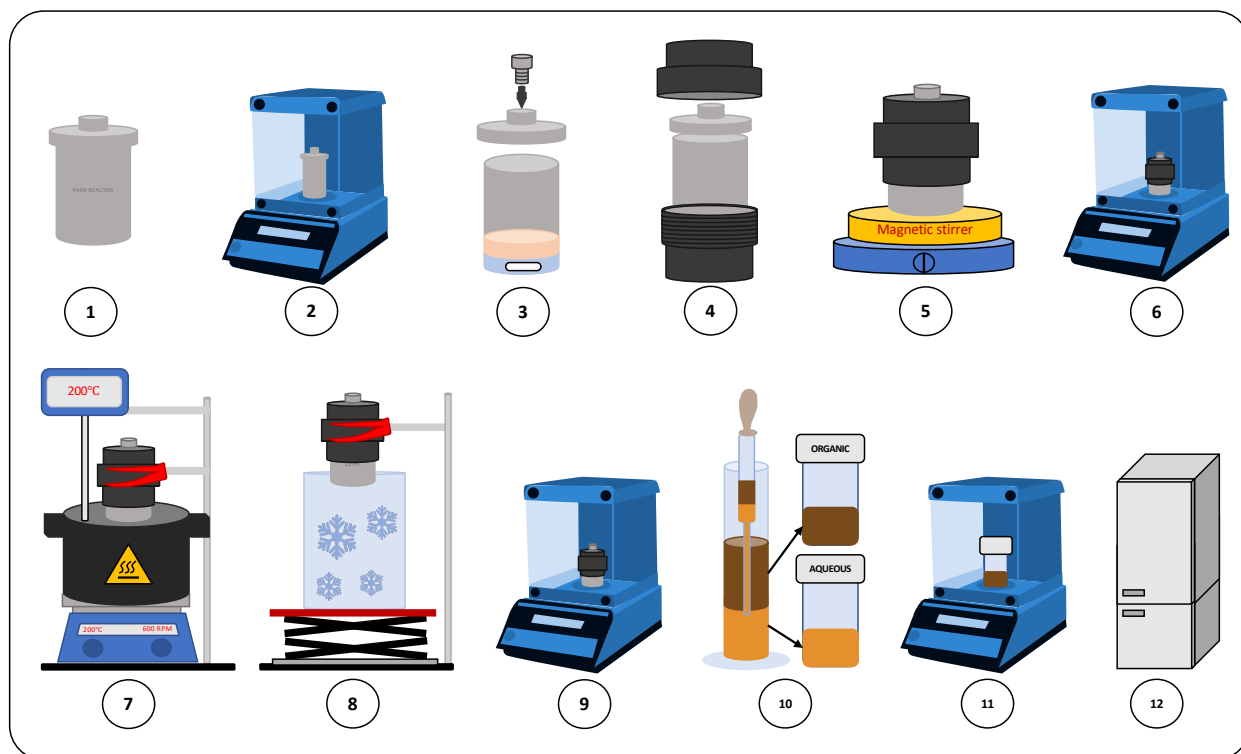
4.3 EXPERIMENTAL

4.3.1 EXPERIMENTAL DESIGN

Sirius PRS 10.0 was used to analyze the results obtained in the experimental designs conducted in this thesis. The acquired responses were analyzed using principal component analysis (PCA) and partial least squares regression (PLS) to identify positive and negative correlations between the main factors, factor interactions, and the measured responses. The results from the multivariate analysis using PCA and PLS are presented and discussed in chapter 5.3.2.1 and 5.3.2.2, respectively.

4.3.2 DEHYDRATION OF D-XYLOSE TO FURFURAL

All experiments were carried out in a Series 4700, 316 Stainless steel batch Parr reactor (22mL) with a polyphenylene lining (Figure K-6, Appendix K). In a typical experiment (Scheme 4-7), the empty reactor (**1**) was initially weighed (**2**) before adding the desired amount of substrate and catalyst to the reactor cup. MilliQ water, organic solvent, and a magnetic stir-bar (**3**) were then added. The reactor was subsequently closed (**4**) and weighed (**5**) before it was placed on a magnetic stirrer (**6**) for approximately 5 minutes to ensure complete dissolution of XYL. The bottom part of the reactor vessel was then submerged in an oil bath (**7**) with a temperature ranging from 150 – 200°C for 30 – 90 minutes while being stirred at 600 revolutions per minute (rpm). The product mixture was immediately quenched after reaction completion by lowering the bottom part of the reactor into an ice bath (**8**). The size of the ice bath was kept constant to ensure a similar cooling rate for all experiments. After reacting room temperature, the reactor was dried and weighed (**9**) to check for potential leakage during the reaction. The product mixture was subsequently transferred into a 10mL graduated cylinder using a VWR 230mm disposable glass pipette, followed by phase separation using the same pipette to minimize loss of product (**10**). The separated organic and aqueous phases were collected in two separate, pre-weighed 20mL Chromacol scintillation sample vials (**10**) to determine mass recovery (**11**). The separated product phases were refrigerated (**12**) prior to qNMR analysis workup. All procedural steps are visualized in Scheme 4-7.



Scheme 4-7: Procedural steps for the synthesis of FUR using a biphasic reaction system.

4.3.3 DEHYDRATION OF F&B REJECTS TO FURFURAL AND 5-HYDROXYMETHYLFURFURAL

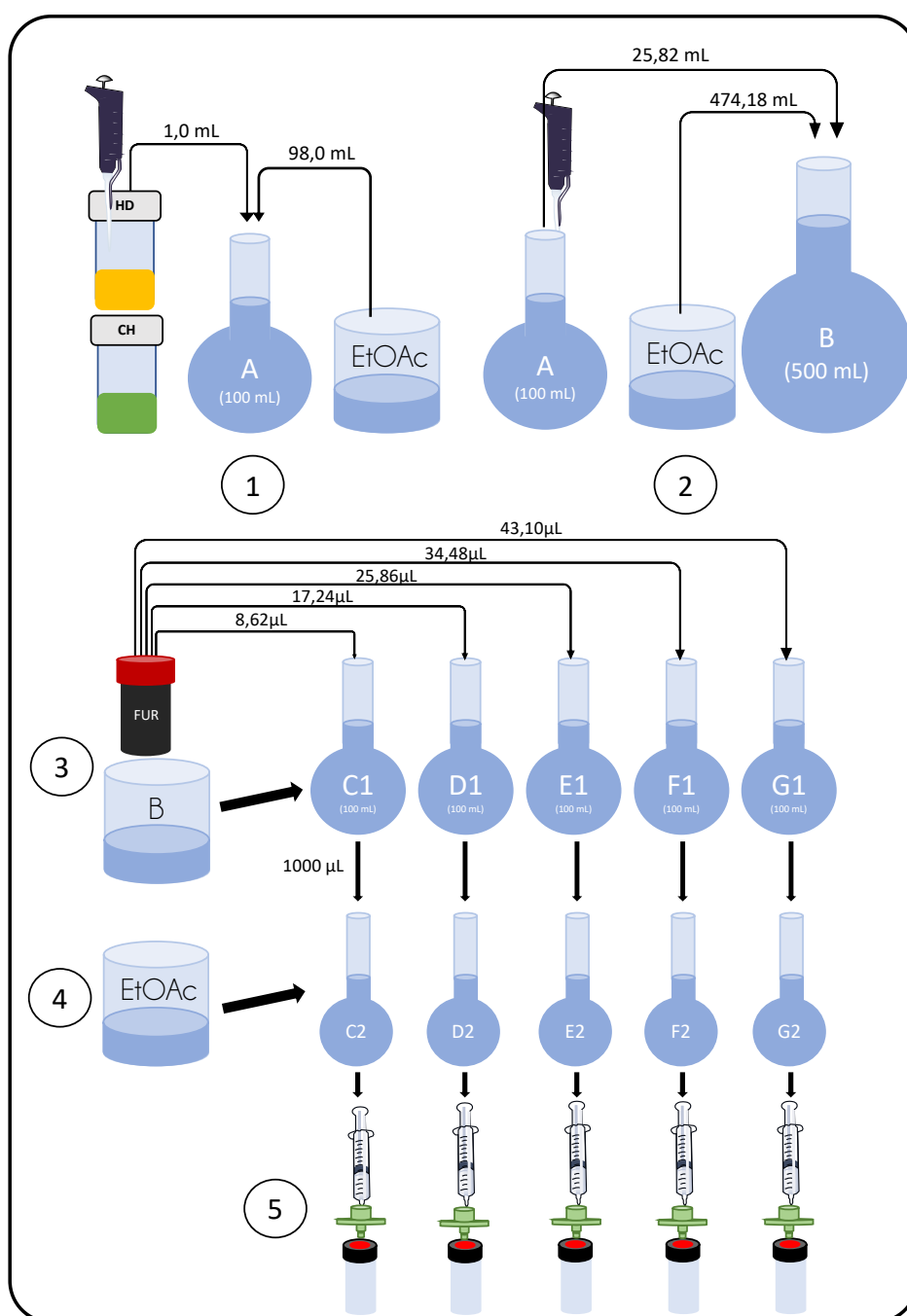
F&B rejects, more specifically plums and cherries, were deseeded before a mortar and pestle were used to make a purée out of the remaining skin and pulp. The subsequent experimental steps were identical to the procedure described in the previous chapter (Chapter 4.3.2), where XYL was used as substrate (Scheme 4-7).

4.3.4 EXPERIMENTAL PROCEDURES - GC-MS

4.3.4.1 PREPARATION AND VALIDATION OF CALIBRATION CURVES FOR GC-MS

Two calibration curves, using two different internal standards (IS) were prepared to evaluate the linearity of GC-MS as an analytical quantification tool for the reaction system used in this thesis. This was done by applying linear regression to the calibration curves using the least-squares method in Microsoft Excel and solving the equations for \hat{y} . Five calibration solutions containing known but increasing amounts of FUR ($9.9\mu\text{g}/\text{mL}$, $20\mu\text{g}/\text{mL}$, $30.8\mu\text{g}/\text{mL}$,

37.5 $\mu\text{g/mL}$, and 50.1 $\mu\text{g/mL}$) and constant amounts of hexadecane (HD) and chlorohexane (CH) (40 $\mu\text{g/mL}$ and 45 $\mu\text{g/mL}$, respectively) were prepared with ethyl acetate as solvent and analyzed using GC-MS. HD and CH served as internal standards. The following preparation and dilution steps were performed to ensure accurate concentrations of each analyte in the five calibration solutions (Scheme 4-8):



Scheme 4-8: Preparation of calibration curves for GC-MS.

In the first step, an Eppendorf autopipette was used to transfer 1000 μ L HD and CH to a 100mL volumetric flask (**1**), which was subsequently filled to the mark with EtOAc (**Solution A**). Solution A containing HD and CH was then diluted to 400 μ g/mL and 455 μ g/mL, respectively, by transferring ~25.8mL of (**A**) to an empty volumetric flask (500mL) using an Eppendorf autopipette (**2**). The flask was then filled to the mark with pure EtOAc (**Solution B**). Five solutions with increasing [FUR] were then prepared by adding different volumes of FUR to empty 100mL volumetric flasks (**3**), yielding concentrations ranging between 100 – 500 μ g/mL (**C1 – G1**). Each flask was weighed before and after the addition of FUR to ensure high concentration accuracy. Each flask was subsequently filled to the mark using solution (**B**).

The five stock solutions (**C1 – G1**), now containing FUR, HD, and CH, were subsequently diluted 1/10 by transferring 1000 μ L of each solution to empty volumetric flasks (10mL) that were filled to the mark with pure EtOAc (**4**), yielding FUR, HD, and CH concentrations ranging between 10 – 50 μ g/mL, 40 μ g/mL, and 45 μ g/mL, respectively (**C2 – G2**). The solutions were ultimately filtered through 0.45 μ m Whatman nylon filters (**5**) and analyzed using an Agilent 7890A GC instrument connected to a 5977A MSD mass spectrometer. The column used for the analysis was a HP-5MS (30m x 0.25mm x 0.25 μ m) GC-column. Samples were analyzed in splitless mode, with an injection volume of 1 μ L and a flow rate of 1mL/min. The temperature program used is given in Table D-3 in Appendix D. Each sample was analyzed twice to enable assessment of peak area reproducibility. The ratio between FUR and the two IS was then computed to calculate the predicted [FUR] in each sample.

To check whether the linear regression models could be used for accurate quantification of FUR in organic product solutions, the calibration curves were used to calculate the predicted [FUR] in a procedural blank where a known amount of FUR was added prior to workup and analysis. The calibration curves were also used to calculate the predicted [FUR] in an experimental series where the catalytic performance of six acid catalysts was compared at identical reaction conditions (Table 5-6, Figure 5-15, and Figure 5-16). The predicted [FUR] was calculated by solving the equation ($\hat{y} = ax + b$) for the linear regression for \hat{y} , where a is the slope, b is the intercept, and x is the measured [FUR] from the GC-MS.

4.3.4.2 SAMPLE PREPARATION FOR GC-MS

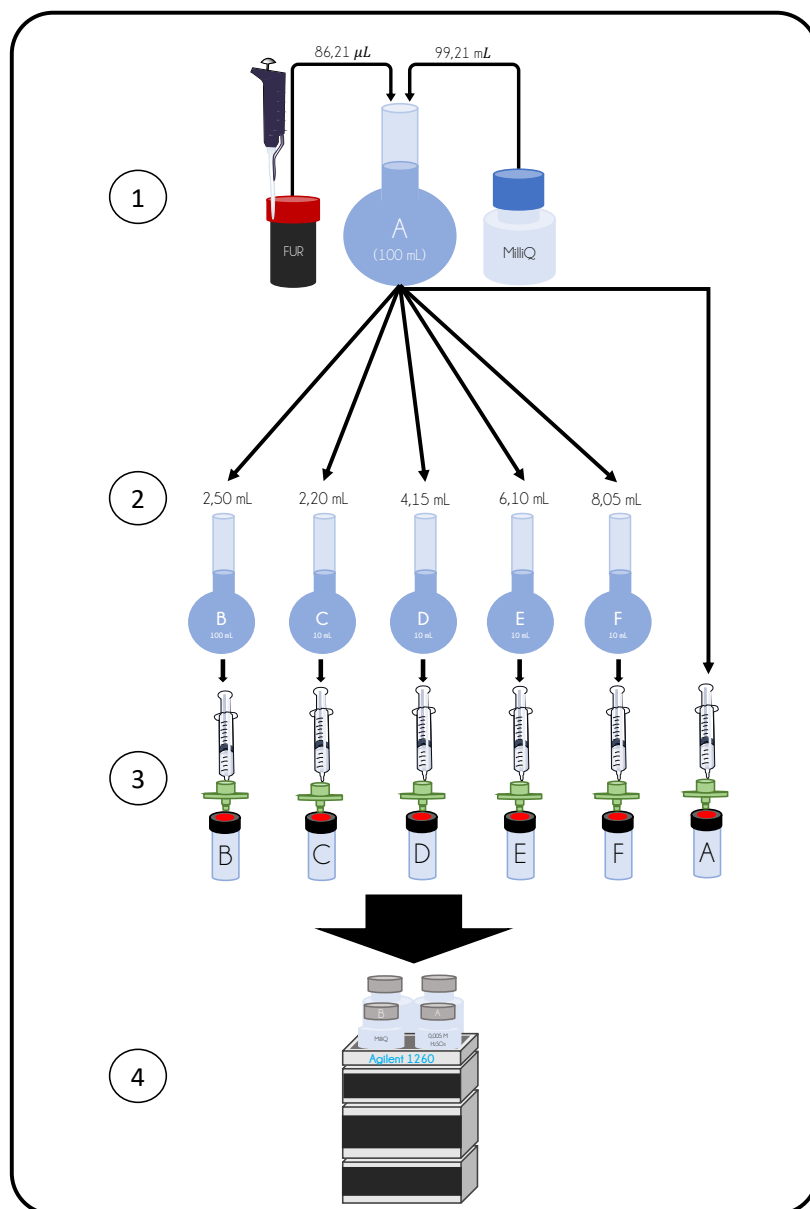
Using a Finn-pipette, the organic phase (100 μ L) was transferred to a volumetric flask (10mL) which was subsequently filled to the mark with ethyl acetate containing HD (40 μ g/mL) and CH (45 μ g/mL) as IS. All samples were filtered through 0,45 μ m Whatman nylon filters and transferred directly to GC-tubes for analysis.

4.3.5 EXPERIMENTAL PROCEDURES – HPLC

4.3.5.1 PREPARATION OF CALIBRATION CURVES FOR HPLC

A six-point calibration curve, spanning a wide concentration area, was prepared to enable accurate quantification of FUR in aqueous samples with varying [FUR]. In order to make a calibration curve covering a sufficiently wide concentration interval, three test solutions with different [FUR] (31 μ g/mL, 163 μ g/mL, and 636 μ g/mL) were initially prepared and analyzed to get a better understanding of the molar absorptivity (ϵ) of FUR, i.e., the ability of FUR to absorb electromagnetic radiation at its reported maximum absorbance wavelength ($\lambda_{max} = 278nm$). This was also done to ensure that the calibration curve was prepared within the upper and lower quantification limit (LoQ) of the DAD-detector coupled to the HPLC instrument.

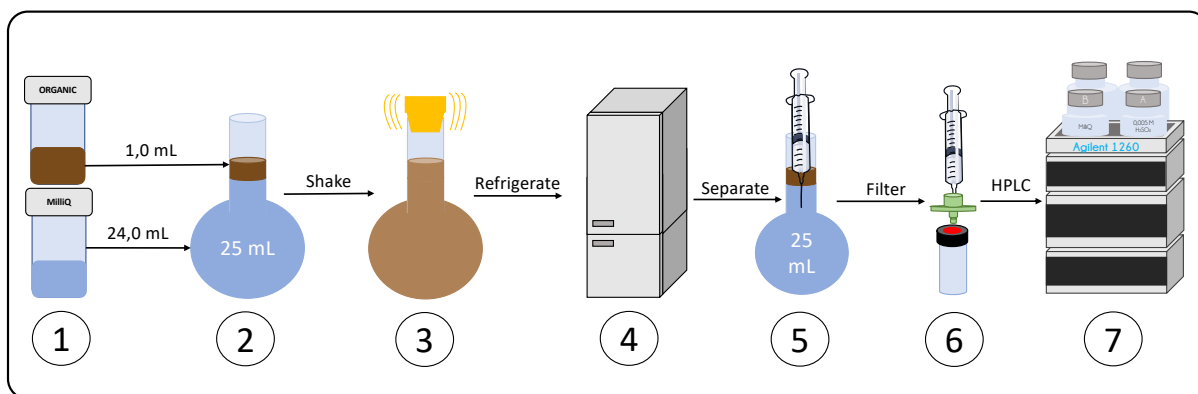
When preparing the calibration solutions, a 100mL stock solution (Scheme 4-9 (A)) containing FUR (~1000 μ g/mL) was initially prepared by transferring 86.2 μ L FUR to a 100mL volumetric flask that was subsequently diluted to the mark using MilliQ water (1). Solution (A) was then used to prepare the remaining five calibration solutions (B-F). All samples were diluted to desired concentrations (25 – 880 μ g/mL) using MilliQ water (2). The six solutions (A-F) were then filtered through 0.2 μ m Pall Acrodisc nylon filters and directly transferred to HPLC autoinjector vials for analysis (3). An Agilent 1260 infinity II HPLC equipped with a vial-sampler, a quaternary pump, and a diode array detector (1260 infinity DAD) was used for the analysis (4) (Scheme 4-9). A Rezex RFQ fast aid column (100 x 7.8mm) was used for sample acquisition. A 0.005M H₂SO₄ solution was used as MP, and the program was set to isocratic elution at 25°C with a flow rate of 0.7 mL/min. The sample injection volume was 10 μ L. All samples were analyzed in triplicates, and the average integration value for each standard solution was used when constructing the calibration curve in Figure 5-2.



Scheme 4-9: Preparation of standard solution for calibration curves.

4.3.5.2 SAMPLE PREPARATION OF ORGANIC PHASES FOR HPLC

An Eppendorf autopipette was used to transfer $\sim 1000\mu\text{L}$ of the recovered organic phase (Scheme 4-10 (1)) to a pre-weighed 25mL volumetric flask. The flask was then filled to the mark with super-distilled water (MilliQ) and weighed (2). The flask was subsequently shaken (3) and refrigerated overnight (4). A disposable syringe was then used to remove the aqueous phase from the extracted organic phase (5). The aqueous phase was subsequently filtered through a $0.2\ \mu\text{m}$ Pall Acrodisc nylon filter and ultimately transferred to an HPLC autoinjector vial for HPLC analysis (Scheme 4-10).



Scheme 4-10: Flow chart showing the preparation of organic phases for HPLC analysis.

4.3.6 EXPERIMENTAL PROCEDURES – NMR

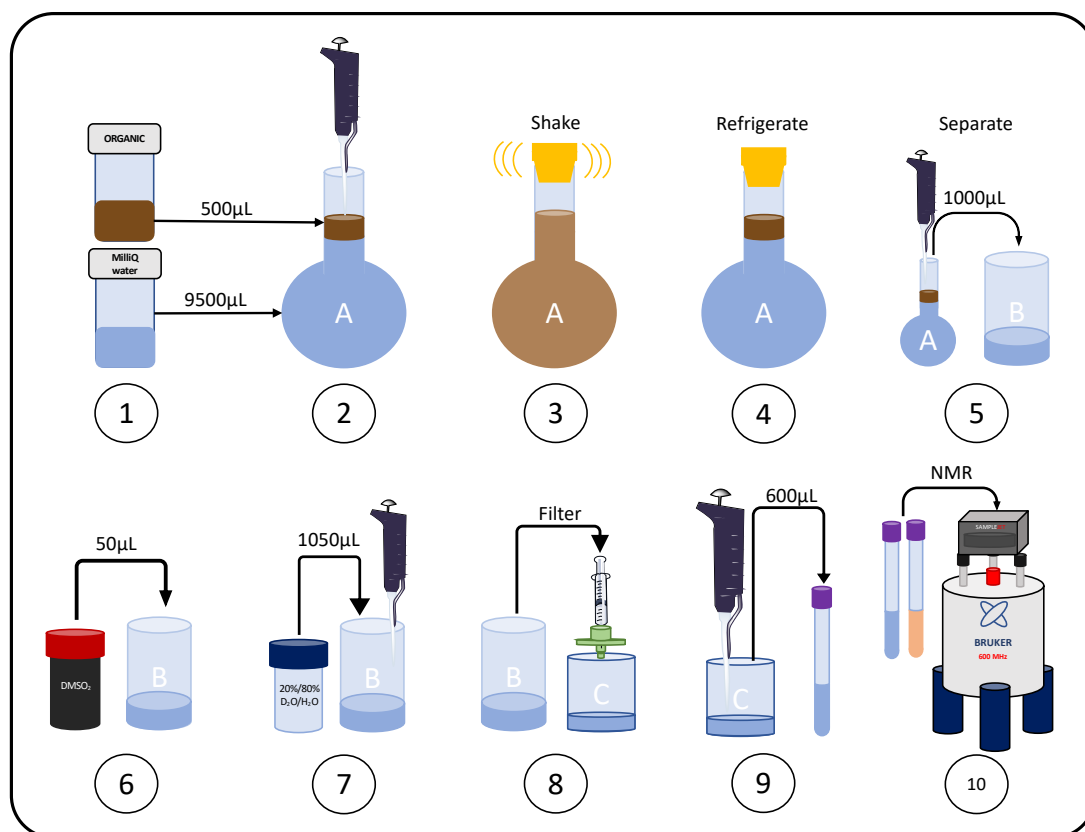
4.3.6.1 PREPARATION OF 10% AND 20% D₂O STOCK SOLUTIONS

A 250mL stock solution containing 20% deuterium oxide (D₂O) was prepared for qNMR analysis of aqueous samples and extracted organic phases. In the first step, 0.4448g sodium phosphate dibasic dihydrate buffer ($\geq 99.0\%$ Na₂HPO₄·2H₂O) was added to a volumetric flask (0.010M in 250mL). Distilled water (120mL) was then added, and the phosphate salt was dissolved using a heating plate and a magnetic stirrer. D₂O (50mL) containing 0.05wt% TSP (3-(Trimethylsilyl)-propionic-2,2,3,3-d₄ acid) sodium salt) was then added, followed by pH adjustment to 7.4 using 1.0 M HCl or 1.0 M NaOH. All pH adjustments were performed using a Metrohm 798 MPT Titrino automatic titrator. Distilled water (80mL) was ultimately added to make the final volume of the stock solution 250mL (Løhre et al., 2021). The 10% D₂O stock solution used for analytical standards was prepared by repeating the same procedure, but instead of adding 50mL D₂O, 25mL was added.

4.3.6.2 SAMPLE PREPARATION FOR qNMR

To enable quantification of FUR in the organic phase, using the workup protocol developed by Løhre et al., the organic phase had to be extracted with water prior to sample preparation (Scheme 4-11, **(1)** - **(4)**). The extraction was performed in a volumetric flask (10mL). In a typical extraction, a capped volumetric flask (**A**) was weighed before transferring the organic phase ($\sim 500\mu\text{L}$) to the flask using an Eppendorf autopipette (**(2)**). The flask was subsequently filled to the mark with MilliQ water ($\sim 9500\mu\text{L}$), followed by vigorous shaking (**(3)**) and

subsequent refrigeration for at least one hour to allow adequate phase separation (**4**). The effect of analyzing the organic phase using different extraction times can be found in Appendix J. Both the organic phase and the water added to the flask were weighed to enable accurate calculation of the dilution factor. The aqueous phase/extracted organic phase (**5**) was prepared for qNMR analysis by transferring 1000 μ L sample to a sample vial (**B**) before adding 50 μ L TraceCERT dimethyl sulfone ((CH₃)₂SO₂/DMSO₂) dissolved in distilled water as the IS ([IS]_{initial} = 2.125 M). The target concentration of DMSO₂ in the sample at this stage is 0.101 M (**6**), as specified by (Løhre et al., 2021). A 20% D₂O stock solution (1050 μ L) (*vide supra*) was then added (**7**) in a 1:1 volume ratio, giving the sample a 10% volume of D₂O. The sample pH was then adjusted to 7.4 followed by subsequent filtration using a 0.2 μ m Pall Acrodisc nylon filter (**8**) The filtered sample (600 μ L) was then transferred to a clean 5.0 \times 103.5mm Samplejet NMR-tube (**9**) (Scheme 4-11). All samples were analyzed with a Bruker BioSpin 600 MHz AVANCE NEO spectrometer equipped with a QCI CryoProbe (Løhre et al., 2021). Samples were stored at 5°C in the autosampler.



Scheme 4-11: Stepwise preparation of organic and aqueous samples for qNMR analysis. Sample preparation of the organic phase starts at (1), while preparation of the aqueous samples starts at (5), as no extraction is required for the aqueous phase.

4.3.6.3 PREPARATION OF STANDARDS FOR QNMR

10 mL solutions, containing 50mM of the desired analytical standard, were prepared using the pre-made 10% D₂O stock solution (*vide supra*). Four standard solutions containing FUR were made by transferring 41 μ L of FUR (~0.048g) to a volumetric flask which was subsequently filled to the mark using the 10% D₂O stock solution. The pH of the four samples were then adjusted to pH = 2.00, 4.80, 7.40, and 10.73 in order to see whether pH affected the chemical shifts of the four peaks associated with FUR in the NMR spectrum. The same procedure was repeated for HMF and XYL by adding 0.063g and 0.075g of each compound, respectively, to each volumetric flask. The pH value for the four HMF standards were adjusted to pH = 1.75, 4.87, 7.40, and 10.81, while the four XYL standards were adjusted to pH = 1.99, 5.18, 7.40, and 11.13. The main objective of analyzing FUR, HMF and XYL at pH values above and below the standard pH value of 7.40 was to see whether acidic and alkaline conditions would alter the peak position of the protons associated with each compound, i.e., whether the peaks would take on different chemical shifts in acidic and basic conditions. Hence, having identical pH values for both FUR, HMF, and XYL standards were not considered critical based on the purpose of the study. All samples were filtered through 0.2 μ m Pall Acrodisc nylon filters before transferring 600 μ L of each sample to clean 5.0 \times 103.5mm Samplejet NMR tubes. NMR-spectra (¹H, ¹³C, COSY, HSQC, HMBC, and H2BC) for FUR, HMF, and XYL standards can be found in Appendix A1-A3. Standard spectra for GVL (Appendix A4), levulinic acid, and formic acid (Appendix A5) were also acquired.

4.3.7 PREPARATION OF PROCEDURAL BLANKS

Procedural blanks were prepared by following steps **(1)** - **(6)** and **(10)** - **(12)** in Scheme 4-7. Initially, distilled water (1.50g) was loaded into a pre-weighed reactor followed by the addition of MIBK (3.00g, 3745 μ L). FUR (~0.05g, 43.1 μ L) and a magnetic stir bar was then added to the reactor. The reactor was subsequently closed and placed on a magnetic stirrer for 5 minutes followed phase separation and analysis using GC-MS, HPLC, and qNMR.

4.3.8 CATALYST TESTING

Six different catalysts were tested at the same reaction conditions (XYL (0.15g), MIBK/H₂O ratio (2:1 (m/m)), catalyst (0.1M aqueous phase), 190°C, and 60 minutes) for all experiments. A blank without the addition of catalyst was also performed to get a better understanding of the catalytic activity of each catalyst. A constant amount of FUR (0.05g, 43.1 μ L) was also added to the reactor prior to heating to get a better understanding of the stability of FUR in the reaction system at elevated temperatures. All experiments were conducted following almost the same workflow shown in Scheme 4-7. The only difference was that the aqueous phase was extracted using an additional 1000 μ L of MIBK to ensure maximum recovery of FUR in the organic phase. The results are presented and discussed in chapter 5.2.2.

4.4 EQUATIONS

The following equations were used to calculate the FUR yield, degree of XYL conversion and reaction selectivity towards FUR formation:

Calculation of FUR yield (mol%):

$$Yield = \frac{m_{FUR,org} + m_{FUR,aq} - m_{FUR,initial}}{m_{xyl,initial}} \times \frac{Mw_{xyl}}{Mw_{FUR}} \times 100\% \quad (\text{Eq. 1})$$

Where $m_{FUR,org}$ and $m_{FUR,initial}$ is the mass of FUR present in the organic and aqueous phase after reaction completion, $m_{FUR,initial}$ and $m_{xyl,initial}$ is the amount of FUR and XYL present in the reaction mixture before heating, and Mw_{FUR} and Mw_{xyl} is the molecular mass of FUR and XYL, respectively.

Calculation of the degree of XYL conversion:

$$Xylose\ conversion = \frac{m_{xyl,initial} - m_{xyl,final}}{m_{xyl,initial}} \times 100\% \quad (\text{Eq. 2})$$

Where $m_{xyl,initial}$ is the mass of XYL added prior to heating and $m_{xyl,final}$ is the mass of XYL remaining after heating.

Calculation of reaction selectivity towards FUR formation:

$$Selectivity = \left(\frac{n_{FUR\ generated}}{n_{XYL\ converted}} \right) \times 100\% \quad (\text{Eq. 3})$$

Where n_{FUR} and is the number of moles of FUR generated and n_{XYL} is the number of moles of converted XYL.

5. RESULTS AND DISCUSSION

This chapter covers the main results and findings acquired over the course of this Master's thesis. The conducted laboratory- and analytical work is divided into four main parts based on the objectives given in chapter 3. The results obtained when comparing GC-MS, HPLC, and qNMR as analytical quantification tools will be presented first. Secondly, the outcomes from the reaction system selection process will be given, i.e., evaluation of different solvents and catalysts. Next, the results attained during the experimental screening process of the chosen reaction system using fractional factorial design will be presented, followed by an in-depth discussion of the relative importance of each main factor. Finally, the results from utilizing F&B rejects as a feedstock for FUR and HMF production will be presented and discussed in light of potential full-scale implementation to lignocellulosic biorefinery concepts.

5.1 COMPARISON OF GC-MS, HPLC, AND qNMR AS QUANTIFICATION TOOLS

Identification of reliable procedures for accurate and precise quantification of FUR, HMF, and XYL in organic and aqueous samples was a central part of this thesis. Since FUR was the main product of interest, a procedural blank containing a known amount of FUR was prepared and analyzed using GC-MS, HPLC, and qNMR to determine which of the three methods was the better analytical tool for reliable quantification. Calibration curves for FUR were prepared and used as quantitative tools for both GC-MS (Figure 5-1) and HPLC (Figure 5-2). For GC-MS, relative peak areas between FUR and two different internal standards (hexadecane (HD) and 1-chlorohexane (CH)) were used in addition to the calibration curves for the quantification. The temperature program used for GC-MS can be found in Table D-3 in Appendix D. For NMR, comprehensive structural elucidations of both FUR, HMF, and XYL using $^1\text{H-NMR}$, $^{13}\text{C-NMR}$, COSY, HSQC, HMBC, and H2BC were performed (Appendix A) to enable accurate identification and quantification of all three compounds using the procedure developed by Løhre et al. (Løhre et al., 2021). Table 4-2 in the previous chapter compares pros and cons associated with each analytical instrument tested in this thesis.

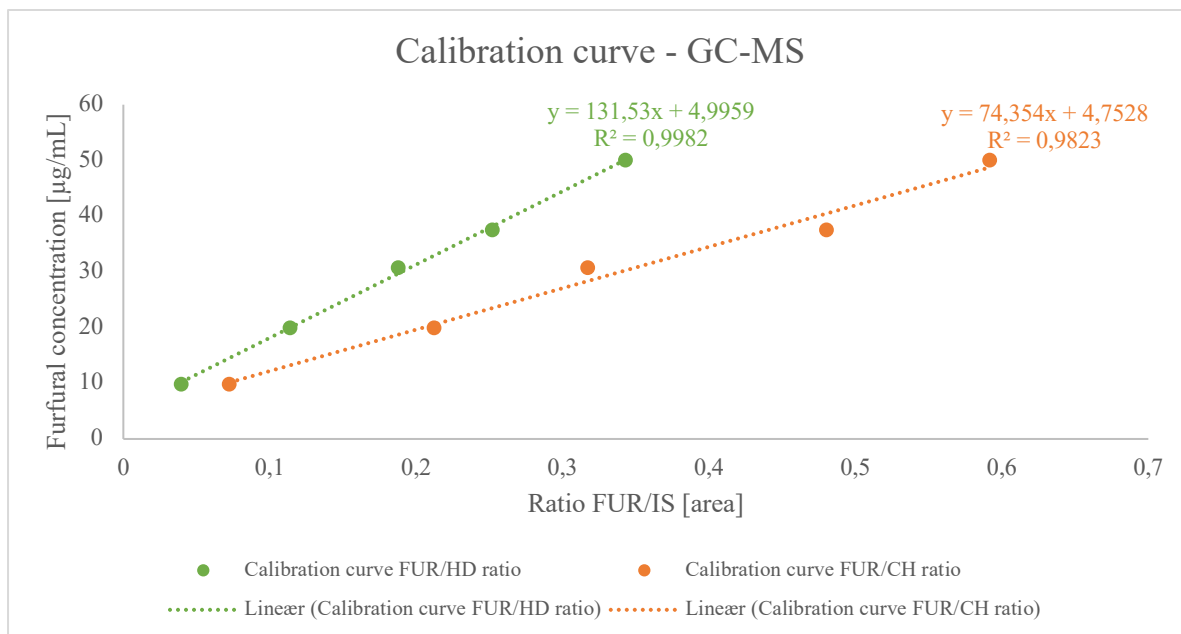


Figure 5-1: Calibration curves for calculating the predicted concentration of FUR in organic samples using GC-MS.

In Figure 5-1, the ratio between peak areas for FUR and IS (x-axis) is plotted against actual concentration of FUR (y-axis). Appendix D contains raw data for constructing the calibration curves (Figure D-2 and Table D-2).

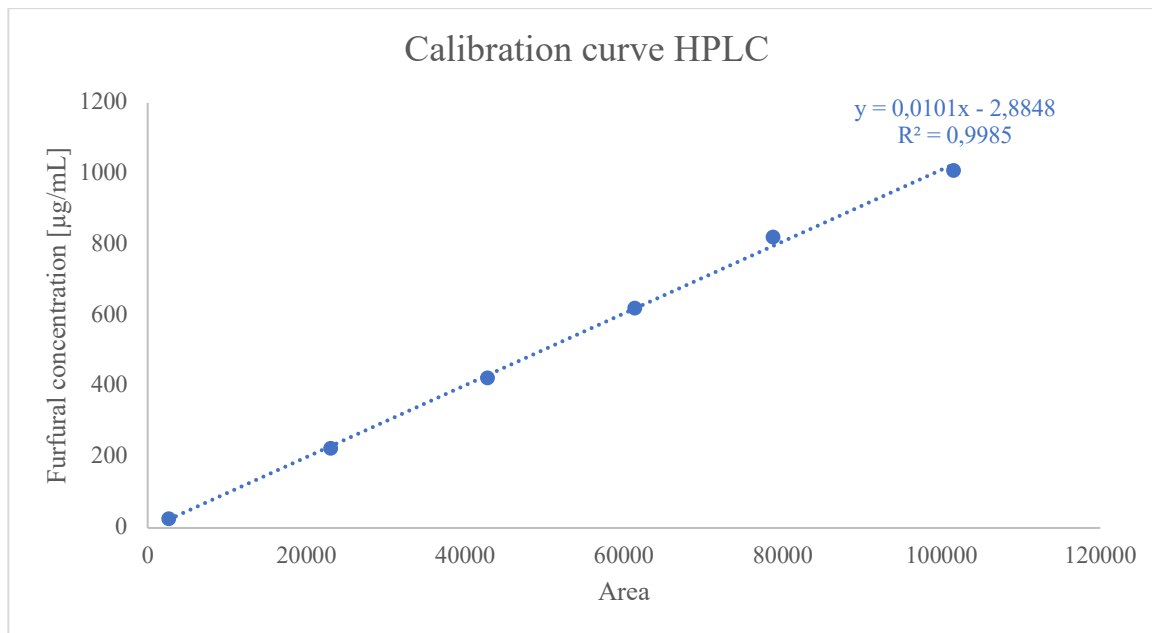


Figure 5-2: Calibration curve used for calculating FUR concentration using HPLC.

In Figure 5-2, the chromatographic peak area (x-axis) is plotted against the measured FUR concentration in the sample (y-axis). All chromatographic peak areas and chromatograms can be found in Appendix D (Figure D-1 and Table D-1).

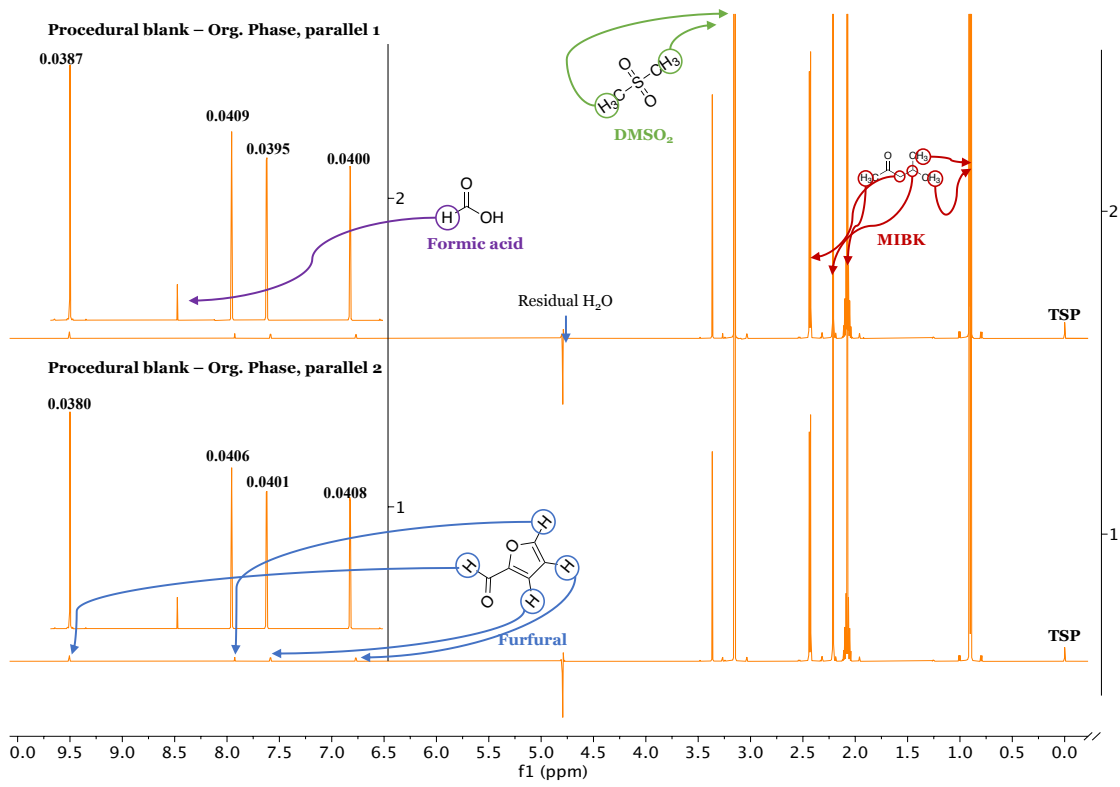


Figure 5-3: Stacked NMR-spectra of the organic phases from the procedural blank. The integration value is given above each peak for both parallels. The integration value of DMSO₂ was set to 6.0.

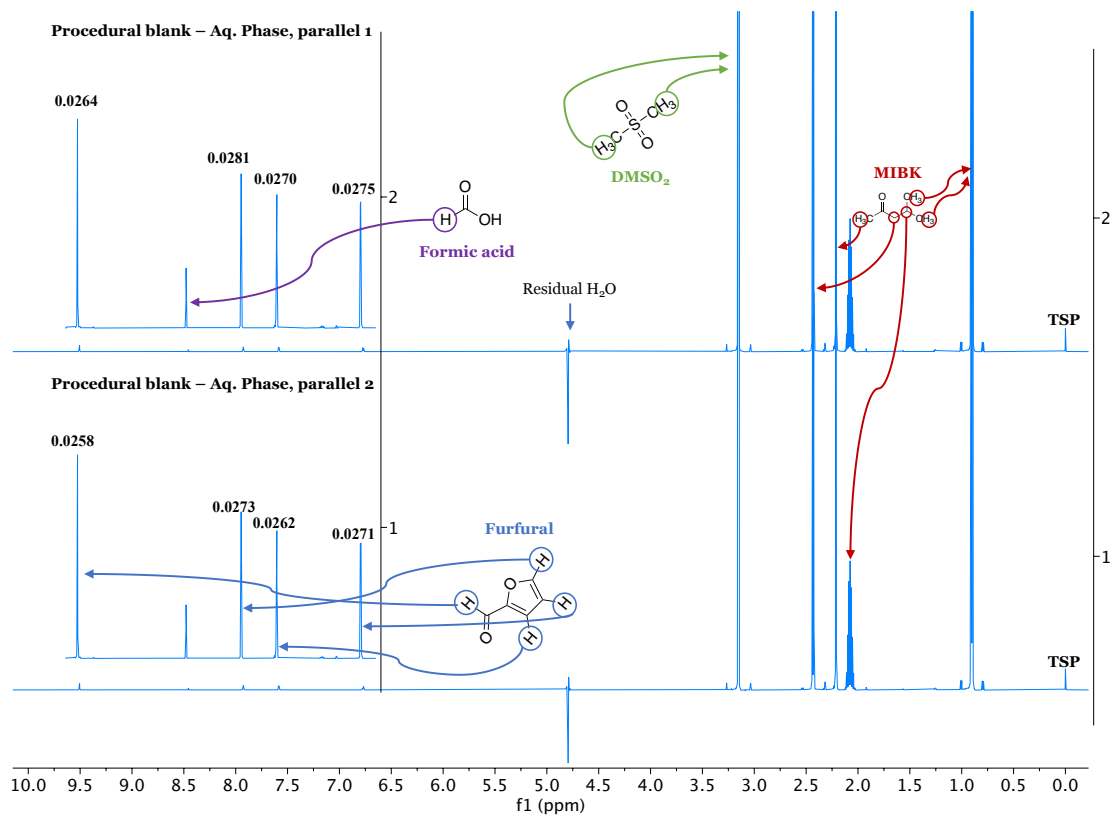


Figure 5-4: Stacked NMR-spectra of the aqueous phases from the procedural blank.

The average integration value of the assigned peaks in the ^1H -spectra in Figure 5-3 and Figure 5-4 was used for the quantification. The results are presented in Table 5-2.

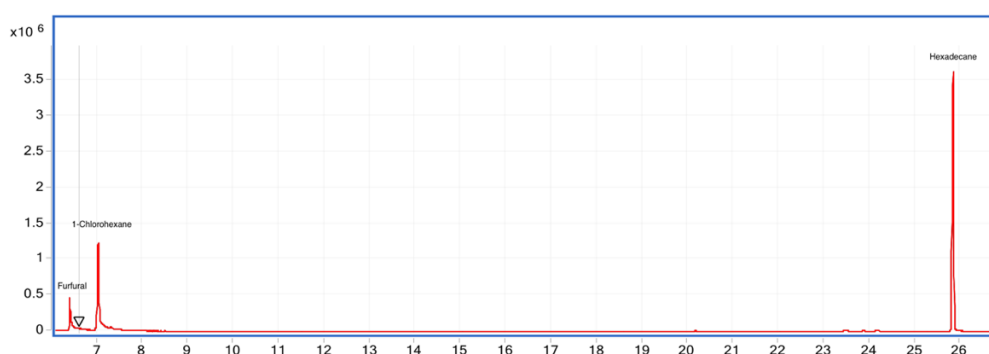


Figure 5-5: GC-MS chromatogram of parallel 1 from the procedural blank.

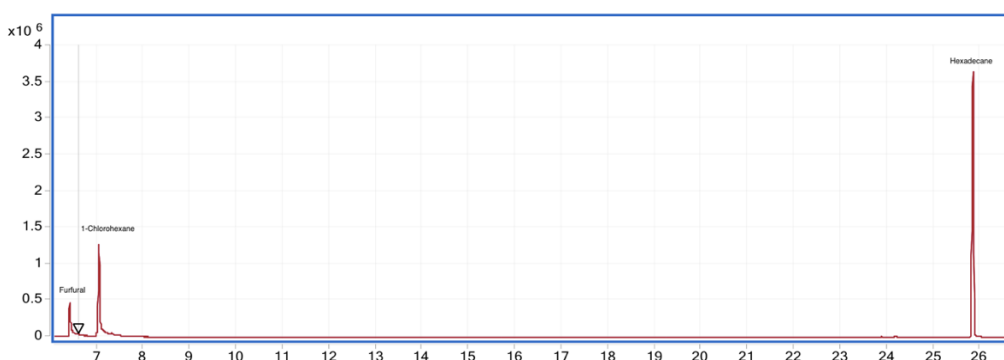


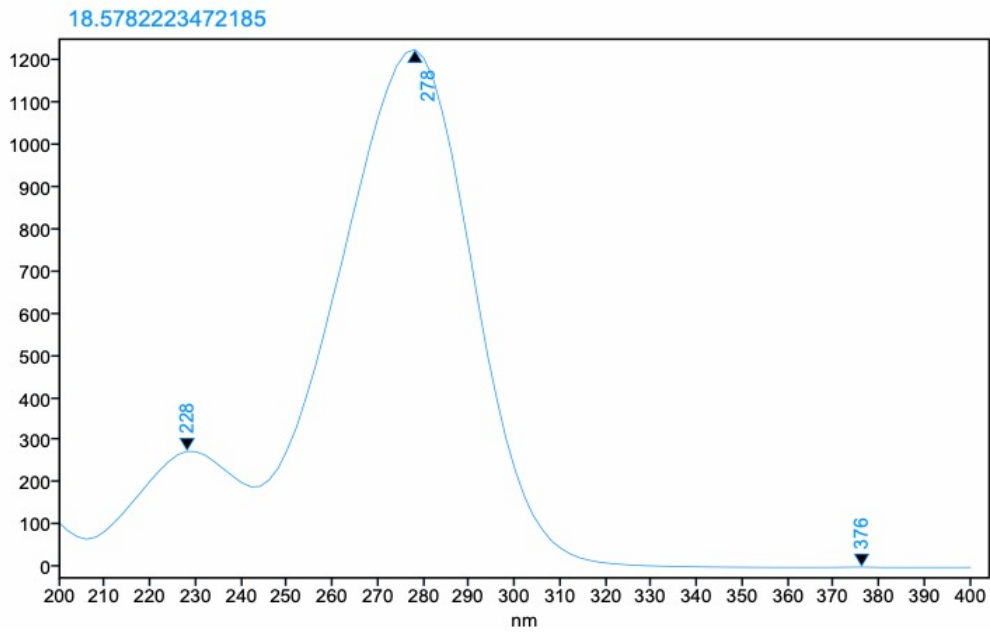
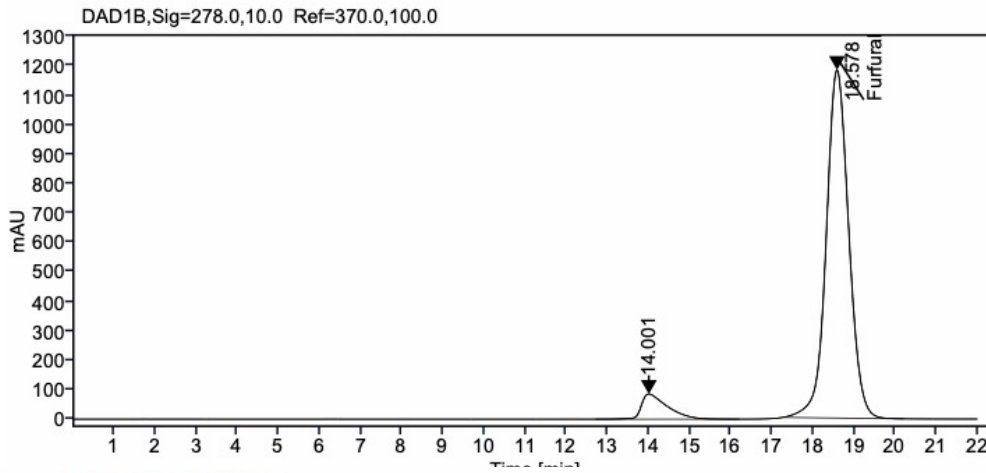
Figure 5-6: GC-MS chromatogram of parallel 2 from the procedural blank.

The measured peak areas for FUR, CH, and HD in Figure 5-5 and Figure 5-6 are given in Table 5-1.

Table 5-1: Chromatographic peak areas for FUR, HD and CH including relative peak areas between FUR and the two internal standards for each parallel.

Parallel	Area FUR	Area HD	Area CH	Ratio FUR/HD	Ratio FUR/CH
1	9149556	91654710	30744257	0.0998	0.2976
2	10865675	95737233	33660390	0.1135	0.3228

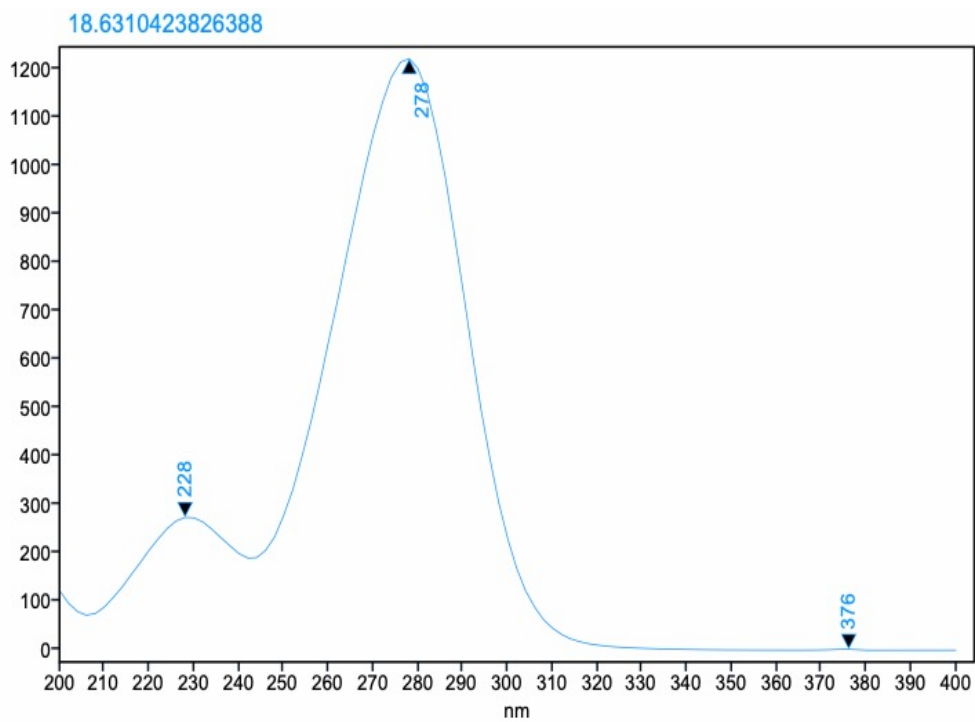
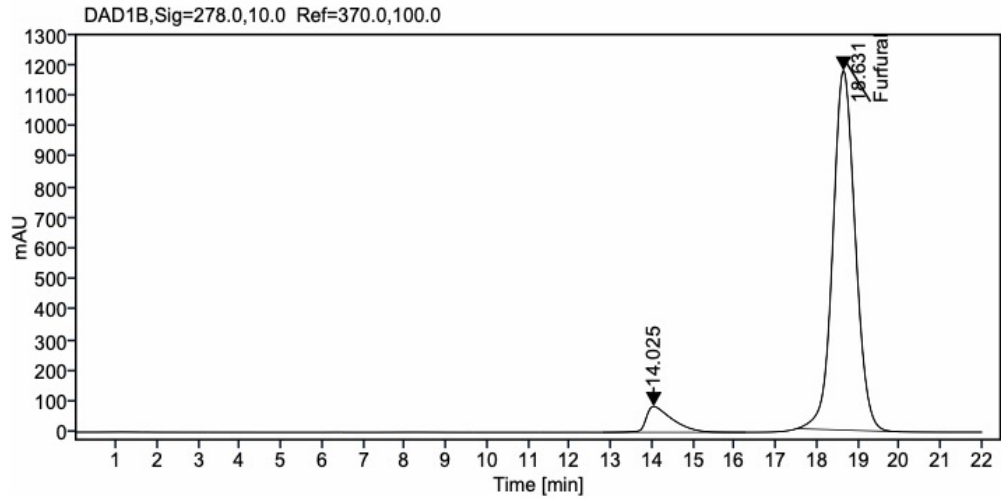
The ratios between FUR/HD and FUR/CH in Table 5-1 were used to predict the concentration of FUR in the procedural blank by solving the two linear equations in Figure 5-1 for y . The results for each parallel is presented in Table 5-2, and the average predicted mass of FUR for each calibration curve is presented in Figure 5-9.



Signal: DAD1B,Sig=278.0,10.0 Ref=370.0,100.0

RT [min]	Width [min]	Area	Height	Area%	Compound Concentration
14.001	3.5060	3744.7653	85.6511	7.6626	
18.578	2.9400	45126.2159	1183.3362	92.3374	450.672
Sum		48870.9812			

Figure 5-7: HPLC-report, parallel 1. The chromatogram and UV-vis spectrum are on the top and bottom, respectively.



Signal: DAD1B,Sig=278.0,10.0 Ref=370.0,100.0

RT [min]	Width [min]	Area	Height	Area%	Compound Concentration
14.025	3.4628	3724.6473	84.9277	7.7158	
18.631	2.5067	44548.4438	1176.1081	92.2842	444.839
Sum		48273.0911			

Figure 5-8: HPLC-report, parallel 2. The chromatogram and UV-vis spectrum are on the top and bottom, respectively.

The chromatographic peak areas from parallel 1 (45126) and parallel 2 (44548) were used to solve the linear equation for the calibration curve in Figure 5-2 for y , which yielded the predicted FUR concentration in the procedural blank for both parallels using HPLC (Table 5-2). The average predicted yields for each quantitative technique relative to the actual mass of FUR added to the procedural blank are presented in Figure 5-9.

Table 5-2: Predicted FUR yields from the procedural blank using HPLC-UV, GC-MS and qNMR as quantification tools.

Quantitative technique	$m_{FUR, predicted}$ [g]	Deviation (Actual vs. predicted) [%]
Mass FUR added	0.0494	-
HPLC parallel 1	0.0530	
HPLC parallel 2	0.0523	
\bar{x}_{HPLC}	0.0526	6.5
NMR parallel 1	0.0487	
NMR parallel 2	0.0488	
\bar{x}_{NMR}	0.0474	-1.4
GC-MS cal. curve FUR/HD parallel 1	0.0356	
GC-MS cal. curve FUR/HD parallel 2	0.0373	
$\bar{x}_{calibration\ curve\ FUR/HD}$	0.0364	-26.3
GC-MS cal. curve FUR/CH Parallel 1	0.0525	
GC-MS cal. curve FUR/CH Parallel 2	0.0537	
$\bar{x}_{calibration\ curve\ FUR/CH}$	0.0531	7.5
GC-MS Area ratio FUR/HD parallel 1	0.0082	
GC-MS Area ratio FUR/HD parallel 2	0.0088	
$\bar{x}_{Ratio\ FUR/HD}$	0.0085	-82.8
GC-MS Area ratio FUR/CH parallel 1	0.0274	
GC-MS Area ratio FUR/CH parallel 2	0.0284	
$\bar{x}_{Ratio\ FUR/CH}$	0.0279	-43.5

*Only one sample was prepared for qNMR and HPLC analysis, i.e., the same sample was analyzed twice, denoted parallel 1 and 2, respectively. For qNMR, parallel 2 was analyzed ~12 hours after the first parallel to see whether the predicted FUR concentration changed as a function of time.

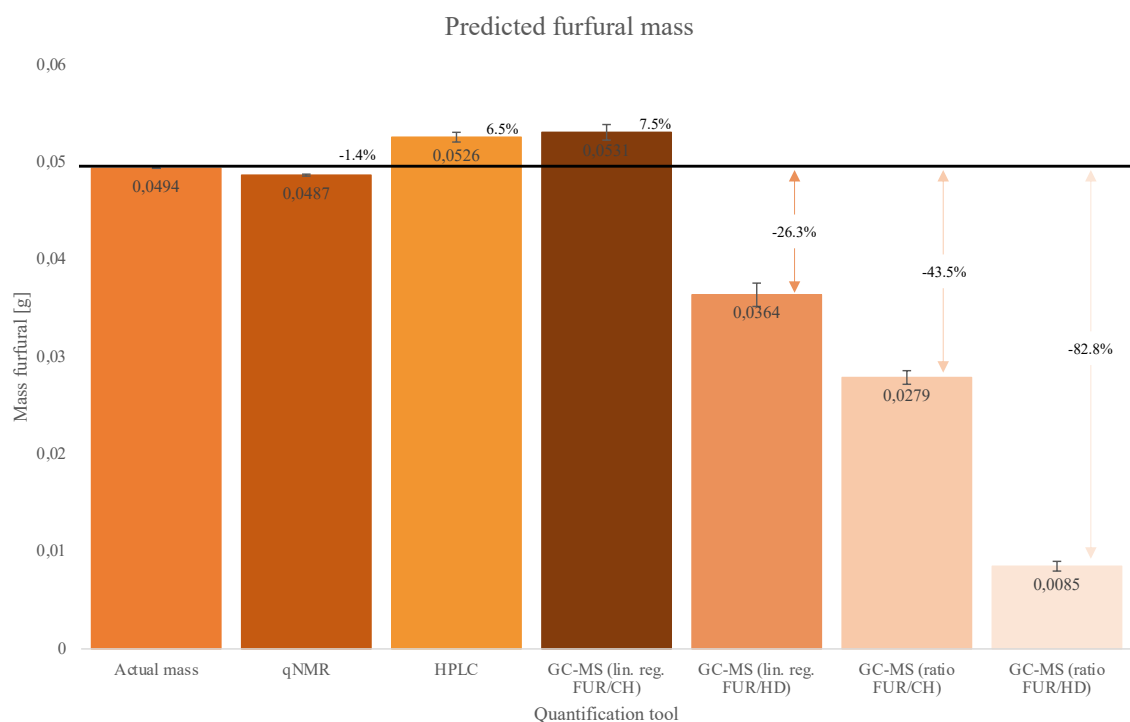


Figure 5-9: Graphical representation of the average predicted FUR yields in the procedural blank using different quantitative techniques. The black line indicates the amount of FUR added to the procedural blank before sample preparation (0.0494g). The percentage deviation (actual vs. predicted) is given above each column.

5.1.1 INTERPRETATION OF RESULTS FROM qNMR

As shown in Figure 5-9 and Table 5-2, qNMR was found to be the most reliable quantification tool of the three analytical modalities tested over the course of this thesis, both in terms of accuracy, i.e., predicted vs. actual FUR mass (-1.4%), and in terms of precision, i.e., the deviation between parallels (0.2%). These results verify that the qNMR workup protocol developed by Løhre et al. (Løhre et al., 2021) is a very reliable tool for accurate and precise quantification of aqueous samples.

A potential disadvantage associated with qNMR compared to HPLC and GC-MS is that samples often require pH adjustments prior to analysis, as pH could drastically influence the chemical shifts of specific protons, causing undesired signal overlap, and consequently, poor quantitative accuracy. Furthermore, the additional step of adjusting the pH to the desired level (typically 7.4) can, in some cases, be time-consuming, making it less desirable for samples containing reactive or unstable compounds like FUR and HMF, which will degrade over time when dissolved in aqueous media (Mellmer et al., 2014). However, the results from the structural elucidations of FUR (Figure A2-2), HMF (Figure A3-2), and XYL (Figure A1-3) in

Appendix A1 – A3 containing the stacked proton spectra of each compound at different pH, showed that pH had little effect on the chemical shifts of the signals associated with each compound, making pH-adjustment prior to analysis redundant.

5.1.2 INTERPRETATION OF RESULTS FROM HPLC

HPLC was the second-best quantification method tested in this thesis, with a calculated accuracy and precision of 6.5% and 1.3%, respectively. These results validate that HPLC can be considered a reliable quantification tool, which agrees with established literature (Miller, 2005). However, the HPLC instrument used in this thesis was equipped with a UV detector, which cannot be used for reliable detection of unreacted XYL, as monomeric sugars have limited UV-absorption due to the lack of chromophores that can efficiently absorb EMR (Debebe et al., 2018). Consequently, derivatization of carbohydrates is often required prior to analysis to ensure sufficient UV sensitivity. This meant that qNMR had to be combined with HPLC in order to quantify both FUR and XYL in both reaction phases accurately. Another disadvantage with HPLC is that it requires preparation of both MP, washing solutions, calibration curves, system purging, etc., before samples can be analyzed. Analysis time is also generally longer when compared to GC-MS and NMR, making it more work-intensive and time-consuming.

5.1.3 INTERPRETATION OF RESULTS FROM GC-MS

When considering GC-MS, the calibration curve for FUR/CH was more than three times as accurate when compared to the calibration curve for FUR/HD (7.5% vs. 26.3% deviation from the original mass of FUR added). The precision associated with the calibration curve for FUR/CH was also more than twice as good when compared to the calibration curve for FUR/HD (2.0% vs. 4.7%). However, when comparing these results with qNMR and HPLC, it becomes obvious that GC-MS cannot be considered a reliable quantification tool, which agrees with established literature (Miller, 2005).

The reason why two different internal standards (IS) were used in combination with FUR when constructing the calibration curves (Figure 5-1) was that the chromatographic peak area of FUR was found to be non-reproducible. It was speculated that this was caused by a varying degree

of evaporation at the injection port of the GC unit due to the low boiling point of the azeotrope formed between FUR and water (97.9°C). In addition, HD and CH had drastically different peak intensities even at similar concentrations (40 µg/mL and 45 µg/mL, respectively) as shown in Figure 5-5 and Figure 5-6. Hence, the predicted concentration of FUR was found to be highly dependent on which IS was used for the quantification (Figure 5-9). However, as can be seen from Figure F-1 in Appendix F, a repeating pattern regarding relative peak intensity between the three compounds can be seen. Consequently, relative peak areas between FUR/IS were used when constructing the calibration curves for GC-MS in this thesis. These results suggest that careful assessment of compounds' physical and chemical properties should be conducted before they are used as IS to make calibration curves, as compound-specific response factors could drastically influence the predicted yield. This claim is supported by the significant quantitative discrepancies between HD and CH used as IS in this thesis, as CH consistently predicted yields significantly higher compared to HD, both when using calibration curves and relative peak areas (Figure 5-9, and Figure F1-2 in Appendix F). In addition, GC-MS could not be used to analyze aqueous samples as water is too polar for the GC column. Liquid-liquid extraction of XYL from the aqueous phase using an organic solvent was also not possible due to the limited solubility of monomeric carbohydrates in most low-boiling organic solvents. Consequently, GC-MS had to be combined with qNMR in order to quantify unreacted XYL and any remaining FUR dissolved in the aqueous phase.

To summarize, the results discussed in this chapter have demonstrated the importance of comparing different quantitative methods in order to establish reliable procedures for accurate and precise quantification of both organic and aqueous samples before time-consuming experimental designs are initiated. Hence, based on the findings presented above, qNMR using the procedure developed by Løhre et al. (Løhre et al., 2021), was chosen as the preferred analytical procedure for this thesis, as it enabled fast and easy sample preparation while providing the best results in terms of quantitative accuracy and precision of both reaction phases.

5.1.4 ¹H-QNMR vs. ¹³C-QNMR

A comparison between ¹H-NMR relative to ¹³C-NMR was performed by preparing two standards containing a known concentration of XYL (~101.9mM) and DMSO₂ (~101.2mM). This was done to assess the quantitative accuracy and precision of ¹H-NMR relative to ¹³C-

NMR. Pros and cons associated with each technique are listed in Table 4-1. Quantitative proton and carbon spectra containing relative integrals for each peak are presented in Figure 5-10 – Figure 5-13. The results are also tabulated in Table 5-3 and Table 5-4.

5.1.4.1 ^1H -QNMR

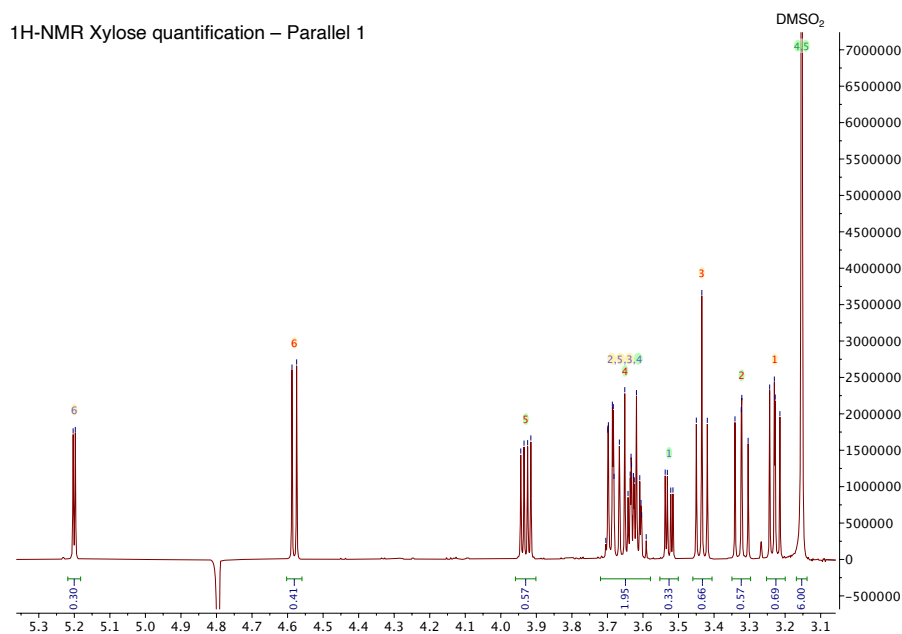


Figure 5-10: ^1H -NMR spectrum (parallel 1) used for XYL quantification. Red and blue numbers are protons associated with the β and α anomer, respectively.

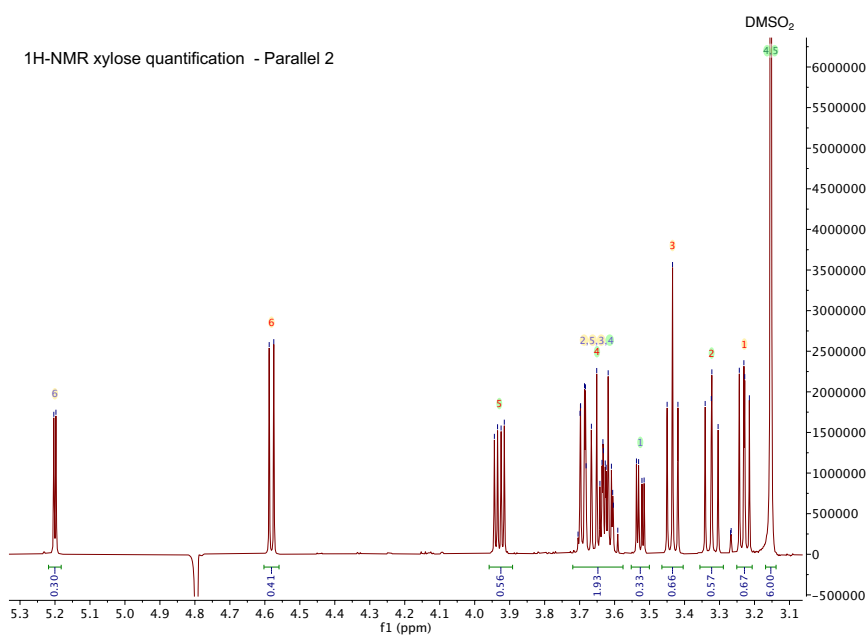


Figure 5-11: ^1H -NMR spectrum (parallel 2) used for XYL quantification.

To enable accurate quantification of XYL, an extensive structural elucidation had to be performed as XYL forms two structural pyranose anomers in aqueous solutions, termed α - and β -D-XYL. Therefore, both coupling constants and relative peak intensities had to be used to differentiate between analogous peaks in the two anomers. As described in chapter 4.1.2.1, the size of the coupling constants is affected by the dihedral torsion angles between protons. For example, the $^3J_{\text{HH}}$ -coupling between proton 1 and 6 (Figure A1-2, Appendix A1) will be $\sim 3.70\text{Hz}$ and $\sim 7.90\text{Hz}$ in the α - and β -anomer, respectively, due to the relative spatial orientation of the hydrogen atoms (Table A1-1). All coupling constants can be found in figure A1-8. When considering peak intensity, Schmidt and colleagues reported that the α -anomer was less stable than the β -anomer. In fact, they found that the relative percentage between the α - and β -anomer present in an aqueous solution after reaching anomeric equilibrium was 35% and 65%, respectively. Applying this knowledge to the $^1\text{H-NMR}$ spectra enables differentiation between the two anomers as the low-intensity peaks must belong to the α -anomer and vice versa (Schmidt et al., 1996). As can be seen in Table 5-3, the measured [XYL] for individual peaks reflects the relative abundance of each anomer. Hence, to obtain the total [XYL] in a sample, the predicted concentration of both α - and β -D-XYL must be added together. This also describes why the measured [XYL] using single peaks in Table 5-3 do not represent the actual [XYL] in the sample (101.9mM). The same logic can also be applied when differentiating between the two anomers in the ^{13}C -spectra. The complete structural elucidation for XYL can be found in Appendix A1.

Table 5-3: Predicted concentrations of XYL using $^1\text{H-qNMR}$. The actual concentration of XYL was $\sim 101.9\text{ mM}$.

Compound	Proton #	Parallel 1				Parallel 2			
		ppm	protons	integral	Concentration [mM]	ppm	protons	integral	Concentration [mM]
DMSO ₂	-	3.15	6	6.00	100.4	3.15	6	6.00	101.2
β -D-xylose	1	3.23	1	0.69	69.3	3.24	1	0.67	67.8
β -D-xylose	2	3.32	1	0.57	57.2	3.32	1	0.57	57.7
β -D-xylose	3	3.43	1	0.66	66.3	3.43	1	0.66	66.8
α -D-xylose	1	3.53	1	0.33	33.1	3.53	1	0.33	33.4
α -D-xylose	2, 3, 4, 4, 5	3.65	5	1.95	39.2	3.65	5	1.93	39.1
β -D-xylose	5	3.93	1	0.57	57.2	3.93	1	0.56	56.7
β -D-xylose	6	4.58	1	0.41	41.2	4.58	1	0.41	41.5
α -D-xylose	6	5.20	1	0.30	30.1	5.20	1	0.30	30.4
α -D-xylose	6*	5.20	1	0.30	102.4*	5.20	1	0.30	101.1*

*Predicted total concentration of XYL using the mathematical relation given below.

As can be seen from Table 5-3, different protons attached to the same anomer predicted slightly different concentrations of XYL due to different integration values. This is especially noticeable for proton 6, which has a reduced signal intensity due to its close proximity to the suppressed water signal ($\sim 4.8\text{ppm}$). This clearly demonstrates the dynamic range problem associated with $^1\text{H-NMR}$, that is, reduced quantitative accuracy of weak signals positioned adjacent to strong solvent peaks. The dynamic range phenomenon is especially problematic when working with aqueous solutions (Davies et al., 1985). Consequently, both peak intensity, chemical shift, and the predisposition for potential overlap for each peak were carefully evaluated to maximize the quantitative accuracy for both anomers. The peaks located at 3.53 ppm and 3.23 ppm in Figure 5-10 and Figure 5-11 (proton 1 for both α - and β -D-XYL) was found to be the best peaks for quantifying α -D-XYL and β -D-XYL, respectively, given no overlapping peaks from other compounds in the spectrum. To obtain the total [XYL] in a given sample, the predicted concentration of both α - and β -D-XYL must be added together. When doing so, the predicted [FUR] using the two peaks located at 3.23ppm and 3.53ppm was 102.4mM for parallel 1, and 101.2mM for parallel 2, which deviates with +0.5% and -0.7% from the true [XYL].

The results also showed that it was possible to quantify the concentration of XYL by only using the peak for α -D-XYL located at 5.20ppm. This was found to be of particular value for spectra that suffers from significant overlap from other compounds in the region below 4.00ppm. From Table 5-3 it is possible to see that the predicted [XYL] using the peak located at 5.20ppm is approximately ~ 3.3 times smaller than the total concentration predicted by the previously discussed peaks. By taking this into consideration, it is possible to formulate a mathematical relation (Eq. 4) that enables accurate quantification of XYL in aqueous samples:

$$C_{xylose} = \frac{I(5,20\text{ ppm}) \times F}{\frac{I(DMSO_2)}{n_{protons}}} \times C_{DMSO_2} \quad (\text{Eq. 4})$$

Where C is the predicted [XYL], I is the integration value of proton 6, and n is the number of protons in DMSO_2 . F is the multiplication factor (~ 3.3) found by summing the integration values for the peaks located at 3.23ppm and 3.53ppm. The acquired sum is subsequently divided by the integration value of proton 6, located at 5.20ppm, which yields the multiplication factor, F , given above (3.3). When applying Eq 4.0 to predict the total [XYL], the predicted concentration for parallel 1 and 2 becomes 102.4mM and 101.1mM, respectively, which is

+0.5% and -0.8% from the actual [XYL], further verifying the high accuracy and precision of ^1H -qNMR, as previously discussed.

5.1.4.2 ^{13}C -QNMR

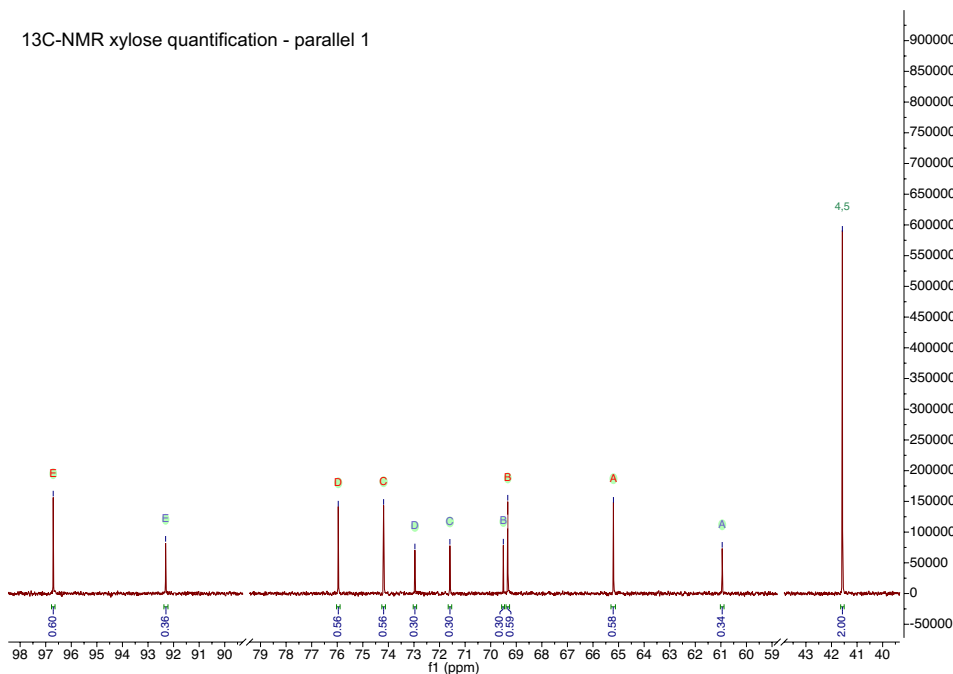


Figure 5-12: ^{13}C -NMR spectra (parallel 1) used for XYL quantification. Red and blue letters are carbons associated with the β and α anomer, respectively.

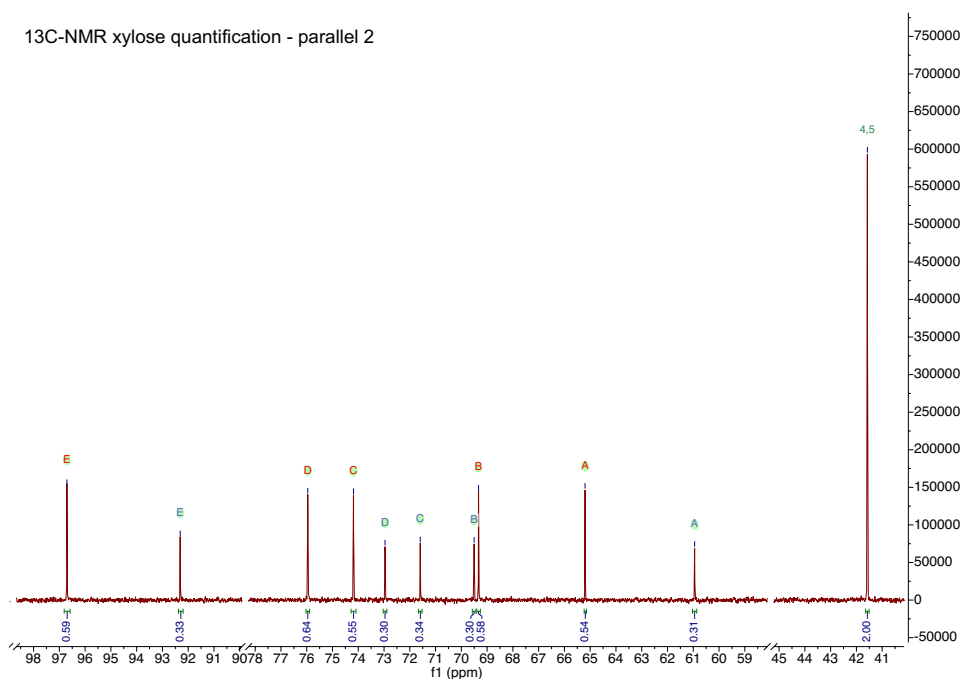


Figure 5-13: ^{13}C -NMR spectra (parallel 2) used for XYL quantification.

Table 5-4: predicted concentrations of XYL using ^{13}C -qNMR. The actual concentration of XYL was ~ 101.9 mM.

Compound	Carbon #	Parallel 1				Parallel 2			
		ppm	carbons	integral	Concentration [mM]	ppm	protons	integral	Concentration [mM]
DMSO ₂	-	41.57	2	2.00	100.4	41.57	2	2.00	101.2
α -D-xylose	A	60.95	1	0.34	34.1	60.95	1	0.31	31.4
β -D-xylose	A	65.20	1	0.58	58.2	65.20	1	0.54	54.6
β -D-xylose	B	69.33	1	0.59	59.2	69.33	1	0.58	58.7
α -D-xylose	B	69.51	1	0.31	31.1	69.51	1	0.30	30.4
α -D-xylose	C	71.60	1	0.30	30.1	71.60	1	0.34	34.4
α -D-xylose	D	72.96	1	0.30	30.1	72.96	1	0.30	30.4
β -D-xylose	C	74.19	1	0.56	56.2	74.19	1	0.55	55.6
β -D-xylose	D	75.96	1	0.56	56.2	75.96	1	0.64	64.8
α -D-xylose	E	92.31	1	0.36	36.1	92.31	1	0.33	33.4
β -D-xylose	E	96.71	1	0.60	60.2	96.71	1	0.59	59.7

From Table 5-4, it is possible to see that carbon NMR generally predicted lower concentrations of XYL compared to proton NMR, which was speculated to be caused by the lower sensitivity associated with ^{13}C -NMR relative to ^1H -NMR. The most accurate result for ^{13}C -NMR was acquired when adding the predicted [XYL] from carbon E in both anomers, yielding a total [XYL] of 96.3mM for parallel 1, and 93.1mM for parallel 2. This equates to -5.4% and -8.7% below the actual [XYL] present in the sample. These results also make sense from a technical perspective, as the NEO-600 spectrometer used during sample acquisition has the ^1H coil situated closest to the sample, meaning that the spectrometer will have increased sensitivity to ^1H -NMR relative to the ^{13}C coil positioned outside of the ^1H coil, making ^1H -NMR a seemingly better quantification tool compared to ^{13}C -NMR.

In summary, ^1H -qNMR was the most reliable and least time-consuming quantitative technique tested and will therefore be used as the preferred quantification method in this thesis.

5.2 REACTION SYSTEM SELECTION

Selecting a reaction system that fulfilled the desired physical and chemical specifications of this thesis, that is, efficient production of FUR using environmentally friendly solvents and catalysts, required a systematic, literature-based approach applying the principles of green chemistry as guidelines. Only variables reported to have a significant impact on FUR production were considered to simplify the selection process. Variables that have been meticulously tested and proven to have an impact on FUR production include:

- Type of substrate and substrate loading
- Use of one or two solvents
- Organic/aqueous ratio
- Type of catalyst and catalyst concentration
- Addition of phase modifiers
- Reaction temperature
- Residence time

The use of modifiers to promote phase separation was excluded from the selection process due to the obvious EHS-related concerns associated with the excessive use of inorganic salts.

5.2.1 SOLVENT SELECTION

Based on literature findings (Table 2-2 and Table 2-1), a biphasic reaction system was chosen as the preferred system for this thesis as it is reported to drastically improve reaction kinetics and product stability compared to monophasic reaction systems (Weingarten et al., 2010b). However, several objectives had to be met when selecting promising organic solvents for this thesis, as physical and chemical solvent properties can influence the desired product yield (Bollar et al., 2018, McBride et al., 2020, Lin et al., 2020). Furthermore, the increasing global environmental awareness in combination with the introduction of new statutory regulations and focus on green chemistry has made EHS criteria increasingly important during the selection process. Consequently, when evaluating the solvents listed in Table 2-1 and Table 2-2 for the production of FUR and HMF, GVL and MIBK were selected for preliminary testing as both

are considered green solvents with promising physicochemical properties, which adhere to the logic of this thesis.

Table 5-5 contains potential pros and cons for both solvents.

Table 5-5: Pros and cons of GVL and MIBK.

Solvent	Pros	Cons
GVL	<ul style="list-style-type: none"> - Green solvent (can produced from FUR and HMF) - Biodegradable - Low toxicity - Does not form an azeotrope with water - Does not form harmful peroxides in the air - Can be used as fuel additive - Lowers activation energy of XYL dehydration - Increases activation energy for FUR degradation - Precursor for food additives, biopolymers and advanced biofuels 	<ul style="list-style-type: none"> - High boiling point (207 – 208°C) causes trouble during work-up and analysis - High water miscibility - Expensive (~1200NOK/kg) - Phase modifier required to form biphasic reaction system
MIBK	<ul style="list-style-type: none"> - Considered a green solvent (can be produced from LCB via acetone) - Low toxicity to aquatic ecosystems (Chemicals, 2012) - Biodegradable and has low potential for bioaccumulation - Almost completely immiscible in water (0.28 wt% at 25°C) → does not require phase modifier - Better extraction properties than other frequently used organic solvents for FUR/HMF production - Low boiling point (117 – 118°C) - Can be used in combination with FUR to produce renewable jet fuels (Pholjaroen et al., 2014, Huber et al., 2005) - Less expensive than GVL (~750NOK/L) 	<ul style="list-style-type: none"> - Highly flammable - Terrestrial contaminant - Can participate in smog formation

GVL was the first solvent to be tested due to its superior physicochemical properties

Table 5-5, Table E-4, Appendix E) combined with the fact that it can be produced directly from both FUR and HMF. However, experimental results from using GVL showed that none of the catalysts chosen for this thesis (*vide infra*) achieved phase separation without saturating the aqueous phase with inorganic salts, which has several EHS-related drawbacks associated with downstream separation and waste handling. Thus, GVL did not fulfill the outlined system requirements for this thesis. These findings did not correspond to the results obtained by Yang et al., which claimed that phase separation between water and GVL was observed quickly after the addition of $Al_2(SO_4)_3$ (Yang et al., 2017), which was one of the tested catalysts. In addition, preliminary experimental results showed that analysis of organic phases using GVL as the extraction solvent was problematic due to its high boiling point (207 – 208°C) and water-

miscibility, making sample preparation and quantification problematic and work-intensive. Hence, water-immiscible MIBK was eventually chosen as the preferred solvent for the liquid-liquid extraction of FUR and HMF as it met the outlined system requirements without using phase modifiers. In addition, its excellent physicochemical properties and good EHS characteristics (

Table 5-5, Table D-3) enabled easy and safe phase separation and subsequent analysis of both organic and aqueous samples.

5.2.2 CATALYST SELECTION

During the catalyst selection process, six different homogenous acid catalysts were considered. A combination of well-established and relatively unexplored catalysts for FUR production were picked for the initial screening using the MIBK/H₂O biphasic solvent system. The selection was based on reported catalytic efficiency from the literature and the chemical properties of the acidic species. Sulfuric acid (H₂SO₄) and hydrochloric acid (HCl) were used as reference catalysts to better understand the catalytic efficiency of the less explored catalysts tested in this screening, as both HCl and H₂SO₄ have been used to produce FUR on an industrial scale for several decades. The other catalysts tested in this thesis included aluminum sulfate (Al₂(SO₄)₃), sulfamic acid (NH₂SO₃H), 2,5-furandicarboxylic acid (FDCA), and formic acid (HCOOH). All catalysts were tested using the same reaction conditions: XYL (0.15 g), H₂O (1.50 g), MIBK (3.00 g), 0.1M catalyst relative to aqueous phase, 190°C, 60min. The reaction parameters were selected based on optimal reaction conditions reported by other authors (Table 2-1 and Table 2-2). The obtained mass of FUR for each catalyst is presented in Table 5-6 and Figure 5-14. Pictures of the product solutions before and after phase separation can also be found in Figure 5-15 and Figure 5-16, respectively.

Table 5-6: Catalytic performance of six different acid catalysts analyzed by GC-MS.

#	Catalyst	XYL added [g]	FUR added [g]	Y_{FUR} (HD) [g]	Y_{FUR} (CH) [g]	$Y_{\text{Theoretical}}$ (g)	Deviation (m_{calc} vs. $m_{\text{theoretical}}$) (HD) [%]	Deviation (m_{calc} vs. $m_{\text{theoretical}}$) (CH) [%]
1	HCl ^a	0.1524	0.039	0.1045	0.1260	0.1014	3.1	24.3
2	H ₂ SO ₄ ^b	0.1519	~0.050 ^g	0.1071	0.1309	0.1122	-4.5	16.7
3	H ₃ NSO ₃ ^c	0.1547	~0.050 ^g	0.0820	0.0990	0.1134	-27.7	-12.7
4	FDCA ^d	0.1491	0.040	0.0609	0.0749	0.1013	-39.9	-26.1
5	Al ₂ (SO ₄) ₃ ^e	0.1495	~0.050 ^g	0.0937	0.1260	0.1112	-15.7	13.3
6	HCOOH ^f	0.1515	0.047	0.0502	0.0653	0.1086	-53.8	-39.9
7	No catalyst	0.1498	0.041	0.0463	0.0677	0.1018	-54.5	-33.5

^aHydrochloric acid, ^bsulfuric acid, ^csulfamic acid, ^d2,5-furandicarboxylic acid, ^ealuminum sulfate, ^fformic acid, ^gMass based on added volume (43.1 μ L)

This experimental series was conducted before it was discovered that the workup protocol developed by Løhre et al. could be used as a reliable quantification tool for both reaction phases by extracting the FUR dissolved in the organic phase with water prior to sample preparation (Chapter 4.2.6.2). Consequently, organic samples were analyzed using GC-MS in combination with the calibration curves in Figure 5-1. Quantification of FUR in the aqueous samples was done using ¹H-qNMR as described by (Løhre et al., 2021). Based on the results discussed in chapter 5.1, the predicted mass of FUR generated in each experiment does not represent realistic yields as GC-MS was found to be very unreliable for accurate quantification of FUR. As a result, the calculated FUR yields were only used to compare the relative catalytic performance of the different catalysts to determine the most promising candidate for further testing. The theoretical yields given in Table 5-6 were calculated by summing the maximum amount of FUR obtainable from the amount of XYL added with the total amount of FUR added prior to heating (see chapter 4.3.8). A description of how the maximum theoretical yield of FUR can be calculated from both XYL and hemicellulose is given in Appendix I.

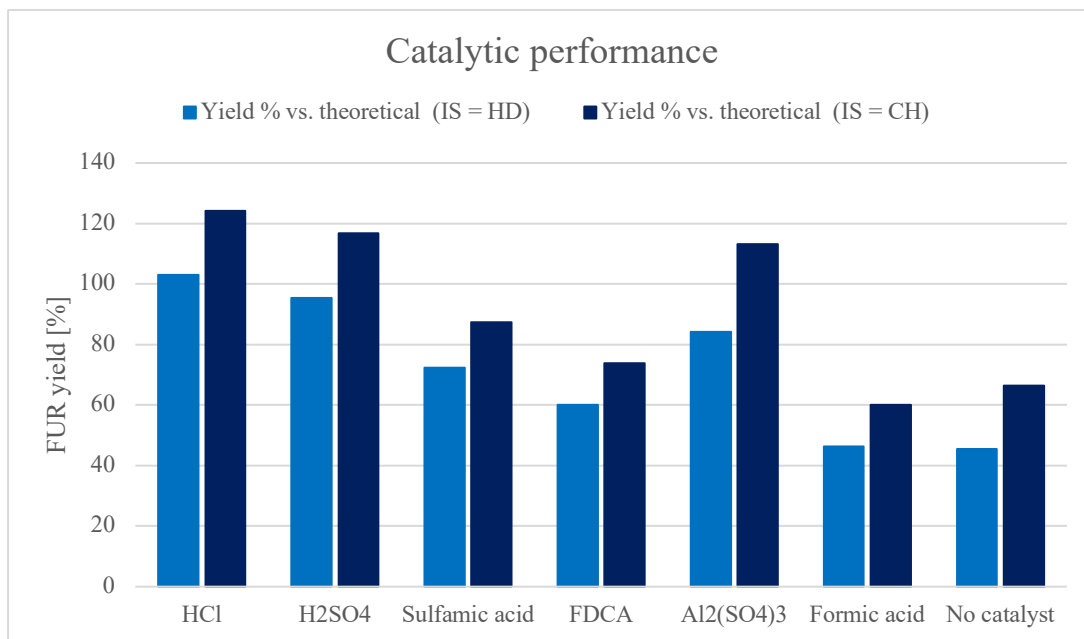


Figure 5-14: Calculated FUR yields for each catalyst, including a blank (autocatalyzed) where no catalyst was added.

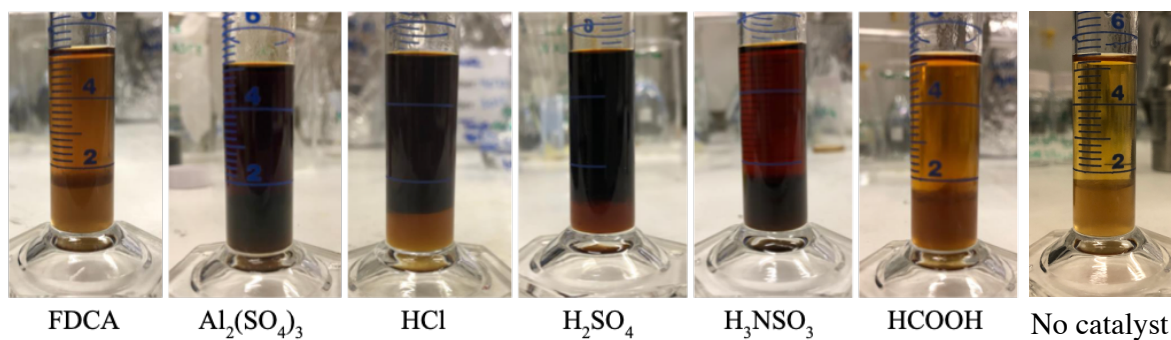


Figure 5-15: Product solutions from the seven experiments testing different catalysts prior to phase separation. The upper phase is organic while the lower phase is aqueous.

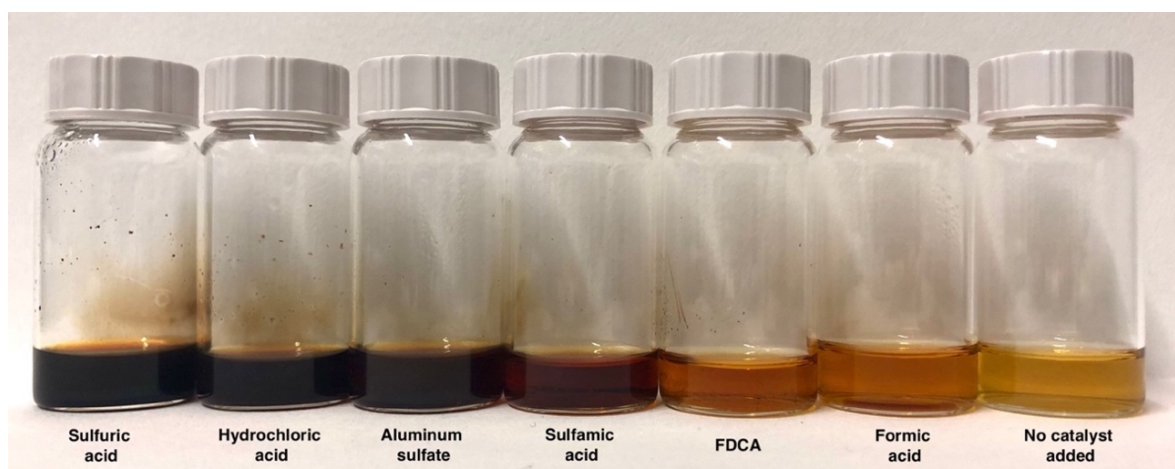


Figure 5-16: Organic samples after phase separation for the experiments employing different catalysts.

When comparing the calculated yields in Table 5-6 with the color saturation of the product solutions in Figure 5-15 and Figure 5-16, a clear positive correlation can be observed, i.e., the darker the sample, the higher the calculated FUR yield. HCl and H₂SO₄, which are both highly potent Brønsted acids, produced the highest yields of all the experiments (Table 5-6, entry 1 and 2, respectively). These results concur with literature findings that claim that BA are thought to be the most efficient at promoting the triple dehydration step that ultimately leads to formation of FUR (Vilonen et al., 2011). This also explains why both HCl and H₂SO₄ have been widely used for large-scale production of FUR for several decades (Xing et al., 2011). However, both catalysts were excluded from further assessment in this thesis due to their obvious EHS-related drawbacks combined with the fact that both HCl and H₂SO₄ have been extensively tested in the literature by many different research groups (Weingarten et al., 2010a, Mittal et al., 2017, Xing et al., 2011, Guo et al., 2020).

Both Aluminum sulfate and sulfamic acid, catalysts reported to exhibit excellent bifunctional catalytic properties (Zhang et al., 2019, Yang et al., 2017, Delbecq et al., 2018), showed promising results when compared to HCl and H₂SO₄ (Table 5-6 entry 5 and 3, respectively). Aluminum sulfate was expected to produce yields comparable to H₂SO₄, as it forms SO₂ anions when dissolved in water, which coincide with the acquired results. However, for the experiment using aluminum sulfate, significant amounts of precipitates formed during the reaction, indicating the occurrence of unwanted side-reactions, making sulfamic acid a seemingly better candidate. The two remaining catalysts, FDCA and formic acid (FA), showed poor catalytic activity when compared to the other catalysts. Both FDCA and FA produced yields that were just slightly better than the yields obtained from the autocatalyzed system where no catalyst was added (Table 5-6, entry 4, 6, and 7, respectively).

To summarize, Sulfuric acid, hydrochloric acid, and aluminum sulfate produced the best FUR yields of all the catalysts tested in this thesis (Figure 5-14). However, due to the many drawbacks associated with these catalysts, sulfamic acid, a non-corrosive bifunctional organic catalyst, was chosen as the preferred catalyst for this thesis due to its excellent physicochemical properties and promising catalytic potential (Veera Swamy Konkala Pramod Kumar, 2017), combined with the fact that no previous studies using sulfamic acid in combination with MIBK were found in the literature.

5.2.3 SUBSTRATE SELECTION

D-Xylose (XYL) was chosen as the preferred substrate for preliminary experimental testing of the chosen reaction system (MIBK/H₂O catalyzed by sulfamic acid) as it is ideal for achieving high yields of FUR. XYL was also used as substrate during the experimental screening process using FFD. However, model compounds like XYL are not considered viable feedstocks for the large-scale production of furanic platform chemicals. Therefore, F&B residues, specifically plum and cherry rejects, were also used as feedstocks in order to outline their potential for producing FUR and HMF in large-scale biorefinery concepts. The results obtained from F&B rejects are presented and discussed in chapter 5.5.

5.3 EXPERIMENTAL DESIGNS

5.3.1 RESULTS FROM THE FIRST EXPERIMENTAL DESIGN

A 2^{5-1} fractional factorial design (FFD) was used during the screening process of the chosen biphasic reaction system. The five variables investigated were:

- Reaction temperature
- Residence time
- Organic/aqueous ratio
- Substrate loading
- Catalyst loading

High and low factor levels were selected based on reported values in the literature. The primary goal of the screening was to explore a broad experimental domain to better understand how each factor and factor interaction affected the measured responses, i.e., FUR yield (mol%), XYL conversion (mol%) and reaction selectivity (%). High and low factor levels for each variable for the experimental design (FFD1) is given in Table 5-7. The results are tabulated in Table 5-8, and graphically presented in Figure 5-17. Pictures of all product solutions prior to phase separation are also given in Figure 5-18. Raw data, including NMR spectra for FFD1 are presented in Appendix C.

Table 5-7: High, low, and CP values for the explored factors in FFD1.

Value	T (°C)	t (min)	Org/aq (V/V)	Substrate (g)	Catalyst (g)
-	150	30	1:4	0.125	0.0125
0	180	60	1:1	0.250	0.0250
+	210	90	4:1	0.375	0.0375

Table 5-8: Calculated FUR yield, XYL conversion, selectivity, and FUR partition for FFD1.

Exp #	FUR yield [mol%]	XYL conversion [mol%]	FUR Selectivity [%]	FUR partition (org/aq)
2	8.5	10.3	82.4	1.5
13	13.6	19.0	71.7	64.4
14	22.7	54.9	41.4	35.3
11	4.5	4.1	~100	1.6
CP1	21.3	48.0	44.4	6.6
7	27.6	52.4	52.6	54.3
21	0.8	~0.0	~0.0	1.8
16a	34.9	~100.0	34.9	51.3
12	36.0	78.6	45.8	1.3
16a	33.8	~100.0	33.8	53.2

Small amounts of formic acid were detected in all experiments, ranging between 0.00001 – 0.002g, depending on reaction conditions. For experiment 11 (Table 5-8), qNMR predicted that the number of moles of FUR generated exceeded the number of moles of XYL that had been converted. The selectivity of the reaction was therefore assumed to be close to 100%. However, the extremely low FUR yield and degree of XYL conversion makes the reaction conditions used in this experiment not relevant for further consideration.

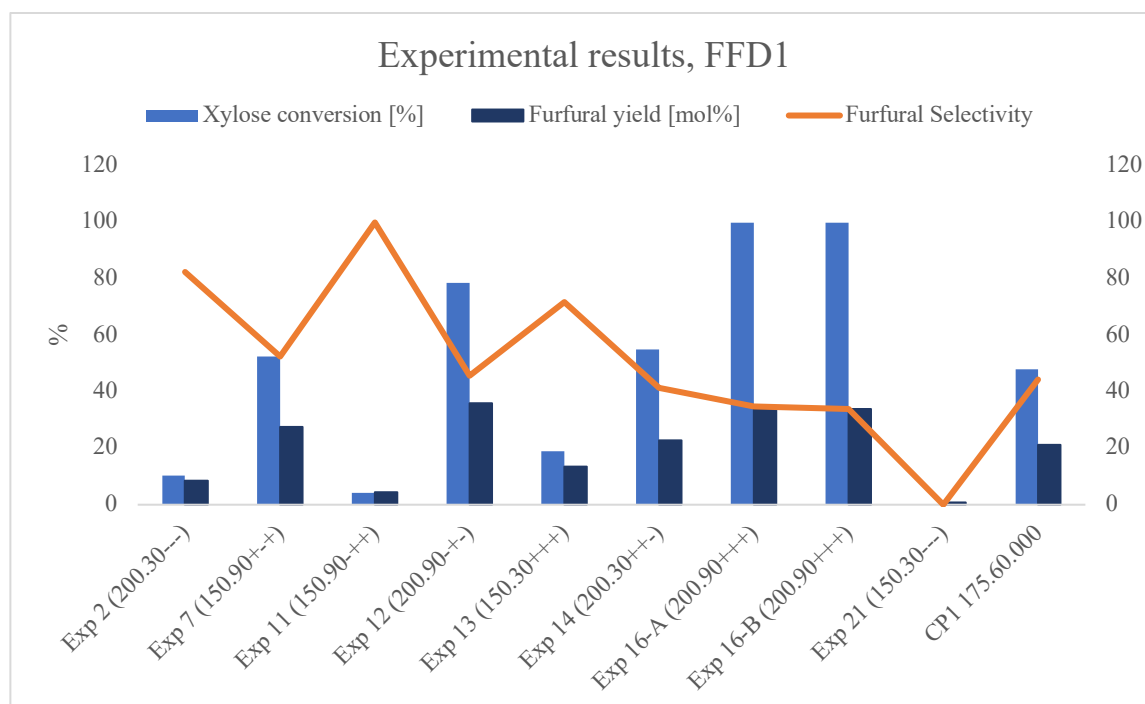


Figure 5-17: FUR yields, XYL conversion, and reaction selectivity for all experiments from FFD1.



Figure 5-18: Product solutions from FFD1. Reaction conditions for each experiment is listed under each picture ($T(^{\circ}\text{C}), t(\text{min}), \text{org}: \text{aq}(\text{vol}/\text{vol}), \text{substrate}(\text{g}), \text{catalyst}(\text{g})$).

It was hypothesized that the factor levels for catalyst loading (Table 5-7) was too high for FFD1 due to excessive formation of precipitates in most of the product solutions (Figure 5-18). Generation of precipitates in the product mixture is associated with undesirable by-product formation through various condensation, fragmentation, and polymerization reactions between FUR, unreacted XYL, and various intermediates, which can have adverse effects on the overall FUR yield (Lamminpaa et al., 2014). To evaluate whether this was the case, FFD1 was paused after ten experiments, and the effect of catalyst loading, more specifically, acid concentration and the associated pH was explored by conducting three center point experiments (CP) containing different amounts of sulfamic acid (Table 5-9). All variables except catalyst loading were kept at a CP levels (Table 5-7). The goal of the following study was to use the acquired responses to make a result-based decision regarding whether FFD1 should be commenced, or if a new FFD with reduced factor levels for catalyst loading should be conducted. Figure 5-19 gives a graphical representation of the calculated results. Pictures of product solutions with associated acid concentrations and pH values can be found in Figure 5-20.

Table 5-9: Calculated results for the three CP experiments with different catalyst loadings^a.

Exp #	Catalyst loading [g]	Concentration [mol/L]	pH	FUR yield [mol%]	XYL conversion [mol%]	Selectivity [%]
CP1	0.0066	0.027	1.59	4.6	8.7	53.3
CP2	0.0249	0.103	1.14	21.3	48.0	44.4
CP3	0.0383	0.158	0.98	33.9	68.0	49.8

^aReaction conditions: XYL (0.250g), distilled H₂O (2.50mL), MIBK (2.50mL), SA (0.025g), 175°C, 60min.

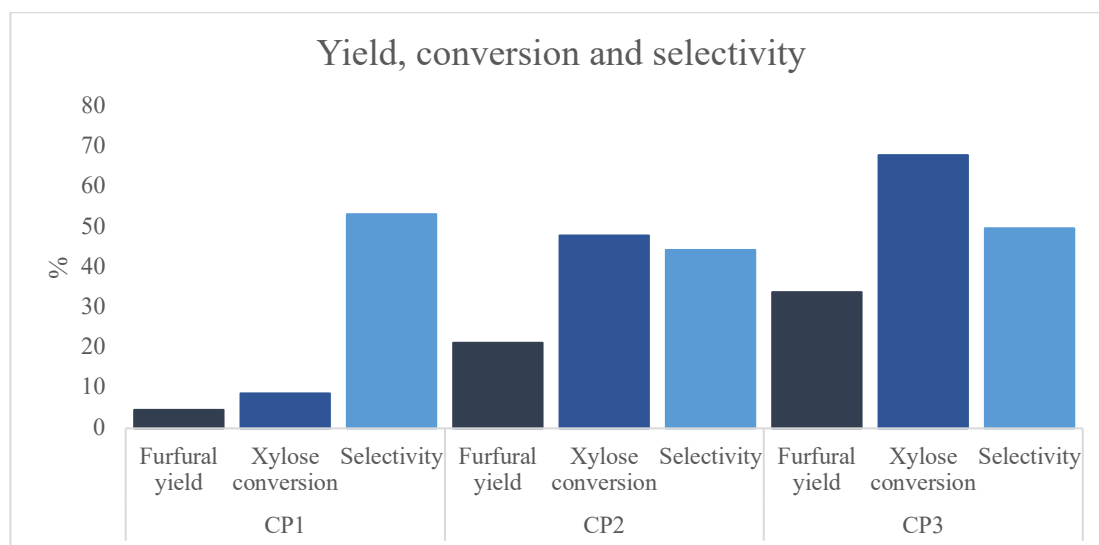


Figure 5-19: FUR yield, XYL conversion and reaction selectivity for the three CPs with different catalyst loadings.

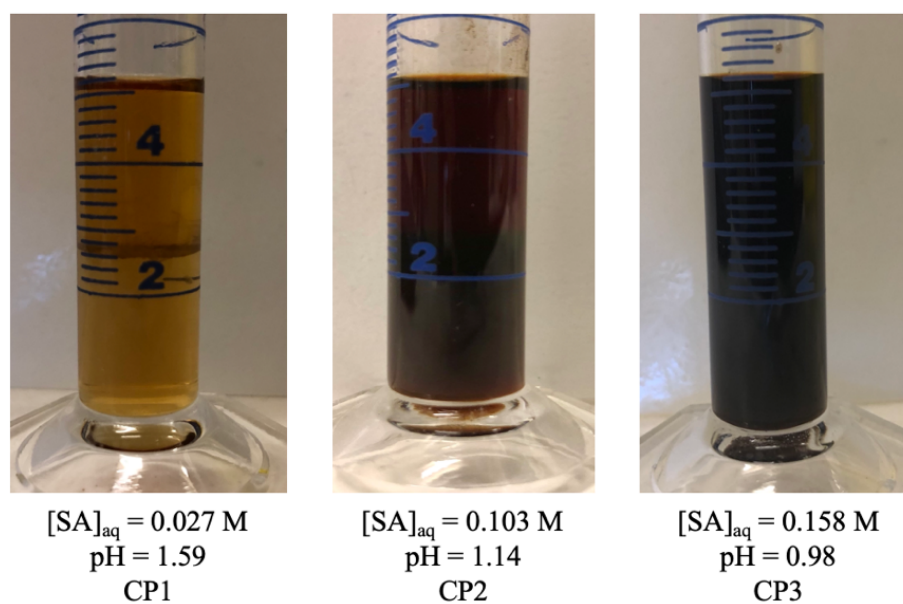


Figure 5-20: Product solutions prior to phase separation for the three CP experiments with different catalyst loadings.

When comparing the results presented in Figure 5-19 with the tabulated values for acid concentration in Table 5-9, a clear positive correlation between FUR yield, XYL conversion, and acidity can be observed. For CP1, which had the lowest acid concentration of the three experiments (0.027M), the degree of XYL conversion (8.7mol%) and FUR yield (4.6mol%) was significantly lower than the obtained yields and conversions for CP2 (21.3mol%, 48.0mol%) and CP3 (33.9mol%, 68.0mol%), which had considerably higher concentrations of sulfamic acid in the aqueous phase (0.103M for CP2 and 0.158M for CP3).

A less distinct trend was observed for selectivity. When the acid concentration was increased from 0.027M (CP1) to 0.103M (CP2), the selectivity dropped from 53.3% to 44.4%. However, when the acid concentration was further increased to 0.158M, the selectivity increased to 49.8%. A visual comparison of the product solutions in Figure 5-20 clearly shows that CP2 and CP3 generated considerable amounts of precipitates relative to CP1, which is a clear sign of concurrent by-product formation. These findings suggest that the acid concentration in the catalytically active aqueous phase should be within a specific range to promote effective dehydration of XYL to FUR while minimizing by-product formation, which is in accordance with literature findings (Xing et al., 2011). These outcomes could also suggest that FUR-associated degradation mechanisms are highly dependent on reaction conditions, i.e., specific mechanisms dominate at different settings. This assumption agrees with the findings done by Rasmussen et al., i.e., that reaction parameters like pH can drastically alter the properties of the aqueous reaction phase, which again can have a significant influence on the initial site of protonation, which is thought to be the determining step for the subsequent degradation pathway of XYL (Rasmussen et al., 2014). It could, for example, be speculated that 3-OH protonation (Scheme K-1, Appendix K) becomes more prevalent when the reaction severity increases, as it results in the formation of fragmentation products that can undergo subsequent polymerization reactions to form various by-products.

To summarize, even though CP3 generated the best results in terms of FUR yield and XYL conversion, significant amounts of precipitates were also observed in the product solution (Figure 5-20). Based on these findings, a new experimental design (FFD2) with reduced factor settings for catalyst loading was planned and conducted. The results from this experimental series are presented in the following chapter.

5.3.2 RESULTS FROM THE SECOND EXPERIMENTAL DESIGN

Based on experimental findings from the previous chapter, a new experimental design (FFD2) with reduced factor settings for catalyst loading was prepared. All other variables were kept at the same levels as for FFD1. This was done to investigate whether reduced acid concentrations in the catalytically active aqueous phase would result in less by-product formation in the form of precipitates while generating FUR yields comparable to FFD1. Decreasing the amount of catalyst added to each experiment would also help reduce the amounts of spent catalyst, improving both atom economy and the costs associated with the reaction system. Factor settings for the new design are listed in Table 5-10. The results presented in Table 5-11 will be analyzed using PCA (chapter 5.3.2.1) and PLS (chapter 5.3.2.2) to identify significant factors and factor interactions with regards to FUR yield, XYL conversion, and reaction selectivity towards FUR formation. Pictures of all product solutions can be found in Figure 5-21, and the results are graphically presented in Figure 5-22. Raw data for FFD2, including NMR spectra, can be found in Table B-1 in Appendix B.

Table 5-10: Second fractional factorial design (FFD2) with high, low, and CP values for each variable investigated.

Value	T (°C)	t (min)	Org/aq (V/V)	Sub (g)	Cat (g)
-	150	30	1:4	0.125	0.0063
0	180	60	1:1	0.250	0.0094
+	210	90	4:1	0.375	0.0125

Table 5-11: Experimental results for all experiments, including replicates, from FFD2 ordered in numerical order.

Exp #	FUR yield [mol%]	XYL conversion [mol%]	FUR selectivity [%]	FUR partition (org/aq)
1	0.7	-0.1	-	1.3
2a	7.7	10.8	71.2	1.5
2b	10.3	26.3	39.3	1.4
3	0.5	1.2	41.7	3.0
4	42.9	88.8	48.3	1.5
5	1.2	5.4	21.7	30.0
6a	37.8	81.1	46.6	22.2
6b	41.4	91.5	45.3	35.9
7	7.1	9.3	76.1	27.5
8	40.0	93.0	43.0	34.6
9	0.2	1.8	13.1	1.4
10	4.4	7.6	57.2	1.4
11	1.8	2.9	60.7	1.5
12a	18.0	18.3	98.0	1.5
12b	35.0	58.7	59.6	1.7
12c	31.4	63.2	49.7	1.8
13	2.5	11.1	22.9	29.5
14a	23.1	64.2	36.0	22.1
14b	19.0	46.4	40.9	29.4
15	3.4	12.4	27.6	40.0
16	41.7	100.0	41.7	37.5
CP1	3.1	6.2	49.4	7.2
CP2	7.3	11.9	61.0	6.3
CP3	5.1	8.6	59.9	6.5
CP4	8.2	18.1	45.4	7.8
CP5	10.7	28.8	37.2	7.1



Figure 5-21: Product solutions from FFD2. Reaction conditions used for each experiment is listed under each picture ($T(^{\circ}\text{C}), t(\text{min}), \text{Org:aq}(\text{vol/vol}), \text{substrate}(\text{g}), \text{catalyst}(\text{g})$).

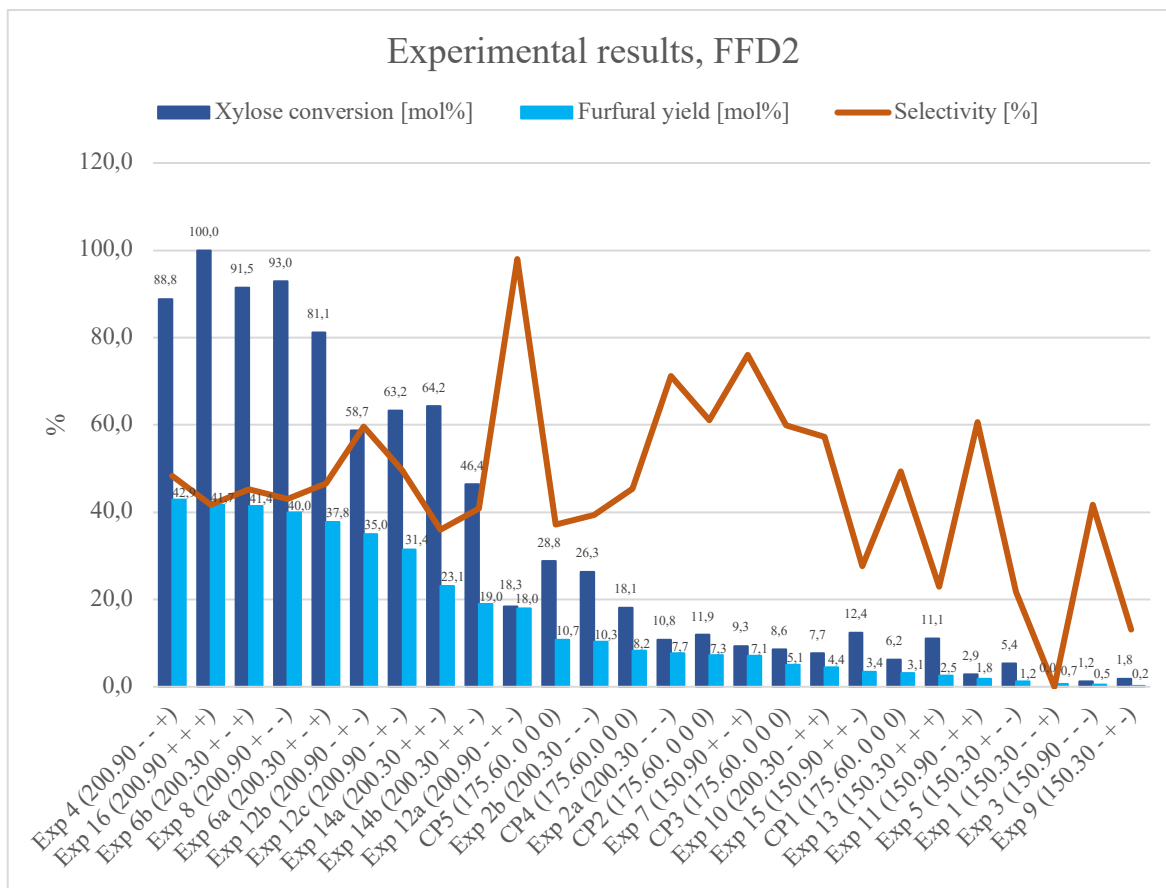


Figure 5-22: FUR yield, XYL conversion and reaction selectivity for all experiments including replicates from FFD2 ordered from best (left) to worst (right) in terms of FUR yield.

5.3.2.1 PRINCIPAL COMPONENT ANALYSIS

Principal component analysis (PCA) was conducted to elucidate how each variable and variable interaction correlated with the measured responses in FFD2, i.e., identify which factors had the biggest influence on FUR yield (mol%), XYL conversion (mol%), and reaction selectivity (%). The data from FFD2, i.e., raw data (Table B-1) and responses for each experiment (Table 5-11) were used to create the plots and graphs presented in the following section. The effect of each main factor, including experimental reproducibility, will be discussed in detail in chapters 5.3.2.3 – 5.3.2.6.

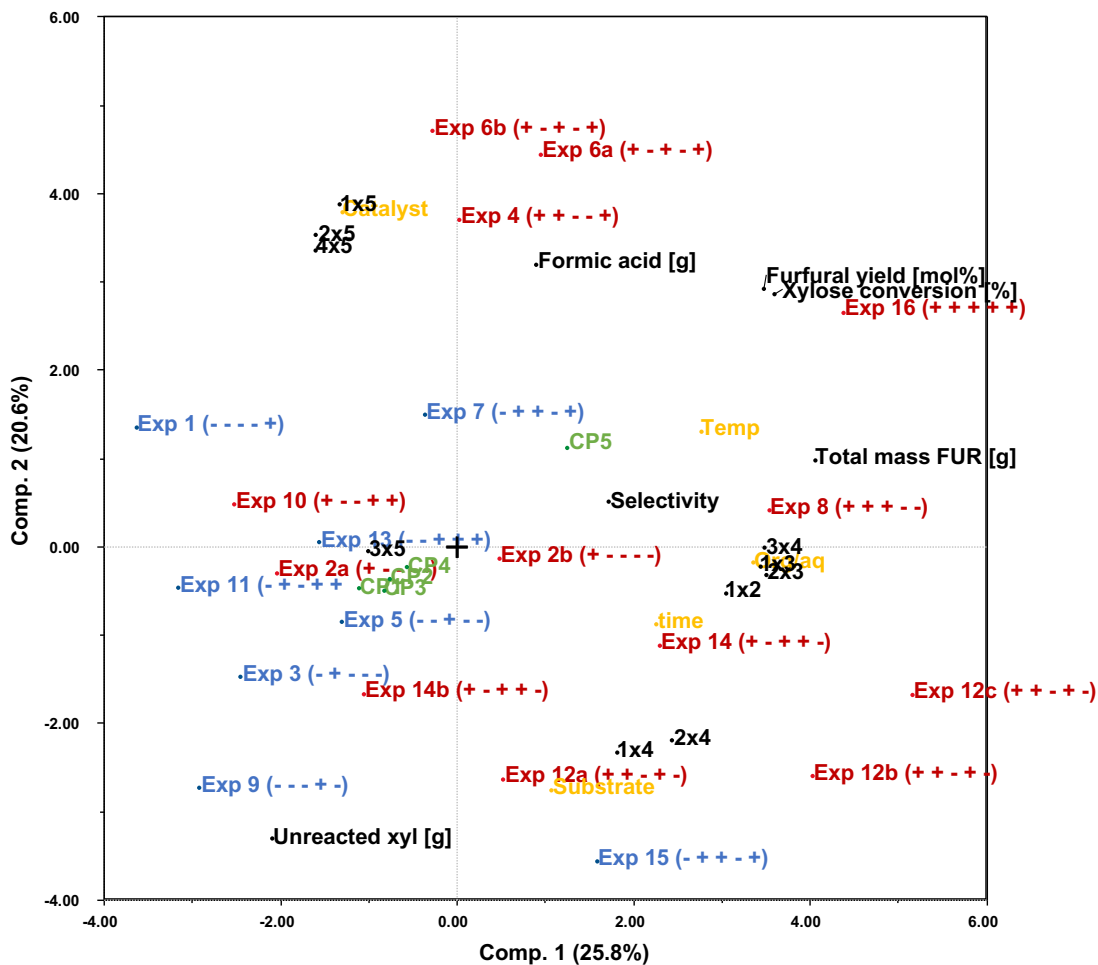


Figure 5-23: PCA biplot for all objects, main factors, two-factor interactions, and measured responses.

The biplot in Figure 5-23 shows how the different experiments, factors, and factor interactions correlate with the measured responses in the plane spanned by the first two principal components. Blue, green, and red objects are experiments conducted at 150°C, 175°C, and 200°C, respectively. The main factors are marked in yellow. The factor levels (Table 5-10) used in each experiment are given in brackets behind each object using the following code: (Temperature, time, org:aq, substrate, catalyst). When all objects, factors, factor interactions, and responses were included in the model, the total explained variance for the dataset was 46.4%, which is insufficient for creating an accurate prediction model using PLS. Consequently, a new biplot containing only the best replicates in terms of FUR yield was created to see whether this would give a better explanation of the dataset (Figure 5-24).

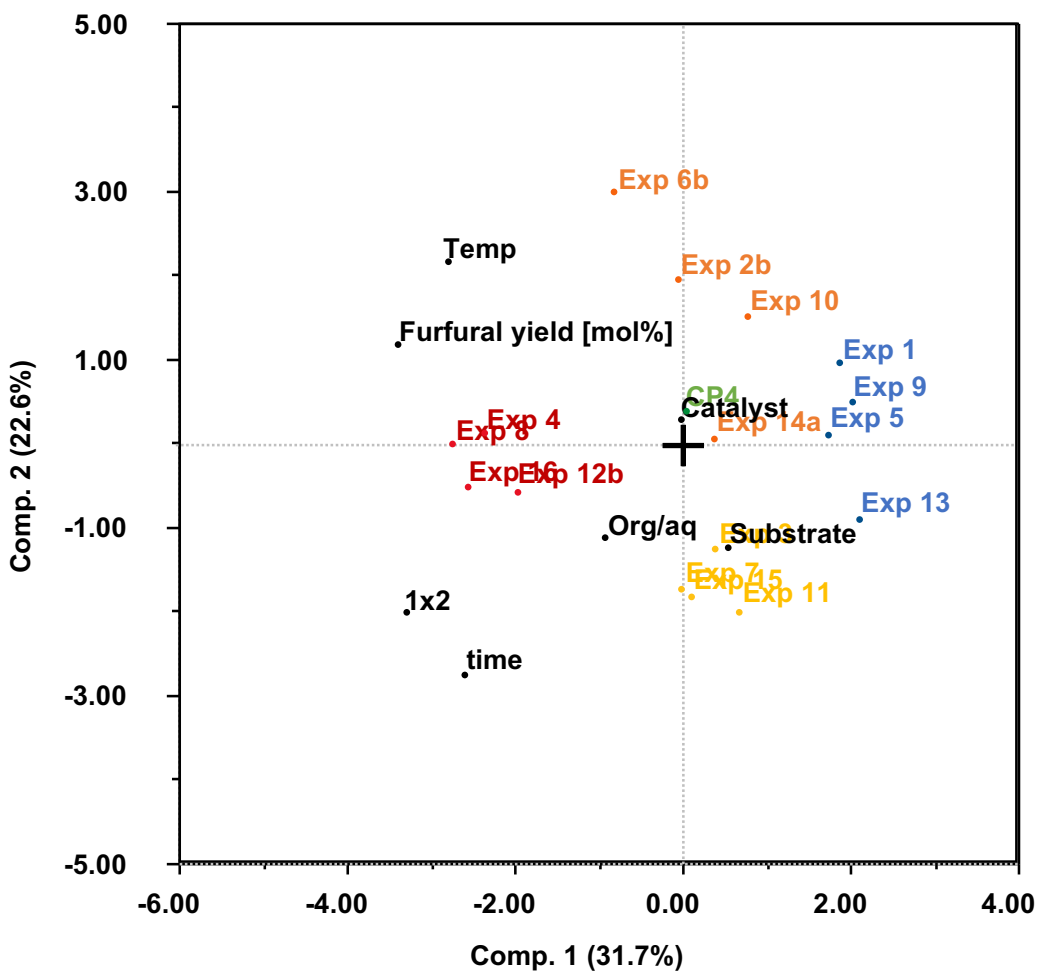


Figure 5-24: Biplot displaying the relative correlations between the best replicates, the five main predictors, and the measured response (FUR yield).

The total explained variance for PC1 and PC2 increased to 54.3% in Figure 5-24 when only the best replicates in terms of FUR yield and the five main factors were included in the PCA. This is still far from optimal for creating an accurate prediction model. However, this was the highest explained variance acquired for FFD2 without sacrificing experimental diversity, i.e., that all experimental variations, including CPs, were used in the PCA. Hence, these objects formed the basis when constructing the regression model using PLS in Figure 5-32.

From Figure 5-24 it is also possible to see four distinct groupings. The red and blue clusters separated along PC1 contains experiments conducted at 200°C for 90 minutes and 150°C for 30 minutes, respectively. The two groups separated along PC2 include experiments conducted at 150°C for 90 minutes (yellow) and experiments conducted at 200°C for 30 minutes (orange).

When comparing the position of these clusters with the loading vectors for the five main predictors and the measured response (FUR yield), it becomes evident that temperature and residence time were the two most important factors for PC1 and PC2, respectively. Temperature was also found to be the most important factor for achieving high FUR yields, whereas catalyst loading was found to be the least influential factor in FFD2. In addition, substrate loading was the only main factor that was found to be negatively correlated with FUR yield.

5.3.2.2 PARTIAL LEAST SQUARE REGRESSION

The goal of the PLS analysis was to formulate a mathematical expression that could be used to estimate the formation of FUR when employing the selected biphasic reaction system. In addition, PLS could also give valuable information on how to approach optimal reaction conditions for the most important variables in order to maximize FUR production. The results from the PLS analysis are presented in Figure 5-25– Figure 5-32 below.

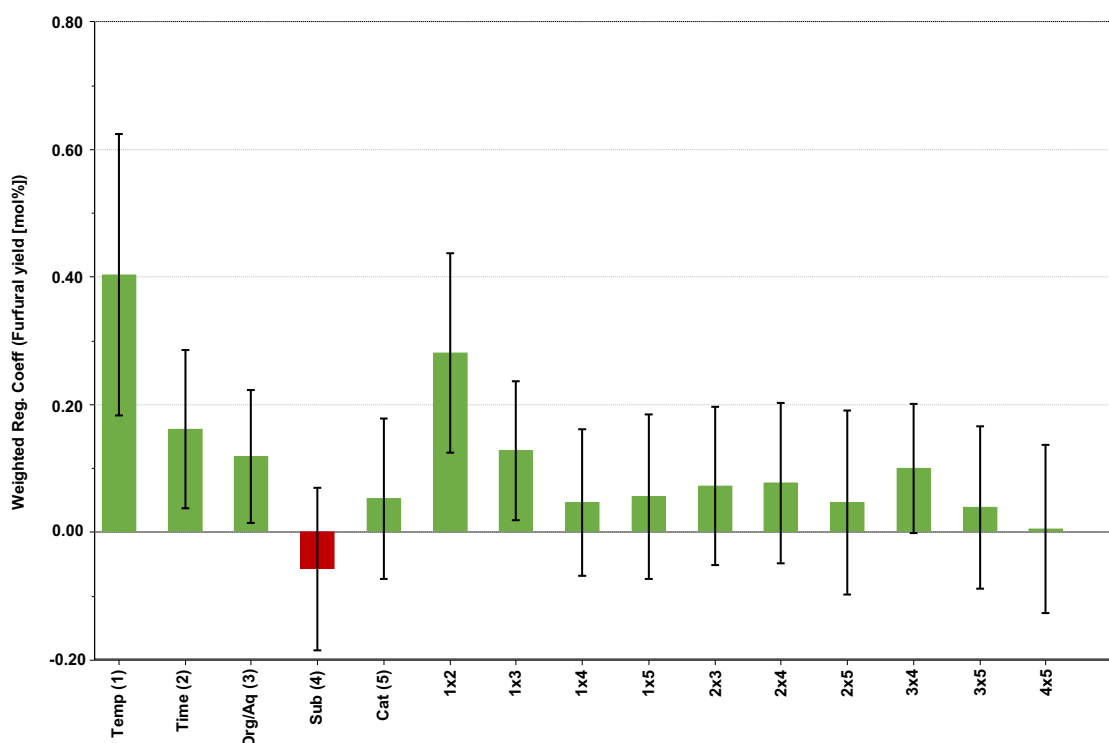


Figure 5-25: Weighted regression coefficients for main factors and two-factor interactions. The number behind each main factor corresponds to the number in each cross-term.

Figure 5-25 contains the weighted regression coefficients for all main factors and two-factor interactions. The plot confirms the trends observed in Figure 5-24, i.e., that temperature was the most important factor for achieving high FUR yields, followed by residence time. The figure also shows that the factor interaction between temperature and time (1 x 2) was the only two-factor interaction with a considerable impact on FUR yield. The importance of this factor interaction is further verified in Figure 5-26, as the two lines are nowhere near parallel, which means that the cross term between time and temperature has a profound effect on the formation of FUR.

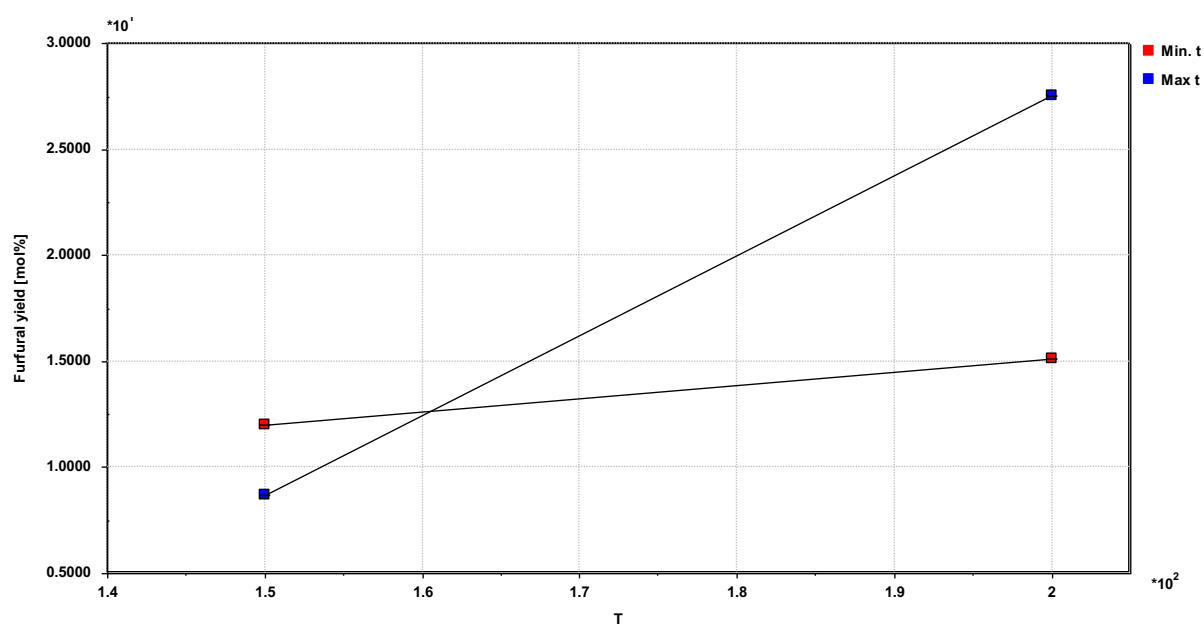


Figure 5-26: Observed trends with regards to FUR yields at different times and temperatures.

According to Figure 5-26, increasing the temperature from 150°C to 200°C had little effect on FUR yield for experiments conducted over 30 minutes, as can be seen from the gentle slope between the two red points in the graph. However, for experiments with residence times of 90 minutes, increasing the reaction temperature proved to have a significant effect on FUR yield, which can be seen from the steep slope between the two blue points. In other words, it appears that residence time only has a major influence on FUR yield when the reaction temperature is above a certain setting.

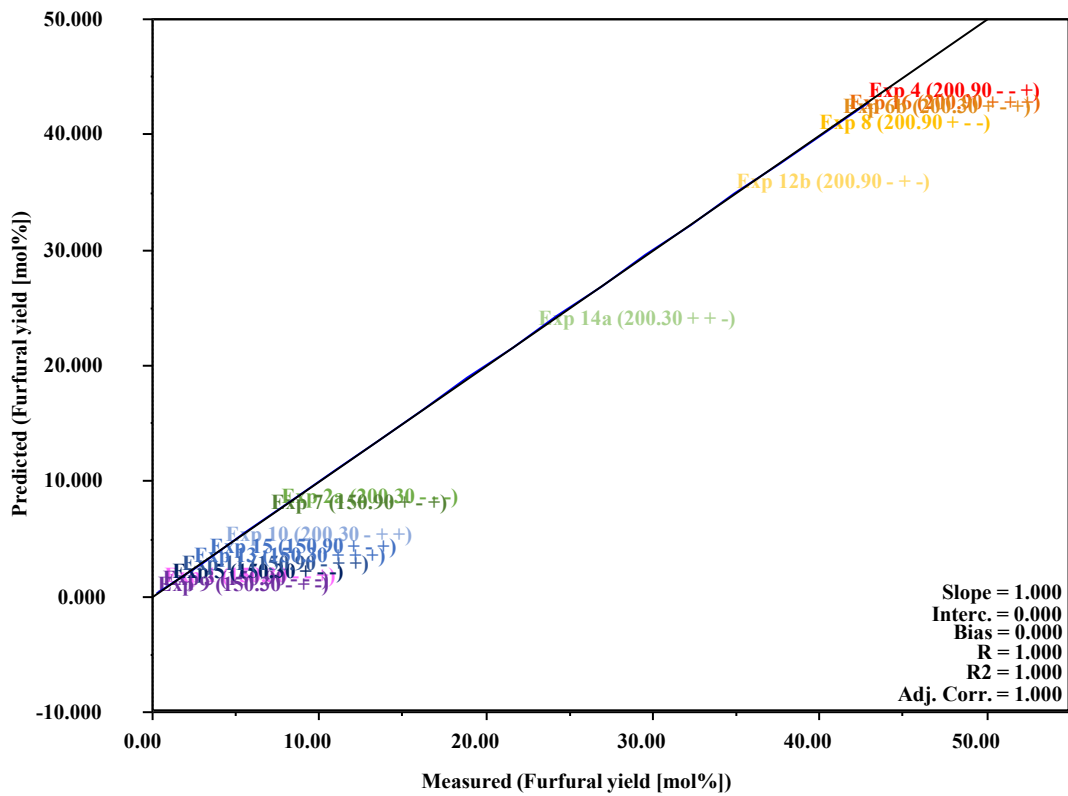


Figure 5-27: Linear regression model testing the orthogonality of the experimental design, excluding CPs.

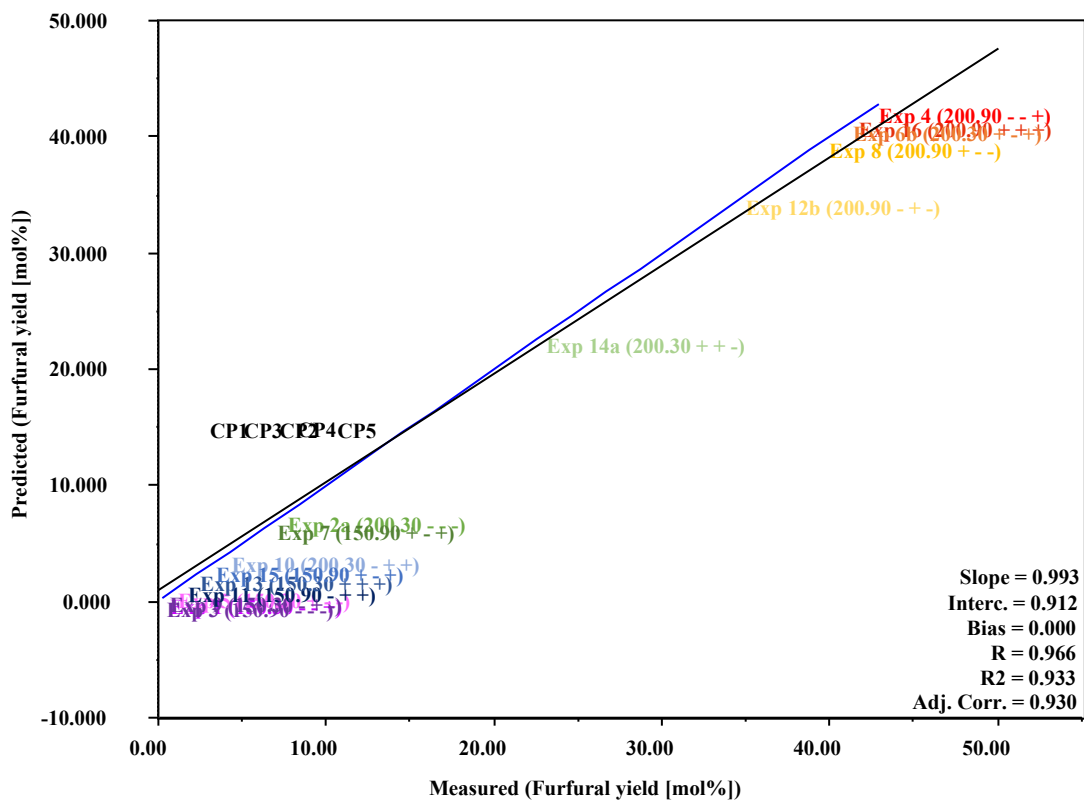


Figure 5-28: Linear regression model testing the orthogonality of the experimental design, including CPs

When comparing Figure 5-27 and Figure 5-28 it is possible to see that the regression model becomes non-linear when CPs are included. This can be seen as the CPs are situated on a horizontal line in Figure 5-28 that follows a deviating trend relative to the other experiments. The reason why the CPs are situated on a horizontal line in Figure 5-28 is because the model predicts the same FUR yield for all CPs. However, the measured FUR yield (Table 5-11) varied for all CPs, causing the CPs to spread along the x-axis. More specifically, the observed trend in Figure 5-28 indicate that the response surface for FUR yield is curved, which is further verified in Figure 5-29 and Figure 5-30. In other words, quadratic terms are required to get a more accurate description of the formation of FUR when using the selected biphasic reaction system. These results validate the importance of performing CPs, as the non-linear relationship detected in the middle of the interval would be missed without including CPs in the experimental design.

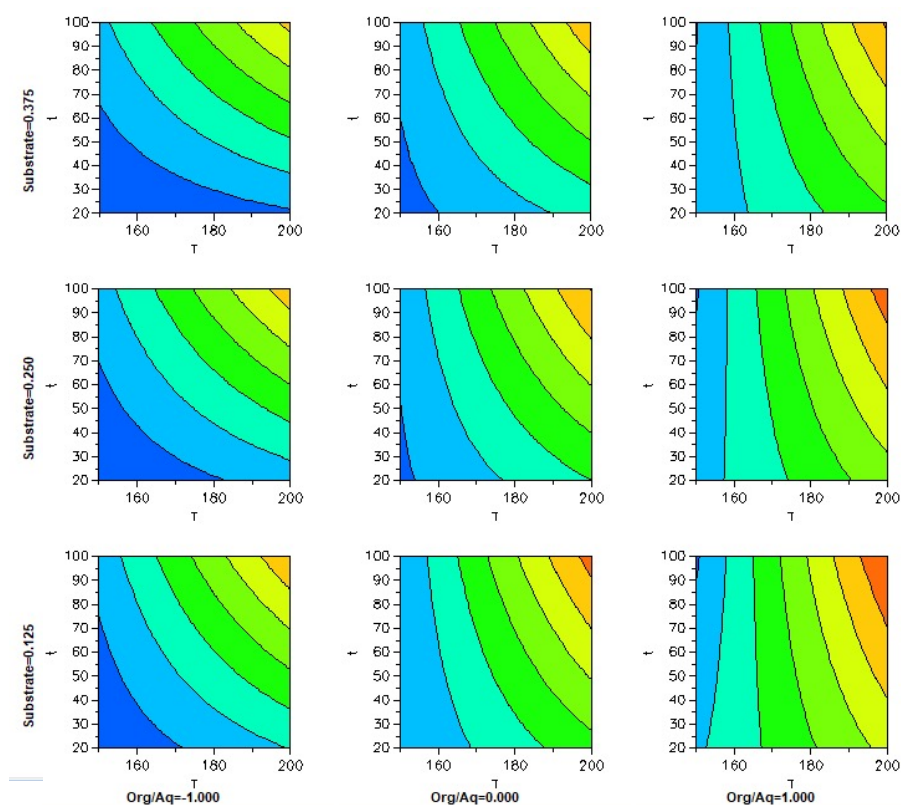


Figure 5-29: Contour plots showing the curvature of the response surface for FUR yield within the explored domain.

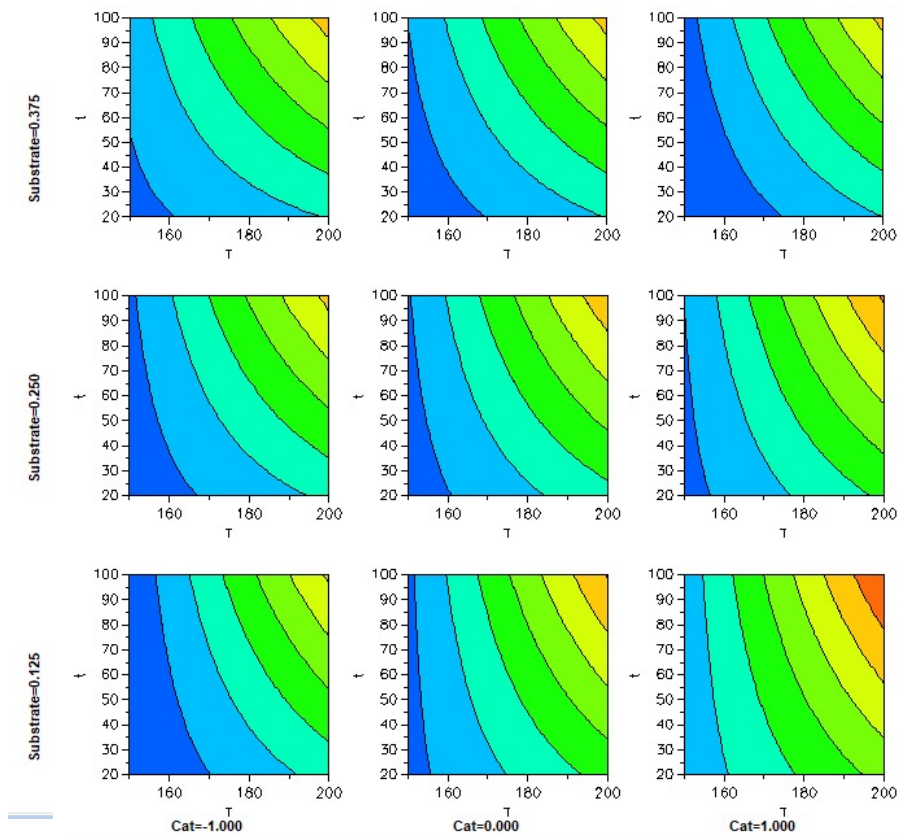


Figure 5-30: Contour plots showing the curvature of the response surface for FUR yield within the explored domain.

In Figure 5-29 and Figure 5-30, temperature and reaction time are plotted on the x- and y-axis, respectively. Each plot in Figure 5-29 shows how different factor settings for substrate loading (vertical axis) and org/aq ratio (horizontal axis) affects the curvature of the response surface with respect to FUR yield. Similarly, Figure 5-30 shows how the curvature of the response surface is affected by altering the factor settings for substrate (vertical axis) and catalyst loading (horizontal axis). As can be seen, the best results (red region) are obtained using a high factor setting for all factors except substrate loading.

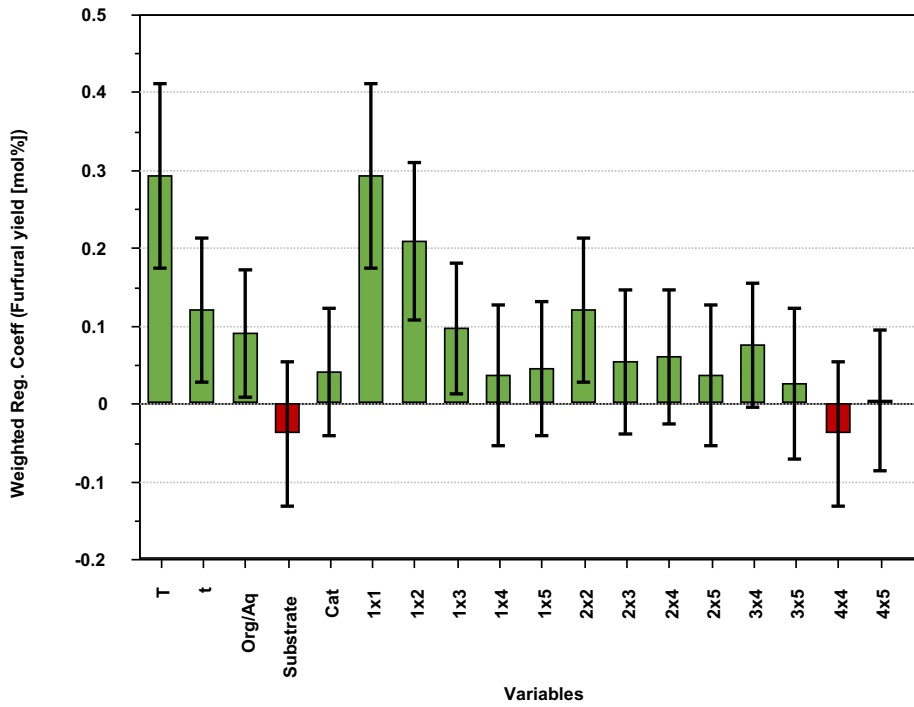


Figure 5-31: Weighted regression coefficients for the model, including quadratic terms.

In Figure 5-31, the weighted regression coefficients for the quadratic terms are included. The plot shows the importance of the squared factor for temperature (1 x 1) in terms of FUR yield, further confirming that temperature seems to be the most influential variable for achieving high FUR yields.

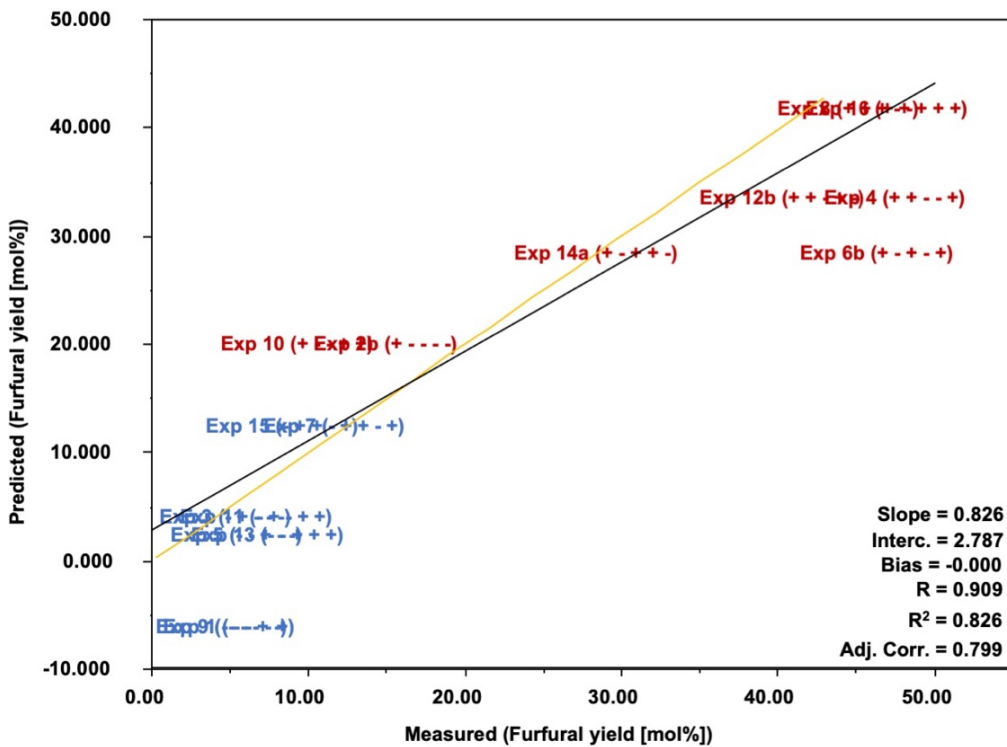


Figure 5-32: Regression model used for predicting the formation of FUR, excluding CPs.

In Figure 5-32, red and blue objects are experiments conducted at 200°C and 150°C, respectively. The yellow line is the fitted regression line for the model. The coefficient of determination (R^2) for the regression model is 0.826, which indicates that the model has some unexplained variability of the response data, i.e., the model is unable to give a perfect description of how the explored factors included in the model affects the formation of FUR. This suggests that other factors not included in the model could play a crucial role in the formation of FUR. The mathematical expression for the prediction model (Eq. 5), excluding insignificant factors and factor combinations, is given below:

$$Y_{FUR[mol\%]} = -3.38 + 0.35T + 0.24org/aq + 0.36T \times t + 0.35T^2 \quad (\text{Eq. 5})$$

Where T is temperature, org/aq is the volumetric ratio between MIBK and water, T x t is the cross-term between temperature and time, and T^2 is the quadratic term for temperature.

5.3.2.3 INFLUENCE OF REACTION TEMPERATURE AND RESIDENCE TIME

Both reaction temperature and residence time were found to have a strong impact on the production of FUR as previously discussed. As shown in the biplot in Figure 5-24, the reaction temperature was by far the most influential factor for converting XYL into FUR. Experiments conducted at 150°C (blue and yellow objects) generated considerably less FUR when compared to experiments conducted at 175°C (CP) and 200°C (red and orange objects, respectively), which is consistent with preceding literature findings, i.e., that temperatures of 150°C or below results in minimal generation of FUR (Zhang et al., 2019). When computing the average FUR yield for all experiments conducted at each temperature setting, a marked increase in FUR production can be observed when the temperature is increased (Figure 5-33).

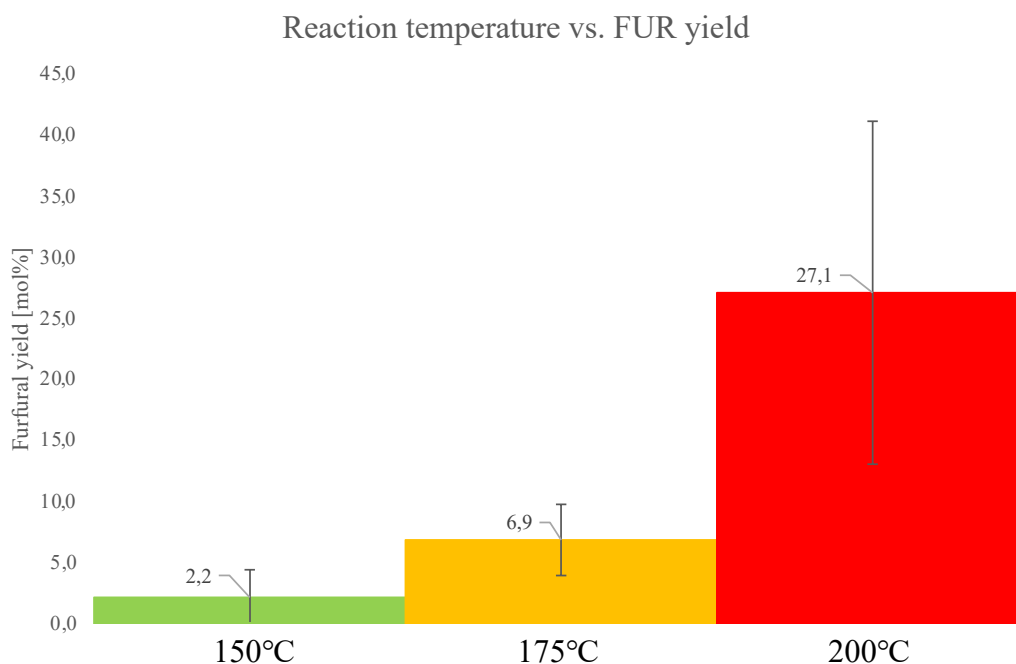


Figure 5-33: Reaction temperature vs. FUR yield.

As can be seen from Figure 5-33, the average FUR yield increased from $2.2 \pm 2.3 \text{ mol\%}$ to $6.9 \pm 2.9 \text{ mol\%}$ to $27.1 \pm 14.0 \text{ mol\%}$ when the temperature was increased from 150 – 175°C and 175 – 200°C, respectively. These findings are consistent with established literature, i.e., that higher temperatures are generally more effective at converting carbohydrates into FUR when using conventional heating methods (Zhang et al., 2019). The low FUR yield associated with the experiments conducted at 150°C can be explained by the fact that the rate-limiting step during the dehydration of XYL is the initial protonation step, which has a relatively high energy barrier (150.8 KJ/mol) (Wang et al., 2015, Rasmussen et al., 2014). Consequently, if the reaction temperature is too low, insufficient protonation will take place, resulting in minimal XYL dehydration and FUR production. However, high reaction temperatures were also associated with increased formation of precipitates (Figure 5-21). These results are in accordance with findings done by Zeitch et al., who found that fragmentation reactions are more prevalent when reaction temperatures exceed 200°C as the “entropy effect” facilitates molecular fragmentation followed by subsequent polymerization reactions, producing by-products commonly referred to as humins (Zeitsch, 2001, Lamminpaa et al., 2014).

When considering residence time, a similar but less dominating trend as for reaction temperature was observed. In general, the longer the reaction time, the higher the FUR yield and degree of XYL conversion. However, as previously discussed, the two-factor interaction between temperature and time had a significant influence on FUR yield, as shown in Figure

5-26. The importance of this interaction becomes even more apparent in Figure 5-34. The figure clearly shows that for experiments conducted at 150°C, the FUR production only increased slightly when the residence time was extended from 30 to 90 minutes. However, when the reaction temperature was increased to 200°C, extending the reaction time resulted in significantly higher FUR yields.

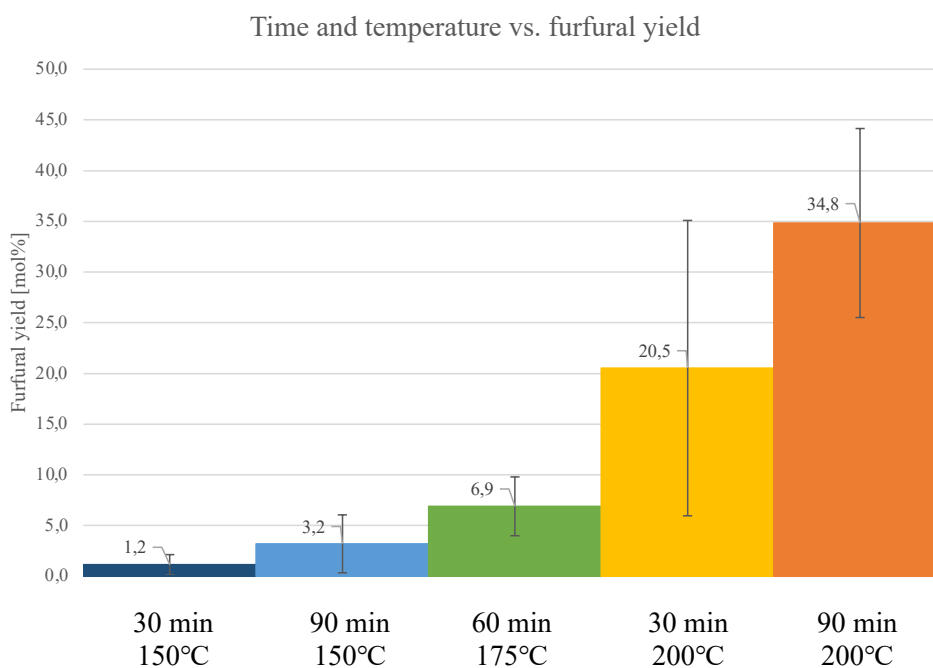


Figure 5-34: Influence of both reaction time and temperature on the production of FUR.

Reaction time also exhibited a positive correlation with regards to reaction selectivity (Figure 5-23), as it went from 41.4% to 50.6% when the reaction time was increased from 30 to 60 minutes. When the reaction time was further increased to 90 minutes, the selectivity only decreased slightly (49.3%). These results contradict findings done by Luo et al., which found that prolonged residence times associated with traditional heating methods tend to increase the number of unwanted side-reactions, thereby decreasing the reaction selectivity (Luo et al., 2017).

In summary, experiments conducted at high reaction temperatures and long residence times clearly produced the highest FUR yields. However, residence time was found to be highly dependent on reaction temperature, i.e., residence time only had a significant impact on the FUR yield at elevated temperatures. However, the results also suggest that if the reaction conditions get too severe, by-products will start to form rapidly, which demonstrates the importance of identifying optimal settings for these factors.

5.3.2.4 INFLUENCE OF SOLVENT RATIO

The effect of the volumetric ratio between MIBK and water was investigated as identification of an optimum ratio between solvent and water is crucial for attaining efficient isomerization and dehydration of XYL while ensuring sufficient FUR extraction from the aqueous reaction medium. Finding an optimal solvent ratio would also help achieve good system economics and improve the overall EHS-characteristics of the reaction system.

As previously mentioned, the organic-to-aqueous ratio was positively correlated with both FUR yield and XYL conversion (Figure 5-23), meaning that a high ratio between solvent and water had a positive effect on the two responses. In fact, according to the reported reaction systems in Table 2-2 and Table 2-1, the optimum solvent-to-aqueous ratio for achieving high FUR yields should be between 2:1 and 4:1, depending on the system. When computing the average FUR yield and XYL conversion for experiments conducted at a high (4:1) and low (1:4) factor setting for org/aq, it becomes evident that having a high solvent ratio resulted in far better system performance (21.7mol% vs. 13.9mol% FUR yield, respectively). This makes sense seen from a kinetic perspective as higher volumes of organic solvent will improve the *in-situ* extraction of FUR, which will help shift the equilibrium in the catalytically active aqueous phase towards FUR formation, thereby improving XYL conversion and FUR yield, which agrees with well-established literature findings (Mittal et al., 2020, Xu et al., 2018). In addition, the organic phase will also help stabilize the product, thus leading to less by-product formation, which ultimately leads to even higher yields (Weingarten et al., 2010a).

However, if the volumetric ratio between organic solvent and water becomes too small relative to the amount of substrate added to the reactor, insufficient dehydration will occur as the extraction rate of FUR into the organic phase becomes inadequate. This could explain the generally poor results obtained for experiments conducted with a low factor setting for org/aq. More specifically, FUR will start to accumulate in the aqueous phase after the organic phase has become saturated. According to Le Chatelier's principle, increased concentrations of FUR in the catalytically active aqueous phase will shift the equilibrium away from FUR production, thereby decreasing the degree of XYL dehydration and selectivity towards FUR formation, which ultimately leads to poor FUR yields.

To further prove the important role of the organic extraction phase, the average partition coefficient of FUR for each solvent ratio was calculated. The partition coefficient went from 1.6 to 6.9 when the volumetric ratio was increased from 1:4 to 1:1. When the ratio was further increased to 4:1, the partition coefficient surged to 30.9. This is thought to be the key advantage of biphasic reaction systems compared to monophasic systems, i.e., the *in-situ* extraction of FUR into the organic phase aid in product stabilization while simultaneously shifting the equilibrium of the reaction towards FUR formation, which increases the overall product yield.

5.3.2.5 INFLUENCE OF CATALYST LOADING

From the biplot in Figure 5-24 and the bar graph showing the weighted regression coefficients for each variable and variable interaction (Figure 5-31), only a weak positive correlation was observed between catalyst loading and FUR yield. In other words, the formation of FUR only increased slightly with elevated acid concentrations for FFD2. These results could indicate that the high and low values for catalyst loading were poorly selected, as very little information was obtained for this factor for the second design.

As is shown in Table 5-7 and Table 5-10, the factor setting for catalyst loading was the only difference between the first (FFD1) and the second (FFD2) experimental design. Hence, comparing experiments with the same numbering from FFD1 and FFD2 could potentially provide additional information regarding how catalyst loading affected the formation of FUR. It may also give increased insight into the apparently unpredictable selectivity response. More specifically, comparing analogous experiments from the two experimental designs could help elucidate whether the observed trends for the previously discussed CP experiments (chapter 5.3.1), where all factor settings except catalyst loading were kept constant, also holds for the experiments where all variables were changed between experiments. Figure 5-35 shows a comparison between FFD1 and FFD2 in terms of FUR yield, XYL conversion and reaction selectivity.

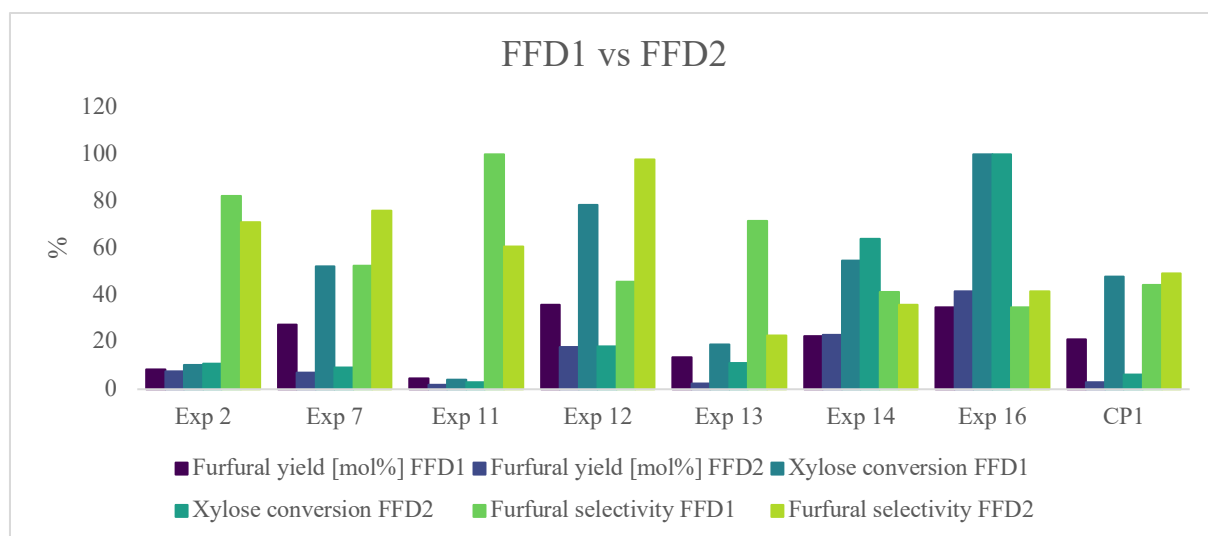


Figure 5-35: Comparison of FFD1 vs. FFD2 in terms of FUR yield, XYL conversion and reaction selectivity.

In general, experiments from FFD1 produced higher FUR yields compared to analogous experiments from FFD2 (Figure 5-35). These findings agree with previously discussed results and literature findings (Xing et al., 2011), meaning that FFD1 was expected to perform better than FFD2 based on the fact that the acid concentrations in FFD1 were significantly higher. In fact, the FUR yield was superior for all experiments in FFD1, except for experiments 14 and 16, where FFD2 showed marginally better results.

A more distinct difference between FFD1 and FFD2 can be observed for experiment 7, both in terms of FUR yield (27.6mol% vs. 7.1mol%) and XYL conversion (52.4 mol% vs. 9.3mol%). When the acid concentration was reduced from 0.386M (pH = 0.66) in FFD1 to 0.129M (pH = 1.00) in FFD2, the FUR yield and XYL conversion decreased by 74.3% and 82.3%, respectively. Experiment 12 exhibited a similar trend, as the FUR yield and XYL conversion decreased by 50.0% and 76.7%, respectively when the catalyst loading was decreased. These results clearly show that acid concentration can have a drastic influence on the formation of FUR if the acid concentration is within a certain range. These results further support the hypothesis that the factor settings for catalyst loading were poorly selected for FFD2, as catalyst was found to have little influence on the overall formation of FUR.

No clear trend was observed between catalyst loading and selectivity when comparing FFD1 and FFD2, which is in accordance with the results obtained from the previously discussed CP experiments. To exemplify, the calculated selectivities for experiments 2, 13, and 14 from FFD1

were higher compared to the same experiments from FFD2. However, experiments 7, 12, 16, and CP1 from FFD1 exhibited an opposing trend, i.e., lower selectivities when compared to FFD2, which had significantly lower acid concentrations than the experimental analogs in FFD1. More specifically, the selectivity for experiment 12 more than doubled (114.0%) when the catalyst loading was reduced from 0.032M (FFD1) to 0.016M (FFD2). However, for experiment 13, the selectivity went from 71.7% to 22.9%, a near 200 % decrease, when the acid concentration was reduced from 0.386M (pH = 0.66) to 0.129M (pH = 1.00). These results do not concur with established literature stating that $\text{pH} < 0.9$ drastically enhances by-product formation, i.e., reduces selectivity (Lamminpaa et al., 2014). Hence, experimental data show an inconsistent trend between catalyst loading and reaction selectivity when experiments from the two experimental designs are compared. These findings could suggest that lurking variables, i.e., unknown factors with a significant effect on one or more responses, have a strong influence on reaction selectivity.

To summarize, FUR yield generally increased with increasing acid concentrations. However, findings suggest that if the aqueous reaction phase is too catalytically active due to excessive catalyst loading, more by-product formation seems to occur as the organic extraction phase cannot remove the generated FUR from the aqueous phase before further side-reactions occur. This can further be ascribed to the fact that FUR is a highly reactive furanic intermediate (Mariscal et al., 2016) formed during the dehydration of carbohydrates, which means that it is susceptible to further degradation if not extracted quickly after its formation. Balancing the catalytic activity of the aqueous reaction phase with the extraction capabilities of the organic extraction phase is therefore essential to maximize XYL conversion and FUR yield while simultaneously minimizing by-product formation.

5.3.2.6 INFLUENCE OF SUBSTRATE LOADING

The effect of substrate loading, i.e., initial concentration of XYL in the aqueous phase was also studied to better understand how much XYL the employed reaction volume could efficiently convert into FUR while maintaining a high degree of conversion. Acquiring information about optimal substrate loading would also help maximize conversion efficiency when dealing with batch reactors.

As previously mentioned, substrate loading was the only main factor that had a negative correlation with FUR yield, i.e., high substrate loadings generally resulted in poor FUR yields (Figure 5-24). The initial XYL concentration in the aqueous phase varied between 0.21 – 2.50M in FFD2. The average XYL conversion and FUR yield for experiments conducted with an initial XYL concentration of 2.50M were 25.0mol% and 15.1mol%, respectively. However, when the XYL concentration in the aqueous phase was at its lowest, i.e., 0.21M, the XYL conversion and FUR yield increased to 55.0mol% and 25.5mol%, respectively, which equates to a 120% increase in XYL conversion and a 68.5% increase in FUR yield. These numbers make sense seen from a stoichiometric perspective, as the number of XYL molecules that must undergo isomerization and subsequent dehydration into FUR is approximately 12 times higher when the XYL concentration in the aqueous phase is 2.50M compared to 0.21M. Since only a finite number of XYL molecules can undergo simultaneous degradation at any given time in a constant reaction volume means if the initial XYL concentration is too high, the system will exhibit reduced performance in terms of conversion and yield as the reaction system will become saturated with FUR before all XYL molecules have been converted.

However, it could be speculated that exploration beyond the explored domain, i.e., increasing factor settings for significant variables like reaction temperature and residence time would result in improved XYL conversions for all experiments in FFD2, independent of initial XYL concentration. However, this would also most likely result in reduced selectivities, as severe reaction conditions are known to promote formation by-products through resinification, fragmentation, and polymerization reactions (Lamminpaa et al., 2014). Therefore, identification of optimal substrate loadings must be done in accordance with both the applied reaction volume and the most significant factors, i.e., temperature and time, as one poorly selected factor setting can have detrimental effects on the final FUR yield. In other words, all variables found to have an impact on the formation of FUR must be balanced in order to maximize the conversion efficiency of the batch process.

5.3.2.7 EXPERIMENTAL REPRODUCIBILITY

In order to determine the reproducibility of the system in terms of FUR yield, selectivity, and XYL conversion, a total of six replicates were conducted for FFD2. For experiments 2, 6, and 14, one replicate was conducted, while for experiment 12 and the CP, two and four replicates were performed, respectively. The results are graphically represented in Figure 5-36. Pictures of product solutions for all replicates can be found in Figure 5-37.

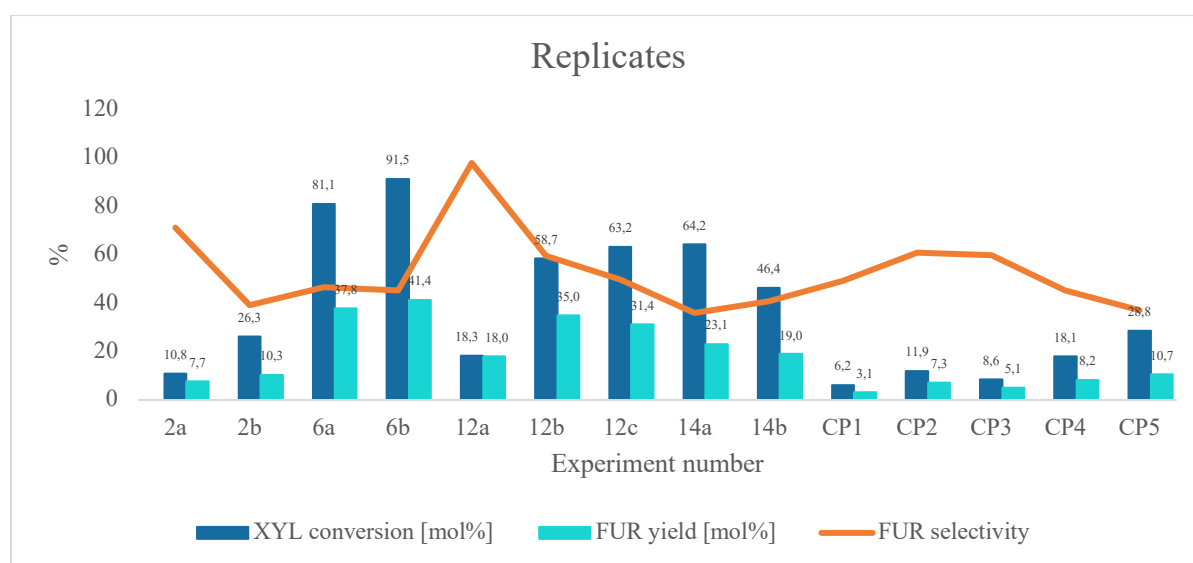


Figure 5-36: Comparison of replicated experiments from the second fractional factorial design (FFD2).

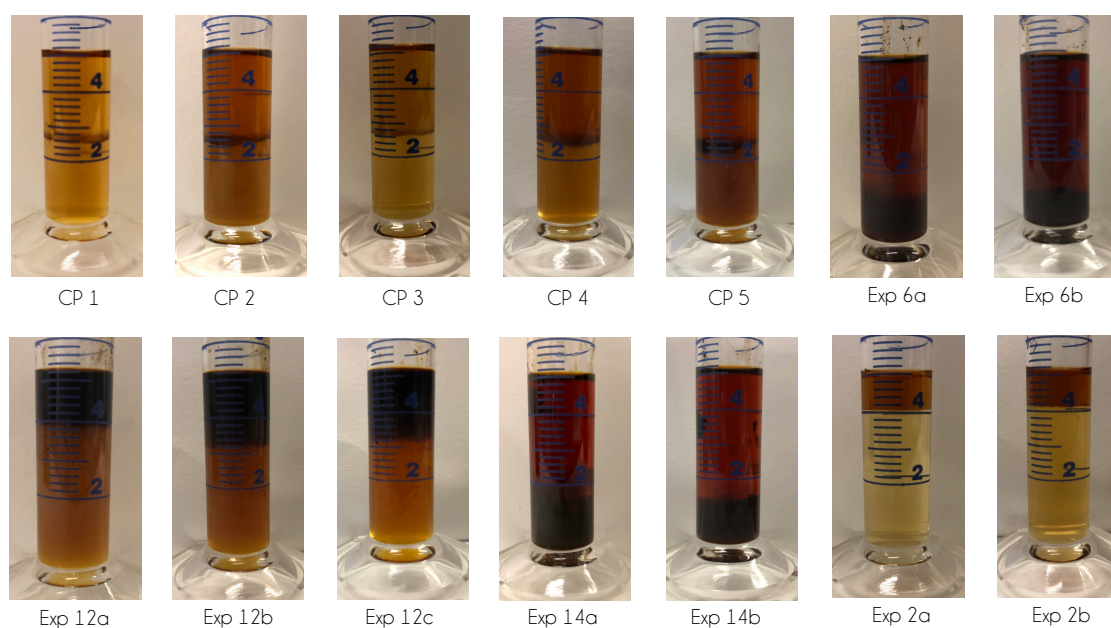


Figure 5-37: Product solutions of replicated experiments from FFD2.

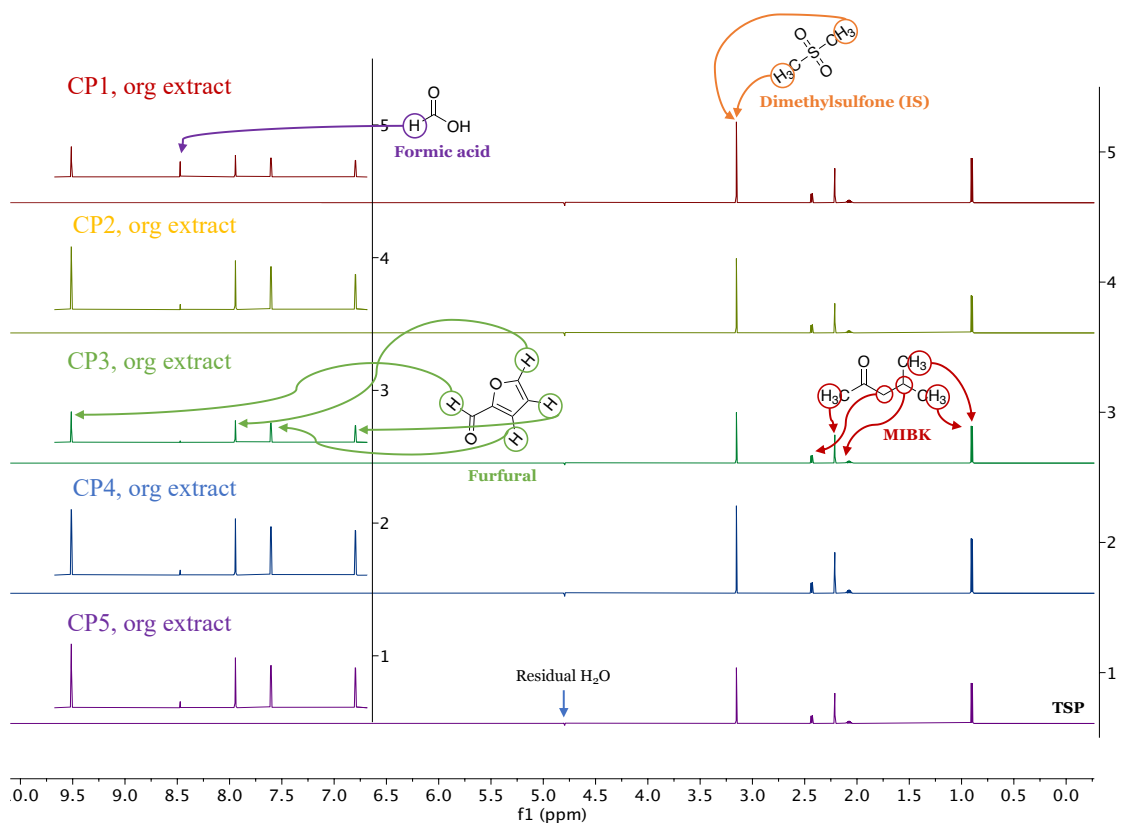


Figure 5-38: Stacked ^1H -NMR spectra of the organic phases from the five CP experiments from FFD2.

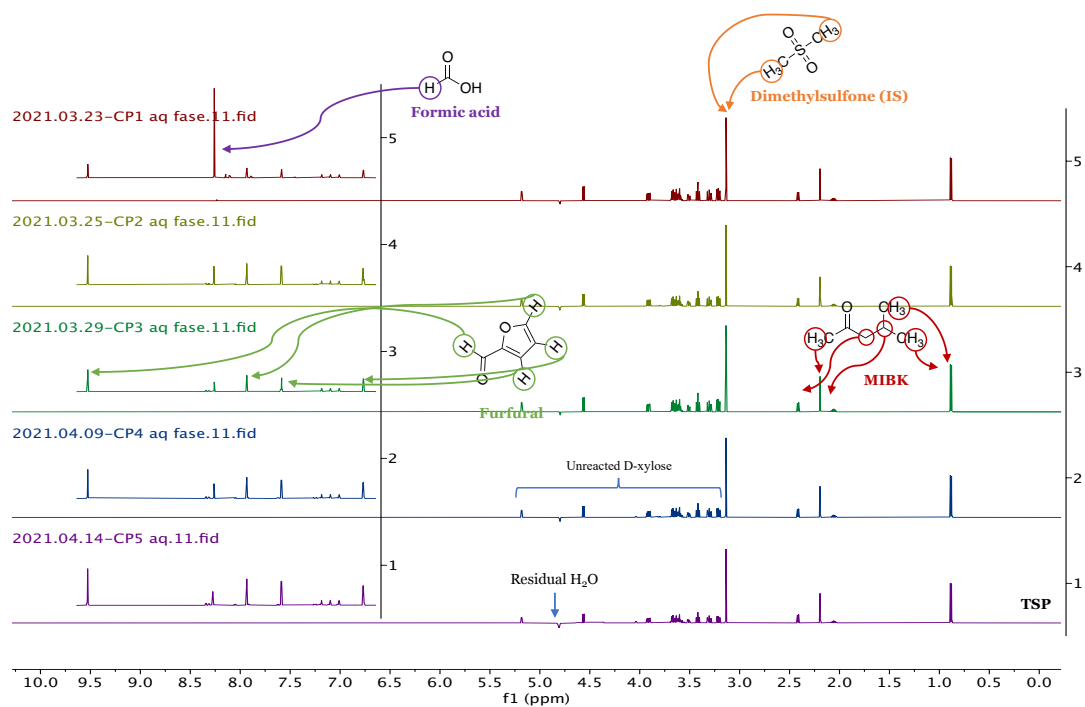


Figure 5-39: Stacked ^1H -NMR spectra of the aqueous phases from the five CP experiments from FFD2.

Stacked NMR spectra for experiment 2a-b, 6a-b, 12a-c, and 14a-b can be found in appendix G.

In general, the reaction system's performance in terms of reproducibility was poor, as can be seen from the graph in Figure 5-36. For experiment 12, the triplicates generated an average FUR yield and degree of XYL conversion of $28.1 \pm 9.0 \text{ mol\%}$ and $46.7 \pm 24.7 \text{ mol\%}$, respectively. The large standard deviations are caused by the significant discrepancies between experiment 12a and the two ensuing parallels (Table 5-11). When focusing on FUR yield, experiment 12b and 12c produced significantly higher FUR yields when compared to experiment 12a (35.0 mol\% and 31.4 mol\% vs. 18.0 mol\% , respectively). Similarly, the degree of XYL conversion for experiments 12b (58.6 mol\%) and 12c (63.2 mol\%) was much higher when compared to experiment 12a (18.3 mol\%). However, the selectivity for experiment 12a (98.0%) was significantly higher when compared to 12b and 12c (59.6% and 49.7% , respectively), which suggest that a negative correlation exists between FUR yield/XYL conversion and reaction selectivity.

Significant deviations between parallels can also be observed for the CPs. In general, FUR yield and XYL conversion increased with run order (Figure 5-36). In addition to producing the worst result in terms of FUR yield, CP1 also produced more than twice the amount of formic acid when compared to the other CPs (Figure 5-39). The reason for the excessive formic acid formation in CP1 was not further investigated in this thesis. However, when performing an outlier detection test for all the CPs (Figure 5-40), both CP1 and CP5 were considered potential outliers due to their high leverage and low residual, i.e., they had a strong influence on the model.

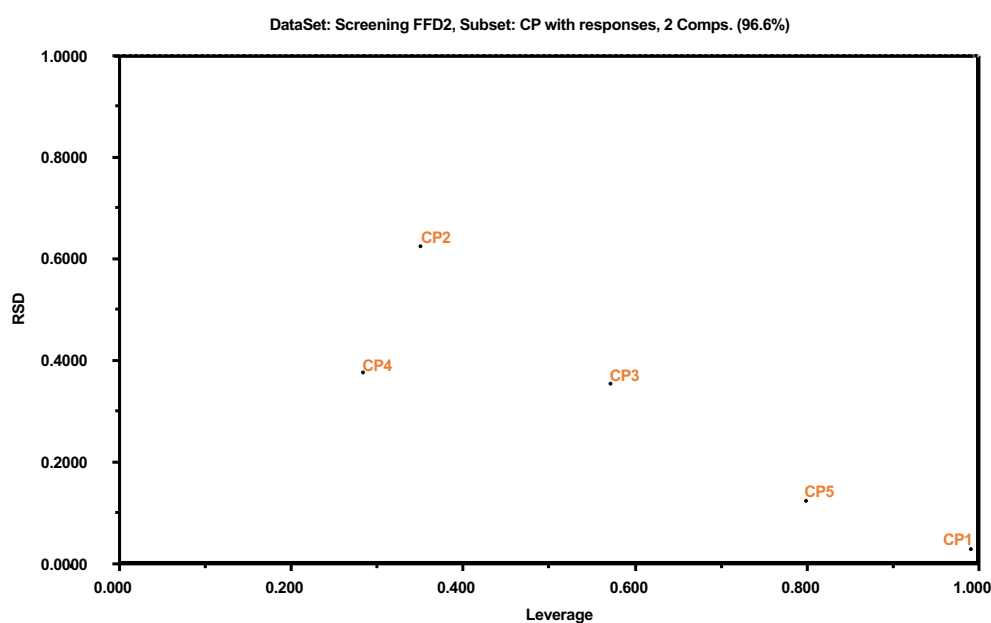


Figure 5-40: Outlier detection for the CP experiments using residual (RSD) vs. leverage.

When the run order (Table B-1, Appendix B) of the different replicates was compared to the measured responses for all replicates (Figure 5-36), an apparent time trend emerged. Hence, the previously detected outliers were not discarded to better illustrate the time trend observed in the dataset. Both FUR yield and XYL conversion generally increased as a function of time, with only a few exceptions. Reaction selectivity exhibited a reverse trend, i.e., it decreased as the experimental design progressed, which agrees with previously discussed findings. It was hypothesized that the time trend was caused by improved catalytic properties of the metal reactor, resulting in increased catalytic activity on the surface of the reactor, thereby increasing XYL conversion and FUR yield as the experimental design progressed. This hypothesis is further supported by the splitting pattern in Figure 5-41, as the dissimilarity between replicates generally increased with increasing time between parallels.

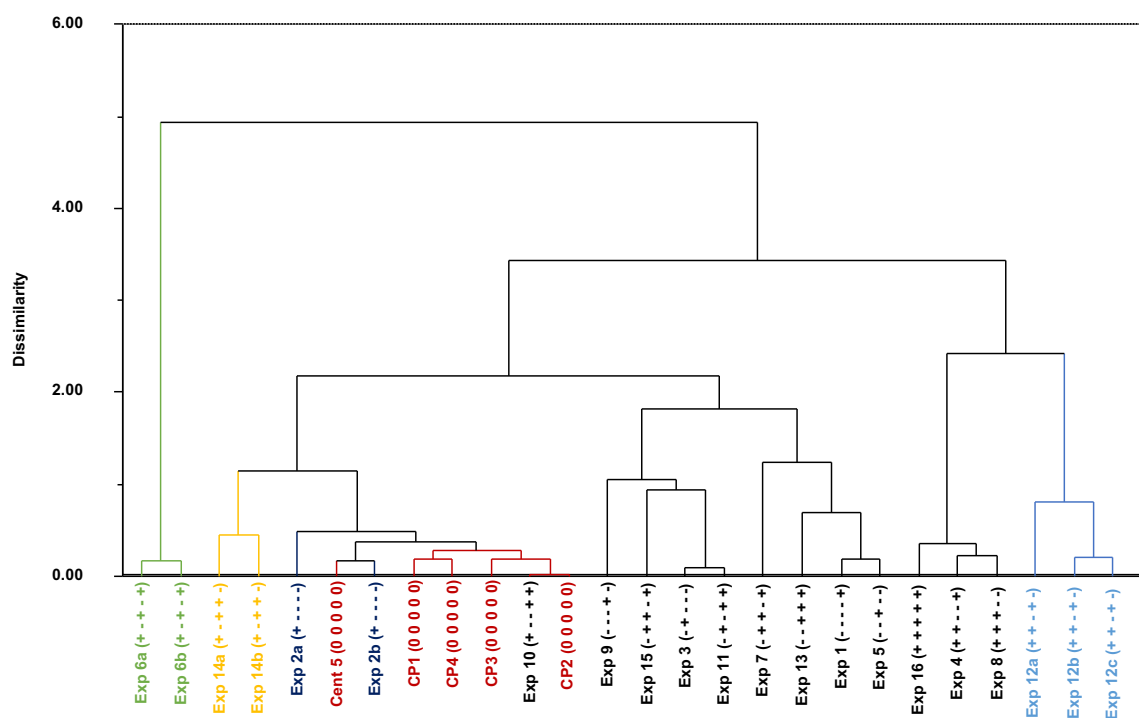


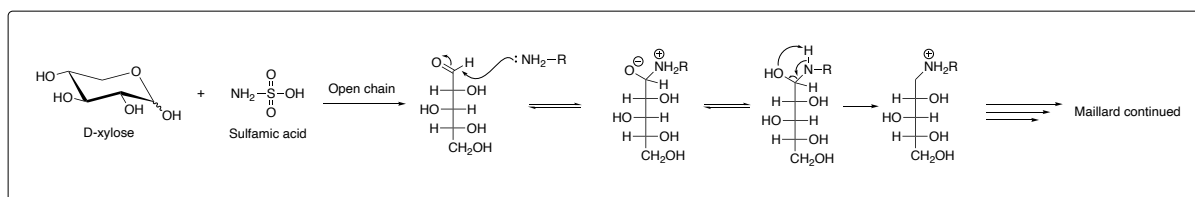
Figure 5-41: Euclidian dendrogram showing experimental dissimilarity for all objects in FFD2 in terms of FUR yield. The lower the connection, the more similar experiments are. The plus and minus signs denote variable settings for the main factors (temp, time, org/aq ratio, substrate loading, catalyst loading).

The dendrogram in Figure 5-41 clearly shows that experiments 2a and 12a, both of which were conducted several weeks prior to their ensuing parallels, are connected at a higher point compared to their experimental analogs, meaning that they are more dissimilar in terms of FUR yield. To exemplify, the FUR yield and XYL conversion for experiments 12b and 12c (conducted over two consecutive days) deviated with 10.3% and 7.8%, respectively. However, when experiment 12a is compared to experiment 12c (conducted three weeks apart), the deviation in yield and conversion soared to 74.4% and 245.0%, respectively. Similarly, for experiments 2a and 2b, which were conducted four weeks apart, the deviation in FUR yield, XYL conversion, and reaction selectivity were 33.8%, 143.5%, and 81.2%, respectively.

To summarize, the system's reproducibility was mediocre when experiments conducted at the beginning of the experimental design are compared to parallels performed at the end of the design. However, when parallels were completed over shorter time intervals, the reproducibility improved significantly but was still far from satisfactory. The low reproducibility suggests that the system is highly unstable, implying that several different reaction mechanisms can occur simultaneously, as has been extensively covered in the literature by several authors (Rasmussen et al., 2014, Lamminpaa et al., 2014, Zeitsch, 2001, Wang et al., 2015). The hypothesis regarding the increased catalytic activity of the reactor walls as a function of time must be explicitly tested by using an inert reactor vessel before it can be verified/falsified.

5.4 HYPOTHESIZED SIDE-REACTIONS

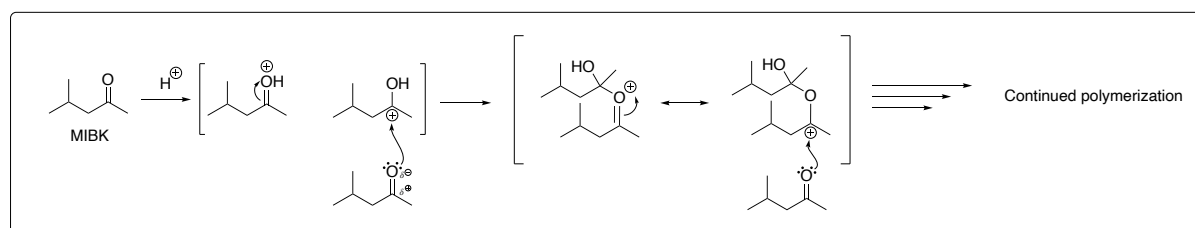
Based on previously discussed experimental findings concerning potential side-reactions and the excessive formation of precipitates, it was speculated that the Maillard reaction between XYL and sulfamic acid could be a participating mechanism resulting in the formation of particulates. The Maillard reaction is known to proceed rapidly between reducing sugars and amino acids at elevated temperatures, resulting in the formation of brown particles. A suggested reaction mechanism between XYL and sulfamic acid is presented in Scheme 5-42.



Scheme 5-42: Proposed Maillard reaction mechanism between XYL and sulfamic acid. (Source: Beate Halsvik, PhD. Candidate, UiB).

However, this hypothesis has yet to be verified, as elemental analysis of precipitates must be performed to see whether nitrogen atoms have been incorporated in the precipitated particles. The presence of nitrogen would imply that sulfamic acid molecules can react with XYL to form solid by-products.

It was also hypothesized that self-polymerization between the solvent molecules could be a possible explanation for the excessive formation of precipitates (Scheme 5-43) as MIBK can undergo polymerization reactions in acidic environments. To test this, two experiments without the addition of substrate were conducted to see whether precipitates would form. The first experiment (blank 1) was conducted using CP values, and the second experiment (blank 2) employed high values for all factors (Table 5-10). Figure 5-44 shows the NMR spectra of the aqueous phases from the conducted experiments. A picture of the product solution for both experiments is also included in the Figure 5-44.



Scheme 5-43: Acid-catalyzed self-polymerization of MIBK. Mechanism proposed by Beate Halsvik, PhD. Candidate at the University of Bergen.

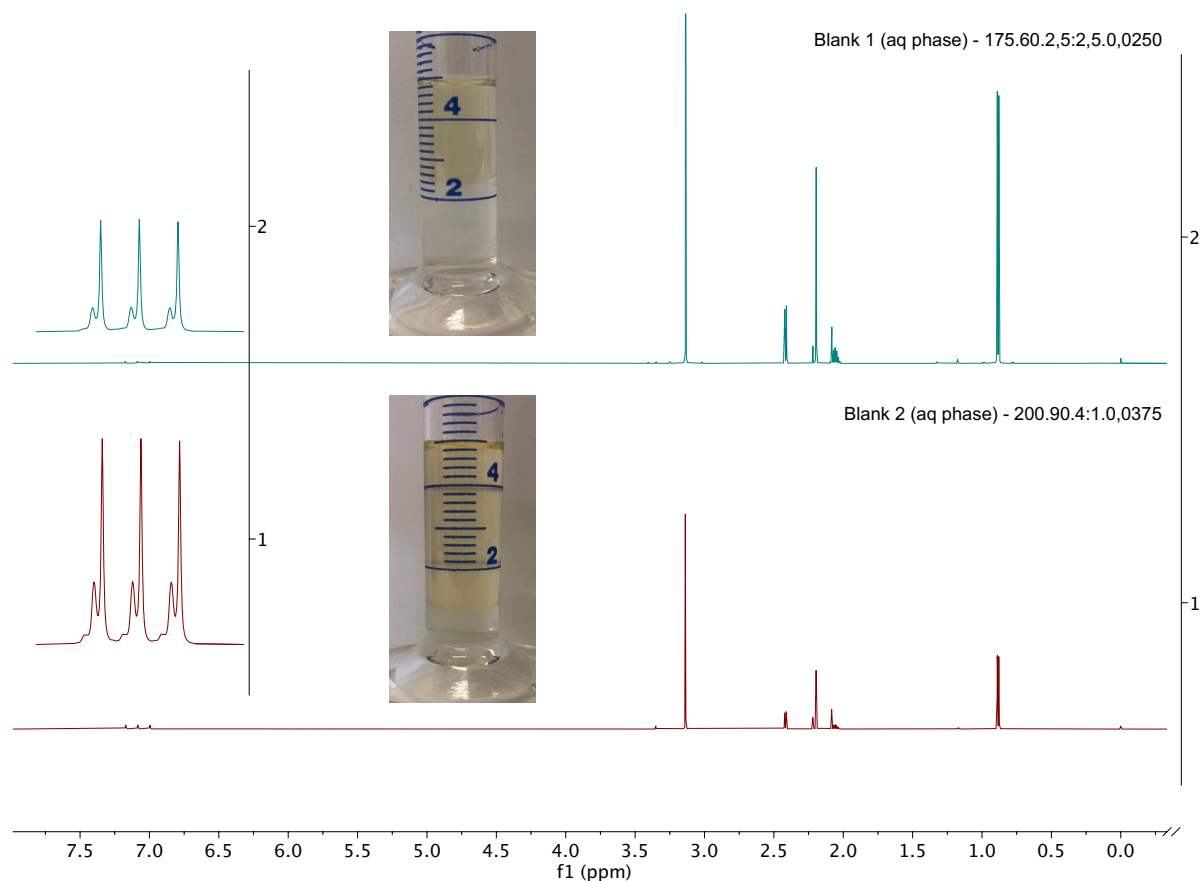


Figure 5-44: NMR spectra of the aqueous phases.

As is apparent from Figure 5-44, no precipitates were observed for any of the experiments, which falsifies the hypothesis that self-polymerization of MIBK molecules participates in the formation of the particulates observed in FFD1. However, the color saturation of the organic phase was significantly higher for blank 2 compared to blank 1. In addition, Figure 5-44 shows that the intensity of the three peaks located between 7.00 – 7.20ppm in the aqueous samples increased for blank 2. Interestingly, these peaks were only observed in the ^1H -NMR spectra for the aqueous phases, indicating that the compound responsible for generating these peaks is insoluble in MIBK. No further investigations regarding these peaks were conducted in this thesis as the only purpose of conducting these experiments was to see whether self-polymerization between MIBK could help explain the formation of precipitates in the product solutions.

5.5 UTILIZATION OF F&B AS FEEDSTOCK FOR PRODUCTION OF FUR AND HMF

The last part of this thesis was to explore whether F&B rejects, more specifically plums and cherries, could be used as potential feedstocks for producing high yields of FUR and HMF using the selected biphasic reaction system. In order to do so, the best reaction parameters identified during the screening process (substrate loading (0.125g), distilled H₂O (4.0mL), MIBK (1.0mL), sulfamic acid (0.0125g), 200°C for 90min) were used when conducting the experiments. The calculated yields are tabulated in Table 5-12 and are graphically presented in Figure 5-45. Pictures of product solutions are shown in Figure 5-46. NMR spectra of organic and aqueous samples, including integration values, can be found in Appendix H. A reaction scheme showing the simultaneous production of FUR and HMF can be found in scheme K-5 in Appendix K. In addition, according to Matvaretabellen.no (Matvaretabellen, 2020), plums and cherries have an average water content of 84% and 83%, respectively. This made it possible to estimate the dry weight of substrate added to each experiment based on the wet mass added prior to heating. The estimated dry weight of substrate added to each experiment was used when calculating the predicted yields given in Table 5-12.

Table 5-12: Added substrate and calculated yields for the experiments using F&B rejects as substrate.

	Cherries	Plums
Substrate (wet) [g]	0.1252	0.1257
Substrate (dry) [g]	0.0213	0.0201
FUR [g]	0.00012	0.00009
HMF [g]	0.0021	0.0024
Formic acid [g]	0.0011	0.0001
Unreacted XYL [g]	0.0032	0.0026
Yield FUR [wt%] ^b	0.56	0.45
Yield HMF [wt%] ^b	9.87	11.93

^bBased on dry weight of substrate.

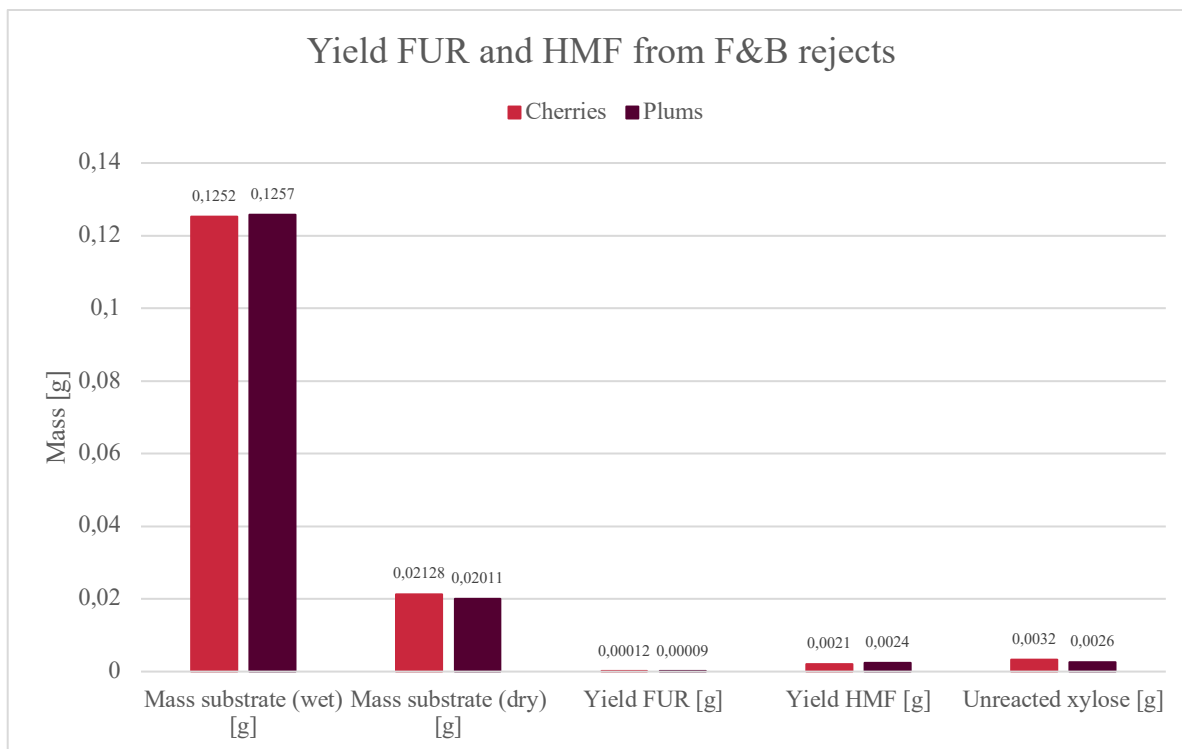


Figure 5-45: Calculated yields for FUR and HMF for the experiments using cherries and plums as feedstock.

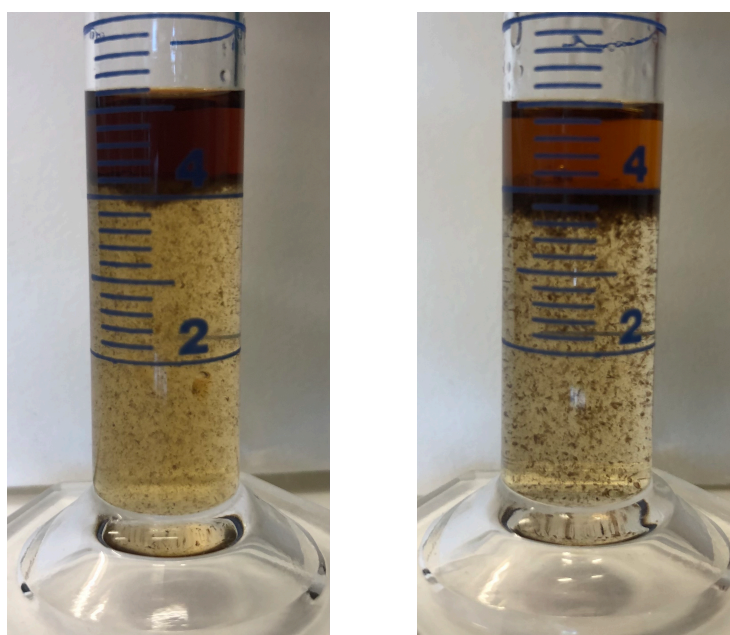


Figure 5-46: Product solutions where cherries (left) and plums (right) were used as substrate instead of XYL.

From Figure 5-46 it is possible to see that both product solutions had significant amounts of solid particles dispersed in the aqueous phase. These particles were assumed to be primarily pomace residues.

The results presented in Table 5-12 and Figure 5-45 show that when cherry rejects were used as a substrate, a total FUR and HMF yield of 0.00012g and 0.0032g were obtained, which equates to 0.6wt% and 9.9wt% based on the dry mass of substrate added before heating. Similarly, the FUR and HMF yield generated from plums was 0.00009g and 0.0024g, which equals 0.5wt% and 11.9wt%, respectively. These yields are, as expected, considerably lower when compared to the yield obtained for XYL using the same reaction conditions, which obtained a total FUR yield of 0.0344g (42.9mol%).

The significantly higher yields of HMF relative to FUR for both experiments suggest that hexoses are more abundant in F&B than pentoses. This coincides with the reported structural composition as glucose and fructose are known to be the predominant sugars found in F&B. In addition to being an abundant free sugar in F&B, glucose is the sole constituent of cellulose as well as being a central component of xyloglycans, a type of hemicellulose, both of which are found in high abundance in F&B. The high amount of fructose present in F&B compared to traditionally used LCB is also favorable for producing HMF as ketoses are far more reactive than aldoses like glucose and mannose, as formerly specified in chapter 2.6.5.2. This means that a substantial fraction of the free sugars present in F&B won't have to undergo isomerization before dehydration, which suggests that production of HMF should be far more efficient when using F&B than conventional LCB, based on kinetic findings in the literature (Guo et al., 2020, Delbecq et al., 2018).

The low yields obtained from F&B rejects compared to when XYL was used as substrate can most likely be explained by the fact that F&B contains significant amounts of lignin, cellulose, and hemicellulose in addition to free sugars and xylooligosaccharides (XOS) (Mitmesser and Combs, 2017, Szymanska-Chargot et al., 2017). The interconnected lignocellulosic matrix present in F&B (Wertz and Bédué, 2013) means that the reaction pathway from hemicellulose and cellulose to FUR and HMF, respectively, must include an additional hydrolytic depolymerization step that converts cellulose and hemicellulose into monomeric sugars before dehydration can take place. This means that the catalytic species present in the reaction phase must promote simultaneous hydrolysis and dehydration when untreated biomass is used as a feedstock. Since the catalyst loading in the aqueous reaction phase for the experiments utilizing F&B rejects was identical to the catalyst loading in the experiment where XYL was used as feedstock means that the number of catalytically active species that are available for dehydration at any given moment will be significantly reduced when concurrent hydrolysis and

dehydration takes place. More specifically, several of the Brønsted acidic species that promoted dehydration into FUR when XYL was used as a substrate will participate in the hydrolysis of glycosidic bonds instead of dehydration when F&B rejects are used as feedstock, as is clearly shown in Scheme 2-12 in chapter 2.6.2. This means that the relative catalytic efficiency regarding FUR and HMF production will be reduced for the experiments where both hydrolysis and dehydration occur simultaneously. In addition, the NMR spectra in Figure H-1 – H-4 in Appendix H also show that significant amounts of unconverted sugars remained in the aqueous phase for both plums and cherries, a clear indication of insufficient catalytic conversion for the employed feedstocks. Therefore, it is likely to assume that increased factor settings for both catalyst loading, reaction temperature and residence time is required to achieve adequate depolymerization and simultaneous dehydration when F&B residues are used as a feedstock to produce furanic derivatives. Increasing the org/aq ratio would most likely also have a positive effect on the final yield as it would improve the *in-situ* extraction of both FUR and HMF.

In summary, even though the yields of FUR and HMF obtained from F&B residues in this thesis are far from satisfactory seen from a biorefinery perspective, it shows that both feedstocks have major potential for generating both FUR and HMF if the reaction system is optimized. Hence, efficient valorization of F&B rejects could potentially serve as a promising contribution towards circular value creation in Norway.

6. CONCLUSION

The primary objective of this thesis was, as stated in chapter 3, to find an efficient, green, biphasic reaction system that could be used to produce high yields of FUR and HMF from both simple sugars and sugar-containing industrial waste streams generated by the F&B industry in Norway. To achieve this, the thesis was divided into four main tasks.

The first task found that ¹H-NMR was the best analytical tool for reliable quantification of FUR when employing biphasic reaction systems, both in terms of accuracy and precision. HPLC had a slightly lower accuracy but a similar reproducibility when compared to qNMR. GC-MS produced the most unreliable results of the three analytical methods, both when using calibration curves and internal standards. These findings clearly show the importance of identifying reliable quantification methods that are compatible with both the products and the applied reaction system before extensive experimental designs are conducted.

In the second task, a sulfamic acid-catalyzed MIBK/H₂O biphasic solvent system was chosen as the preferred reaction system for this thesis based on literature findings and preliminary experimental testing, combined with the fact that both MIBK and sulfamic acid have excellent physicochemical properties and good EHS characteristics, which concurred with the desired specifications of this thesis.

In the third task, the interpretation of the measured responses and how they correlated with the explored factors and factor interactions within the explored domain revealed that a potential progression towards optimum conditions could be achieved by increasing the factor settings for the most significant variables, i.e., reaction temperature and residence time. Solvent ratio and acid concentration only had a small positive effect on the FUR yield, while substrate loading was found to have a slightly negative influence on the overall yield. The curved response surfaces of the contour plots in Figure 5-29 and Figure 5-30 clearly show that the best yields were obtained close to the outer border of the experimental domain, i.e., when reaction temperature, residence time, org/aq ratio, and catalyst loading were high, and when substrate loading was low. Consequently, it is reasonable to postulate that increasing the factor settings

for the most significant variables, i.e., time and temperature, potentially could improve the overall formation of FUR.

The poor reproducibility of the reaction system suggests that isomerization and subsequent dehydration of pentoses to FUR is a complex process that is sensitive to minor changes in both physical and chemical system properties, which coincide with kinetic studies conducted by Rasmussen et al. (Rasmussen et al., 2014). Therefore, it can be hypothesized that all of the mechanistic pathways proposed in Scheme 2-11 could be involved in the formation of FUR. However, their relative importance is most likely dependent on the applied reaction conditions. Hence, identifying optimal reaction parameters is critical to ensure that the most favorable reaction pathways in terms of conversion efficiency are the predominating mechanisms involved during thermochemical conversion of carbohydrates to FUR. This would also help improve the overall energy efficiency of the process while enhancing the EHS characteristics of the reaction system, which align with the principles of green chemistry.

The best reaction conditions with regards to FUR yield, XYL conversion, and selectivity within the experimental domain were identified to be 200°C, 90 min, with a sulfamic acid concentration of 0.032M, MIBK/water ratio of 1:4, and a [XYL] of 0.83M. Under these conditions, a total FUR yield of 42.9mol% was achieved in combination with a XYL conversion and reaction selectivity of 88.8mol% and 48.3%, respectively. These results are relatively poor compared to previously reported reaction systems employing MIBK as the extraction solvent, as yields exceeding 80% have been reported when using conventional heating methods (Zhang et al., 2013).

In the final task, when F&B rejects were used as feedstock and subjected to the best reaction conditions identified during the experimental screening process, the performance in terms of FUR and HMF yield was drastically reduced. More specifically, when plum rejects were used as feedstock, the obtained yields of FUR and HMF were 0.45wt% and 11.93wt%, respectively, while cherries produced a total FUR and HMF yield of 0.56wt% and 9.87wt%, respectively. These yields are also relatively poor compared to reported yields obtained from untreated LCB where conventional heating modes were employed. In fact, simultaneous FUR and HMF yields of 41.0% and 50.0% from wheat straw in a MIBK/water solvent system have been reported (Mirzaei and Karimi, 2016). However, given the fact that the FUR and HMF yields presented in this thesis were achieved under sub-optimal reaction conditions suggest that significant

improvements in terms of yield may be obtained if the system is optimized. Hence, efficient utilization of bio-wastes generated from industrial processing of F&B to produce FUR and HMF could be a small step towards meeting the ambitious sustainable development goals, as well as accelerating the ongoing sustainable transformation as we transition from a fossil-based to a renewable society.

7. FURTHER WORK

- Perform a response surface design, e.g., a central composite design (CCD) containing axial points (star points) for the two most significant variables, i.e., temperature and time. The addition of axial points would help get a more accurate description of the response surface curvature of the initial model acquired from FFD2. Each axial point experiment would be identical to the CPs except for one factor, which would take on a new factor setting above and below the explored factor range used in the experimental design in FFD2
- The results obtained from the CCD could be used to further optimize the formation of FUR by conducting a sequential simplex search by adjusting the most significant variables, viz. temperature and time. In other words, a near-optimum domain could potentially be located by following the slope of the response surface acquired from the second FFD and the CCD.
- Use microwave-assisted heating (MWAH) instead of conventional heating. This will give insights into how residence time and heating rate affect the FUR yield and reaction selectivity, as microwaves have been reported to produce high yields of both FUR and HMF in significantly shorter times than traditional heating modes (Hansen et al., 2009, Le Guenic et al., 2015). It has also been reported that MWAH can enhance reaction selectivity and reduce the necessity of LCB pretreatment.
- Conduct a Life Cycle Assessment (LCA) to evaluate the environmental impact of the different inputs and outputs of the reaction system. Elucidation of potential measures that could help make the system as environmentally friendly and energy-efficient as possible would be highly desirable, seen from the perspective of green chemistry.
- Estimate the energy efficiency of the reaction to see whether the reaction system has potential for viable large-scale production of furanic derivatives.

- Test alternative acid catalysts, both homogeneous and heterogeneous, to see whether better yields can be obtained using less severe reaction conditions, which would be beneficial seen from both an energy- and an EHS-perspective.
- Test the reaction system on alternative bio-based feedstocks. This will give valuable information regarding how effective the reaction system is at producing furanic derivatives from biomass with different structural compositions and origins. Obtaining information on system efficacy will also help evaluate if the system has potential for being used in large-scale biorefinery concepts in the future.
- Conduct a kinetic study focusing on what mechanisms are predominant at different reaction conditions. This will help reveal how the applied factor settings can be adjusted to shift reaction selectivity towards FUR formation.
- Conduct an experimental design in an inert reactor to test the hypothesis that speculated that the catalytic properties of the metallic reactor walls changed over time, which was thought to be the main factor for the poor reproducibility of the system.
- Reuse the recovered aqueous phase to see how it affects the formation of FUR. Efficient recycling of the aqueous phase would also drastically reduce the amount of spent catalyst.
- Retest the catalytic performance of the six catalysts tested during the selection process using qNMR as a quantification tool instead of GC-MS. Duplicates/triplicates of the best performing catalysts should also be performed to check for system reproducibility.

8. BIBLIOGRAPHY

- ABDI, H. & WILLIAMS, L. J. 2010. Principal component analysis. *WIREs Computational Statistics*, 2, 433-459.
- ABOU-YOUSEF, H. & HASSAN, E. 2014. Efficient utilization of aqueous phase bio-oil to furan derivatives through extraction and sugars conversion in acid-catalyzed biphasic system. *Fuel*, 137, 115-121.
- ACHEAMPONG, M., ERTEM, F. C., KAPPLER, B. & NEUBAUER, P. 2017. In pursuit of Sustainable Development Goal (SDG) number 7: Will biofuels be reliable? *Renewable and Sustainable Energy Reviews*, 75, 927-937.
- AGIRREZABAL-TELLERIA, I., GANDARIAS, I. & ARIAS, P. L. 2014. Heterogeneous acid-catalysts for the production of furan-derived compounds (furfural and hydroxymethylfurfural) from renewable carbohydrates: A review. *Catalysis Today*, 234, 42-58.
- AL GHATTA, A., ZHOU, X., CASARANO, G., WILTON-ELY, J. D. E. T. & HALLETT, J. P. 2021. Characterization and Valorization of Humins Produced by HMF Degradation in Ionic Liquids: A Valuable Carbonaceous Material for Antimony Removal. *ACS Sustainable Chemistry & Engineering*, 9, 2212-2223.
- ANASTAS, P. T. & WARNER, J. C. 1998. *Green chemistry : theory and practice*, Oxford, Oxford University Press.
- ANTO, S., MUKHERJEE, S. S., MUTHAPPA, R., MATHIMANI, T., DEVIRAM, G., KUMAR, S. S., VERMA, T. N. & PUGAZHENDHI, A. 2020. Algae as green energy reserve: Technological outlook on biofuel production. *Chemosphere*, 242.
- ARIAS, P. L., CECILIA, J. A., GANDARIAS, I., IGLESIAS, J., GRANADOS, M. L., MARISCAL, R., MORALES, G., MORENO-TOST, R. & MAIRELES-TORRES, P. 2020. Oxidation of lignocellulosic platform molecules to value-added chemicals using heterogeneous catalytic technologies. *Catalysis Science & Technology*, 10, 2721-2757.
- ARPIA, A. A., CHEN, W. H., LAM, S. S., ROUSSET, P. & DE LUNA, M. D. G. 2021. Sustainable biofuel and bioenergy production from biomass waste residues using microwave-assisted heating: A comprehensive review. *Chemical Engineering Journal*, 403.
- ATALLA, R. H., HACKNEY, J. M., UHLIN, I. & THOMPSON, N. S. 1993. Hemicelluloses as structure regulators in the aggregation of native cellulose. *International Journal of Biological Macromolecules*, 15, 109-112.
- BARDALEN, A. 2016. Jordbrukets bidrag til bioøkonomien - En vurdering av jordbruks- og matsektorens bidrag til vekst i norsk bioøkonomi.
- BOLLAR, N. V., ZIMMERMANN, C. J., WETTSTEIN, S. G., ROMO, J. E., BOLLAR, N. V., ZIMMERMANN, C. J. & WETTSTEIN, S. G. 2018. Conversion of Sugars and Biomass to Furans Using Heterogeneous Catalysts in Biphasic Solvent Systems. Weinheim, Germany .:
- BORREGAARD 2021. Business areas.
- CARLSON, R. & CARLSON, J. E. 2005. *Design and optimization in organic synthesis*, Amsterdam, Elsevier.
- CHEMICALS, S. 2012. MIBK - Product stewardship summary.
- CHERUBINI, F. 2010. The biorefinery concept: Using biomass instead of oil for producing energy and chemicals. *Energy Conversion and Management*, 51, 1412-1421.
- CHHEDA, J. N., ROMÁN-LESHKOV, Y. & DUMESIC, J. A. 2007. Production of 5-hydroxymethylfurfural and furfural by dehydration of biomass-derived mono- and poly-saccharides. *Green chemistry : an international journal and green chemistry resource : GC*, 9, 342-350.
- CLIMENT, M. J., CORMA, A. & IBORRA, S. 2014. Conversion of biomass platform molecules into fuel additives and liquid hydrocarbon fuels. *Green Chemistry*, 16, 516-547.
- DANON, B., MARCOTULLIO, G. & DE JONG, W. 2014. Mechanistic and kinetic aspects of pentose dehydration towards furfural in aqueous media employing homogeneous catalysis. *Green Chemistry*, 16, 39-54.

- DAS, D. 2015. *Algal Biorefinery: An Integrated Approach*. 1st ed. 2015. ed. Cham: Springer International Publishing : Imprint: Springer.
- DAVIES, S., BAUER, C., BARKER, P. & FREEMAN, R. 1985. The dynamic range problem in NMR. *Journal of Magnetic Resonance (1969)*, 64, 155-159.
- DE JONG, E., HIGSON, A., WALSH, P. & WELLISCH, M. 2012. Bio-based chemicals value added products from biorefineries. *IEA Bioenergy, Task42 Biorefinery*, 34.
- DEBEBE, A., TEMESGEN, S., REDI-ABSHIRO, M., CHANDRAVANSI, B. S. & ELE, E. 2018. Improvement in Analytical Methods for Determination of Sugars in Fermented Alcoholic Beverages. *Journal of analytical methods in chemistry*, 2018, 4010298-4010298.
- DELBECQ, F., WANG, Y. T. & LEN, C. 2016. Conversion of xylose, xylan and rice husk into furfural via betaine and formic acid mixture as novel homogeneous catalyst in biphasic system by microwave-assisted dehydration. *Journal of Molecular Catalysis a-Chemical*, 423, 520-525.
- DELBECQ, F., WANG, Y. T., MURALIDHARA, A., EL OUARDI, K., MARLAIR, G. & LEN, C. 2018. Hydrolysis of Hemicellulose and Derivatives-A Review of Recent Advances in the Production of Furfural. *Frontiers in Chemistry*, 6.
- DOE, U. S. 2015. *Systems Biology to Advance Understanding of Carbon Cycling and Other Biogeochemical Processes*.
- EDENHOFER, O., INTERGOVERNMENTAL PANEL ON CLIMATE CHANGE. WORKING GROUP, P. & WORKING GROUP, I. I. I. T. S. U. 2014. *Climate change 2014 : mitigation of climate change : Working Group III contribution to the Fifth assessment report of the Intergovernmental Panel on Climate Change*. New York, New York: Cambridge University Press.
- FAVA, F., TOTARO, G., DIELS, L., REIS, M., DUARTE, J., CARIOCA, O. B., POGGI-VARALDO, H. M. & FERREIRA, B. S. 2015. Biowaste biorefinery in Europe: opportunities and research & development needs. *New Biotechnology*, 32, 100-108.
- GARCÍA-SANCHO, C., SÁDABA, I., MORENO-TOST, R., MÉRIDA-ROBLES, J., SANTAMARÍA-GONZÁLEZ, J., LÓPEZ-GRANADOS, M. & MAIRELES-TORRES, P. 2013. Dehydration of Xylose to Furfural over MCM-41-Supported Niobium-Oxide Catalysts. *ChemSusChem*, 6, 635-642.
- GÓMEZ MILLÁN, G., BANGALORE ASHOK, R. P., OINAS, P., LLORCA, J. & SIXTA, H. 2020. Furfural production from xylose and birch hydrolysate liquor in a biphasic system and techno-economic analysis. *Biomass Conversion and Biorefinery*.
- GÓMEZ MILLÁN, G., PHIRI, J., MÄKELÄ, M., MALONEY, T., BALU, A. M., PINEDA, A., LLORCA, J. & SIXTA, H. 2019. Furfural production in a biphasic system using a carbonaceous solid acid catalyst. *Applied catalysis. A, General*, 585, 117180.
- GUNST, R. F. & MASON, R. L. 2009. Fractional factorial design. *Wiley interdisciplinary reviews. Computational statistics*, 1, 234-244.
- GUO, W., HEERES, H. J. & YUE, J. 2020. Continuous synthesis of 5-hydroxymethylfurfural from glucose using a combination of AlCl₃ and HCl as catalyst in a biphasic slug flow capillary microreactor. *Chemical Engineering Journal*, 381, 122754.
- GÜRBÜZ, E. I., GALLO, J. M. R., ALONSO, D. M., WETTSTEIN, S. G., LIM, W. Y. & DUMESIC, J. A. 2013. Conversion of Hemicellulose into Furfural Using Solid Acid Catalysts in γ -Valerolactone. *Angew Chem Int Ed Engl*, 52, 1270-1274.
- HALLERAKER, H. V. & BARTH, T. 2020. Quantitative NMR analysis of the aqueous phase from hydrothermal liquefaction of lignin. *Journal of Analytical and Applied Pyrolysis*, 151, 104919.
- HANSEN, T. S., WOODLEY, J. M. & RIISAGER, A. 2009. Efficient microwave-assisted synthesis of 5-hydroxymethylfurfural from concentrated aqueous fructose. *Carbohydrate Research*, 344, 2568-2572.
- HITA, I., GHOREISHI, S., SANTOS, J. I., BARTH, T. & HEERES, H. J. 2021. Hydrothermal liquefaction versus catalytic hydrodeoxygenation of a bioethanol production stillage residue to platform chemicals: A comparative study. *Fuel Processing Technology*, 213, 106654.
- HOFFMANN, P. A. J., M. A. 1989. How wood is composed of cellulose: Structure and degradation process for waterlogged archaeological wood.

- HUA, D. R., WU, Y. L., LIU, Y. F., CHEN, Y., YANG, M. D., LU, X. N. & LI, J. 2016. Preparation of furfural and reaction kinetics of xylose dehydration to furfural in high-temperature water. *Petroleum Science*, 13, 167-172.
- HUANG, Y. B. & FU, Y. 2013. Hydrolysis of cellulose to glucose by solid acid catalysts. *Green Chemistry*, 15, 1095-1111.
- HUBBERT, M. K. Nuclear Energy and the Fossil Fuel. *Drilling and Production Practice*, 1956. API-56-007.
- HUBER, G. W., CHHEDA, J. N., BARRETT, C. J. & DUMESIC, J. A. 2005. Production of liquid alkanes by aqueous-phase processing of biomass-derived carbohydrates. *Science*, 308, 1446-1450.
- HUBER, G. W., IBORRA, S. & CORMA, A. 2006. Synthesis of transportation fuels from biomass: Chemistry, catalysts, and engineering. *Chemical Reviews*, 106, 4044-4098.
- HÜLSEY, M. J. 2018. Shell biorefinery: A comprehensive introduction. *Green Energy & Environment*, 3, 318-327.
- IEA 2020a. Sustainable Development Scenario, World Energy Model, IEA, Paris
- IEA 2020b. World Energy Outlook 2020, IEA, Paris.
- IPCC 2018. Global Warming of 1.5 °C : an IPCC special report on the impacts of global warming of 1.5 °C above pre-industrial levels and related global greenhouse gas emission pathways, in the context of strengthening the global response to the threat of climate change, sustainable development, and efforts to eradicate poverty. Sveits: IPCC.
- IROEGBU, A. O., SADIKU, E. R., RAY, S. S. & HAMAM, Y. 2020. Sustainable Chemicals: A Brief Survey of the Furans. *Chemistry Africa*, 3, 481-496.
- IUPAC 1997. Compendium of Chemical Terminology, 2nd ed. (the "Gold Book"). Compiled by A. D. McNaught and A. Wilkinson. *Blackwell Scientific Publications*.
- JIN, Z. F., KATSUMATA, K. S., LAM, T. B. T. & IYAMA, K. 2006. Covalent linkages between cellulose and lignin in cell walls of coniferous and nonconiferous woods. *Biopolymers*, 83, 103-110.
- KLEINERT, M. & BARTH, T. 2008. Phenols from Lignin. *Chemical Engineering & Technology*, 31, 736-745.
- KOUPAIE, E. H., DAHADHA, S., LAKEH, A. A. B., AZIZI, A. & ELBESHBISHY, E. 2019. Enzymatic pretreatment of lignocellulosic biomass for enhanced biomethane production-A review. *Journal of Environmental Management*, 233, 774-784.
- KUHNS, R. J. & SHAW, G. H. 2018. Navigating the Energy Maze : The Transition to a Sustainable Future. 1st ed. 2018. ed. Cham: Springer International Publishing : Imprint: Springer.
- KUMAR, B. & VERMA, P. 2021. Biomass-based biorefineries: An important archetype towards a circular economy. *Fuel*, 288.
- LAMMINPAA, K., AHOLA, J. & TANSKANEN, J. 2014. Kinetics of furfural destruction in a formic acid medium. *Rsc Advances*, 4, 60243-60248.
- LANCASTER, M. & CHEMISTRY, R. S. O. 2016. *Green chemistry : an introductory text*, Cambridge, Royal Society of Chemistry.
- LE GUENIC, S., DELBECQ, F., CEBALLOS, C. & LEN, C. 2015. Microwave-assisted dehydration of D-xylose into furfural by diluted inexpensive inorganic salts solution in a biphasic system. *Journal of Molecular Catalysis a-Chemical*, 410, 1-7.
- LEVITT, M. H. 2008. *Spin dynamics : basics of nuclear magnetic resonance*, Chichester, Wiley.
- LI, W., ZHU, Y., LU, Y., LIU, Q., GUAN, S., CHANG, H.-M., JAMEEL, H. & MA, L. 2017. Enhanced furfural production from raw corn stover employing a novel heterogeneous acid catalyst. *Bioresour Technol*, 245, 258-265.
- LI, Y. J., CAO, X. F., SUN, S. N., YUAN, T. Q., WEN, J. L., WANG, X. L., XIAO, L. P. & SUN, R. C. 2020. An integrated biorefinery process to comprehensively utilize corn stalk in a MIBK/water/Al(NO₃)₃center dot 9H(2)O biphasic system: Chemical and morphological changes. *Industrial Crops and Products*, 147.
- LIN, Q., LIAO, S., LI, L., LI, W., YUE, F., PENG, F. & REN, J. 2020. Solvent effect on xylose conversion under catalyst-free conditions: insights from molecular dynamics simulation and experiments Electronic supplementary information (ESI) available. See DOI: 10.1039/c9gc03624e. 22, 532-539.

- LIU, C., WEI, L. S., YIN, X. Y., WEI, M., XU, J. M., JIANG, J. C. & WANG, K. 2020. Selective conversion of hemicellulose into furfural over low-cost metal salts in a gamma-valerolactone/water solution. *Industrial Crops and Products*, 147.
- LIU, F., BOISSOU, F., VIGNAULT, A., LEME, L., MARINKOVIC, S., ESTRINE, B., DE OLIVEIRA VIGIER, K. & JRME, F. 2014a. Conversion of wheat straw to furfural and levulinic acid in a concentrated aqueous solution of betane hydrochloride. *RSC Adv.*, 4, 28836-28841.
- LIU, H. T., HU, H. R., BAKTASH, M. M., JAHAN, M. S., AHSAN, L. & NI, Y. H. 2014b. Kinetics of furfural production from pre-hydrolysis liquor (PHL) of a kraft-based hardwood dissolving pulp production process. *Biomass & Bioenergy*, 66, 320-327.
- LUNDSTEDT, T., SEIFERT, E., ABRAMO, L., THELIN, B., NYSTRÖM, Å., PETERSEN, J. & BERGMAN, R. 1998. Experimental design and optimization. *Chemometrics and Intelligent Laboratory Systems*, 42, 3-40.
- LUO, Y., LI, Z., LI, X., LIU, X., FAN, J., CLARK, J. H. & HU, C. 2019. The production of furfural directly from hemicellulose in lignocellulosic biomass: A review. *Catalysis today*, 319, 14-24.
- LUO, Y., LI, Z., ZUO, Y., SU, Z. & HU, C. 2017. A Simple Two-Step Method for the Selective Conversion of Hemicellulose in Pubescens to Furfural. *ACS Sustainable Chemistry & Engineering*, 5, 8137-8147.
- LØHRE, C. 2021. Personal communication.
- LØHRE, C., KLEINERT, M. & BARTH, T. 2017. Organosolv extraction of softwood combined with lignin-to-liquid-solvolytic as a semi-continuous percolation reactor. *Biomass and Bioenergy*, 99, 147-155.
- LØHRE, C., LAUGERUD, G.-A. A., HUIJGEN, W. J. J. & BARTH, T. 2018. Lignin-to-Liquid-Solvolytic (LtL) of Organosolv Extracted Lignin. *ACS Sustainable Chemistry & Engineering*, 6, 3102-3112.
- LØHRE, C., UNDERHAUG, J., BRUSLETTO, R. & BARTH, T. 2021. A Workup Protocol Combined with Direct Application of Quantitative Nuclear Magnetic Resonance Spectroscopy of Aqueous Samples from Large-Scale Steam Explosion of Biomass. *ACS Omega*.
- MARCOTULLIO, G. & DE JONG, W. 2010. Chloride ions enhance furfural formation from d-xylose in dilute aqueous acidic solutions. *Green Chemistry*, 12, 1739-1746.
- MARISCAL, R., MAIRELES-TORRES, P., OJEDA, M., SÁDABA, I. & LÓPEZ GRANADOS, M. 2016. Furfural: a renewable and versatile platform molecule for the synthesis of chemicals and fuels. *Energy & Environmental Science*, 9, 1144-1189.
- MARISCAL, R., OJEDA, M., LOPEZ GRANADOS, M., CAMPOS MOLINA, M. J., MARISCAL, R., OJEDA, M. & LÓPEZ GRANADOS, M. 2012. Cyclopentyl methyl ether: A green co-solvent for the selective dehydration of lignocellulosic pentoses to furfural. [New York, NY] :.
- MARKETSANDMARKETS 2019. Furfural Market by Raw Material (Sugarcane Bagasse, Corncob, Rice Husk and Others), Application (Derivatives (Furfural Alcohol and Other Derivatives), solvent) and Region (Asia-Pacific, Americas, Europe, Middle East and Africa) - Global Forecast to 2024, Report Code: CH 7382.
- MATSAGAR, B. M., MUNSHI, M. K., KELKAR, A. A. & DHEPE, P. L. 2015. Conversion of concentrated sugar solutions into 5-hydroxymethyl furfural and furfural using Bronsted acidic ionic liquids. *Catalysis Science & Technology*, 5, 5086-5090.
- MATVARETABELLEN 2020.
- MAZAR, A., JEMAA, N., AL DAJANI, W. W., MARINOVA, M. & PERRIER, M. 2017. Furfural production from a pre-hydrolysate generated using aspen and maple chips. *Biomass & Bioenergy*, 104, 8-16.
- MAZAR, A., JEMAA, N., AL DAJANI, W. W., MARINOVA, M. & PERRIER, M. 2018. Comparative study: Furfural production from two types of pre-hydrolysates produced using aspen and maple chips. *Biomass & Bioenergy*, 111, 103-113.
- MCBRIDE, K., SUNDMACHER, K. & LINKE, S. 2020. Systematic Green Solvent Selection for the Hydroformylation of Long-Chain Alkenes. Washington, DC :.
- MELLMER, M. A., SENNER, C., GALLO, J. M. R., LUTERBACHER, J. S., ALONSO, D. M. & DUMESIC, J. A. 2014. Solvent Effects in Acid-Catalyzed Biomass Conversion Reactions. *Angewandte Chemie-International Edition*, 53, 11872-11875.

- MILLAN, G. G., HELLSTEN, S., LLORCA, J., LUQUE, R., SIXTA, H. & BALU, A. M. 2019. Recent Advances in the Catalytic Production of Platform Chemicals from Holocellulosic Biomass. *Chemcatchem*, 11, 2022-2042.
- MILLER, J. M. 2005. *Chromatography : concepts and contrasts*, Hoboken, N.J, Wiley.
- MIRZAEI, H. M. & KARIMI, B. 2016. Sulphanilic acid as a recyclable bifunctional organocatalyst in the selective conversion of lignocellulosic biomass to 5-HMF. *Green Chemistry*, 18, 2282-2286.
- MITMESSER, S. & COMBS, M. 2017. Chapter 23 - Prebiotics: Inulin and Other Oligosaccharides. In: FLOCH, M. H., RINGEL, Y. & ALLAN WALKER, W. (eds.) *The Microbiota in Gastrointestinal Pathophysiology*. Boston: Academic Press.
- MITTAL, A., BLACK, S. K., VINZANT, T. B., O'BRIEN, M., TUCKER, M. P. & JOHNSON, D. K. 2017. Production of Furfural from Process-Relevant Biomass-Derived Pentoses in a Biphasic Reaction System. *ACS Sustainable Chem. Eng*, 5, 5694-5701.
- MITTAL, A., PILATH, H. M. & JOHNSON, D. K. 2020. Direct Conversion of Biomass Carbohydrates to Platform Chemicals: 5-Hydroxymethylfurfural (HMF) and Furfural. *Energy & Fuels*, 34, 3284-3293.
- MIZELL, J. 2021. Diode-Array Detection can be used to identify unknown peaks observed in chromatography.
- MORAIS, A. R. C., MATUCHAKI, M., ANDREAUS, J. & BOGEL-LUKASIK, R. 2016. A green and efficient approach to selective conversion of xylose and biomass hemicellulose into furfural in aqueous media using high-pressure CO₂ as a sustainable catalyst. *Green Chemistry*, 18, 2985-2994.
- MOTAGAMWALA, A. H., WON, W. Y., SENER, C., ALONSO, D. M., MARAVELIAS, C. T. & DUMESIC, J. A. 2018. Toward biomass-derived renewable plastics: Production of 2,5-furandicarboxylic acid from fructose. *Science Advances*, 4.
- NOAA 2020.
- PALLARDY, S. G. & KOZLOWSKI, T. T. 2008. *Physiology of woody plants*. 3rd ed. ed. Amsterdam ;,Boston: Elsevier.
- PANIAGUA, M., MELERO, J. A., IGLESIAS, J., JUAREZ, P., LÓPEZ-AGUADO, C., MELERO, J. A., JUÁREZ, P., LÓPEZ GRANADOS, M. & MORALES, G. 2020. Stable Continuous Production of γ -Valerolactone from Biomass-Derived Levulinic Acid over Zr-Al-Beta Zeolite Catalyst. Basel, Switzerland :.
- PATIL, S. K. R. & LUND, C. R. F. 2011. Formation and Growth of Humins via Aldol Addition and Condensation during Acid-Catalyzed Conversion of 5-Hydroxymethylfurfural. *Energy & Fuels*, 25, 4745-4755.
- PAVIA, D. L. 2015. *Introduction to spectroscopy*, Stamford, Conn, Cengage Learning.
- PAWAR, H. S. 2020. Purification of 5-Hydroxymethyl Furfural from Side Products of Fructose Dehydration Reaction in a Green Solvent. *ChemistrySelect (Weinheim)*, 5, 6851-6855.
- PELETEIRO, S., GALLETTI, A. M. R., ANTONETTI, C., SANTOS, V. & PARAJO, J. C. 2018. Manufacture of Furfural from Xylan-containing Biomass by Acidic Processing of Hemicellulose-Derived Saccharides in Biphasic Media Using Microwave Heating. *Journal of Wood Chemistry and Technology*, 38, 198-213.
- PHOLJAROEN, B., LI, N., YANG, J. F., LI, G. Y., WANG, W. T., WANG, A. Q., CONG, Y., WANG, X. D. & ZHANG, T. 2014. Production of Renewable Jet Fuel Range Branched Alkanes with Xylose and Methyl Isobutyl Ketone. *Industrial & Engineering Chemistry Research*, 53, 13618-13625.
- PINO, N., BUITRAGO-SIERRA, R. & LÓPEZ, D. 2020. Conversion of Biomass-Derived Furans to Fuel-Range Hydrocarbons: Use of Palm Oil Empty Fruit Bunches. *Waste and Biomass Valorization*, 11, 565-577.
- QI, L., MUI, Y. F., LO, S. W., LUI, M. Y., AKIEN, G. R. & HORVATH, I. T. 2014. Catalytic Conversion of Fructose, Glucose, and Sucrose to 5-(Hydroxymethyl)furfural and Levulinic and Formic Acids in gamma-Valerolactone As a Green Solvent. *Acs Catalysis*, 4, 1470-1477.
- QI, Z., WANG, Q., LIANG, C., YUE, J., LIU, S., MA, S., WANG, X., WANG, Z., LI, Z. & QI, W. 2020. Highly Efficient Conversion of Xylose to Furfural in a Water-MIBK System Catalyzed by Magnetic Carbon-Based Solid Acid. *Industrial & Engineering Chemistry Research*, 59, 17046-17056.

- RASMUSSEN, H., SORENSEN, H. R. & MEYER, A. S. 2014. Formation of degradation compounds from lignocellulosic biomass in the biorefinery: sugar reaction mechanisms. *Carbohydrate Research*, 385, 45-57.
- ROMO, J. E., BOLLAR, N. V., ZIMMERMANN, C. J. & WETTSTEIN, S. G. 2018. Conversion of Sugars and Biomass to Furans Using Heterogeneous Catalysts in Biphasic Solvent Systems. *Chemcatchem*, 10, 4819-4830.
- SADHUKHAN, J., NG, K. S. & HERNANDEZ, E. M. 2014. *Biorefineries and Chemical Processes : Design, Integration and Sustainability Analysis*, New York, UNITED KINGDOM, John Wiley & Sons, Incorporated.
- SAHU, R. & DHEPE, P. L. 2012. A One-Pot Method for the Selective Conversion of Hemicellulose from Crop Waste into C5 Sugars and Furfural by Using Solid Acid Catalysts. *Chemsuschem*, 5, 751-761.
- SCHMIDT, R. K., KARPLUS, M. & BRADY, J. W. 1996. The Anomeric Equilibrium in d-Xylose: Free Energy and the Role of Solvent Structuring. *Journal of the American Chemical Society*, 118, 541-546.
- SCHOBERT, H. 2013. *Chemistry of Fossil Fuels and Biofuels*, Cambridge University Press.
- SEEMALA, B., HARITOS, V. & TANKSALE, A. 2016. Levulinic Acid as a Catalyst for the Production of 5-Hydroxymethylfurfural and Furfural from Lignocellulose Biomass. *Chemcatchem*, 8, 640-647.
- SENER, C., GALLO, J. M. R., LUTERBACHER, J. S., ALONSO, D. M., MELLMER, M. A., GALLO, J. M. R., LUTERBACHER, J. S. & DUMESIC, J. A. 2014. Solvent Effects in Acid-Catalyzed Biomass Conversion Reactions. International ed. in English. ed. Weinheim/Bergstr. .:
- SHELDON, R. A. 2014. Green and sustainable manufacture of chemicals from biomass: state of the art. *Green Chemistry*, 16, 950-963.
- SHI, N., LIU, Q. Y., WANG, T. J., ZHANG, Q., MA, L. L. & CAI, C. L. 2015. Production of 5-Hydroxymethylfurfural and Furfural from Lignocellulosic Biomass in Water-Tetrahydrofuran Media with Sodium Bisulfate. *Chinese Journal of Chemical Physics*, 28, 650-656.
- SIGMA-ALDRICH 2020. Furfural.
- SUNDARAM, S. 2015. Biorefineries and chemical processes: design, integration and sustainability analysis. *Green Processing and Synthesis*, 4, 65-66.
- SWEYGERS, N., DEPUYDT, D. E. C., VAN VUURE, A. W., DEGREVE, J., POTTERS, G., DEWIL, R. & APPELS, L. 2020. Simultaneous production of 5-hydroxymethylfurfural and furfural from bamboo (*Phyllostachys nigra* "Boryana") in a biphasic reaction system. *Chemical Engineering Journal*, 386.
- SZYMANSKA-CHARGOT, M., CHYLINSKA, M., GDULA, K., KOZIOL, A. & ZDUNEK, A. 2017. Isolation and Characterization of Cellulose from Different Fruit and Vegetable Pomaces. *Polymers*, 9.
- THE NORWEGIAN GOVERNMENT, M. O. T., INDUSTRY AND FISHERIES 2016. Kjente ressurser - uante muligheter - Regjeringens bioøkonomistrategi.
- TIMOKHIN, B. V., BARANSKY, V. A. & ELISEEVA, G. D. 1999. Levulinic acid in organic synthesis. *Uspekhi Khimii*, 68, 80-93.
- UNDERHAUG, J. 2004. An NMR study of α -lactalbumin pKa-determinations and structural calculations. The University of Bergen.
- VEERA SWAMY KONKALA PRAMOD KUMAR, D. 2017. Sulfamic acid as a green, reusable catalyst for stepwise, tandem & one-pot solvent-free synthesis of pyrazole derivatives. *Chinese Chemical Letters*, 28, 1571-1576.
- VILLAS-BOAS, S. G., ESPOSITO, E. & DE MENDONCA, M. M. 2003. Bioconversion of apple pomace into a nutritionally enriched substrate by *Candida utilis* and *Pleurotus ostreatus*. *World Journal of Microbiology & Biotechnology*, 19, 461-467.
- VILONEN, K., NIEMELA, M., KARINEN, R. & NIEMELÄ, M. 2011. Biorefining: Heterogeneously Catalyzed Reactions of Carbohydrates for the Production of Furfural and Hydroxymethylfurfural. Weinheim, Germany .:
- WANG, M., LIU, C., LI, Q. B. & XU, X. X. 2015. Theoretical insight into the conversion of xylose to furfural in the gas phase and water. *Journal of Molecular Modeling*, 21.

- WANG, Q., QI, W., WANG, W., ZHANG, Y., LEKSAWASDI, N., ZHUANG, X., YU, Q. & YUAN, Z. 2019. Production of furfural with high yields from corncob under extremely low water/solid ratios. *Renewable Energy*, 144, 139-146.
- WEINGARTEN, R., CHO, J., CONNER, J. W. C. & HUBER, G. W. 2010a. Kinetics of furfural production by dehydration of xylose in a biphasic reactor with microwave heating. *Green chemistry : an international journal and green chemistry resource : GC*, 12, 1423-1429.
- WEINGARTEN, R., CHO, J., CONNER, W. & HUBER, G. 2010b. Kinetics of furfural production by dehydration of xylose in a biphasic reactor with microwave heating. *Green Chem.*, 12, 1423-1429.
- WERPY, T., PETERSEN, G., ADEN, A., BOZELL, J., HOLLADAY, J., WHITE, J., MANHEIM, A., ELIOT, D., LASURE, L., JONES, S. & DEPARTMENT OF ENERGY WASHINGTON, D. C. 2004. Top Value Added Chemicals From Biomass. Volume 1 - Results of Screening for Potential Candidates From Sugars and Synthesis Gas.
- WERTZ, J.-L. & BÉDUÉ, O. 2013. *Lignocellulosic Biorefineries*.
- WILLIAMS, D. L. H. 2004. Chapter 2 - Nitrosation at nitrogen centres. In: WILLIAMS, D. L. H. (ed.) *Nitrosation Reactions and the Chemistry of Nitric Oxide*. Amsterdam: Elsevier Science.
- WRIGSTEDT, P., KESKIVÄLI, J. & REPO, T. 2016. Microwave-enhanced aqueous biphasic dehydration of carbohydrates to 5-hydroxymethylfurfural. *RSC Advances*, 6, 18973-18979.
- XING, R., QI, W. & HUBER, G. W. 2011. Production of furfural and carboxylic acids from waste aqueous hemicellulose solutions from the pulp and paper and cellulosic ethanol industries. *Energy & environmental science*, 4, 2193.
- XING, R., SUBRAHMANYAM, A. V., OLCAY, H., QI, W., VAN WALSUM, G. P., PENDSE, H. & HUBER, G. W. 2010. Production of jet and diesel fuel range alkanes from waste hemicellulose-derived aqueous solutions Electronic supplementary information (ESI) available: Tables S1 and S2. See DOI: 10.1039/c0gc00263a. 12, 1933-1946.
- XU, C., PAONE, E., RODRIGUEZ-PADRÓN, D., LUQUE, R. & MAURIELLO, F. 2020a. Recent catalytic routes for the preparation and the upgrading of biomass derived furfural and 5-hydroxymethylfurfural. *Chemical Society Reviews*, 49, 4273-4306.
- XU, C., PAONE, E., RODRÍGUEZ-PADRÓN, D., LUQUE, R. & MAURIELLO, F. 2020b. Recent catalytic routes for the preparation and the upgrading of biomass derived furfural and 5-hydroxymethylfurfural. *Chemical Society Reviews*, 49, 4273-4306.
- XU, S. Q., PAN, D. H., WU, Y. F., SONG, X. H., GAO, L. J., LI, W. Q., DAS, L. & XIAO, G. M. 2018. Efficient production of furfural from xylose and wheat straw by bifunctional chromium phosphate catalyst in biphasic systems. *Fuel Processing Technology*, 175, 90-96.
- YANG, T., ZHOU, Y.-H., ZHU, S.-Z., PAN, H. & HUANG, Y.-B. 2017. Insight into Aluminum Sulfate-Catalyzed Xylan Conversion into Furfural in a γ -Valerolactone/Water Biphasic Solvent under Microwave Conditions. *ChemSusChem*, 10, 4066-4079.
- YANG, W., LI, P., BO, D. & CHANG, H. 2012a. The optimization of formic acid hydrolysis of xylose in furfural production. *Carbohydr Res*, 357, 53-61.
- YANG, Y., HU, C.-W. & ABU-OMAR, M. M. 2012b. Synthesis of Furfural from Xylose, Xylan, and Biomass Using $AlCl_3 \cdot 6H_2O$ in Biphasic Media via Xylose Isomerization to Xylulose. *ChemSusChem*, 5, 405-410.
- YOUNG, R. A. 1985. Cellulose chemistry and its applications : edited by T.P. Nevell and S. Haig Zeronian, Ellis Horwood, Chichester, Sussex, 1985, 544 pages + Subject Index, £55.00. Elsevier Ltd.
- ZANG, G., SHAH, A. & WAN, C. 2020. Techno-economic analysis of an integrated biorefinery strategy based on one-pot biomass fractionation and furfural production. *Journal of Cleaner Production*, 260, 120837.
- ZEITSCH, K. J., LI, JOSHUA Q. 2001. The Chemistry and Technology of Furfural and its Many By-products: Karl J. Zeitsch; Elsevier, 2000, 358 pp, US\$ 235.00 (hardback), ISBN: 0-444-50351-X. *Chemical Engineering Journal*, 81, 338-339.
- ZHANG, Q., WANG, C., MAO, J., RAMASWAMY, S., ZHANG, X. & XU, F. 2019. Insights on the efficiency of bifunctional solid organocatalysts in converting xylose and biomass into furfural in a GVL-water solvent. *Industrial Crops and Products*, 138, 111454.

- ZHANG, T. Y., KUMAR, R. & WYMAN, C. E. 2013. Enhanced yields of furfural and other products by simultaneous solvent extraction during thermochemical treatment of cellulosic biomass. *Rsc Advances*, 3, 9809-9819.
- ZHENG, Y., ZHAO, J., XU, F. & LI, Y. 2014. Pretreatment of lignocellulosic biomass for enhanced biogas production. *Progress in energy and combustion science*, 42, 35-53.

APPENDICES

APPENDIX A – STRUCTURAL ELUCIDATIONS

APPENDIX A1 – STRUCTURAL ELUCIDATION OF α AND β -D-XYLOSE

The following color-coding has been used throughout the structural elucidation of D-xylose: **Blue = α - D - Xylose**. **Red = β - D - Xylose**. Both coupling constants and relative peak intensity was used in order to differentiate between certain peaks in the two anomers. As described in chapter 4.1.2, The Karplus equation describes the relationship between the 3J -coupling constants and dihedral torsion angles in NMR spectroscopy. The closer this torsion angle is to 90° , the smaller the vicinal coupling constant ($^3J_{\text{HH}}$). The closer the torsion angle is to 0° and 180° , the larger the coupling constant will be. As a result, the $^3J_{\text{HH}}$ -coupling between hydrogen 1 and 6 in the α - and β -anomer will be $\sim 3.70\text{Hz}$ and $\sim 7.90\text{Hz}$, respectively, due to the relative spatial orientation of the hydrogen atoms in the two anomers (table A1-1). In 1996, Schmidt and colleagues published an article describing the anomeric equilibrium of D-xylose in aqueous solutions. They found that the α -anomer is less stable than the β -anomer. Consequently, the relative percentage between the α - and β -pyranoid anomer present in an aqueous solution is 35% and 65%, respectively. By applying this knowledge to the ^1H -NMR spectrum (Figure A1-2), it is possible to say that the doublet located downfield at 5.20ppm belongs to the α -anomer, while the doublet at 4.58ppm belongs to the β -anomer (Schmidt et al., 1996). The high chemical shift of proton 6 in the two anomers is caused by proton deshielding due to the electron withdrawing effect of the pyranose-oxygen and the OH-group located on opposite sides of the proton.

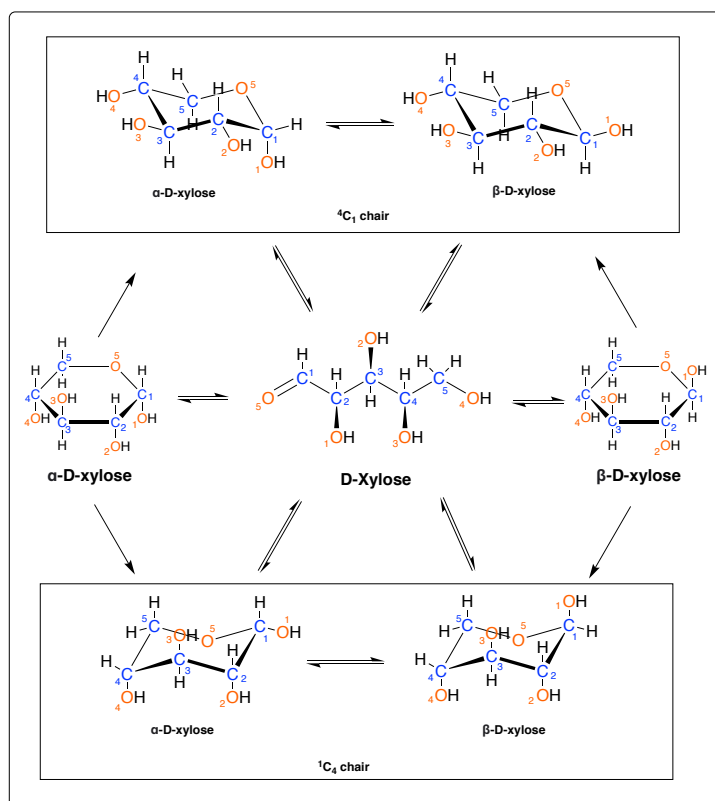


Figure A1-1: 4C_1 and 1C_4 -chair conformations of α - and β -D-xylose.

Table A1-1: ¹H-NMR chemical shifts for D-xylose standards at different pH (Neo-600 MHz).

Chemical environment	Chemical shift. pH-adjusted (7.40) [ppm]	Chemical shift pH = 1.99 [ppm]	Chemical shift pH = 5.19 [ppm]	Chemical shift. pH = 11.13 [ppm]	Multiplicity	Peaks Exponential multiplication	Coupling constant. J [Hz]	Integration value	Atom number	Position
1	3.23	3.21	3.23	3.22	dd		9.39. 7.89	1H	1	
2	3.32	3.31	3.32	3.32	dd		11.57. 10.64	1H	2	
3	3.43	3.42	3.43	3.43	t		9.26. 9.26	1H	3	
4	3.53	3.51	3.52	3.52	dd		9.43. 3.69	1H	1	
5	3.65	3.63	3.64	3.65	m		-	5H	4, 4, 2, 3, 5	
6	3.93	3.91	3.93	3.92	dd		11.55. 5.48	1H	5	
7	4.58	4.56	4.58	4.59	d		7.90	1H	6	
8	5.20	5.18	5.20	5.20	d		3.68	1H	6	

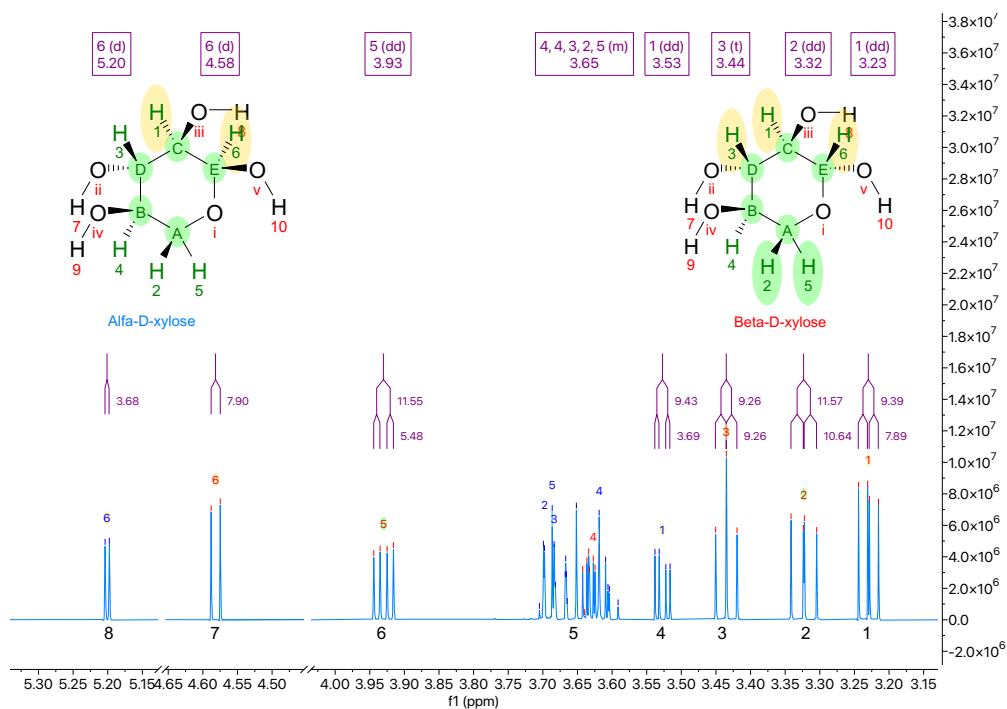


Figure A1-2: $^1\text{H-NMR}$ spectrum of xylose standard. pH adjusted (pH = 7.40). The sample contains both the α and the β anomer of D-xylose.

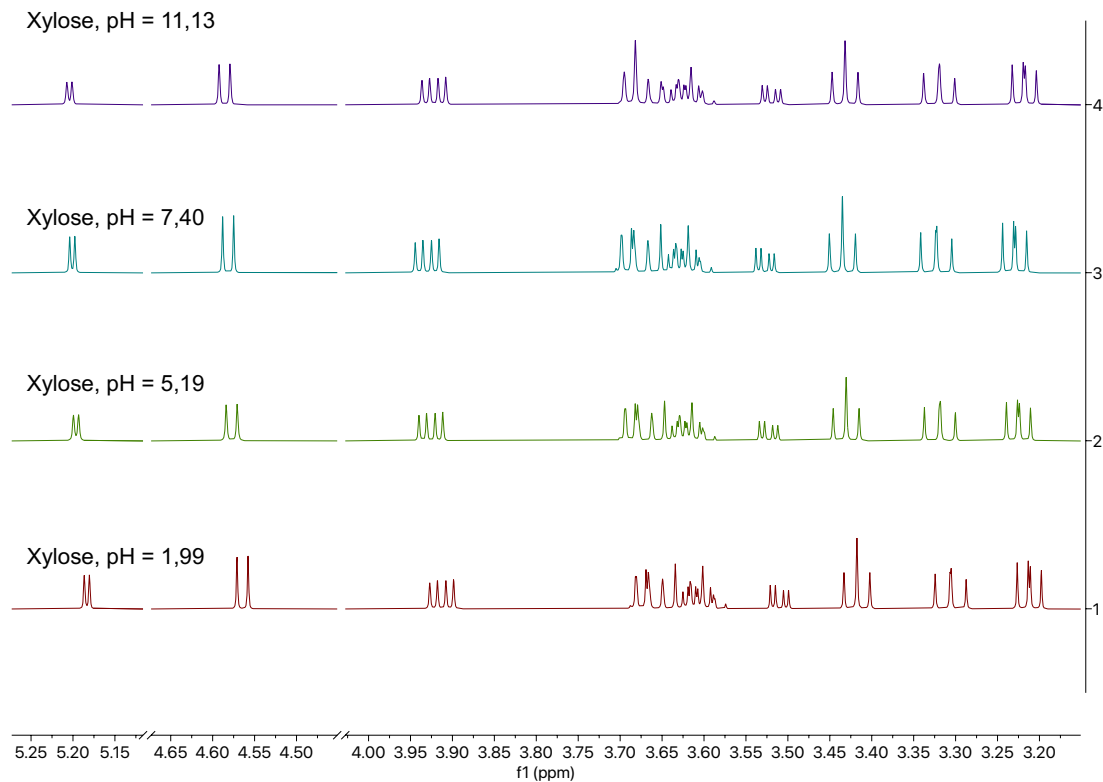


Figure A1-3: Chemical shifts (α - and β -D-xylose at different pH values. The figure clearly show that pH has minimal effect on the chemical shifts and relative positions of the peaks. The chemical shifts of the peaks slightly decreased when the pH was adjusted to 1.99.

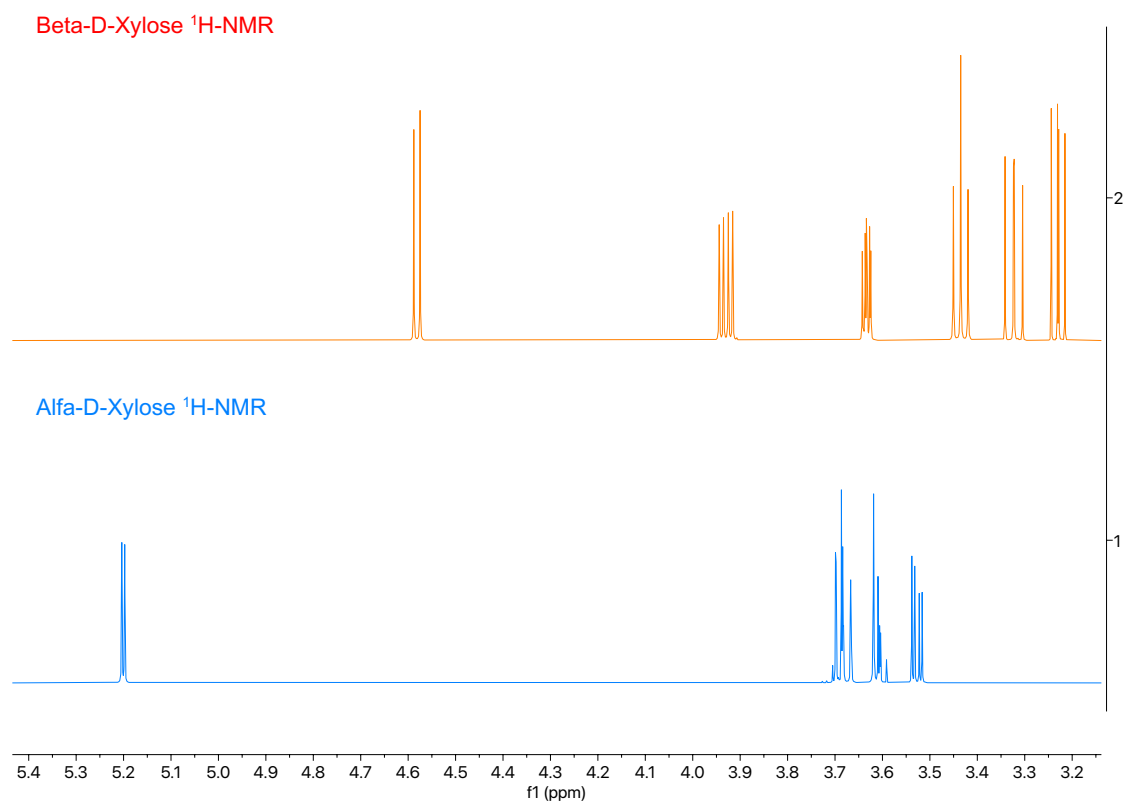
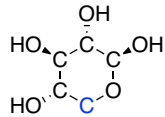
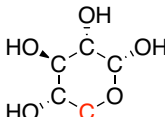
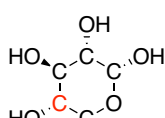
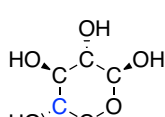
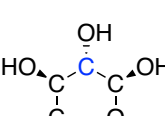
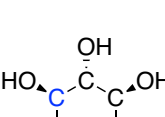


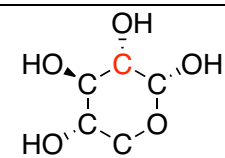
Figure A1-4: Separated/filtered ¹H-NMR spectra for α - and β -D-xylose. The chemical shifts of proton 2 and 5 in α -D-xylose are almost identical (0.001ppm difference).

Table A1-2: ^{13}C -NMR chemical shifts for D-xylose.

Chemical environment	Chemical shift	Position
A	63.70	
A	67.96	
B	72.12	
B	72.26	
C	74.35	
D	75.72	

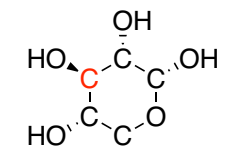
C

76.94



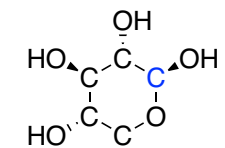
D

78.72



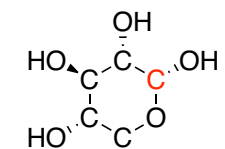
E

95.07



E

99.46



Blue = α - D - Xylose. Red = β - D - Xylose

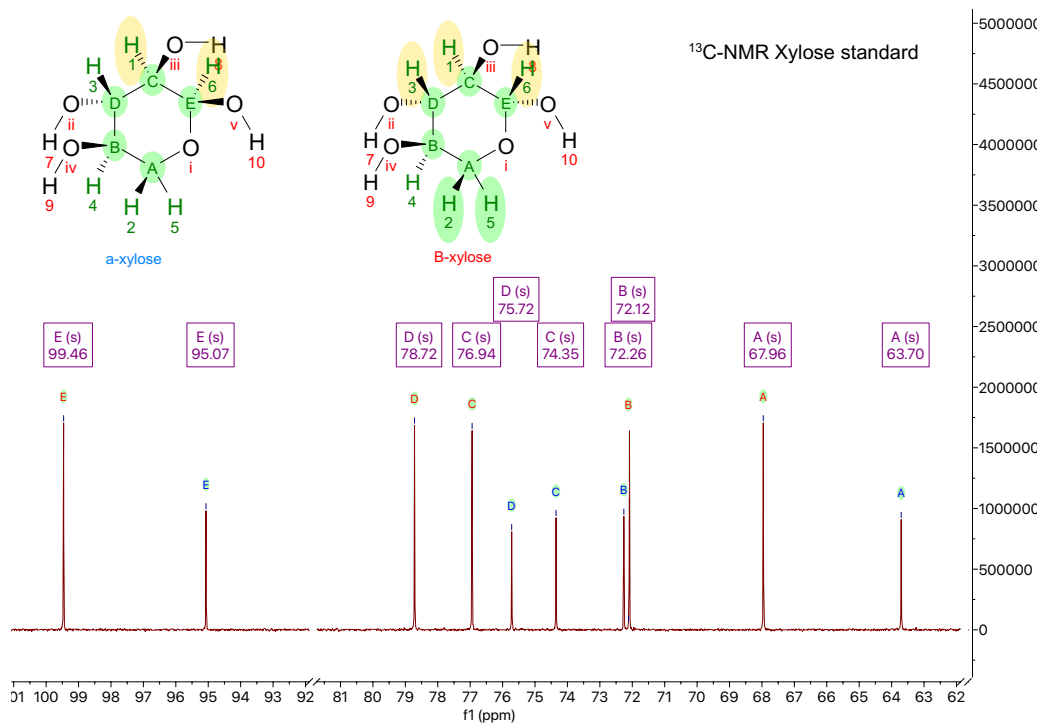


Figure A1-5: ¹³C-NMR spectra (D-xylose standard).

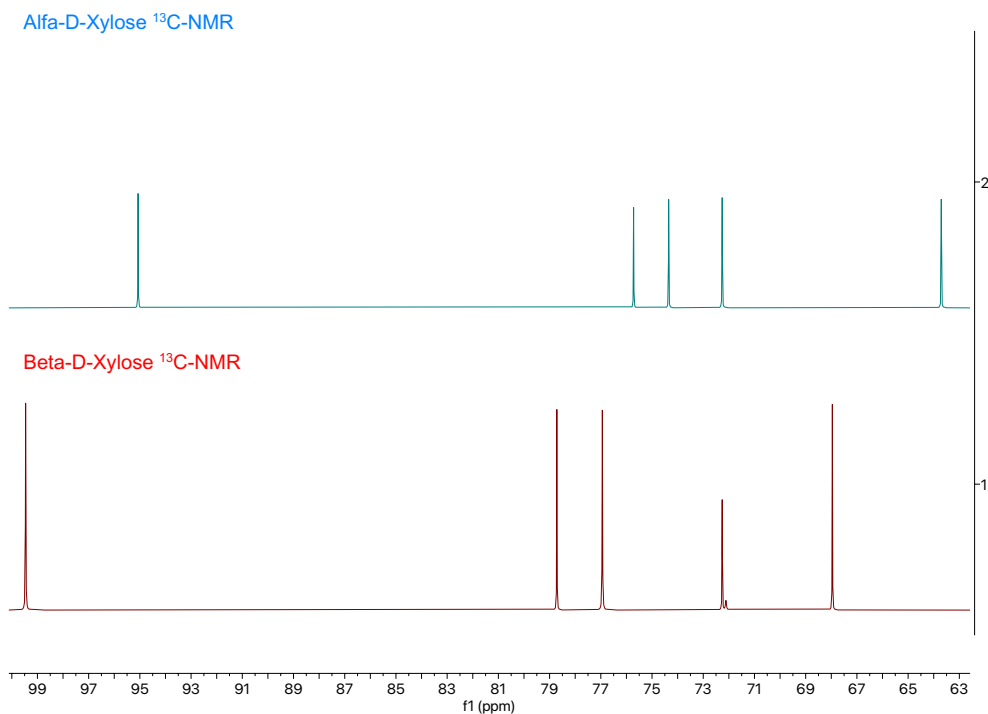


Figure A1-6: Separated (filtered) ¹³C-NMR spectra for α - and β -D-xylose.

COSY, Xylose standard

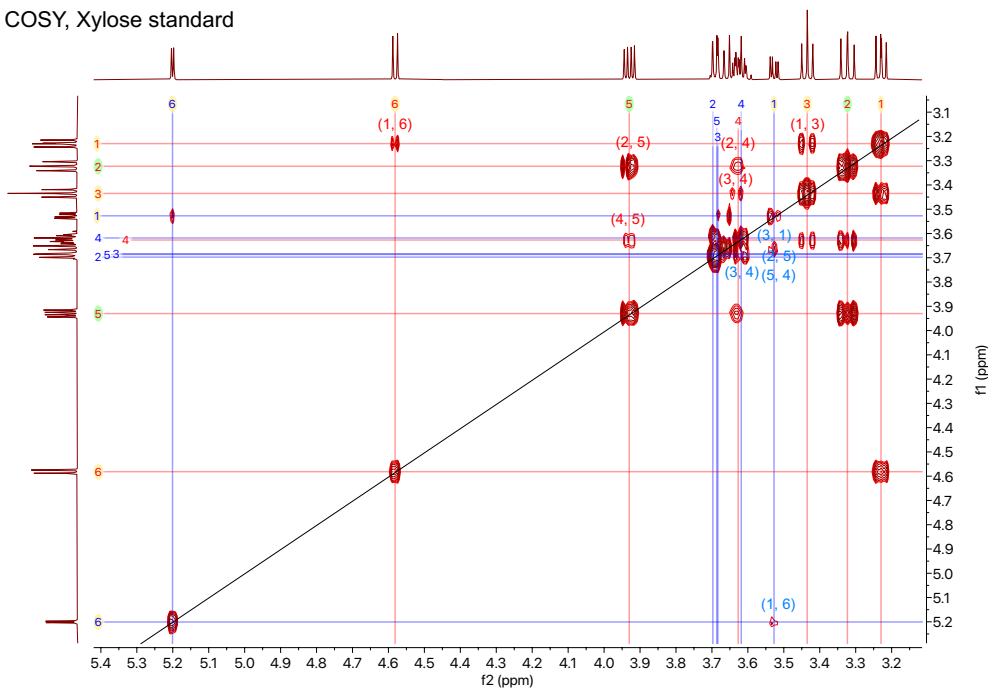


Figure A1-7: COSY (D-xylose standard).

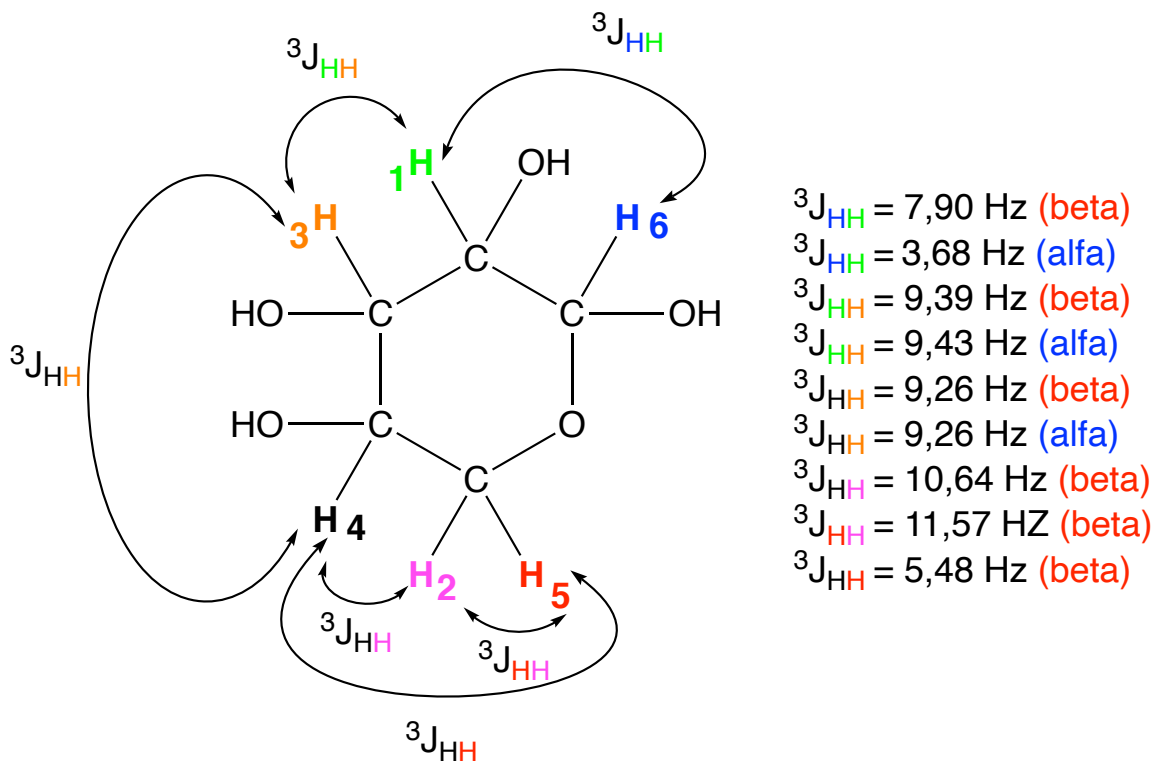
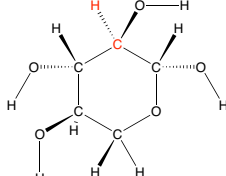
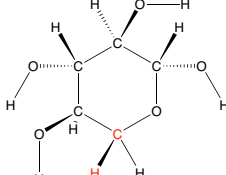
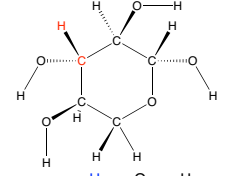
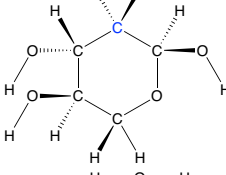
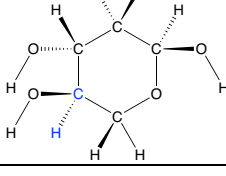
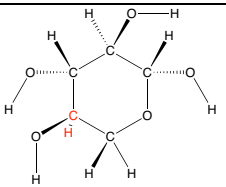
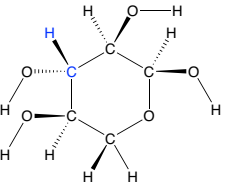
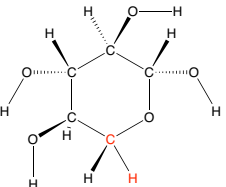
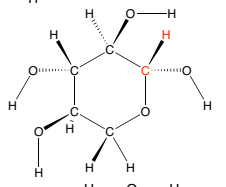
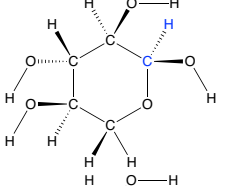
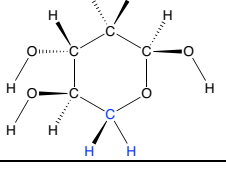


Figure A1-8: Coupling constants (D-xylose-standard).

Table A1-3: Cross-peak identification from high resolution HSQC. Focus area decreased from 165 to 55 ppm. number of points increased from 256 to 1024 and 25% non-uniform sampling (NOS) were used to decrease analysis time. Peak (k) is from the normal HSQC (figure A1-9).

Crosspeak #	¹ H-peak	¹³ C-peak	Anomer	Position
(a)	1 (3.23)	C (76.93)	<i>β</i> - D - Xylose	
(b)	2 (3.33)	A (67.96)	<i>β</i> - D - Xylose	
(c)	3 (3.43)	D (78.70)	<i>β</i> - D - Xylose	
(d)	1 (3.53)	C (74.35)	<i>α</i> - D - Xylose	
(e/f)	4 (3.62)	B (72.25)	<i>α</i> - D - Xylose	

(e/f)	4 (3.63)	B (72.09)	$\beta - D - Xylose$	
(g)	3 (3.67)	D (75.69)	$\alpha - D - Xylose$	
(h)	5 (3.94)	A (67.96)	$\beta - D - Xylose$	
(i)	6 (4.58)	E (99.43)	$\beta - D - Xylose$	
(j)	6 (5.20)	E (95.08)	$\alpha - D - Xylose$	
(k) (only appear in the normal HSQC)	2. 5(3.67)	A (63.60)	$\alpha - D - Xylose$	

HSQC, Xylose standard

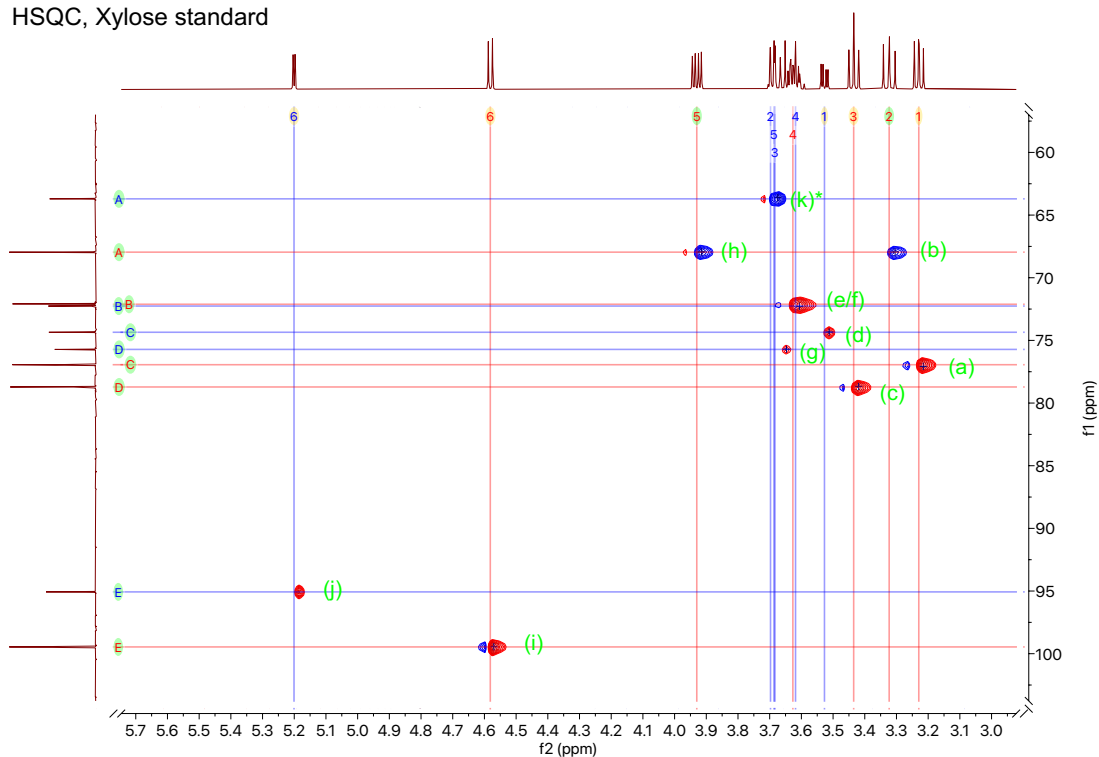


Figure A1-9: HSQC (D-xylose standard). Peak (k) was not visible in the high-resolution HSQC (figure A1-10).

High resolution HSQC,
Xylose std, 600 MHz

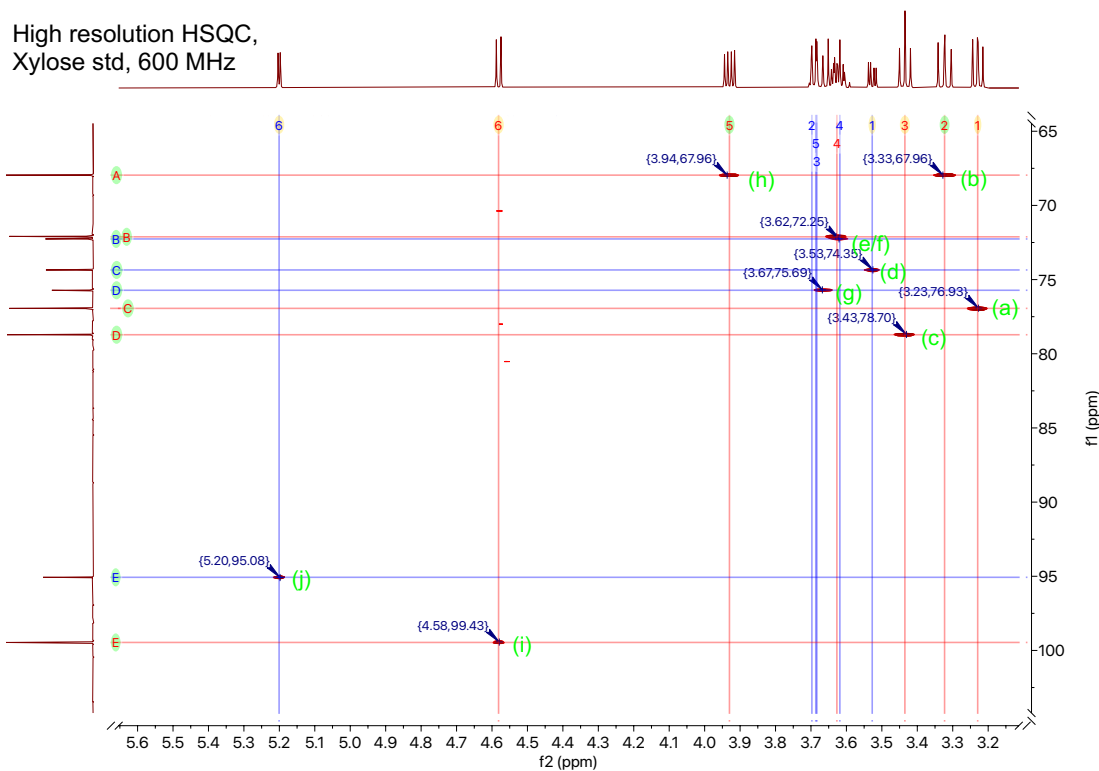


Figure A1-10: High resolution HSQC (D-xylose standard).

High resolution HSQC, zoomed

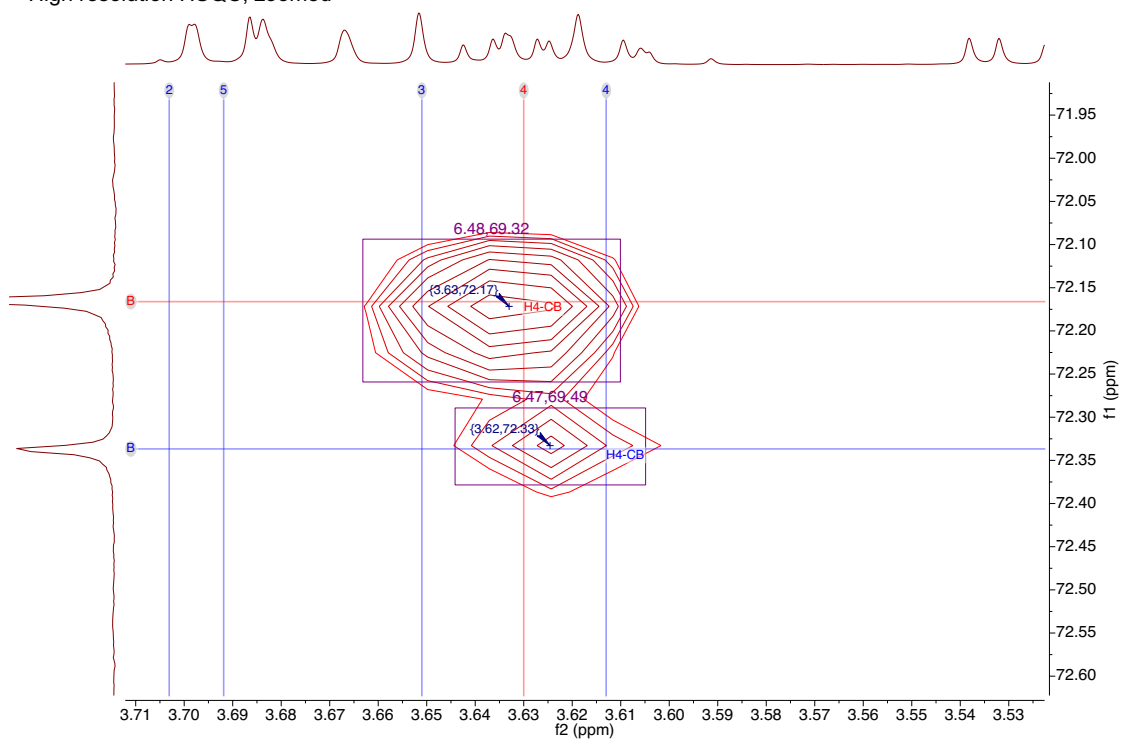
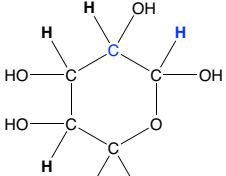
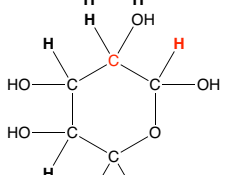
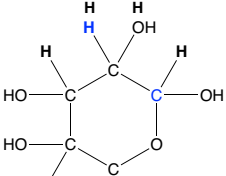
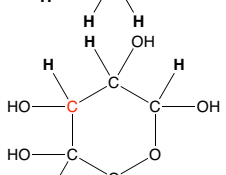
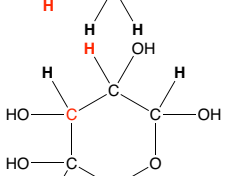
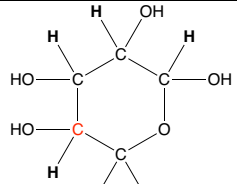
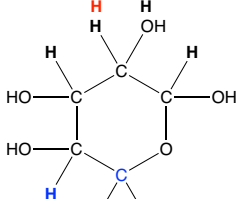
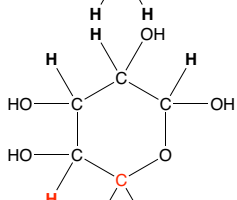
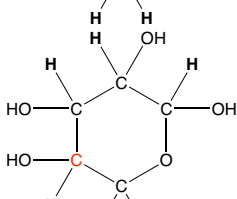
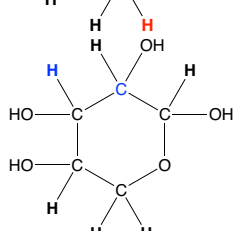
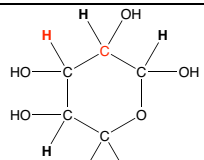
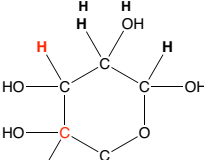
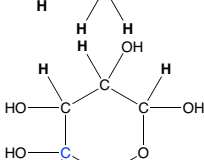
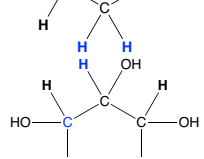
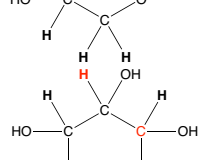


Figure A1-11: High resolution HSQC showing cross peaks between carbon B and proton 4 in both anomers.

Table A1-4: Cross peak identification from H2BC (D-xylose standard).

Cross-peak	(¹ H, ¹³ C)	Anomer	Position
A	(6.C)	<i>α</i> - D - Xylose	
B	(6.C)	<i>β</i> - D - Xylose	
C	(1.E)	<i>α</i> - D - Xylose	
D	(4.D)	<i>β</i> - D - Xylose	
E	(1.D)	<i>β</i> - D - Xylose	

F	(2.B)	<i>β - D - Xylose</i>	
G	(4.A)	<i>α - D - Xylose</i>	
H	(4.A)	<i>β - D - Xylose</i>	
I	(5.B)	<i>β - D - Xylose</i>	
J	(3.C)	<i>α - D - Xylose</i>	

K	(3.C)	<i>β - D - Xylose</i>	
L	(3.B)	<i>β - D - Xylose</i>	
M	(2/5.B)	<i>α - D - Xylose</i>	
N	(1.D)	<i>α - D - Xylose</i>	
O	(1.E)	<i>β - D - Xylose</i>	

H2BC specter Xylose

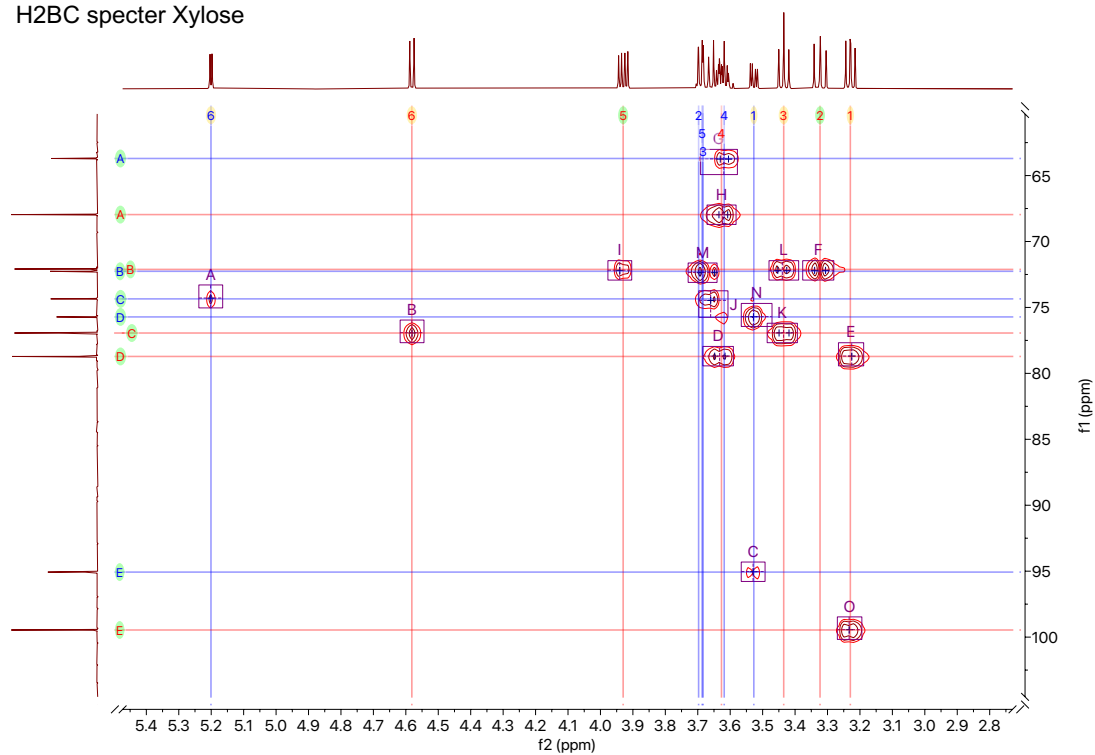
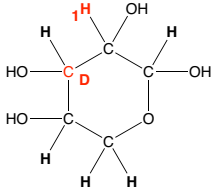
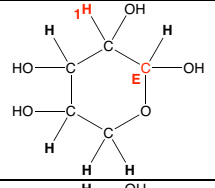
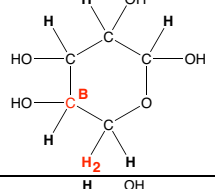
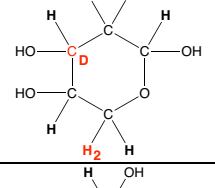
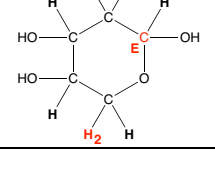
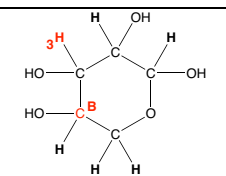
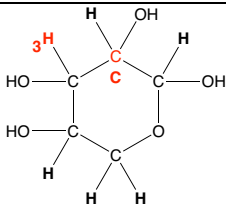
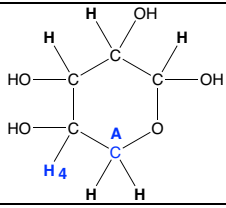
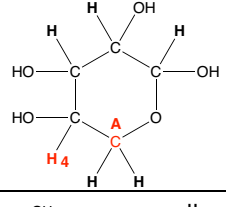
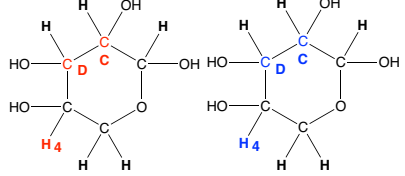
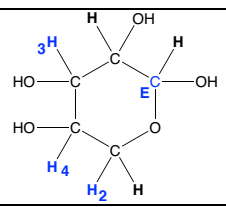
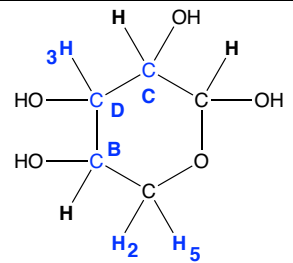
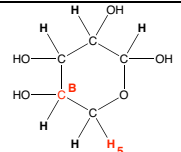
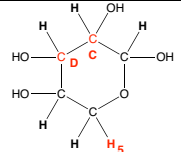
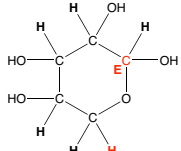
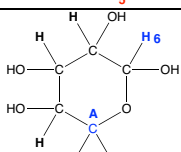
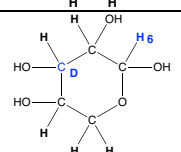


Figure A1-12: H2BC (D-xylose standard).

Table A1-5: Crosspeak identification from HMBC (D-xylose standard).

Cross peak #	(¹ H, ¹³ C)	Coupling	Anomer	Position
A	(1.D)	² J _{HC}	<i>β</i> - D - Xylose	
B	(1.E)	² J _{HC}	<i>β</i> - D - Xylose	
C	(2.B)	² J _{HC}	<i>β</i> - D - Xylose	
D	(2.D)	³ J _{HC}	<i>β</i> - D - Xylose	
E	(2.E)	³ J _{HC}	<i>β</i> - D - Xylose	

F	(3.B)	${}^2J_{\text{HC}}$	<i>$\beta - D - \text{Xylose}$</i>	
G	(3.C)	${}^2J_{\text{HC}}$	<i>$\beta - D - \text{Xylose}$</i>	
H	(4.A)	${}^2J_{\text{HC}}$	<i>$\alpha - D - \text{Xylose}$</i>	
I	(4.A)	${}^2J_{\text{HC}}$	<i>$\beta - D - \text{Xylose}$</i>	
J	(4.C)	${}^3J_{\text{HC}}$	<i>$\alpha - D - \text{Xylose}$</i>	
	(4.D)	${}^2J_{\text{HC}}$	<i>$\alpha - D - \text{Xylose}$</i>	
	(4.C)	${}^3J_{\text{HC}}$	<i>$\beta - D - \text{Xylose}$</i>	
	(4.D)	${}^2J_{\text{HC}}$	<i>$\beta - D - \text{Xylose}$</i>	
K	(2.E)	${}^3J_{\text{HC}}$	<i>$\alpha - D - \text{Xylose}$</i>	
	(3.E)	${}^3J_{\text{HC}}$		
	(4.E)	${}^4J_{\text{HC}}$		

L	(2.B)	${}^2J_{\text{HC}}$	<i>α-D-Xylose</i>	
	(2.C)	${}^4J_{\text{HC}}$		
	(2.D)	${}^3J_{\text{HC}}$		
	(3.B)	${}^2J_{\text{HC}}$		
	(3.C)	${}^2J_{\text{HC}}$		
	(5.B)	${}^2J_{\text{HC}}$		
M	(5.C)	${}^4J_{\text{HC}}$	<i>β-D-Xylose</i>	
	(5.D)	${}^3J_{\text{HC}}$		
N	(5.B)	${}^2J_{\text{HC}}$	<i>β-D-Xylose</i>	
	(5.C)	${}^4J_{\text{HC}}$		
O	(5.D)	${}^3J_{\text{HC}}$	<i>β-D-Xylose</i>	
	(5.E)	${}^3J_{\text{HC}}$		
P	(6.A)	${}^3J_{\text{HC}}$	<i>α-D-Xylose</i>	
Q	(6.D)	${}^3J_{\text{HC}}$	<i>α-D-Xylose</i>	

HMBC, Xylose standard

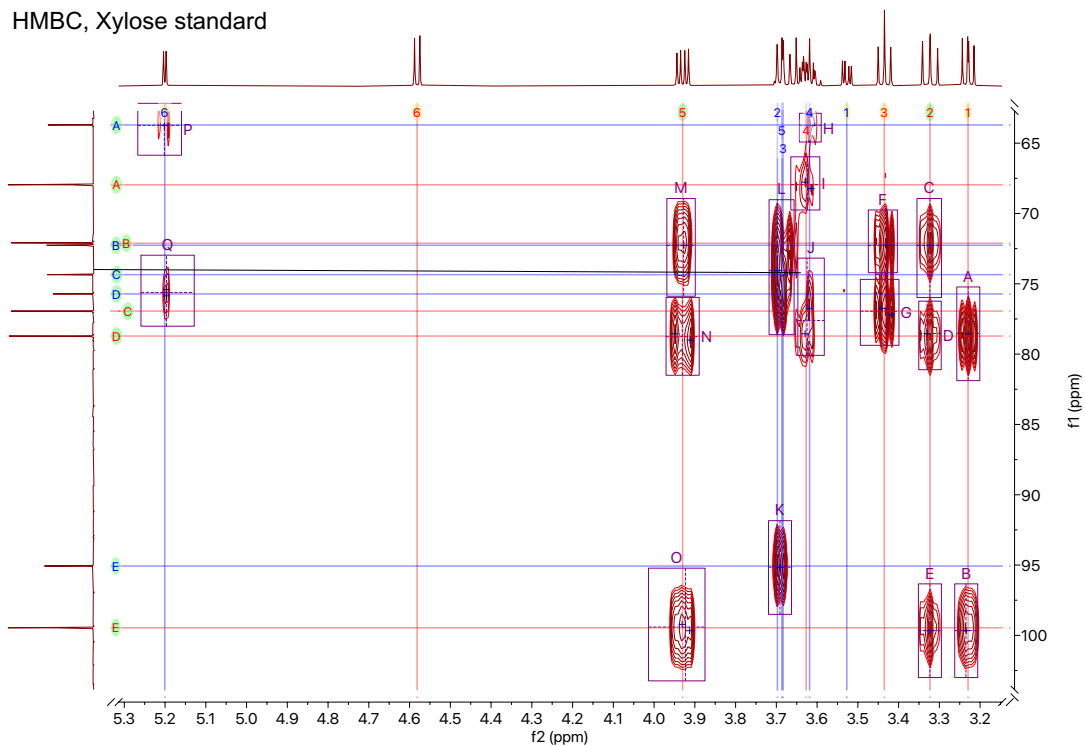


Figure A1-13: HMBC (D-xylose standard).

J-Resolved, 850 MHz

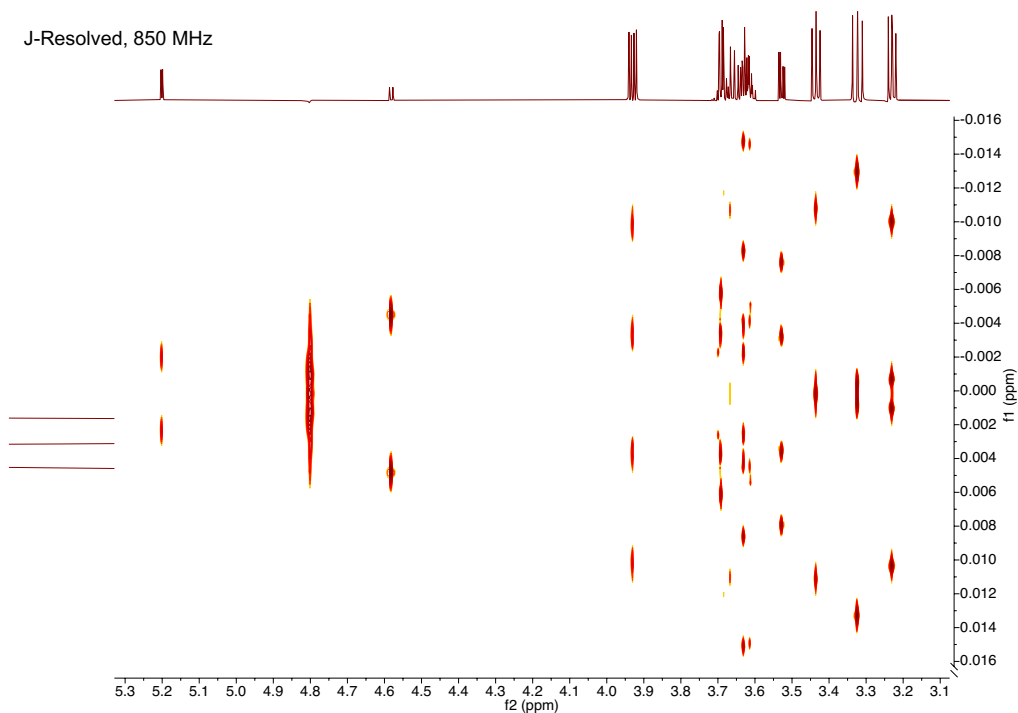


Figure A1-14: J-Resolved spectrum of D-xylose (2D-experiment where the indirect dimension (f1) is the coupling constant). Combining a ^1H -NMR spectrum (850 MHz) with a J-resolved experiment almost made it possible to extract the coupling constant for proton 4 in the two anomers (figure A1-15).

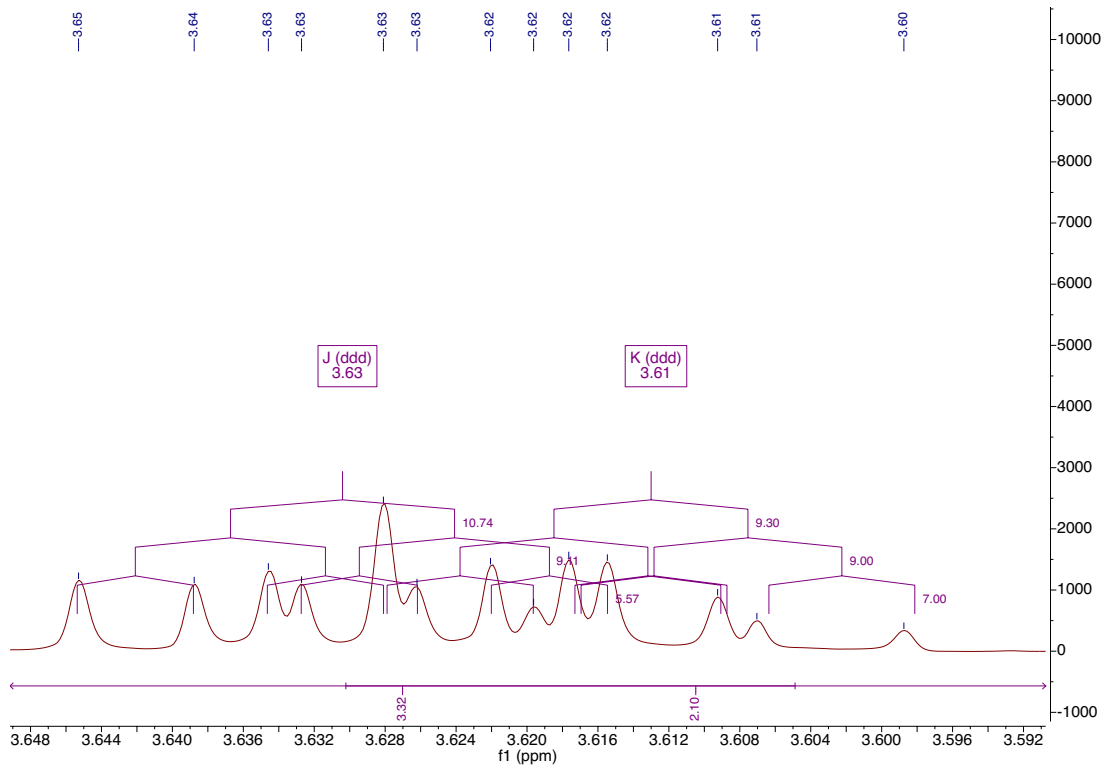


Figure A1-15: J-tree showing coupling constants between individual peaks in the complex multiplet.

APPENDIX A2 – STRUCTURAL ELUCIDATION OF FURFURAL

Furfural standard, pH = 7,40, 600 MHz

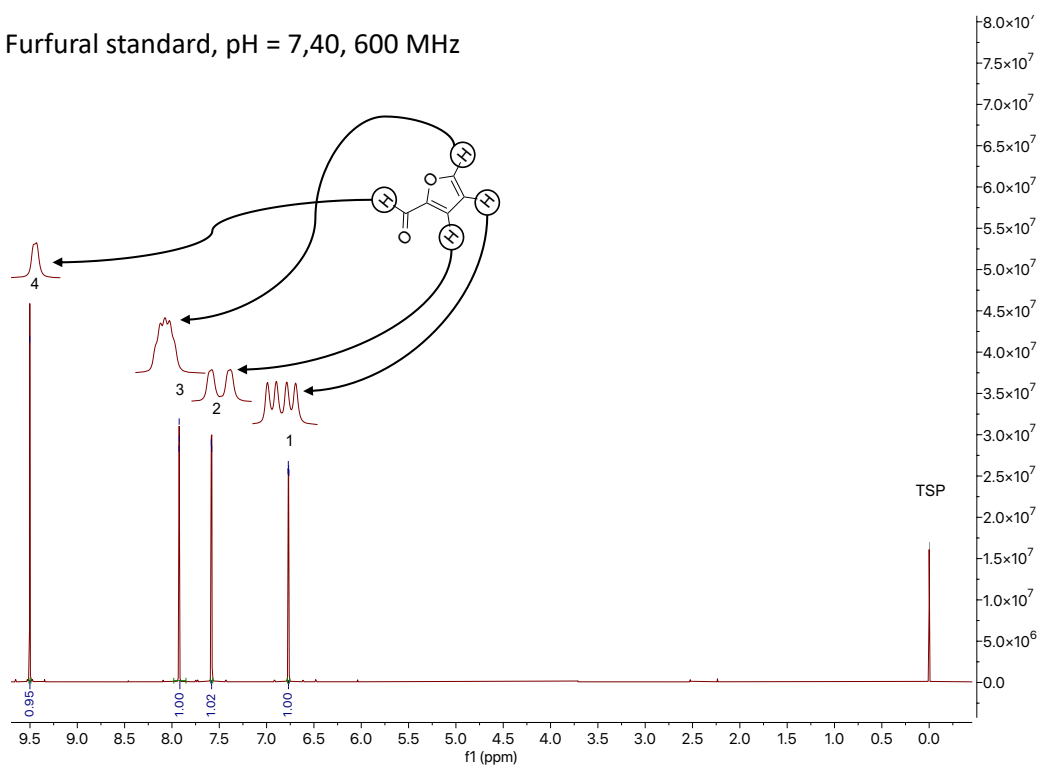
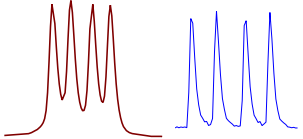
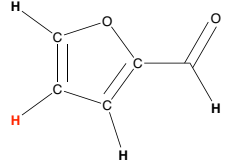
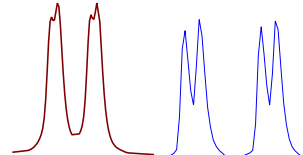
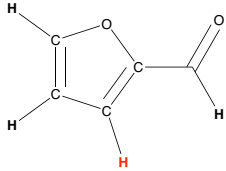
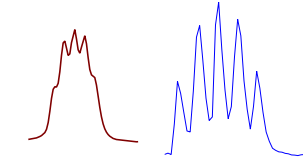
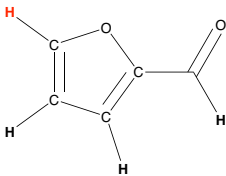
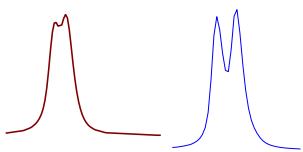
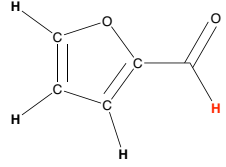


Figure A2-1: $^1\text{H-NMR}$ spectrum of FUR standard (pH adjusted to 7.40).

Splitting patterns and integration values for the different chemical environments in FUR:

- $\delta = 6.77$ ppm. **H1**: Doublet of doublets (dd) due to different $^3J_{\text{HH}}$ bonds to H2 and H3.
- $\delta = 7.58$ ppm. **H2**: Doublet of doublets (dd) due to $^3J_{\text{HH}}$ to H1 and $^4J_{\text{HH}}$ to the aldehydic proton.
- $\delta = 7.92$ ppm. **H3**: Complex multiplet (m) due to $^3J_{\text{HH}}$ to H1 and $^4J_{\text{HH}}$ to H2. Maybe even $^5J_{\text{HH}}$ to the aldehydic proton.
- $\delta = 9.50$ ppm. **H4**: Doublet (d). Aldehydic proton. The peak is split due to $^4J_{\text{HH}}$ to H2.

Table A2-1 ¹H-NMR chemical shifts for FUR standards at different pH (Neo-600 MHz).

Chemical environment	Chemical shift, not pH-adjusted (pH = 7.38) [ppm]	Chemical shift, pH-adjusted (7.40) [ppm]	Chemical shift pH = 2.00 [ppm]	Chemical shift pH = 4.80 [ppm]	Chemical shift, pH = 10.73 [ppm]	Chemical shift, Chemdraw [ppm]	Multi-plicity	Peaks Exponential multiplication	Peaks Lorentz Gauss transformation (Gaussian = 0.2 Zero Filling = 128k)	Coupling constant. J [Hz]	Integration value	Functional group	Position
1	6.77	6.77	6.75	6.77	6.77	6.84	dd			3.7. 1.7	1H	-CH-	
2	7.58	7.59	7.56	7.58	7.58	7.47	dd			3.7. 0.8	1H	-CH-	
3	7.92	7.92	7.91	7.92	7.92	8.18	m			1.7. 0.9	1H	CH-O	
4	9.50	9.50	9.49	9.50	9.50	9.68	d			0.9	1H	-CH=O	

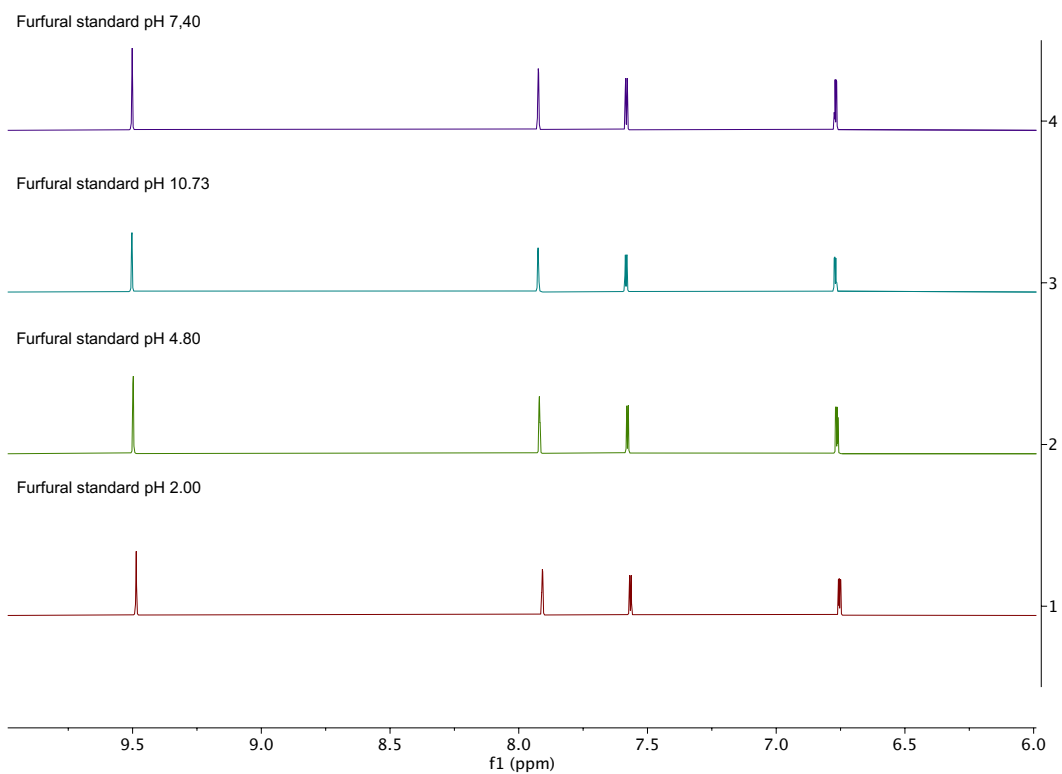


Figure A2-2: stacked $^1\text{H-NMR}$ spectra of FUR standards at different pH.

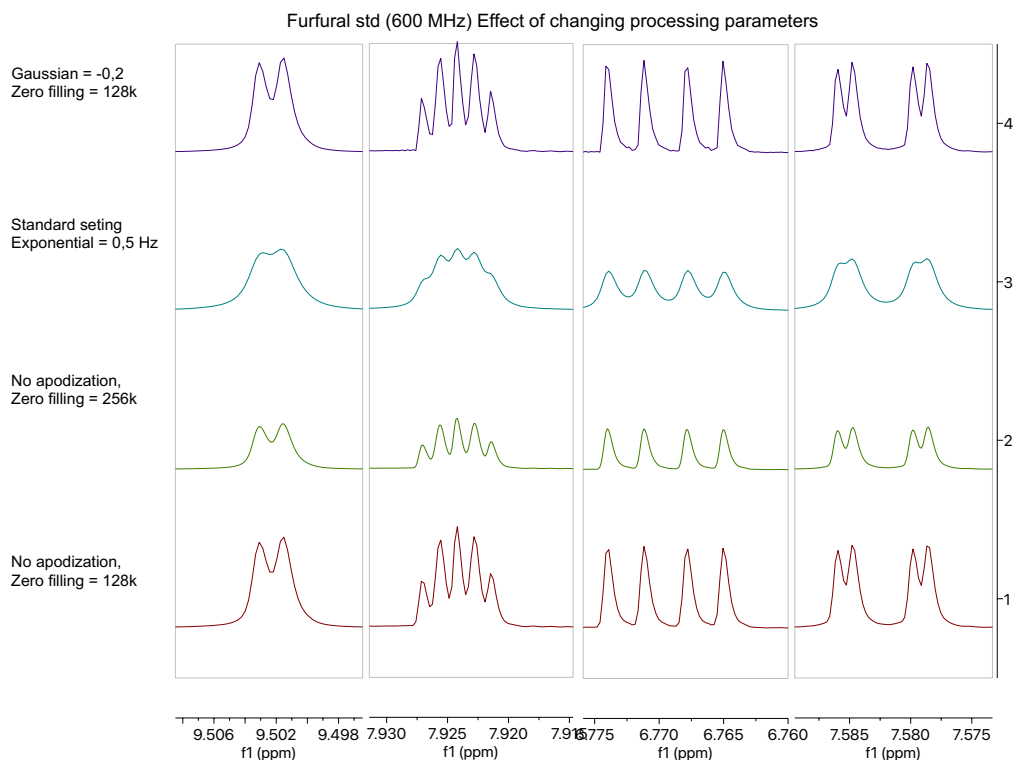
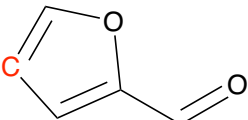
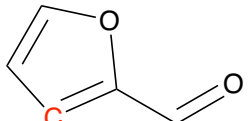
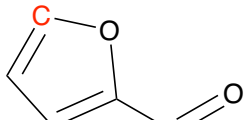
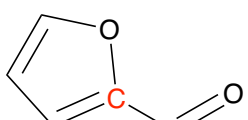
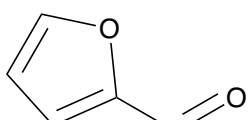


Figure A2-3: $^1\text{H-NMR}$ FUR std. Different processing parameters affects peak resolution. Best resolution achieved with Gaussian = 0.2 and zero filling set to 128k.

Table A2-2: ^{13}C -NMR chemical shifts for FUR.

Chemical environment	Chemical shift	Chemical shift (Chemdraw)	Functional group	Position
a	113.27	112.60	-CH-	
b	125.89	121.10	-CH-	
c	150.22	147.10	-CH-	
d	152.10	153.30	-C-	
e	180.73	178.10	CH=O	

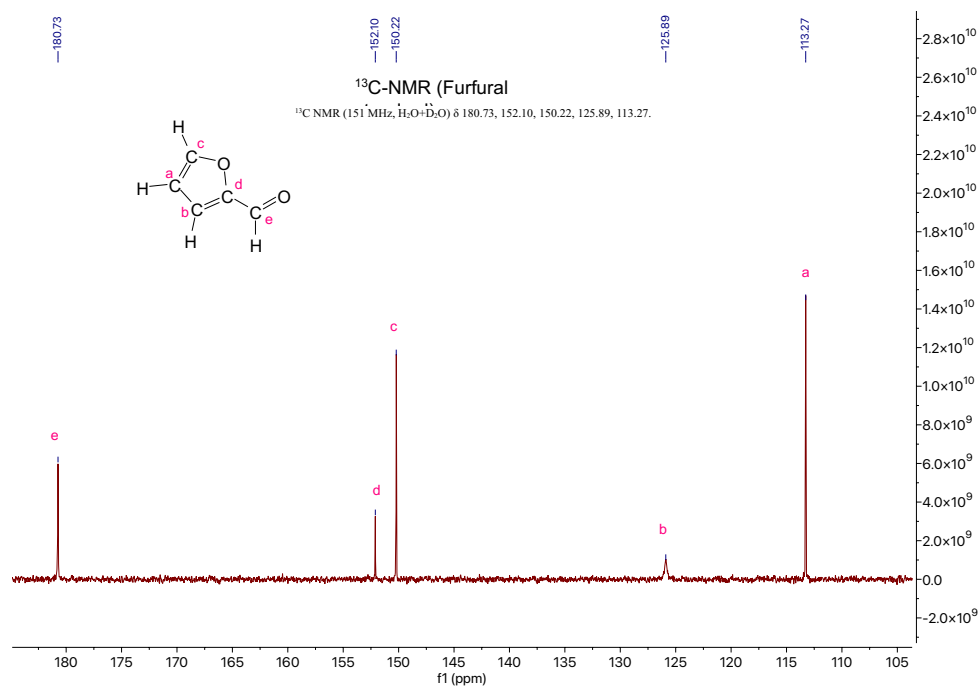


Figure A2-4: ¹³C-NMR (FUR standard). The reduced integration intensity of peak d could be a result of the nuclear overhauser effect (NOE) as no proton is directly connected to the carbon.

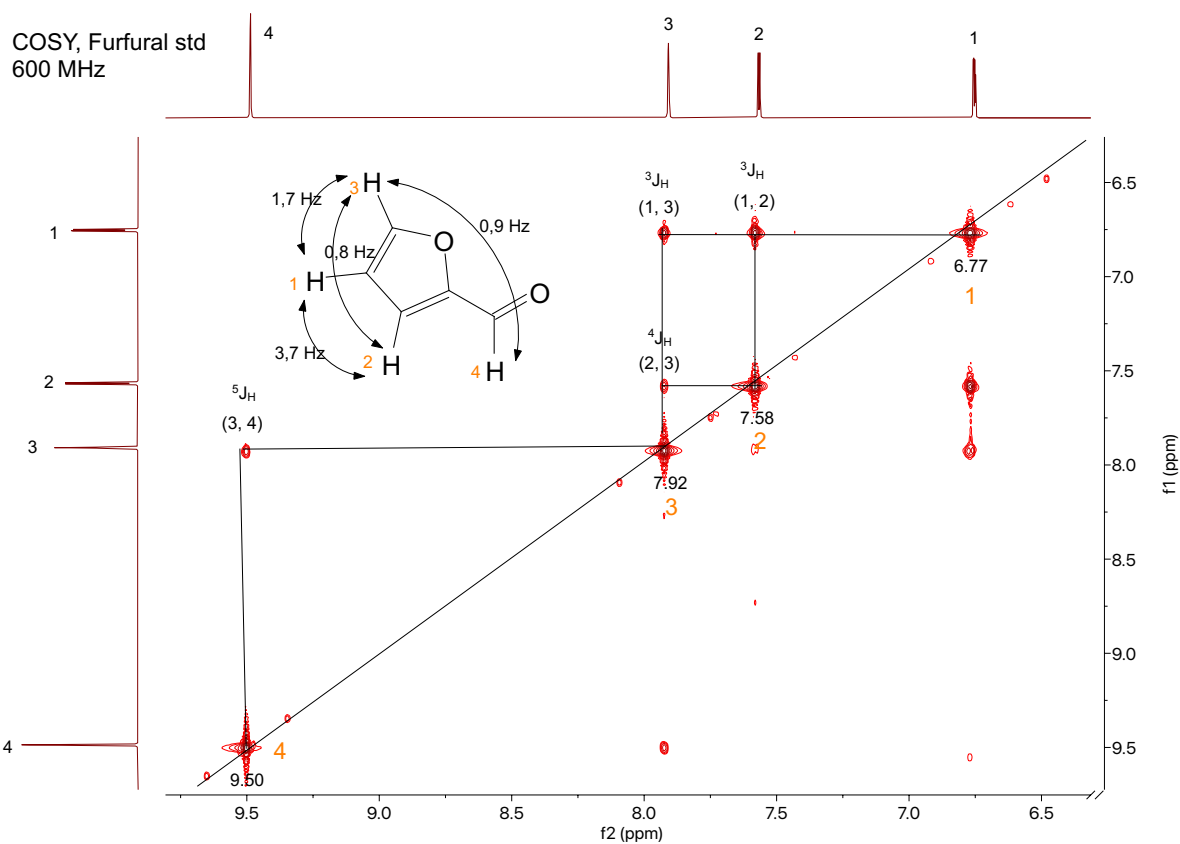


Figure A2-5: COSY spectrum of FUR standard with coupling constants.

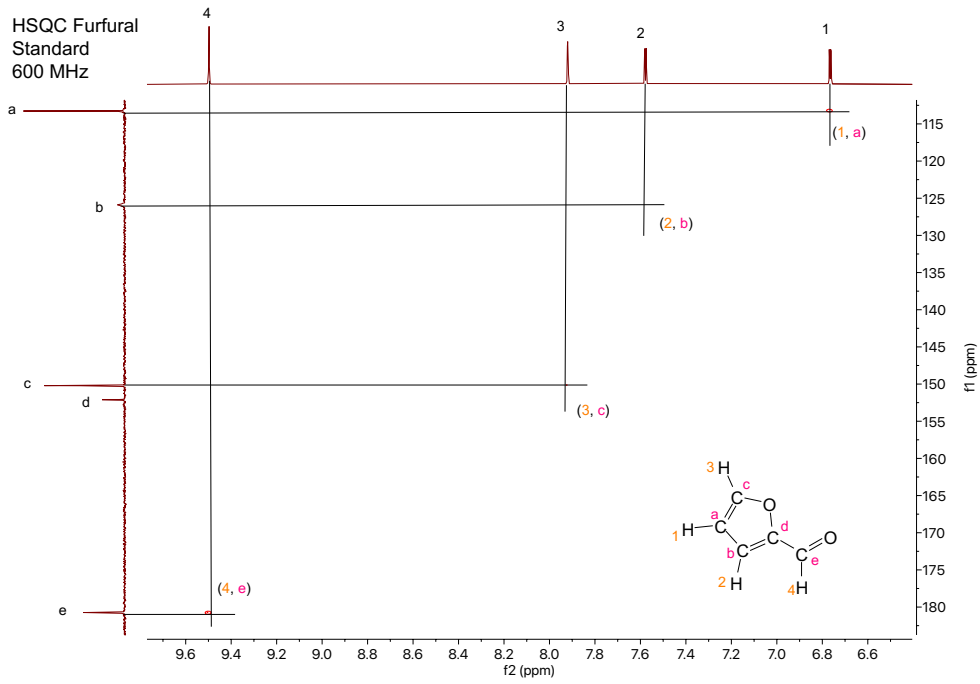


Figure A2-6: HSQC (FUR standard).

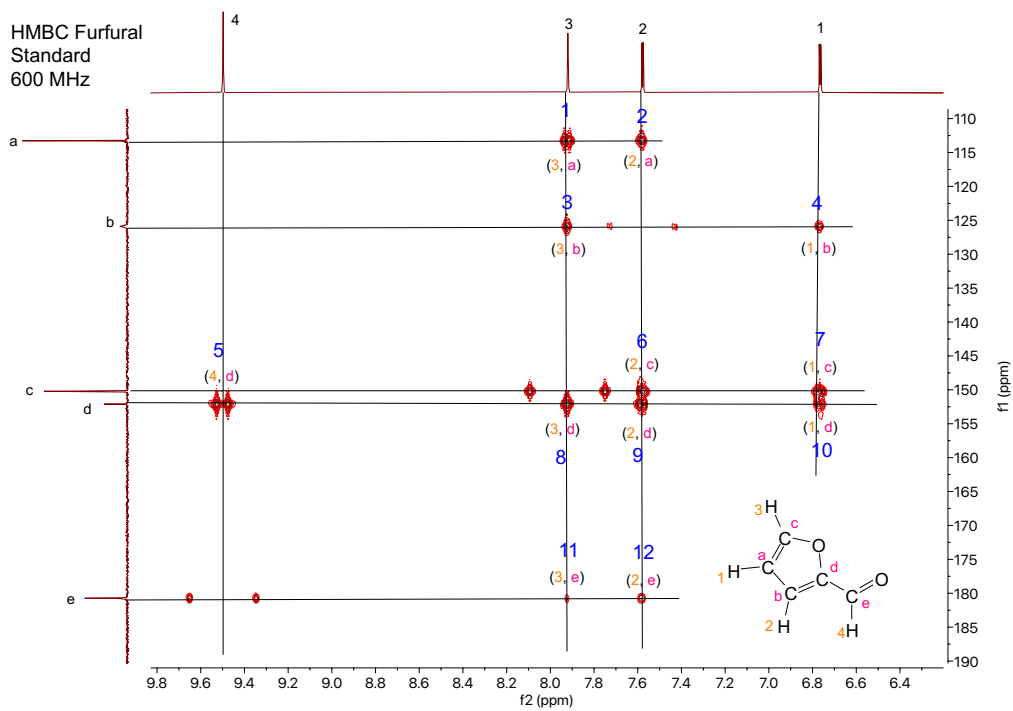


Figure A2-7: HMBC (FUR standard). The peaks without numbers located at (4, e) and (2, b) are satellite peaks from ^{13}C , and are of little analytical value.

Table A2-3: Cross-peak identification from HMBC (FUR standard).

Crosspeak #	¹ H-peak	¹³ C-peak	Identity	Signal strength	Coupling
4	1 (6.77)	b (125.89)	C-H	Strong	² J _{HC}
7		c (150.22)	C-H	Strong	² J _{HC}
10		d (152.10)	C-H	Medium	³ J _{HC}
2	2 (7.58)	a (113.27)	C-H	Strong	² J _{HC}
6		c (150.22)	C-H	Strong	³ J _{HC}
9		d (152.10)	C-H	Medium	² J _{HC}
12		e (180.73)	C-H (aldehyde)	Weak	³ J _{HC}
1	3 (7.92)	a (113.27)	C-H	Strong	³ J _{HC}
3		b (125.89)	C-H	Medium	³ J _{HC}
8		d (152.10)	C-H	Strong	³ J _{HC}
11		e (180.73)	C-H (aldehyde)	Weak	⁴ J _{HC}
5	4 (9.50)	d (152.10)	C-H	Strong	² J _{HC}

APPENDIX A3 – STRUCTURAL ELUCIDATION OF 5-HYDROXYMETHYLFURFURAL

5-Hydroxymethylfurfural standard, pH = 7,40, 600 MHz

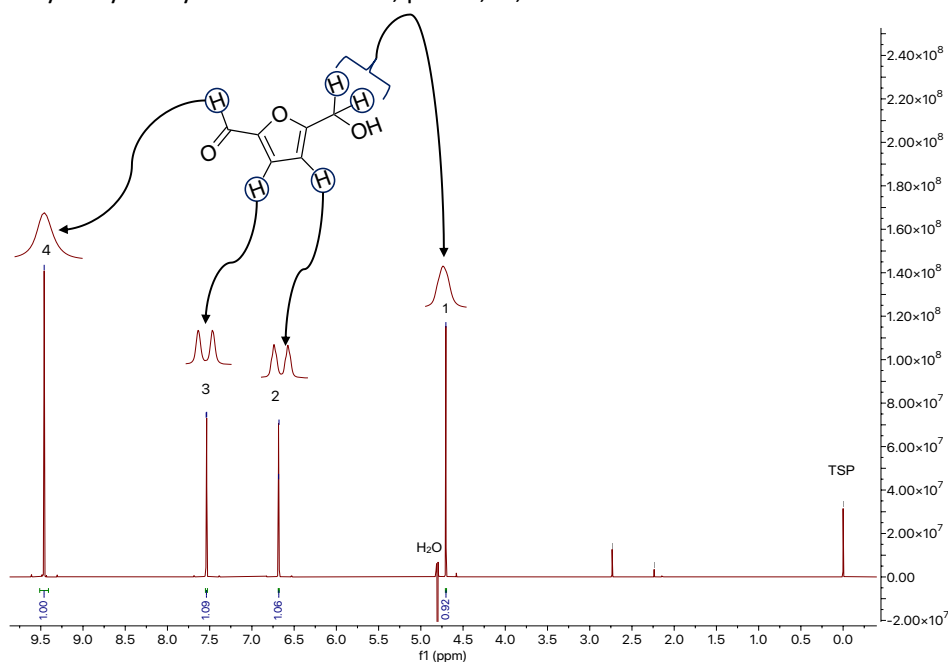


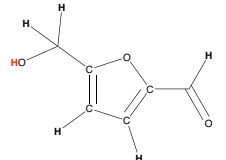
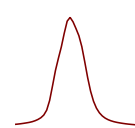
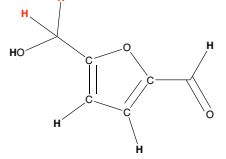
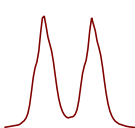
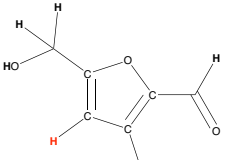
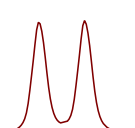
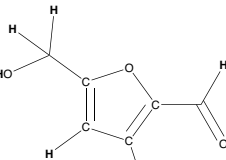
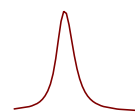
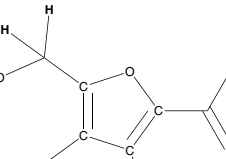
Figure A3-1: ¹H-NMR spectrum of 5-HMF standard. pH adjusted (pH = 7.40).

Splitting patterns and integration values for the different chemical environments in 5-hydroxymethylfurfural (HMF):

- **$\delta = 4.70$ ppm. H1:** Singlet (s). No neighboring protons. Integration value of this peak should be 2 (methylene group). Unfortunately, the methylene resonance is very close to the H₂O resonance (60Hz). The small integration value is a result of spillover from the presaturation on the H₂O resonance and over to the CH₂ resonance. This causes saturation of the peak and the signal intensity is consequently reduced. The integration value varied for all spectra. It was not reproducible, but consistently too small.
- **$\delta = 6.68$ ppm. H2:** Doublet (d). One neighboring proton $^3J_{HH}$ to H3. Integration value = 1
- **$\delta = 7.54$ ppm. H3:** Doublet (d). One neighboring proton $^3J_{HH}$ to H2. Integration value = 1
- **$\delta = 9.46$ ppm. H4:** Singlet (s). High chemical shift due to the proximity to a carbonyl group. Integration value = 1

The OH-group does not appear in the spectrum since the OH-proton is rapidly exchanged with the solvent, especially when D₂O is used as a solvent.

Table A3-1: ¹H-NMR chemical shifts for 5-HMF standards at different pH (Neo-600 MHz).

Chemical environment	Chemical shift. δ pH not adjusted (pH=7.46)	Chemical shift. δ pH-adjusted (pH=7.40)	Chemical shift. δ (pH=1.75)	Chemical shift. δ (pH=4.87)	Chemical shift. δ (pH=10.81)	Chemical shift. δ Predicted Chemdraw	Multiplicity	Peaks	Coupling constant. J [Hz]	Integration value	Functional group	Position
*	-	-	-	-	-	5.12	-	-	-	1H	HO-	
1	4.70	4.70	4.69	4.70	4.70	4.39	s		-	2H	-CH ₂ -	
2	6.68	6.68	6.67	6.68	6.69	6.73	d		3.6	1H	-CH-	
3	7.54	7.54	7.53	7.54	7.54	7.42	d		3.6	1H	-CH-	
4	9.46	9.46	9.44	9.45	9.46	9.68	s		-	1H	-CH=O	

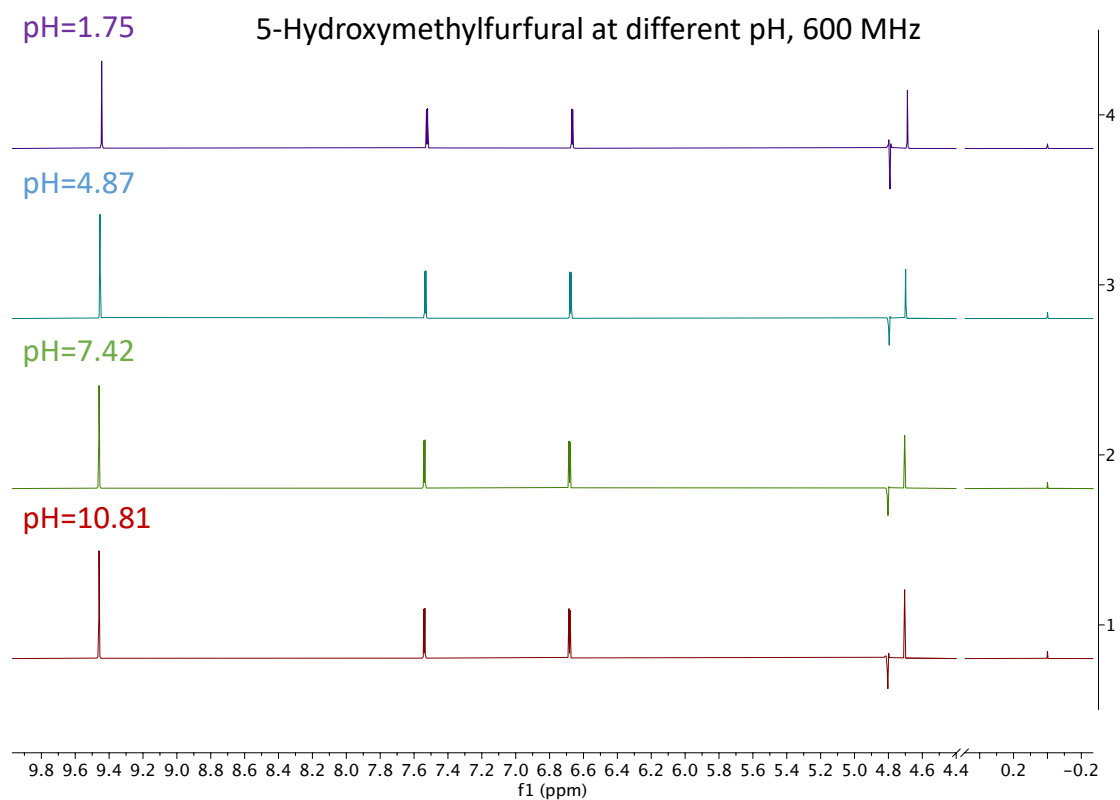


Figure A3-2: Stacked $^1\text{H-NMR}$ spectra of HMF measured at different pH to see how it affected the chemical shifts of the different peaks.

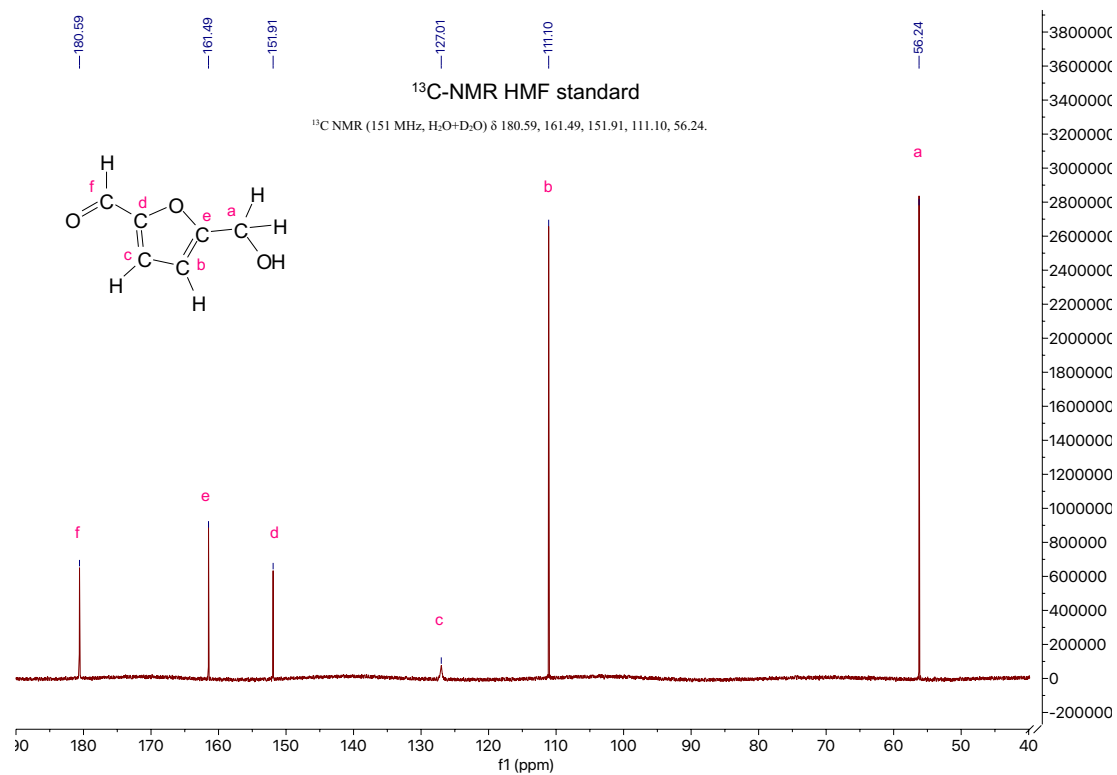
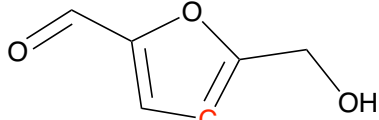
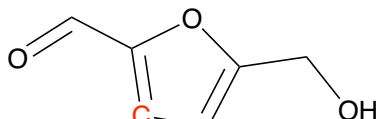
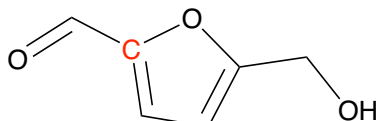
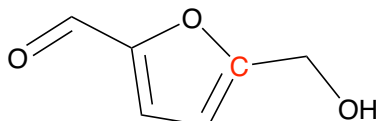


Figure A3-3: $^{13}\text{C-NMR}$ (HMF-standard)

Table A3-2: ^{13}C -NMR chemical shifts for HMF.

Chemical environment	Chemical shift	Chemical shift (Chemdraw)	Functional group	Position
a	56.24	57.00	$-\text{CH}_2\text{-OH}$	
b	111.10	111.60	$-\text{CH}-$	
c	127.01	121.90	$-\text{CH}-$	
d	151.91	153.10	$-\text{C}-$	
e	161.49	161.60	$-\text{C}-$	
f	180.59	178.10	CH=O	

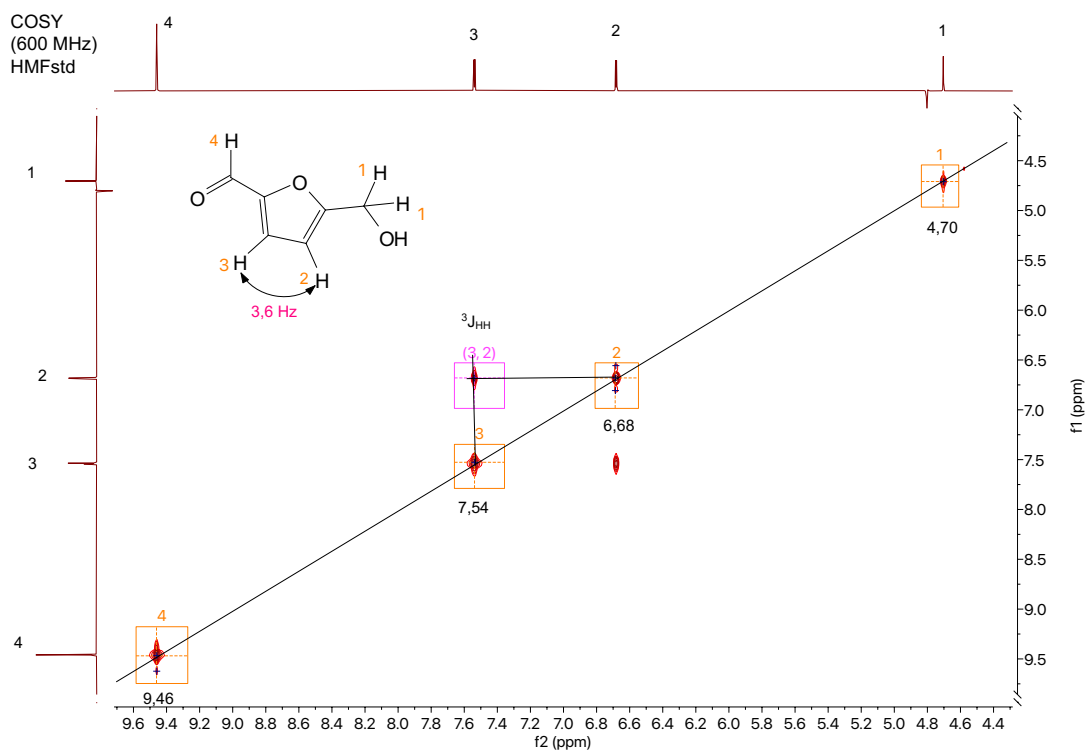


Figure A3-4: COSY spectrum of HMF standard.

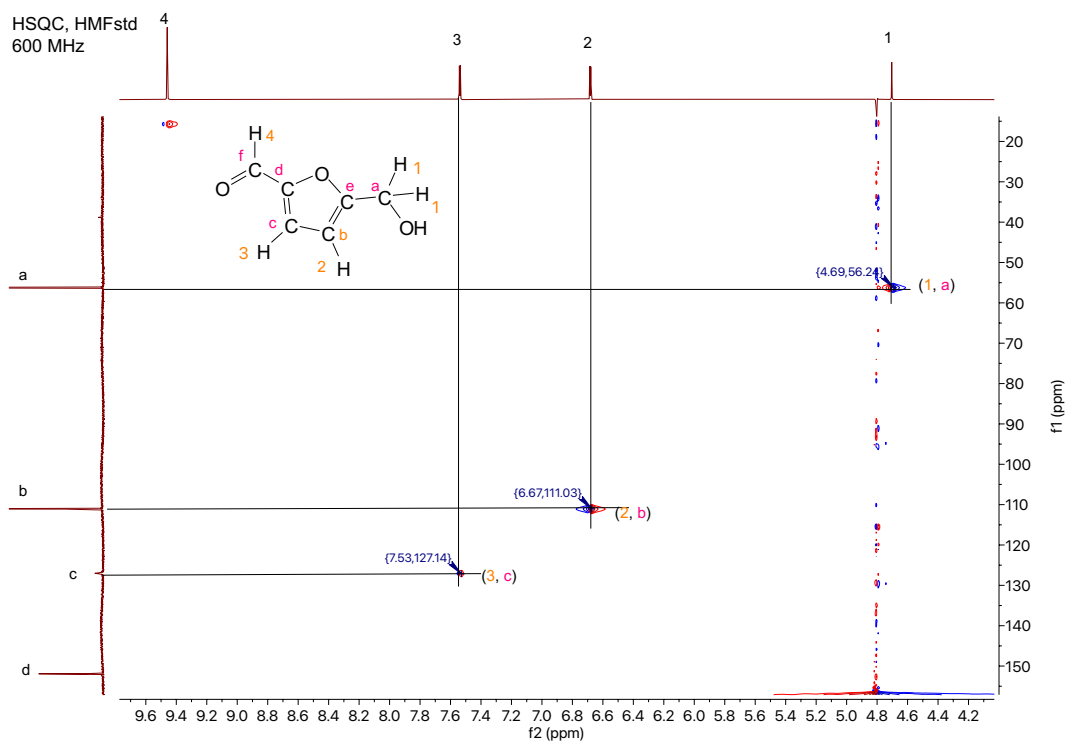


Figure A3-5: HSQC (HMF standard).

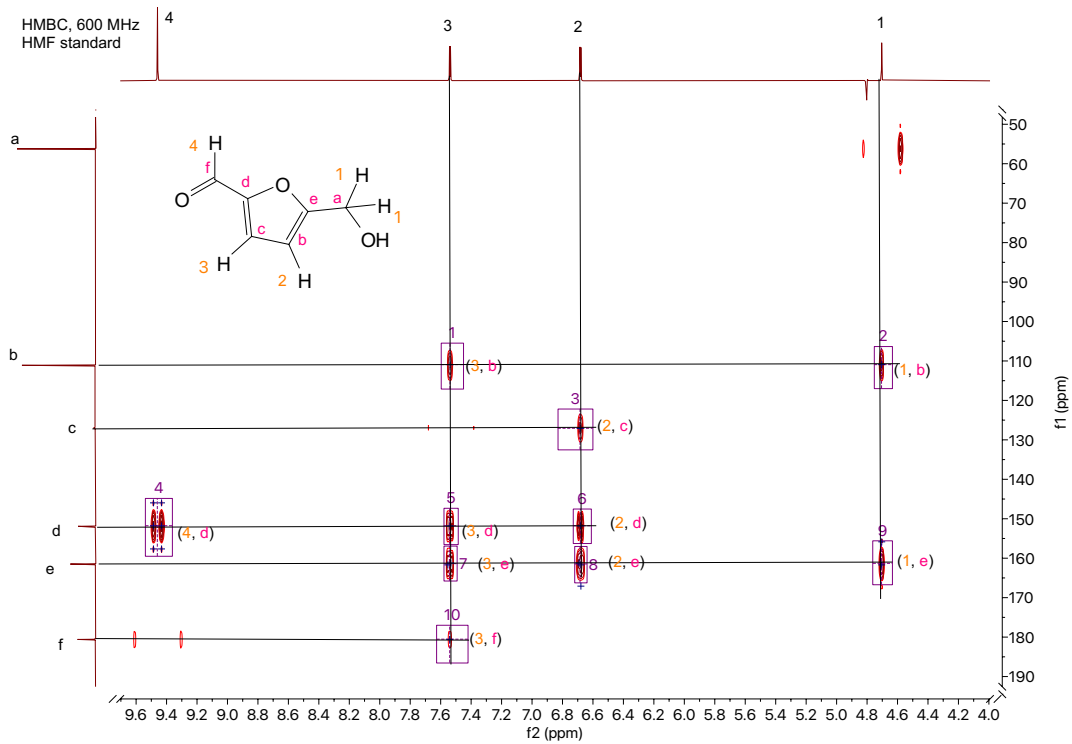


Figure A3-6: HMBC (HMF standard).

Table A3-3: Cross-peak identification from HMBC (HMF standard).

Crosspeak #	¹ H-peak	¹³ C-peak	Identity	Signal strength	Coupling
2	1 (4.70)	b (111.10)	C-H	Medium	³ J _{HC}
9		e (161.49)	C-H	Medium	² J _{HC}
3	2 (6.68)	c (127.01)	C-H	Medium	² J _{HC}
6		d (151.91)	C-H	Strong	³ J _{HC}
8		e (161.49)	C-H	Strong	² J _{HC}
1	3 (7.54)	b (111.10)	C-H	Medium	² J _{HC}
5		d (151.91)	C-H	Strong	² J _{HC}
7		e (161.49)	C-H	Strong	³ J _{HC}
10		f (180.59)	C-H (aldehyde)	Weak	³ J _{HC}
4	4 (9.46)	d (151.91)	C-H	Strong	² J _{HC}

APPENDIX A4 – STRUCTURAL ELUCIDATION OF GAMMA-VALEROLACTONE (GVL)

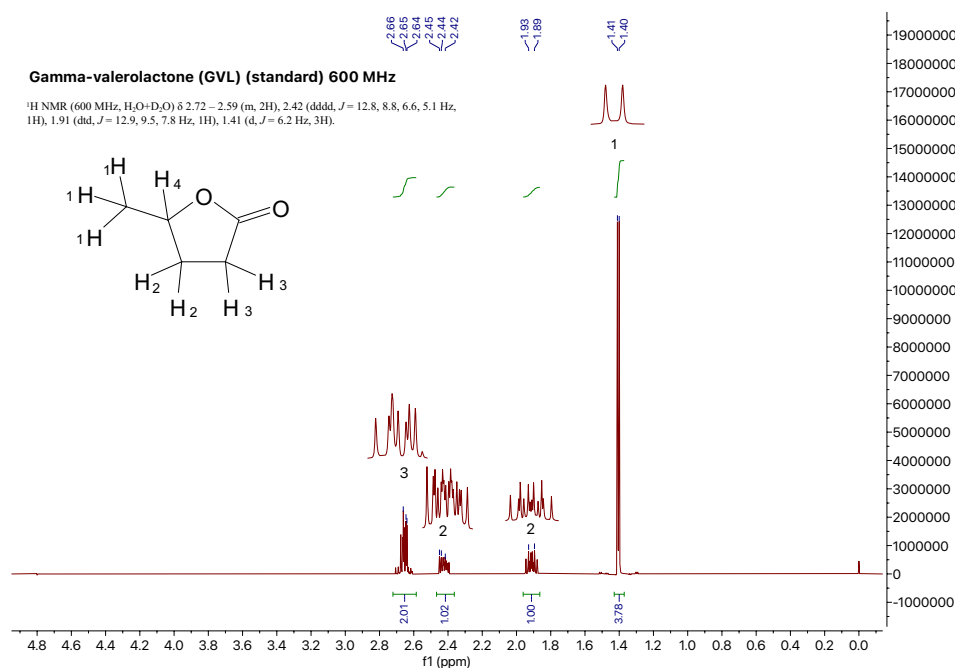
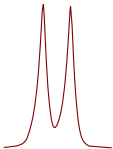
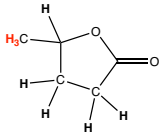
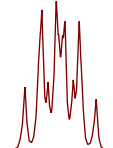
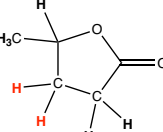
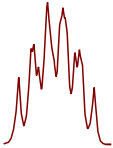
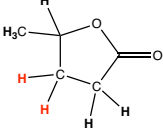
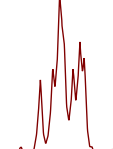
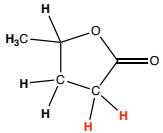
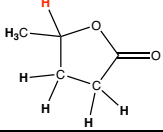


Figure A4-1: ¹H-NMR spectrum of GVL standard measured at pH = 7.40 (600 MHz)

The complex splitting pattern is a result of tautomerization of the GVL molecule. The non-planar nature of the furanic ring gives rise to different chemical shifts for the protons directly attached to the ring due to continuously changing spatial orientations of the protons. Consequently, different protons can couple to other protons in the ring depending on the relative spatial orientation of all the protons in the furanic ring.

- **$\delta = 1.40$ ppm, H1:** Doublet (d). Methyl group (integration value should be equal to 3). Split due to ³J_{HH} bond to H4. The integration value in figure A4-1 is too big due to signal overlap. This could probably be solved by using CDCl₃ as solvent, as this will solve the problem regarding signal overlap with water
- **$\delta = 1.91$ ppm and 2.43 ppm, H2:** Multiplet (m). Methylene group in the furanic ring. The signal is split into two separate multiplets.
- **$\delta = 2.66$ ppm, H3:** Complex multiplet (m). second methylene group attached to the furanic ring. Integration value = 2
- **H4:** Does not appear in the spectrum due to overlap with water. Predicted chemical shift from chemdraw is 4.40 ppm, which is very close to the signal for water, which has been suppressed by water suppression.

Table A4-1: ¹H-NMR chemical shifts for γ-valerolactone (GVL) standard (Neo-600 MHz).

Chemical environment	Chemical shift, not pH-adjusted (pH = 7,46) [ppm]	Chemical shift, predicted by Chemdraw [ppm]	Multiplicity	Peaks	Coupling constant, J [Hz]	Integration value	Functional group	Position
1	1.40	1.30	m		-	3H	CH ₃ -	
2	1.93	1.92	m		-	1H	-CH ₂ -	
2	2.43	2.17	m		-	1H	-CH ₂ -	
3	2.66	2.25, 2.35	m		-	2H	-CH ₂ -	
4	-	4.40	-	-	-	1H	-CH-	

APPENDIX A5 - ADDITIONAL STANDARD SPECTRA (NMR)

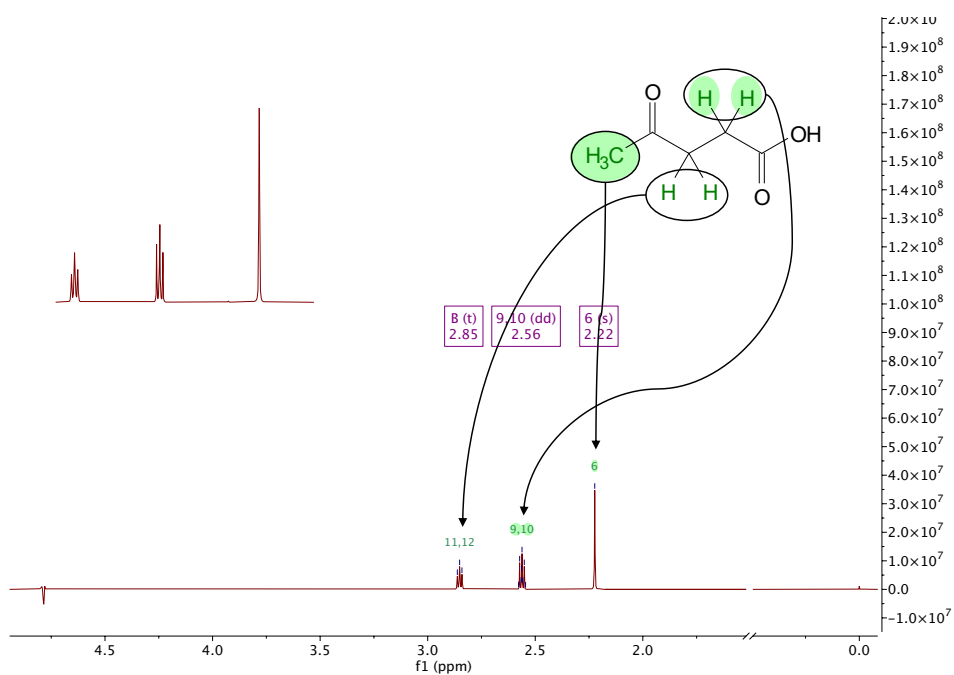


Figure A5-1: Levulinic acid standard (600 MHz).

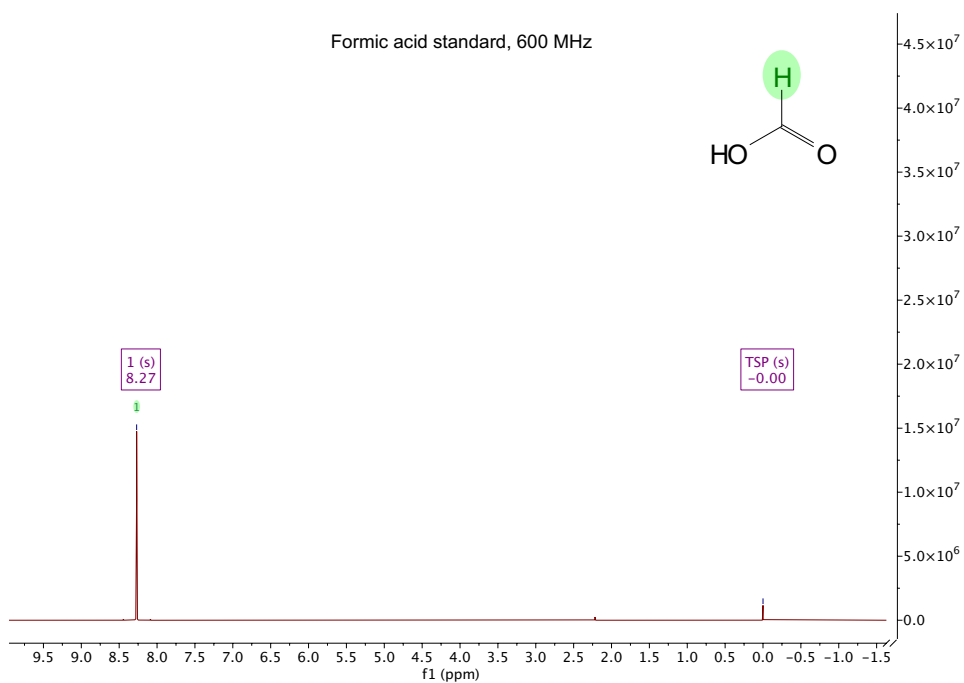


Figure A5-2: Formic acid standard (600 MHz).

APPENDIX B – RAW DATA FROM THE SECOND EXPERIMENTAL DESIGN

Table B-1: Experimental setup for FFD2 with added masses of substrate and catalyst for each experiment.

Experiment #	Temperature [°C]	Time [min]	Org/Aq [v/v]	Substrate [g]	Catalyst [g]	Run Order
1	150	30	1:4	0.1250	0.0133	2a
2a	200	30	1:4	0.125	0.0066	13
3	150	90	1:4	0.1249	0.0061	14a
4	200	90	1:4	0.1254	0.0123	11
5	150	30	4:1	0.1256	0.0062	CP1
6a	200	30	4:1	0.1249	0.0124	7
7	150	90	4:1	0.1253	0.0124	12a
8	200	90	4:1	0.1250	0.0062	6a
9	150	30	1:4	0.3750	0.0063	3
10	200	30	1:4	0.3753	0.0125	CP2
11	150	90	1:4	0.3741	0.0131	5
12a	200	90	1:4	0.3747	0.0062	4
13	150	30	4:1	0.3750	0.0127	15
14a	200	30	4:1	0.3747	0.0063	1
15	150	90	4:1	0.3752	0.0063	CP3
16	200	90	4:1	0.3747	0.0125	16
CP1*	175	60	1:1	0.2494	0.0094	9
CP2*	175	60	1:1	0.2498	0.0093	8
CP3*	175	60	1:1	0.2501	0.0093	10
CP4*	175	60	1:1	0.2503	0.0094	CP4
14b	200	30	4:1	0.3751	0.0065	14b
12b	200	90	1:4	0.3749	0.0064	12b
12c	200	90	1:4	0.3754	0.0063	12c
CP5*	175	60	1:1	0.2497	0.0094	CP5
2b	200	30	1:4	0.1254	0.0062	2b
6b	200	30	4:1	0.1253	0.0123	6b

*Center point experiments

Table B-2: Integration values, predicted concentrations and calculated yields for all experiments from FFD2.

Exp #	Compound	Organic phase					Aqueous phase			
		Protos	Integral	Concentration [mM]	Factor	Yield [g]	Integral	Concentration [mM]	Factor	Yield [g]
1	Furfural	1	0.0020	0.2034	-	0.00032	0.0061	0.6204	-	0.00025
	DMSO ₂	6	6.0000	102.9800	0.00971	-	6.0000	101.7100	0.00983	-
	α and β D-Xylose	2	-	-	-	-	1.9121	194.4797	-	0.1251
	Formic acid	1	-	-	-	-	0.0092	0.9219	-	0.00006
2a	Furfural	1	0.0213	2.1771	-	0.0037	0.0572	5.8066	-	0.0025
	DMSO ₂	6	6.0000	102.0900	0.00979	-	6.0000	101.4700	0.00986	-
	α and β D-Xylose	2	-	-	-	-	1.7019	172,6918	-	0.1122
	Formic acid	1	-	-	-	-	0.0083	0.8422	-	0.0002
2b	Furfural	1	0.0263	2.7197	-	0.0048	0.0838	8.3926	-	0.0035
	DMSO ₂	6	6.0000	103.51	0.0097	-	6.0000	100.1800	0.0100	-
	α and β D-Xylose	2	-	-	-	-	1.4334	143.5980	-	0.0923
	Formic acid	1	-	-	-	-	0.0110	1.1020	-	0.0002
3	Furfural	1	0.0010	0.1012	-	0.0002	0.0416	0.0001	-	0.0001
	DMSO ₂	6	6.0000	103.8221	0.0096	-	6.0000	103.7132	0.0096	-
	α and β D-Xylose	2	-	-	-	-	2.0753	215.2294	-	0.1359
	Formic acid	1	-	-	-	-	0.0326	3.3809	-	0.0006
4	Furfural	1	0.1068	11.1719	-	0.0204	0.3622	37.4246	-	0.0144
	DMSO ₂	6	6.0000	104.6348	0.0096	-	6.0000	103.3435	0.0097	-
	α and β D-Xylose	2	-	-	-	-	0.2250	23.2515	-	0.0140
	Formic acid	1	-	-	-	-	0.0760	7.8538	-	0.0014
5	Furfural	1	0.0011	0.1145	-	0.0009	0.0028	0.2817	-	0.00003
	DMSO ₂	6	6.0000	104.0734	0.0096	-	6.0000	99.7194	0.0100	-
	α and β D-Xylose	2	-	-	-	-	7.9161	789.3935	-	0.1268
	Formic acid	1	-	-	-	-	0.0074	0.7379	-	0.00004
6a	Furfural	1	0.1423	14.3139	-	0.0289	0.3796	37.5588	-	0.0013
	DMSO ₂	6	6.0000	103.9469	0.0096	-	6.0000	102.3382	0.0098	-
	α and β D-Xylose	2	-	-	-	-	4.5066	461.2054	-	0.0236
	Formic acid	1	-	-	-	-	0.0944	9.6609	-	0.0083
6b	Furfural	1	0.0375	3.9570	-	0.0323	0.1044	10.4580	-	0.0009
	DMSO ₂	6	6.0000	105.5926	0.0095	-	6.0000	100.2246	0.0100	-
	α and β D-Xylose	2	-	-	-	-	0.8028	80.4566	-	0.0106
	Formic acid	1	-	-	-	-	0.0899	9.0098	-	0.0074
7	Furfural	1	0.0068	0.7083	-	0.0055	0.0139	1.3949	-	0.0002
	DMSO ₂	6	6.0000	104.1566	0.0096	-	6.0000	100.5308	0.0099	-
	α and β D-Xylose	2	-	-	-	-	7.0969	713.4514	-	0.1136
	Formic acid	1	-	-	-	-	0.0380	3.8201	-	0.0002
8	Furfural	1	0.0395	4.0705	-	0.0311	0.1123	11.6917	-	0.0009
	DMSO ₂	6	6.0000	104.0539	0.0097	-	6.0000	104.0765	0.0096	-

	α and β D-Xylose	2	-	-	-	-	0.6900	71.8152	-	0.0088
	Formic acid	1	-	-	-	-	0.1016	10.5745	-	0.0004
9	Furfural	1	0.0020	0.2066	-	0.0003	0.0057	0.5660	-	0.0002
	DMSO ₂	6	6.0000	105.9432	0.0094	-	6.0000	99.2954	0.0101	-
	α and β D-Xylose	2	-	-	-	-	5.6300	559.0590	-	0.3680
	Formic acid	1	-	-	-	-	0.0051	0.5064	-	0.00001
10	Furfural	1	0.0319	3.3288	-	0.0061	0.1038	10.4767	-	0.0044
	DMSO ₂	6	6.0000	104.3481	0.0096	-	6.0000	100.9757	0.0099	-
	α and β D-Xylose	2	-	-	-	-	5.1848	523.5611	-	0.3466
	Formic acid	1	-	-	-	-	0.0041	0.4140	-	0.00008
11	Furfural	1	0.0140	1.4659	-	0.0025	0.0377	3.8139	-	0.0017
	DMSO ₂	6	6.0000	104.5248	0.0096	-	6.0000	101.3020	0.0099	-
	α and β D-Xylose	2	-	-	-	-	5.5491	562.1238	-	0.3633
	Formic acid	1	-	-	-	-	0.0224	2.2691	-	0.0004
12a	Furfural	1	0.0368	3.8176	-	0.0260	0.1324	13.3418	-	0.0171
	DMSO ₂	6	6.0000	103.8121	0.0096	-	6.0000	100.7466	0.0099	-
	α and β D-Xylose	2	-	-	-	-	1.6468	165.9151	-	0.3060
	Formic acid	1	-	-	-	-	0.0962	9.6922	-	0.0020
12b	Furfural	1	0.2540	26.5048	-	0.0527	0.7695	74.8823	-	0.0312
	DMSO ₂	6	6.0000	104.3617	0.0096	-	6.0000	101.9535	0.0098	-
	α and β D-Xylose	2	-	-	-	-	2.4476	249.5328	-	0.1550
	Formic acid	1	-	-	-	-	0.0935	9.5323	-	0.0018
12c	Furfural	1	0.2479	25.8659	-	0.0486	0.6465	65.7400	-	0.0269
	DMSO ₂	6	6.0000	104.3355	0.0096	-	6.0000	101.6852	0.0098	-
	α and β D-Xylose	2	-	-	-	-	2.1190	215.4811	-	0.1380
	Formic acid	1	-	-	-	-	0.0946	9.6199	-	0.0019
13	Furfural	1	0.0073	0.7706	-	0.0059	0.0147	1.3833	-	0.0002
	DMSO ₂	6	6.0000	105.2000	0.0095	-	6.0000	94.4200	0.0106	-
	α and β D-Xylose	2	-	-	-	-	18.7237	1767.8918	-	0.3333
	Formic acid	1	-	-	-	-	0.0094	0.8875	-	0.00005
14a	Furfural	1	0.0684	7.0808	-	0.0530	0.2282	21.7520	-	0.0024
	DMSO ₂	6	6.0000	103.5199	0.0097	-	6.0000	95.3186	0.0105	-
	α and β D-Xylose	2	-	-	-	-	8.9753	855.5256	-	0.1318
	Formic acid	1	-	-	-	-	0.1268	12.0866	-	0.00006
14b	Furfural	1	0.0498	5.2199	-	0.4066	0.1405	13.3489	-	0.0015
	DMSO ₂	6	6.0000	104.8728	0.0095	-	6.0000	95.0126	0.0105	-
	α and β D-Xylose	2	-	-	-	-	11.9054	1131.1321	-	0.2009
	Formic acid	1	-	-	-	-	0.0343	3.2588	-	0.0001
15	Furfural	1	0.0098	1.0106	-	0.0080	0.0155	1.4500	-	0.0002
	DMSO ₂	6	6.0000	103.6486	0.0096	-	6.0000	93.8474	0.0107	-
	α and β D-Xylose	2	-	-	-	-	17.8414	1674.4154	-	0.3287

	Formic acid	1	-	-	-	-	0.0502	4.7113	-	0.0003
16	Furfural	1	0.1255	13.1171	-	0.0975	0.4722	44.9983	-	0.0026
	DMSO ₂	6	6.0000	104.5615	0.0096	-	6.0000	95.2982	0.0105	-
	α and β D-Xylose	2	-	-	-	-	-	-	-	0.0000
	Formic acid	1	-	-	-	-	0.5353	51.0141	-	0.0014
CP1	Furfural	1	0.0085	0.8892	-	0.0043	0.0253	2.5467	-	0.0006
	DMSO ₂	6	6.0000	105.2322	0.0095	-	6.0000	100.7635	0.0099	-
	α and β D-Xylose	2	-	-	-	-	6.1372	618.3843	-	0.2339
	Formic acid	1	-	-	-	-	0.0903	9.0986	-	0.0011
CP2	Furfural	1	0.0201	2.1012	-	0.0100	0.0590	5.8565	-	0.0016
	DMSO ₂	6	6.0000	104.7996	0.0095	-	6.0000	99.2172	0.0101	-
	α and β D-Xylose	2	-	-	-	-	5.3369	529.5272	-	0.2201
	Formic acid	1	-	-	-	-	0.0261	2.5896	-	0.0003
CP3	Furfural	1	0.0140	1.4794	-	0.0071	0.0416	4.1687	-	0.0011
	DMSO ₂	6	6.0000	105.6697	0.0095	-	6.0000	100.2102	0.0100	-
	α and β D-Xylose	2	-	-	-	-	5.5699	558.1597	-	0.2287
	Formic acid	1	-	-	-	-	0.0092	0.9219	-	0.00001
CP4	Furfural	1	0.0217	2.3155	-	0.0117	0.0565	5.6661	-	0.0015
	DMSO ₂	6	6.0000	106.8252	0.0094	-	6.0000	100.2432	0.0100	-
	α and β D-Xylose	2	-	-	-	-	5.0339	504.5981	-	0.2049
	Formic acid	1	-	-	-	-	0.0178	1.7843	-	0.0002
CP5	Furfural	1	0.0307	3.1280	-	0.0153	0.0807	8.1032	-	0.0021
	DMSO ₂	6	6.0000	101.7830	0.0098	-	6.0000	100.3797	0.0100	-
	α and β D-Xylose	2	-	-	-	-	4.3090	432.5374	-	0.1778
	Formic acid	1	-	-	-	-	0.0405	4.0654	-	0.0005

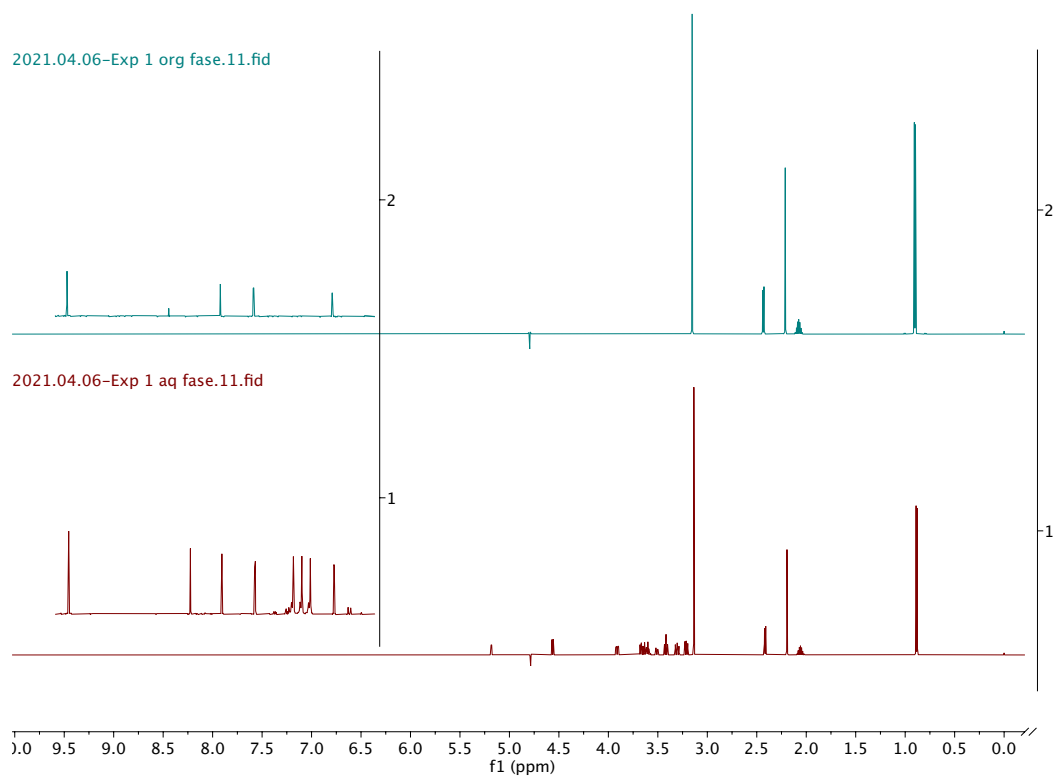


Figure B-1: ^1H -NMR-spectra of the organic and aqueous phases for experiment 1.

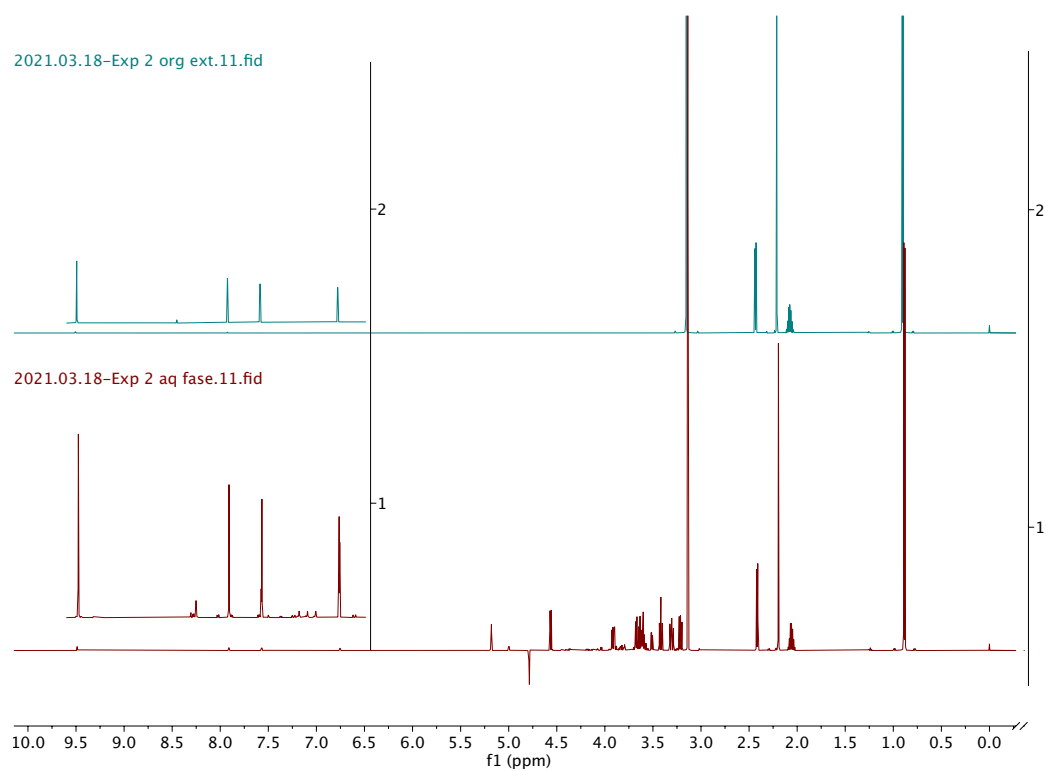


Figure B-2: ^1H -NMR-spectra of the organic and aqueous phases for experiment 2a.

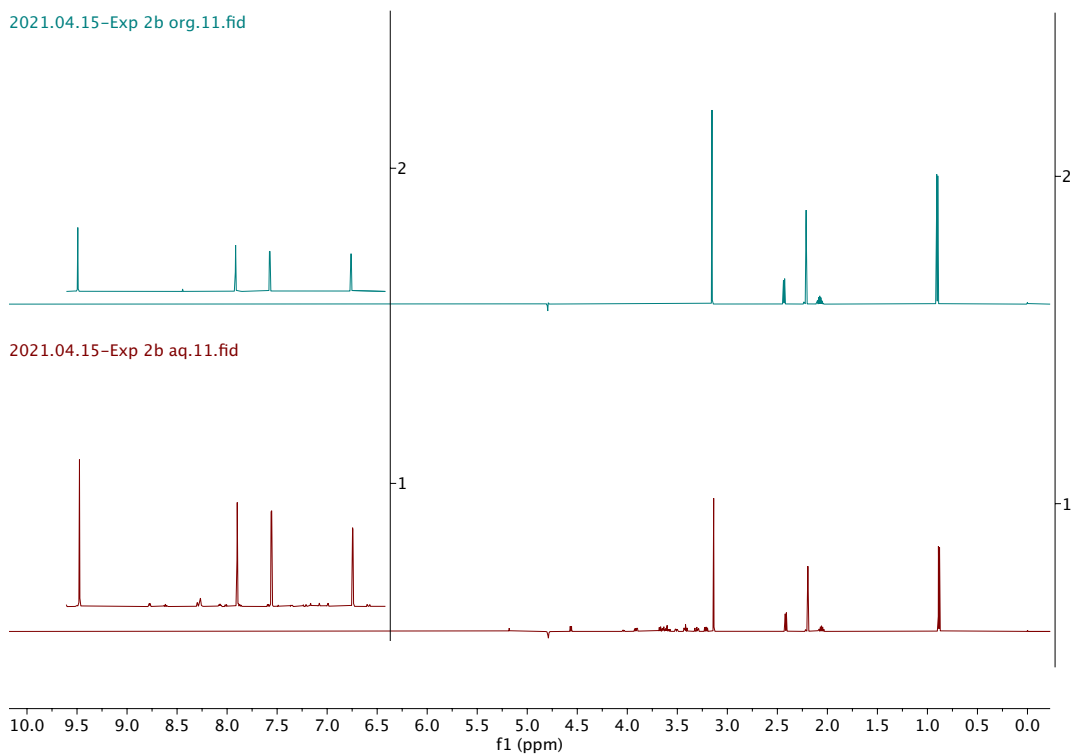


Figure B-3: ^1H -NMR-spectra of the organic and aqueous phases for experiment 2b.

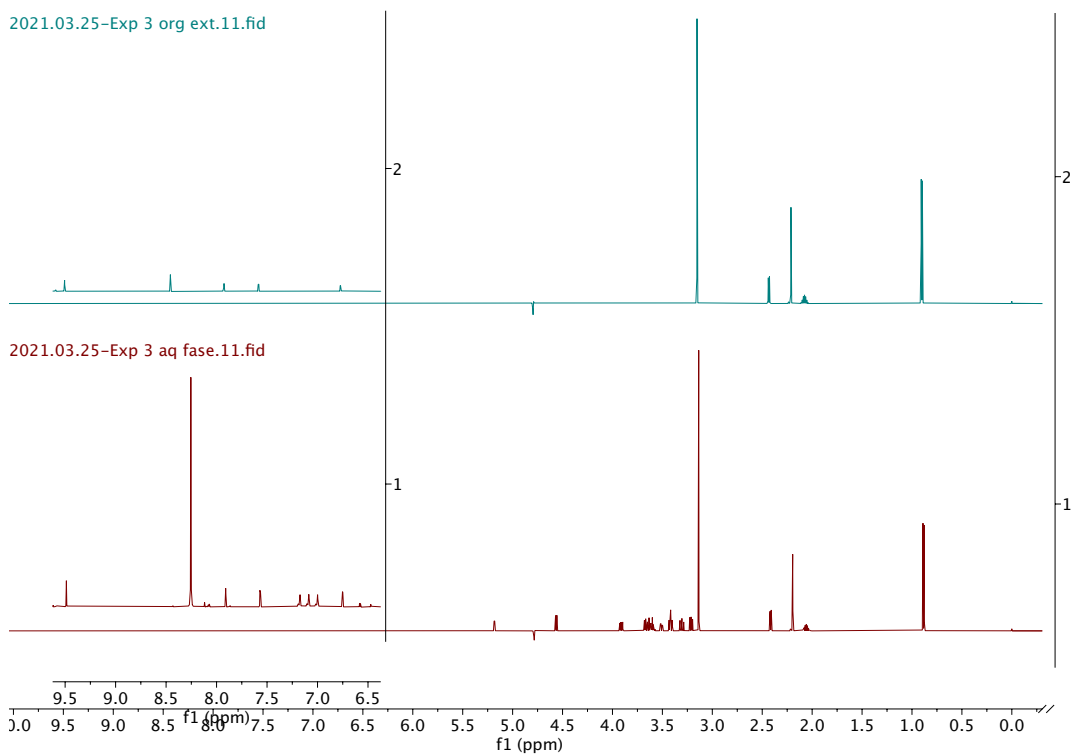


Figure B-4: ^1H -NMR-spectra of the organic and aqueous phases for experiment 3.

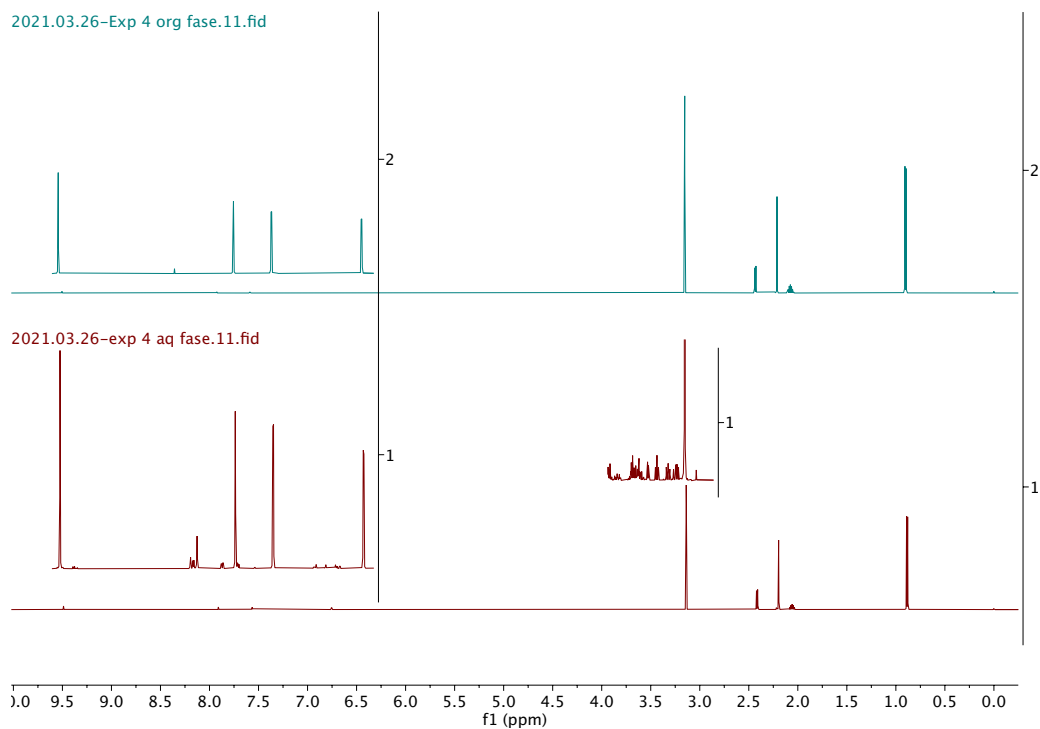


Figure B-5: $^1\text{H-NMR}$ -spectra of the organic and aqueous phases for experiment 4.

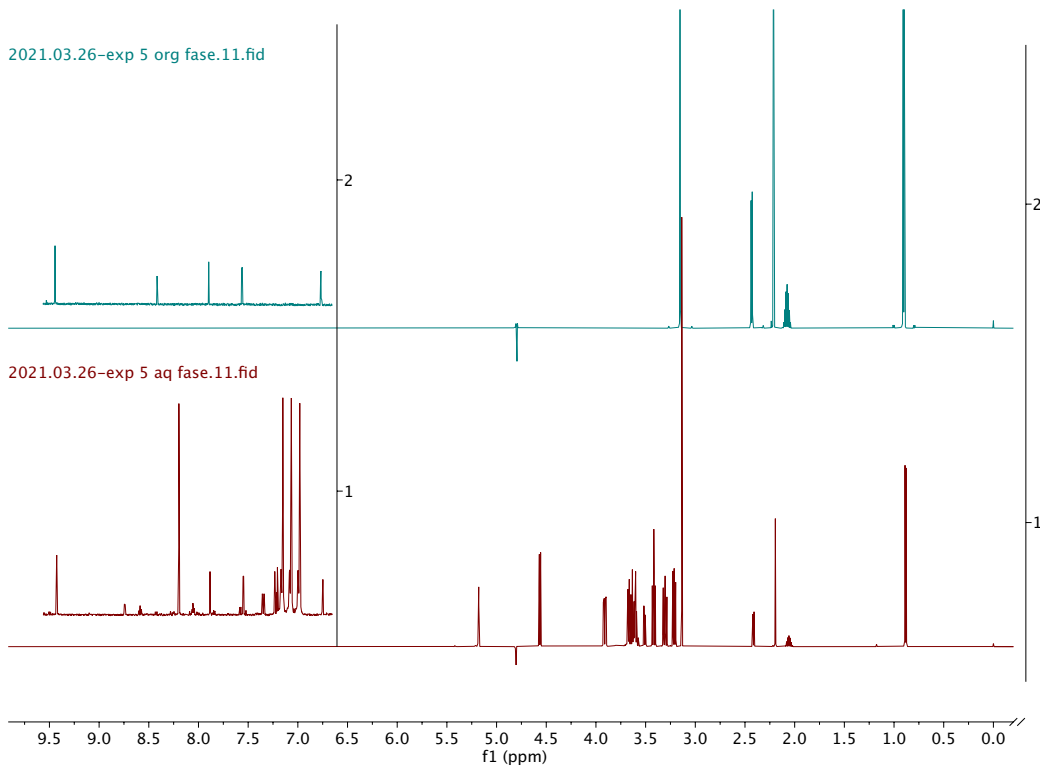


Figure B-6: $^1\text{H-NMR}$ -spectra of the organic and aqueous phases for experiment 5.

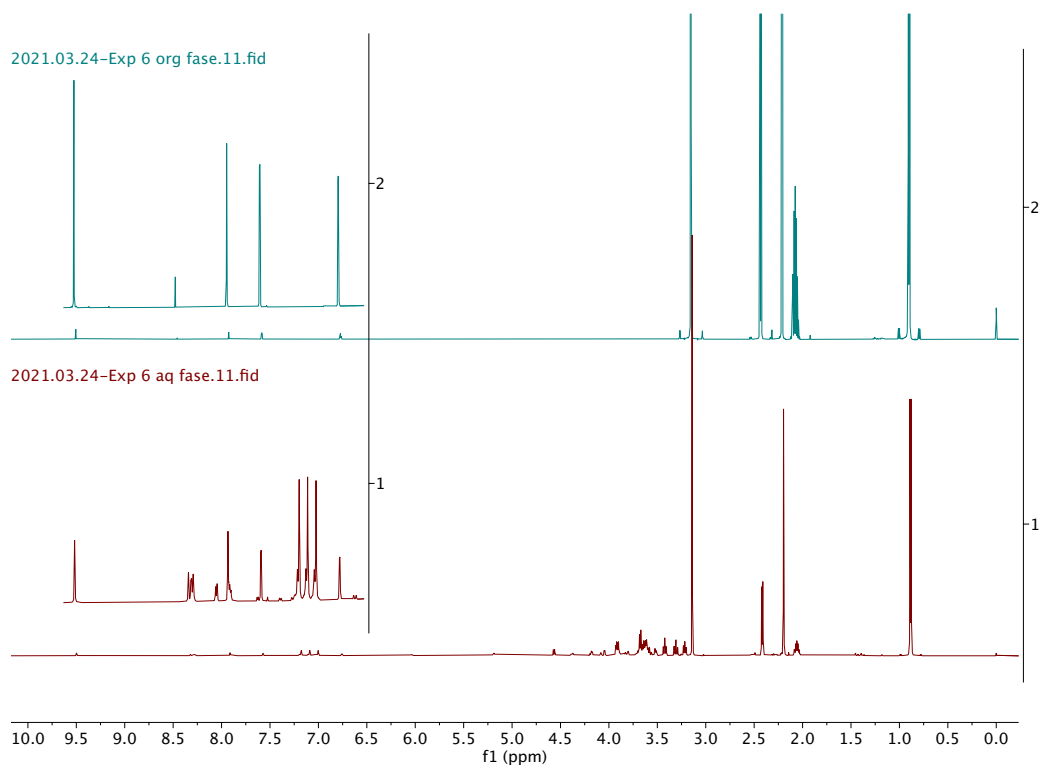


Figure B-7: $^1\text{H-NMR}$ -spectra of the organic and aqueous phases for experiment 6a.

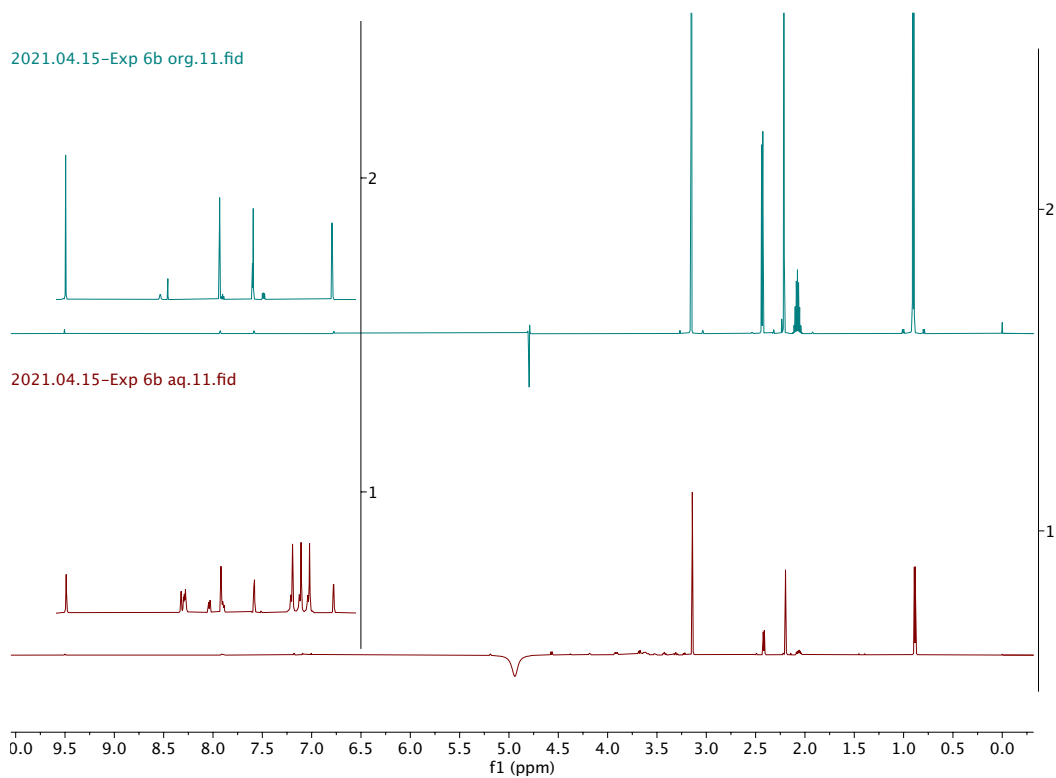


Figure B-8: $^1\text{H-NMR}$ -spectra of the organic and aqueous phases for experiment 6b.

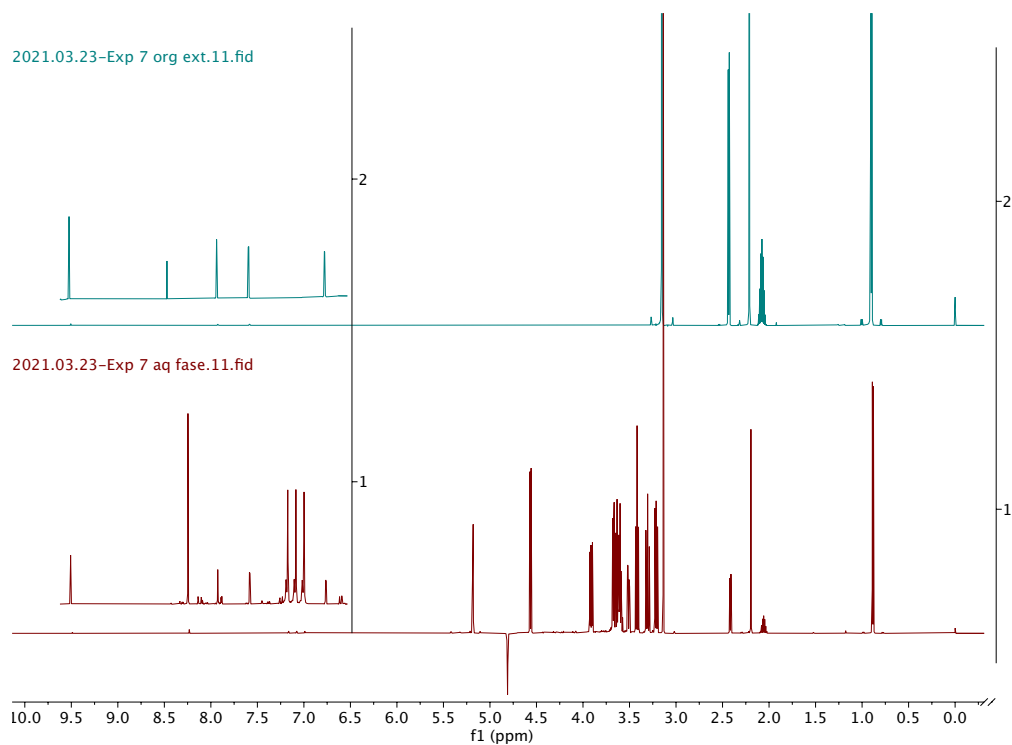


Figure B-9: $^1\text{H-NMR}$ -spectra of the organic and aqueous phases for experiment 7.

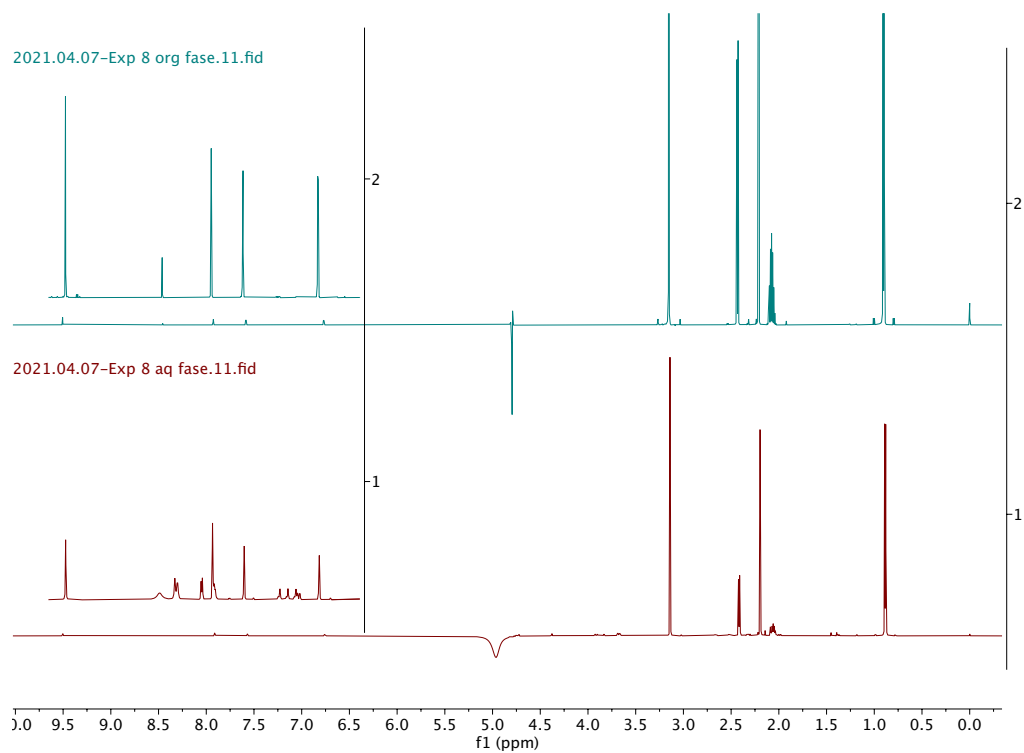


Figure B-10: $^1\text{H-NMR}$ -spectra of the organic and aqueous phases for experiment 8.

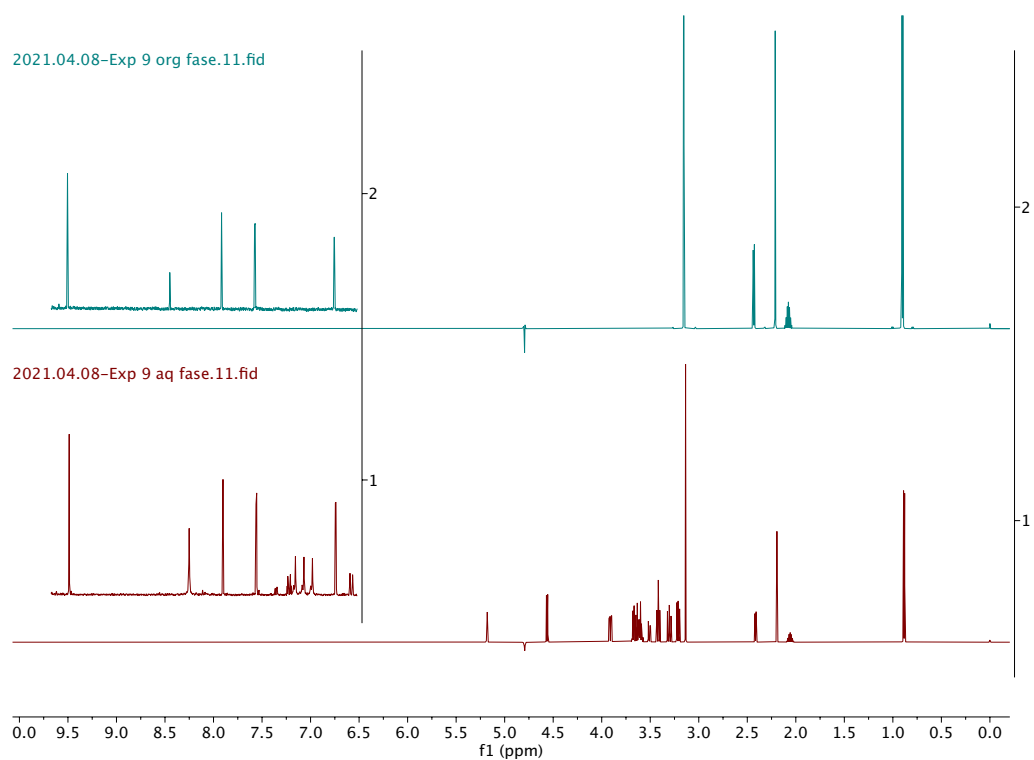


Figure B-11: $^1\text{H-NMR}$ -spectra of the organic and aqueous phases for experiment 9.

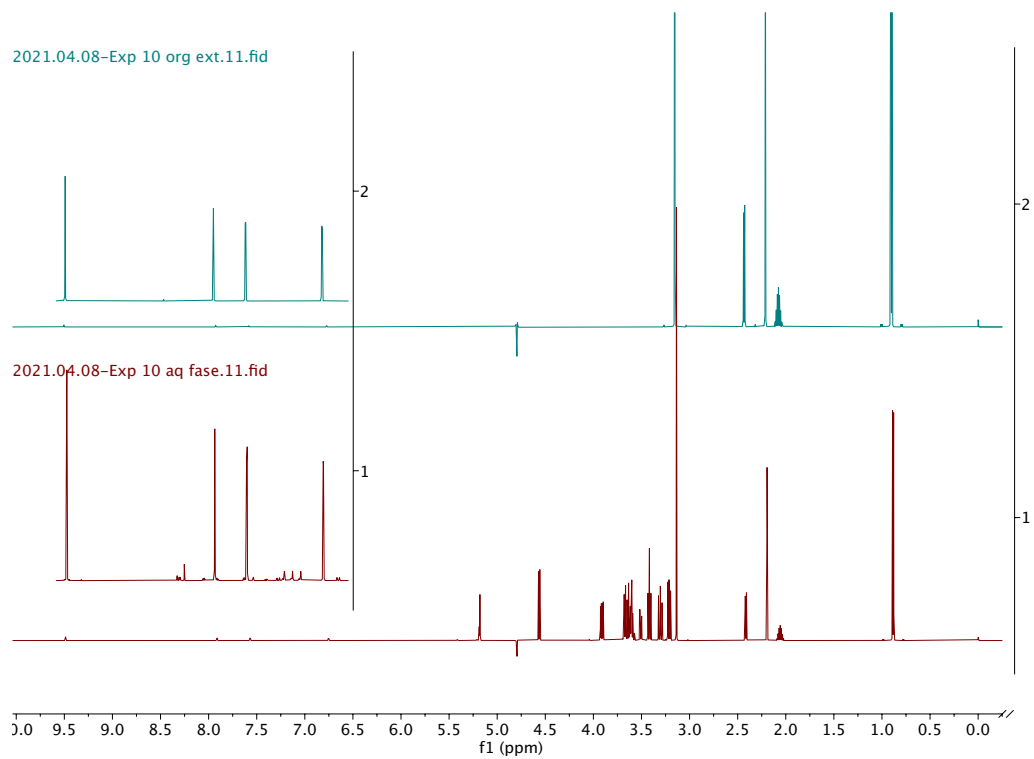


Figure B-12: $^1\text{H-NMR}$ -spectra of the organic and aqueous phases for experiment 10.

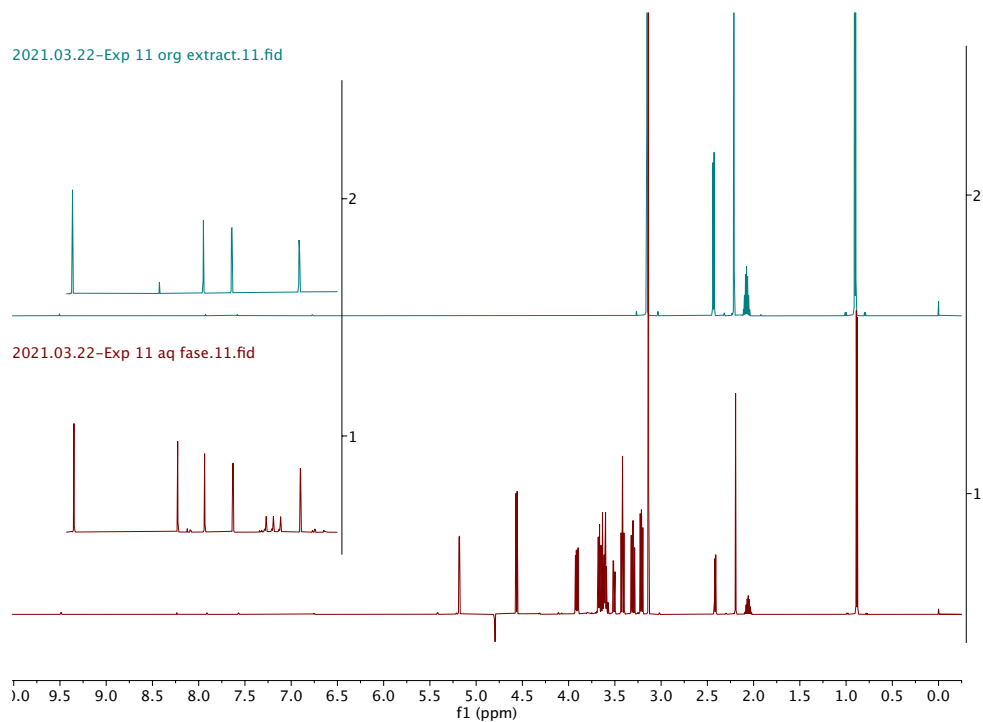


Figure B-13: $^1\text{H-NMR}$ -spectra of the organic and aqueous phases for experiment 11.

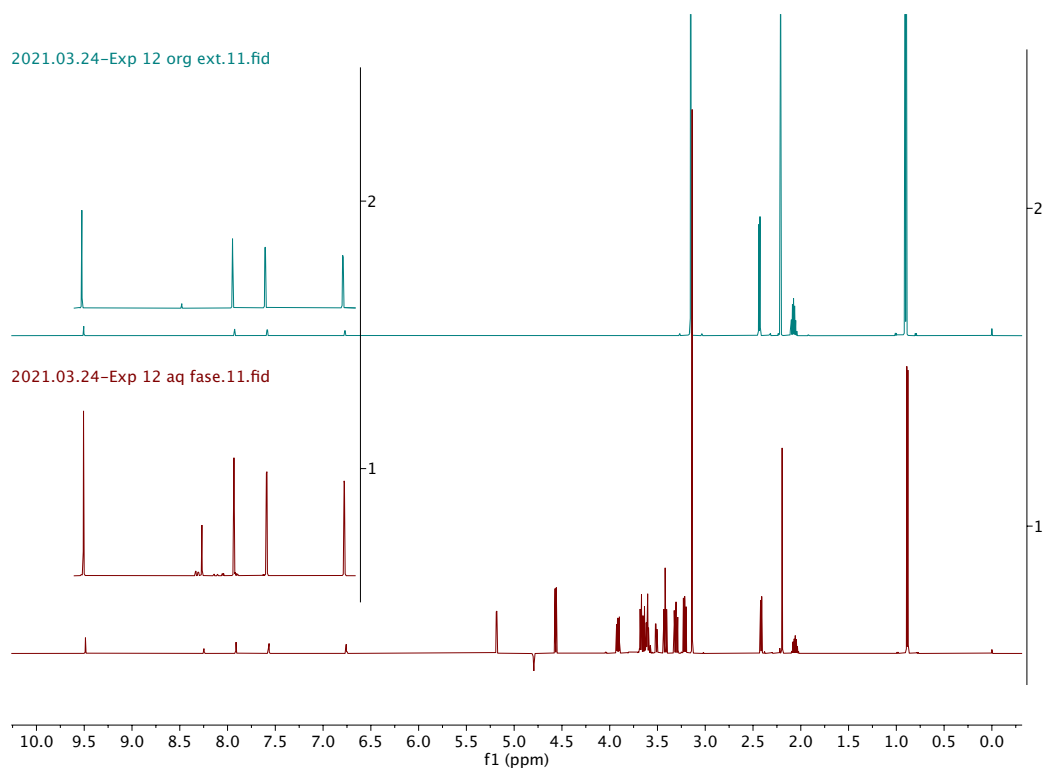


Figure B-14: $^1\text{H-NMR}$ -spectra of the organic and aqueous phases for experiment 12a.

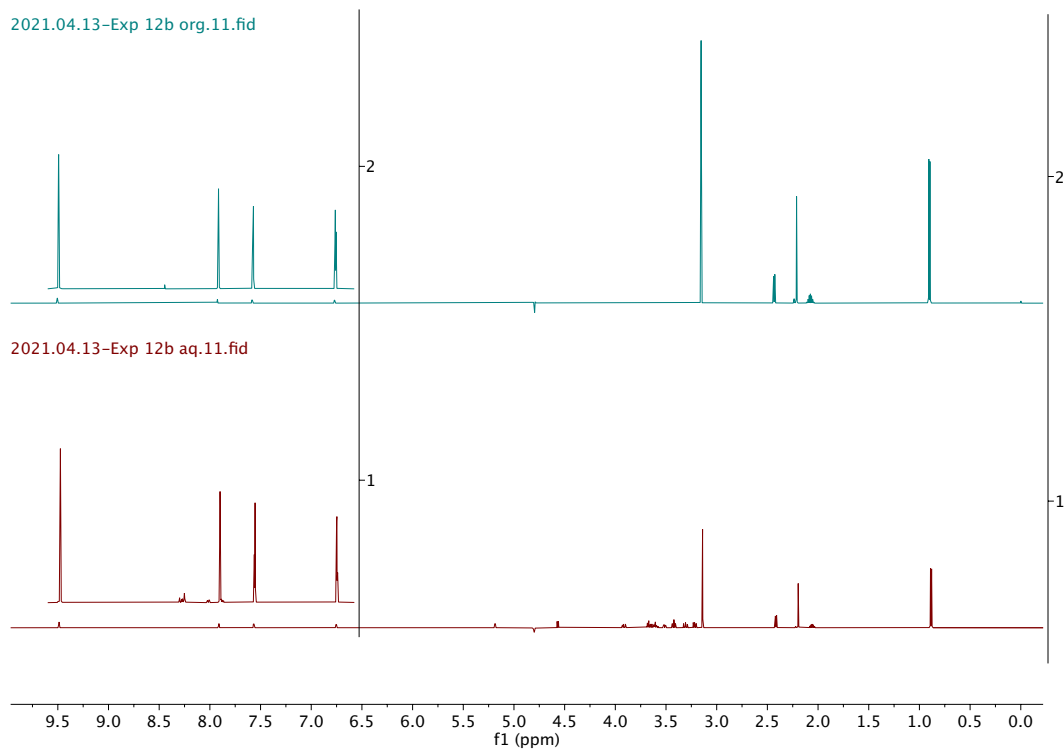


Figure B-15: ^1H -NMR-spectra of the organic and aqueous phases for experiment 12b.

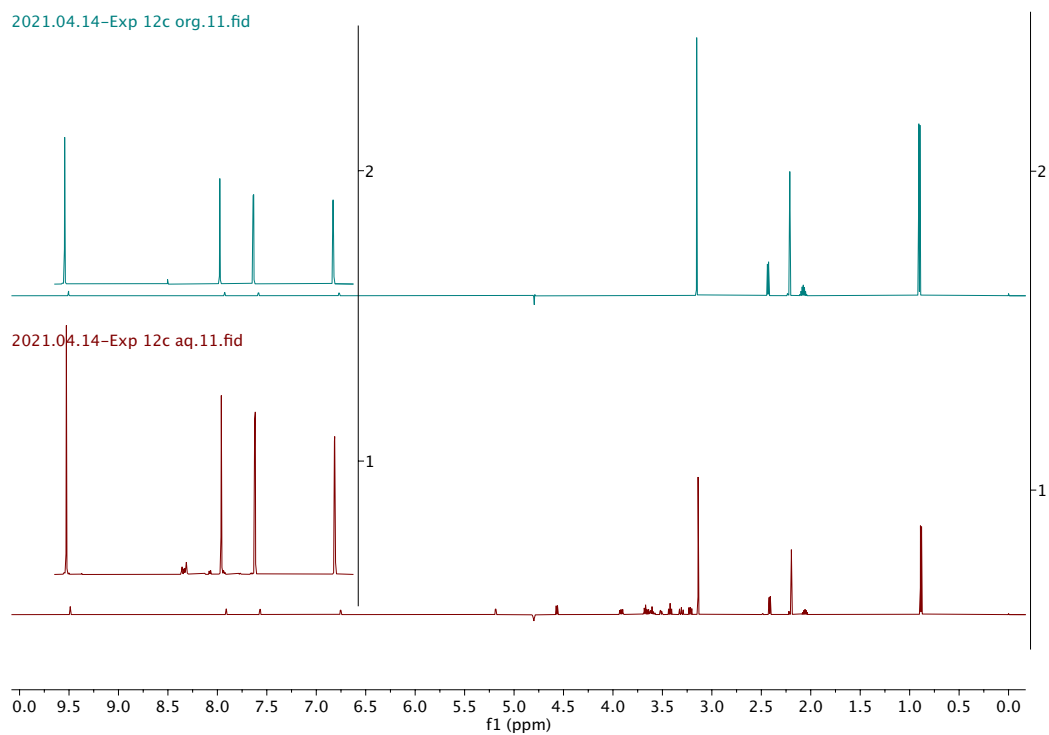


Figure B-16: ^1H -NMR-spectra of the organic and aqueous phases for experiment 12c.

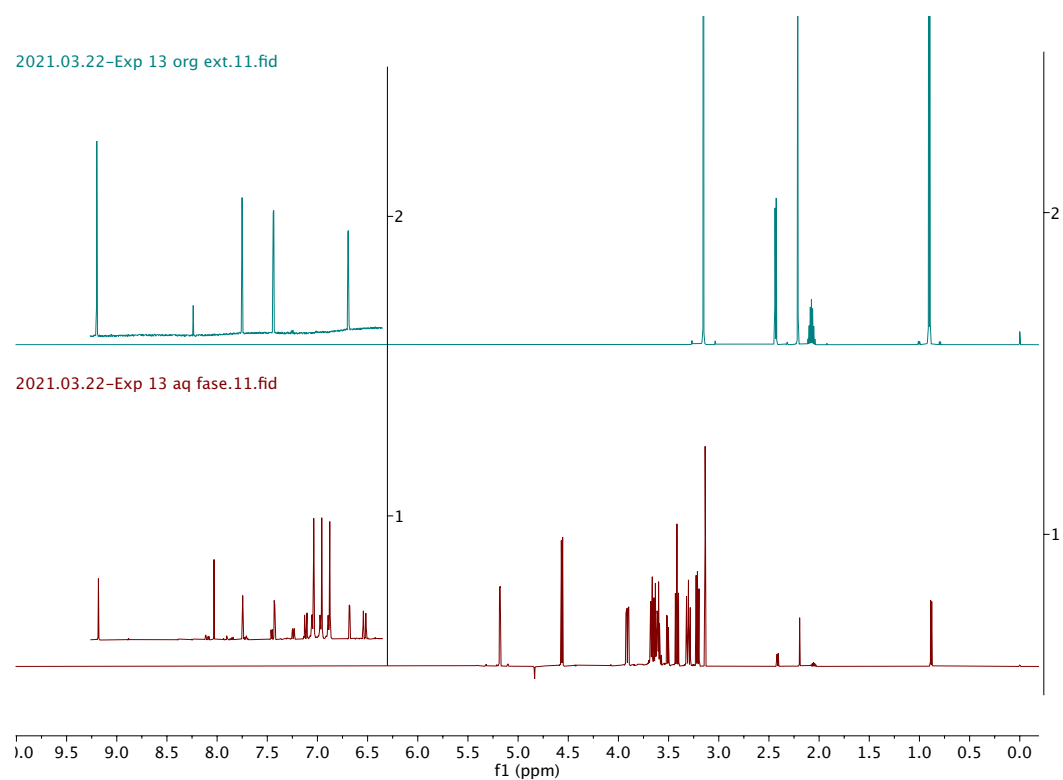


Figure B-17: $^1\text{H-NMR}$ -spectra of the organic and aqueous phases for experiment 13.

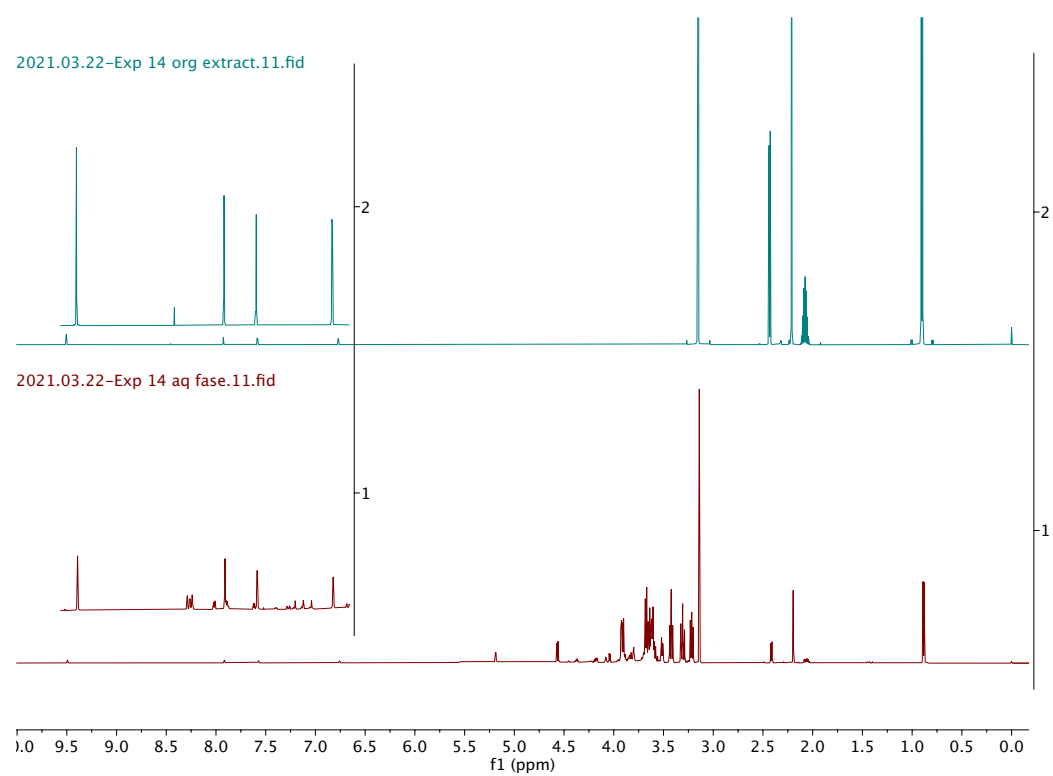


Figure B-18: $^1\text{H-NMR}$ -spectra of the organic and aqueous phases for experiment 14a.

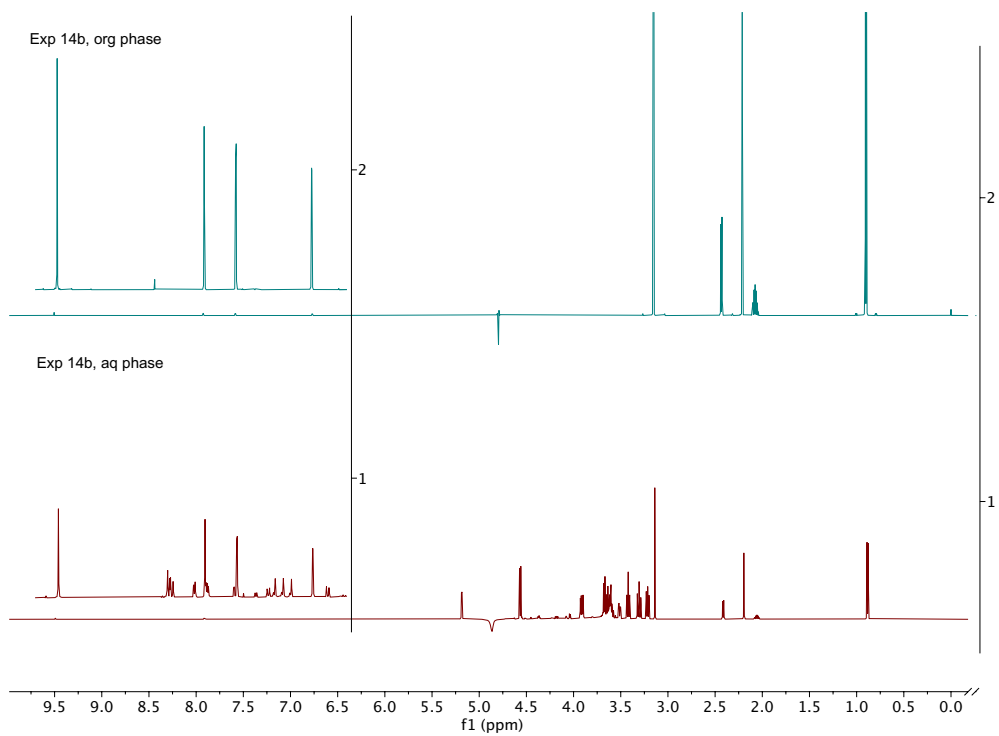


Figure B-19: ¹H-NMR-spectra of the organic and aqueous phases for experiment 14b.

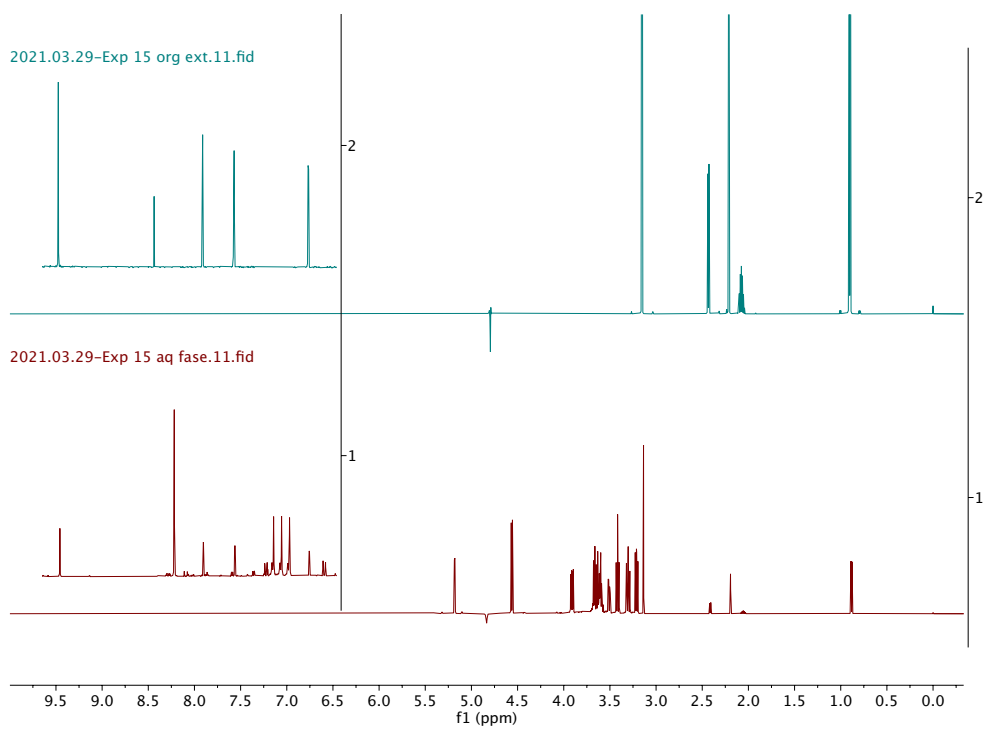


Figure B-20: ¹H-NMR-spectra of the organic and aqueous phases for experiment 15.

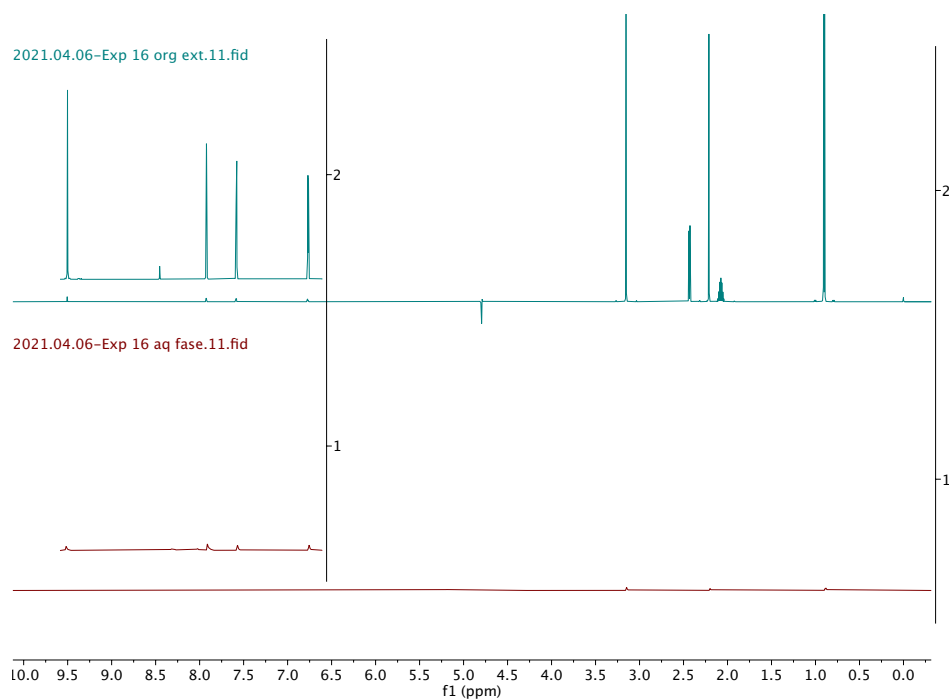


Figure B-21: ^1H -NMR-spectra of the organic and aqueous phases for experiment 16.

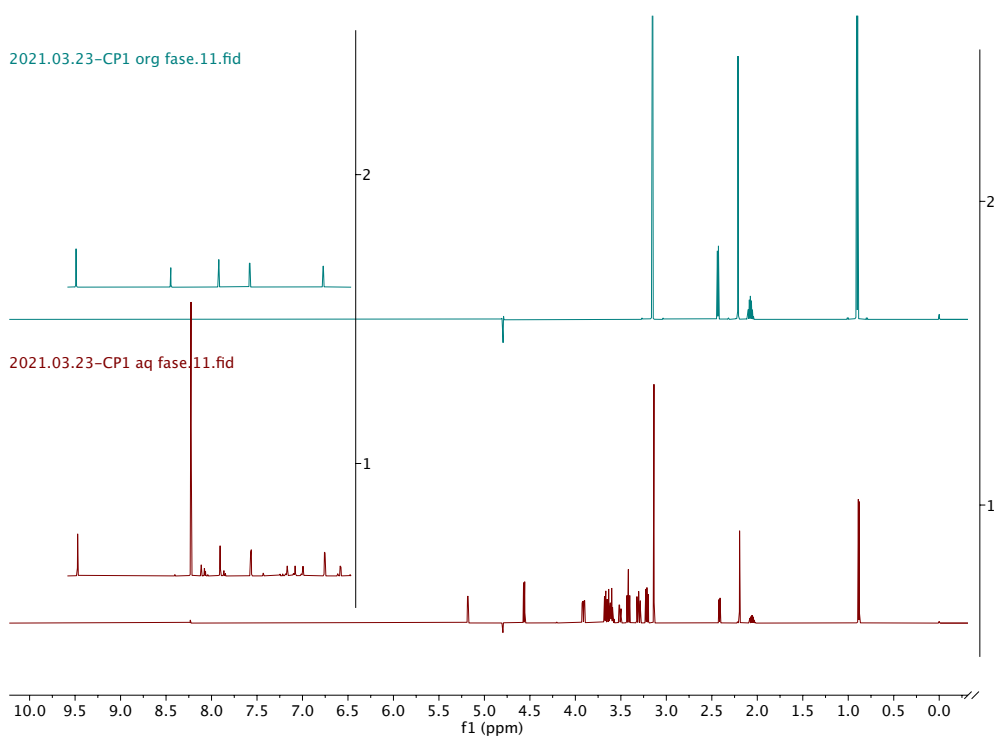


Figure B-22: ^1H -NMR-spectra of the organic and aqueous phases for experiment CP1.

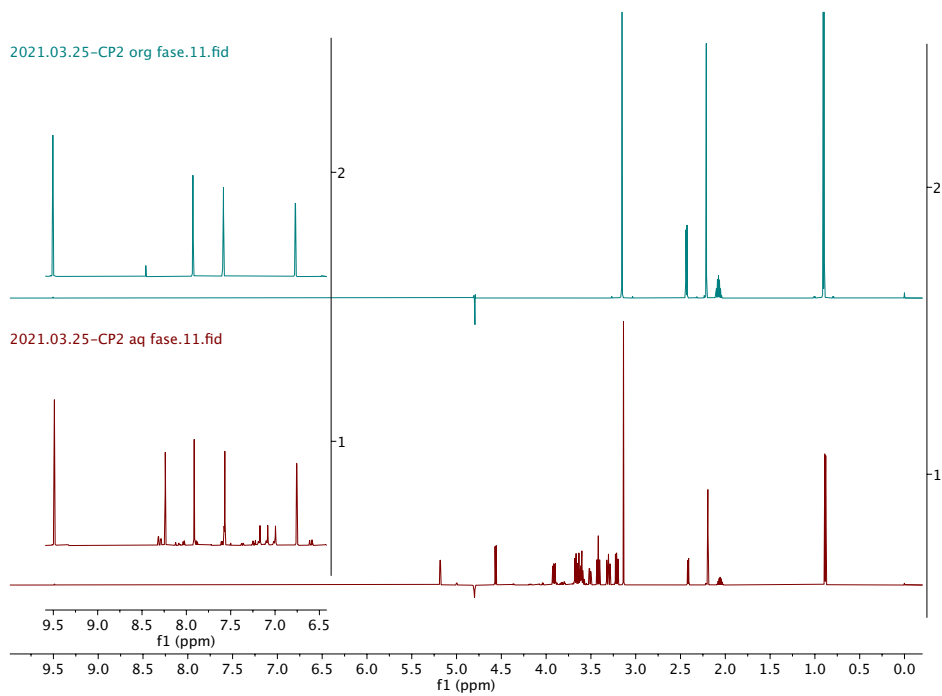


Figure B-23: ^1H -NMR-spectra of the organic and aqueous phases for experiment CP2.

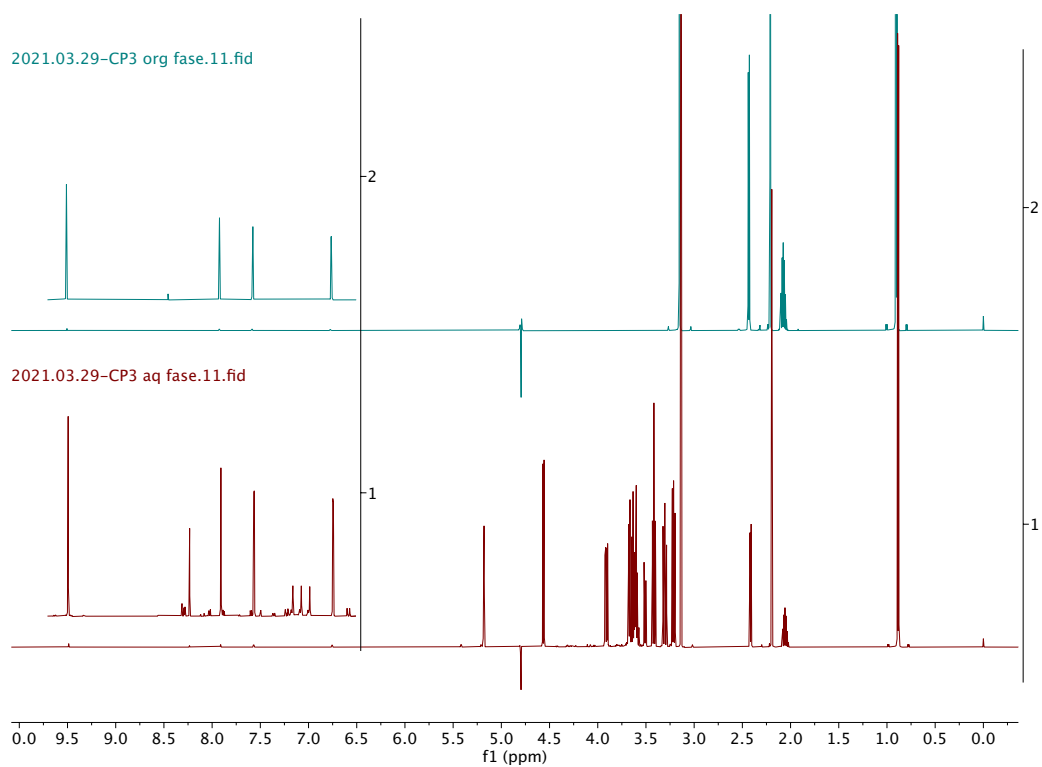


Figure B-24: ^1H -NMR-spectra of the organic and aqueous phases for experiment CP3.

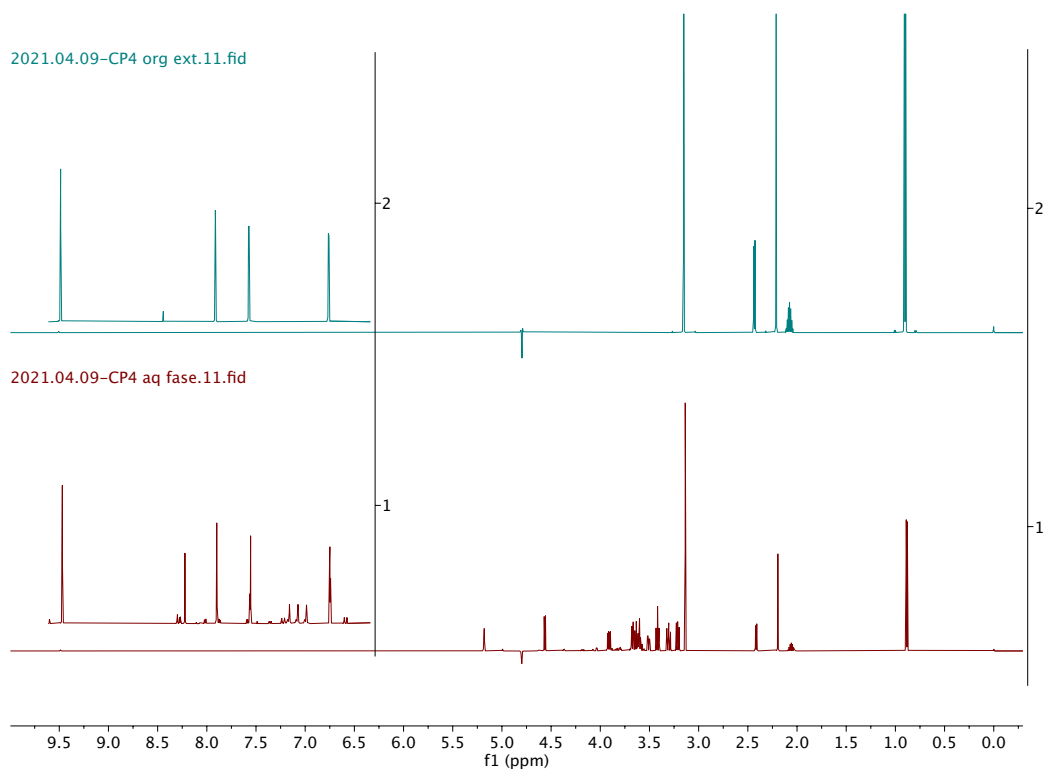


Figure B-25: ^1H -NMR-spectra of the organic and aqueous phases for experiment CP4.

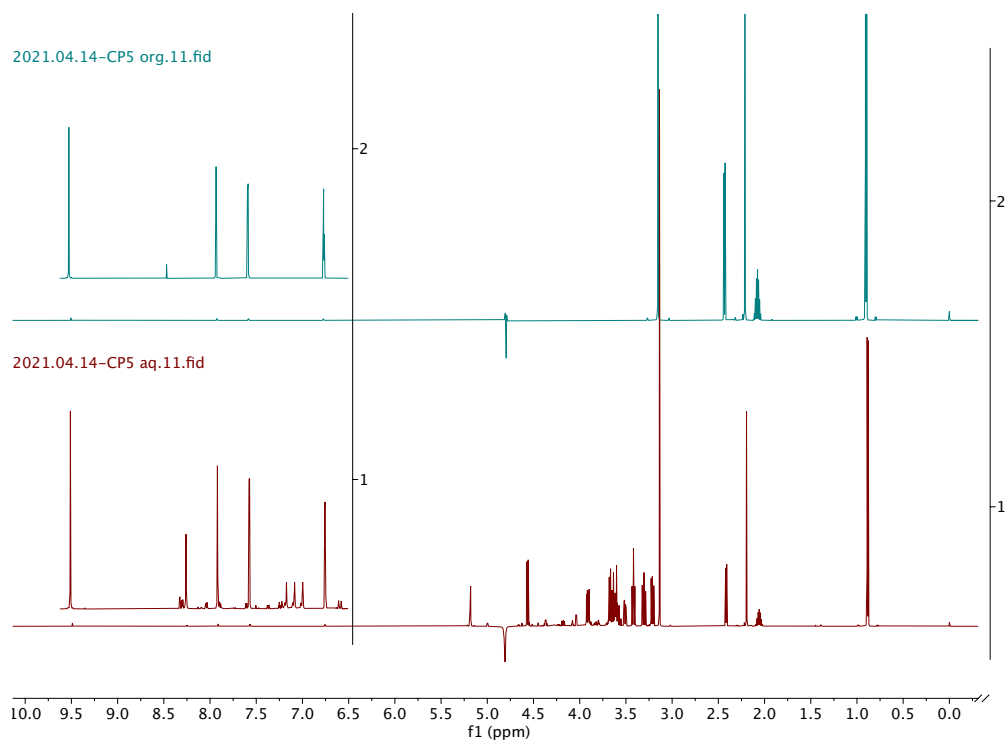


Figure B-26: ^1H -NMR-spectra of the organic and aqueous phases for experiment CP5.

APPENDIX C – RAW DATA FROM THE FIRST EXPERIMENTAL DESIGN

Table C-1: Raw data for FFD1 with added masses of substrate and catalyst for each experiment.

Experiment #	Temperature [°C]	Time [min]	Org/Aq [v/v]	Substrate [g]	Catalyst [g]
2	200	30	1:4	0.1253	0.0127
13	150	30	4:1	0.3753	0.0374
14	200	30	4:1	0.3743	0.0125
11	150	90	1:4	0.3751	0.0375
CP1	175	60	1:1	0.2499	0.0249
7	150	90	4:1	0.1252	0.0371
21	150	30	1:4	0.1252	0.0121
16a	200	90	4:1	0.3752	0.0373
12	200	90	1:4	0.3752	0.0126
16b	200	90	1:4	0.3753	0.0373

Table C-2: Integration values, predicted concentrations and calculated yields for all experiments from FFD1.

Exp #	Compound	Organic phase					Aqueous phase			
		Protons	Integral	Conc. [mM]	Factor	Yield [g]	Integral	Conc. [mM]	Factor	Yield [g]
2	Furfural	1	0.0218	2.2548	-	0.0041	0.0628	6.5469	-	0.0027
	DMSO ₂	6	6.0000	103.4300	0.0096	-	6.0000	104,2500	0.0096	-
	α and β D-Xylose	2	-	-	-	-	1.6930	174,7304	-	0.1124
13	Furfural	1	0.0399	4.1275	-	0.0322	0.0401	4,1275	-	0.0005
	DMSO ₂	6	6.0000	101.4800	0.0098	-	6.0000	102.5000	0.0097	-
	α and β D-Xylose	2	-	-	-	-	16.1998	1676.8414	-	0.3040
14	Furfural	1	0.0684	6.9109	-	0.0530	0.1601	15.2334	-	0.0015
	DMSO ₂	6	6.0000	101.25	0.0099	-	6.0000	96.2000	0.0105	-
	α and β D-Xylose	2	-	-	-	-	11.4589	1090.3066	-	0.1689
11	Furfural	1	0.0346	3.5601	-	0.0066	0.0937	9.5589	-	0.0041
	DMSO ₂	6	6.0000	103.25	0.0097	-	6.0000	101.6200	0.0098	-
	α and β D-Xylose	2	-	-	-	-	5.3093	537,1372	-	0.3599
CP1	Furfural	1	0.0605	6.3515	-	0.0296	0.1726	16.9047	-	0.0045
	DMSO ₂	6	6.0000	105.38	0.0095	-	6.0000	95.6800	0.0105	-
	α and β D-Xylose	2	-	-	-	-	3.2889	314.2904	-	0.1300
7	Furfural	1	0.0262	2.7159	-	0.0217	0.0432	4.2966	-	0.0004
	DMSO ₂	6	6.0000	103.56	0.0096	-	6.0000	96.48	0.0104	-
	α and β D-Xylose	2	-	-	-	-	4.4081	425.2935	-	0.0596
21	Furfural	1	0.0022	0.2375	-	0.0004	0.0055	0.5854	-	0.0002
	DMSO ₂	6	6.0000	106.73	0.0094	-	6.0000	105.9600	0.0094	-
	α and β D-Xylose	2	-	-	-	-	1.8860	195.6551	-	0.1274
16a	Furfural	1	0.1139	11.4609	-	0.0821	0.3979	42.1112	-	0.0016
	DMSO ₂	6	6.0000	100.60	0.0099	-	6.0000	93.11	0.0107	-
	α and β D-Xylose	2	-	-	-	-	0.0000	0.0000	-	0.0000
12	Furfural	1	0.2946	29.6317	-	0.0495	0.8822	93.4779	-	0.0369
	DMSO ₂	6	6.0000	103.92	0.0096	-	6.0000	97.6900	0.0102	-
	α and β D-Xylose	2	-	-	-	-	1.3312	130.4044	-	0.0803
16b	Furfural	1	0.1123	11.2949	-	0.0798	0.3799	40.2489	-	0.0015
	DMSO ₂	6	6.0000	103.16	0.0099	-	6.0000	103.3400	0.0107	-
	α and β D-Xylose	2	-	-	-	-	0.0000	0.0000	-	0.0000

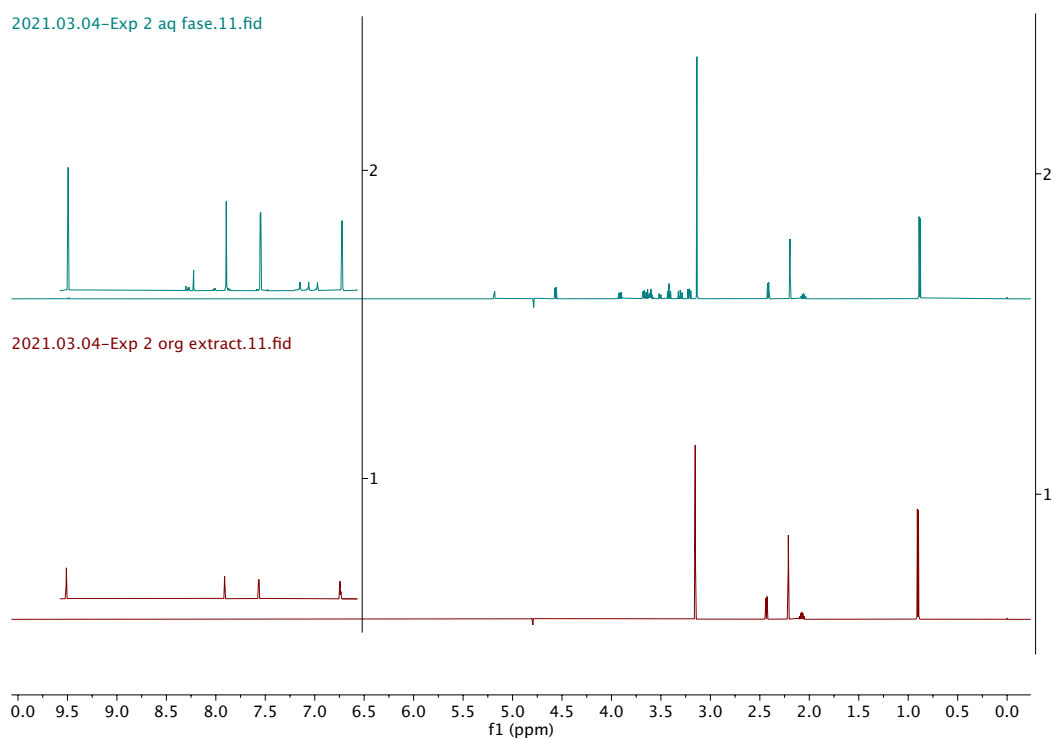


Figure C-1: ^1H -NMR-spectra of the organic and aqueous phases for experiment 2.

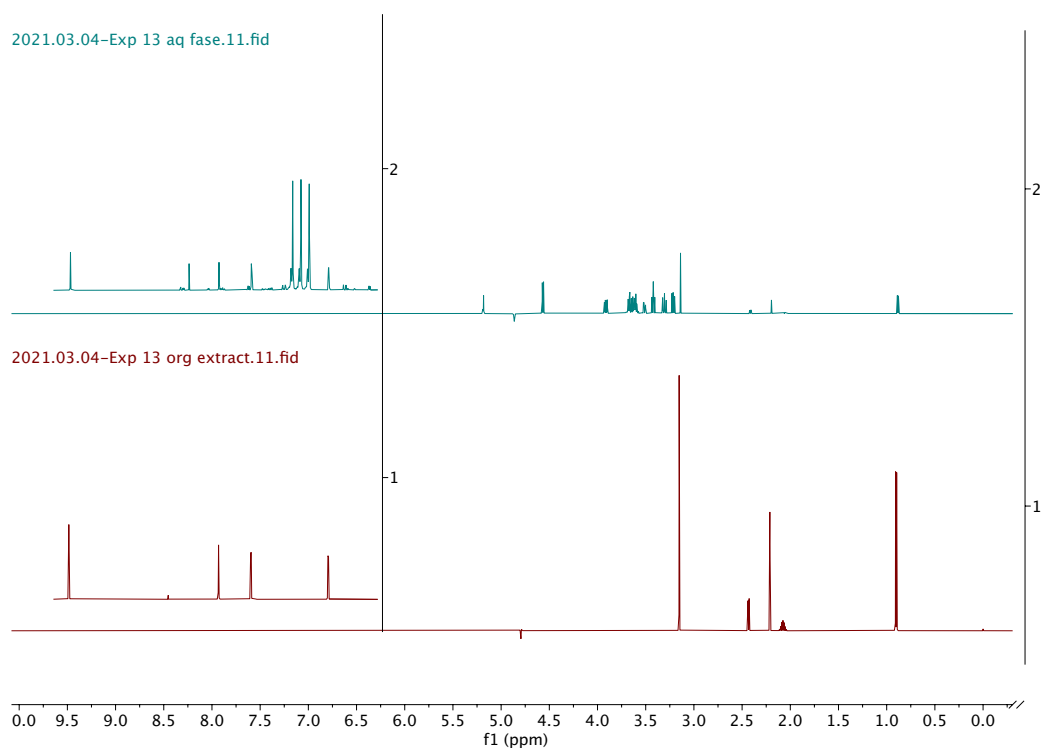


Figure C-2: ^1H -NMR-spectra of the organic and aqueous phases for experiment 13.

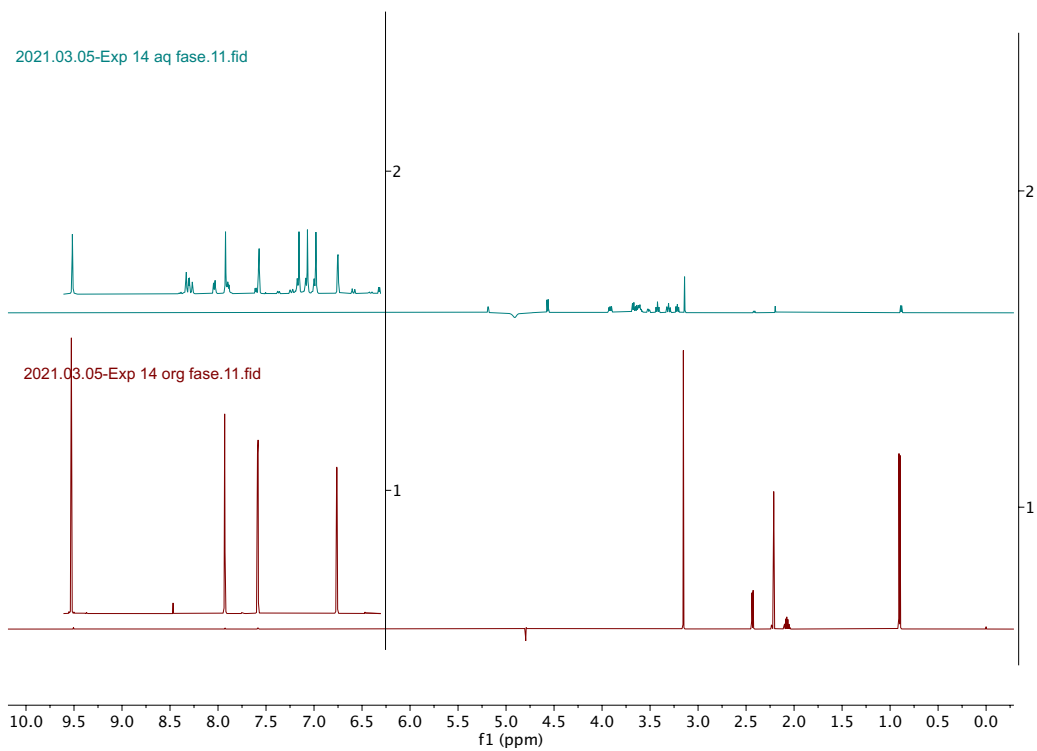


Figure C-3: ^1H -NMR-spectra of the organic and aqueous phases for experiment 14.

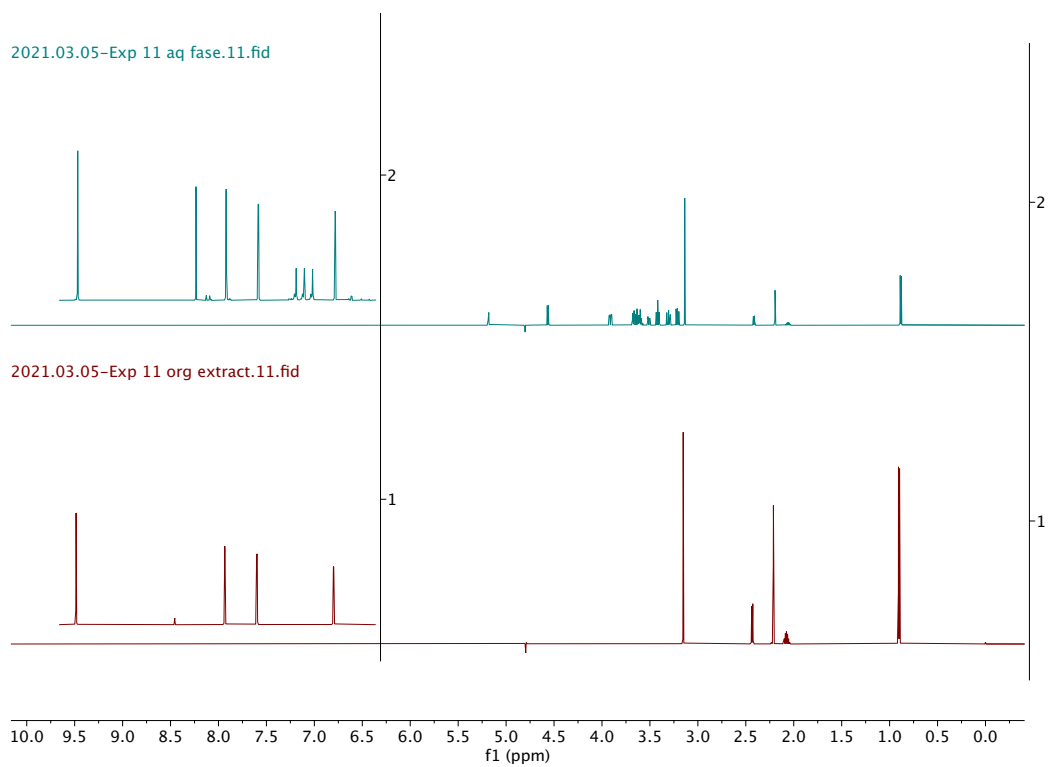


Figure C-4: ^1H -NMR-spectra of the organic and aqueous phases for experiment 11.

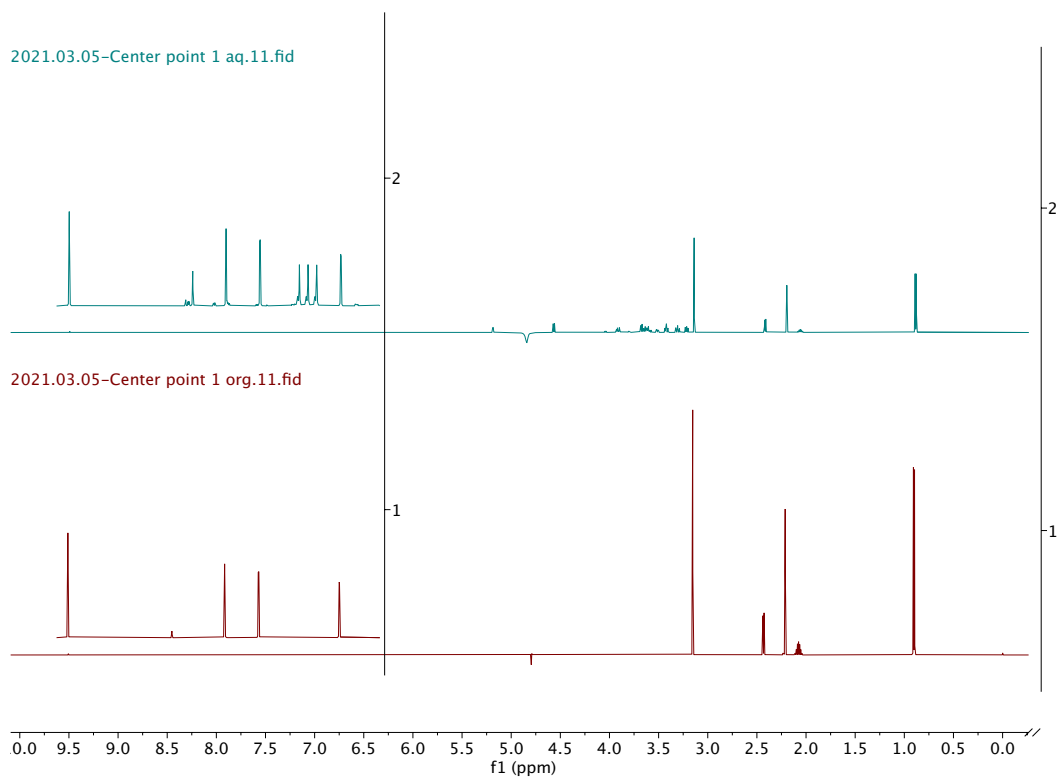


Figure C-5: $^1\text{H-NMR}$ -spectra of the organic and aqueous phases for CPI.

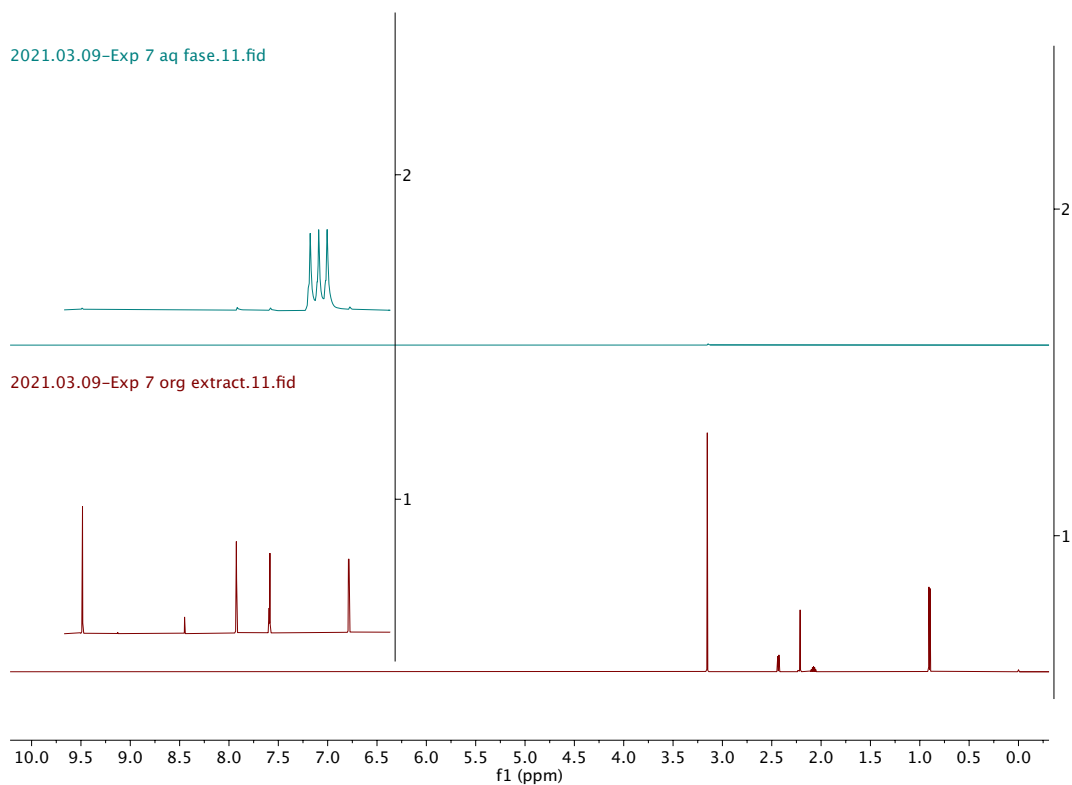


Figure C-6: $^1\text{H-NMR}$ -spectra of the organic and aqueous phases for experiment 7.

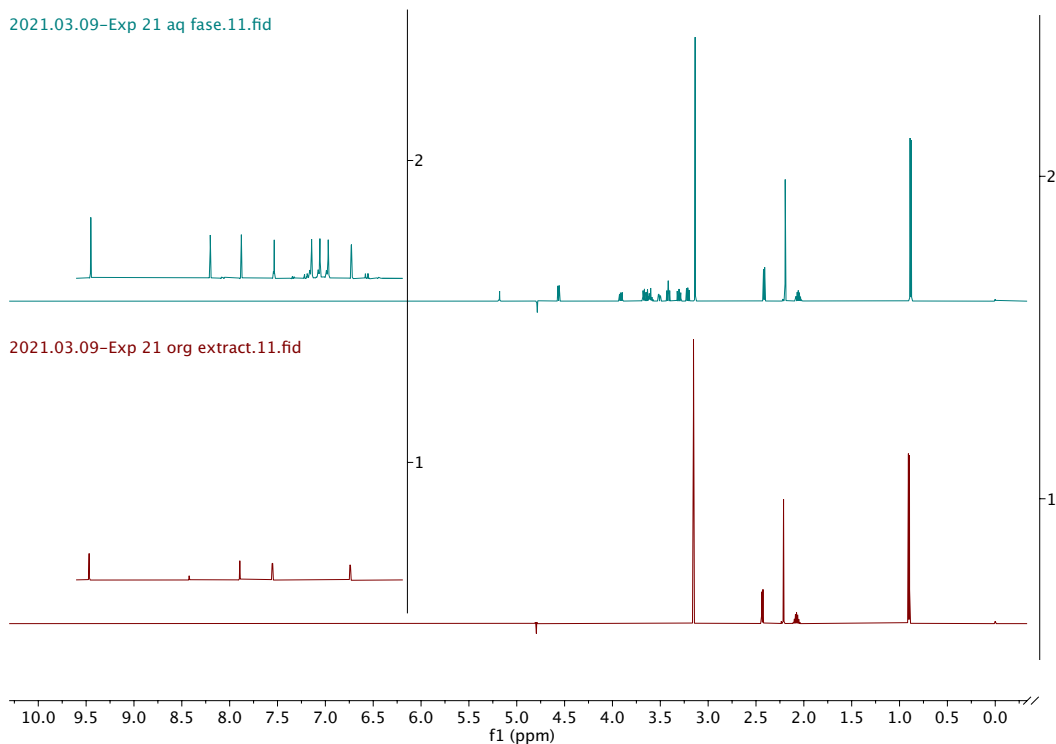


Figure C-7: ^1H -NMR-spectra of the organic and aqueous phases for experiment 21.

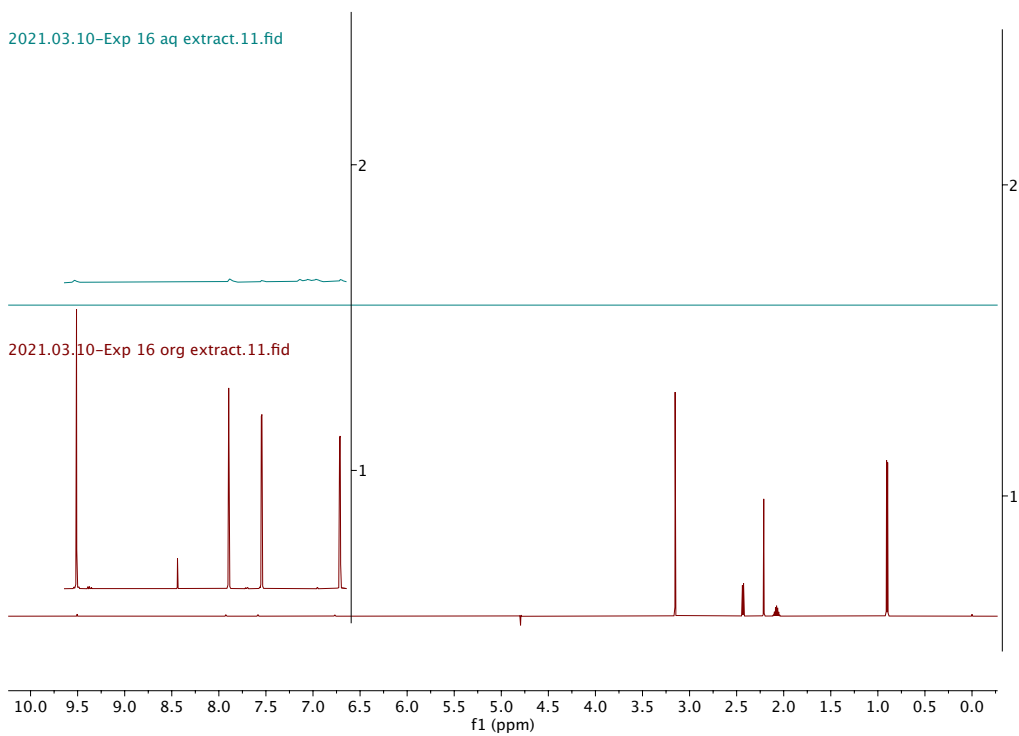


Figure C-8: ^1H -NMR-spectra of the organic and aqueous phases for experiment 16a.

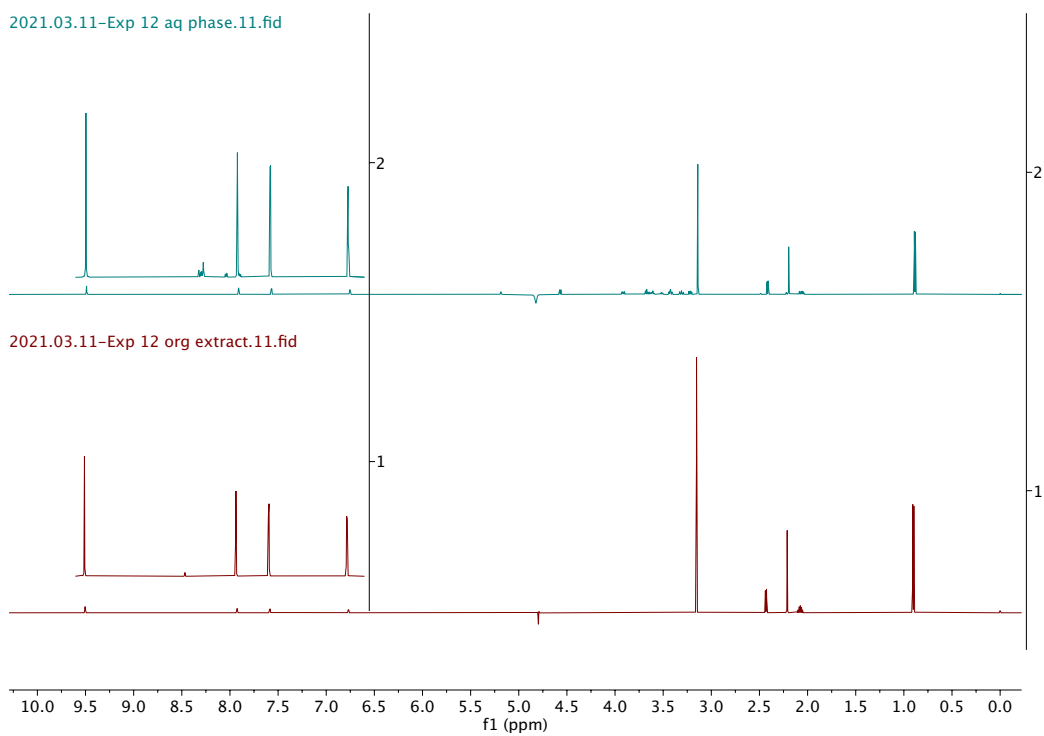


Figure C-9: ^1H -NMR-spectra of the organic and aqueous phases for experiment 12.

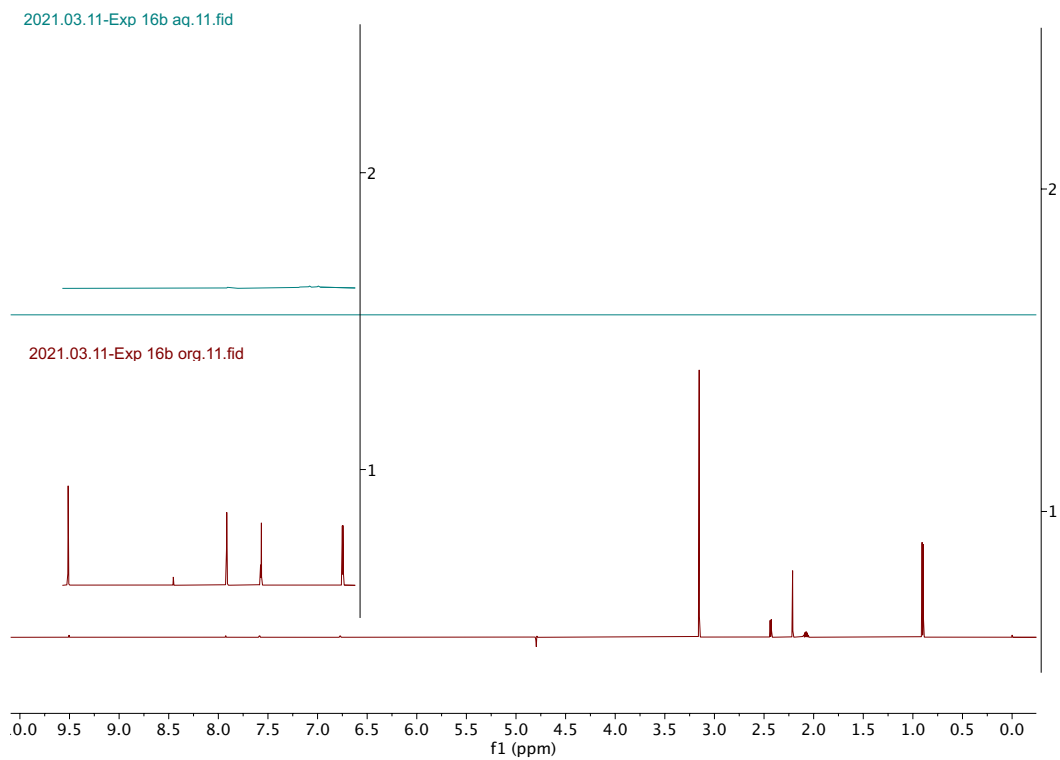


Figure C-10: ^1H -NMR-spectra of the organic and aqueous phases for experiment 16b.

APPENDIX D – RAW DATA – HPLC, GC-MS

Tabell D-1: Peak areas used when making the calibration curve for HPLC.

Concentration [$\mu\text{g/mL}$]	Parallel	Area
25.40	1	2638.55
25.40	2	2633.94
25.40	3	2628.91
\bar{x}		2633.80
s		4.82
224.95	1	23031.96
224.95	2	23022.67
224.95	3	22976.06
\bar{x}		23010.23
s		29.95
424.26	1	42742.34
424.26	2	42813.43
424.26	3	42708.82
\bar{x}		42754.86
s		53.41
621.10	1	61395.18
621.10	2	61411.35
621.10	3	61285.44
\bar{x}		61363.99
s		68.51
821.51	1	78675.95
821.51	2	78814.92
821.51	3	78696.74
\bar{x}		78729.20
s		74.96
1009.05	1	101388.35
1009.05	2	101549.74
1009.05	3	101495.93
\bar{x}		101478.01
s		82.18

*Samples were analyzed in triplicates in order to enable calculation of average peak area (\bar{x}) and standard deviation (s). The average peak area for each calibration solution was used when creating the calibration curve.

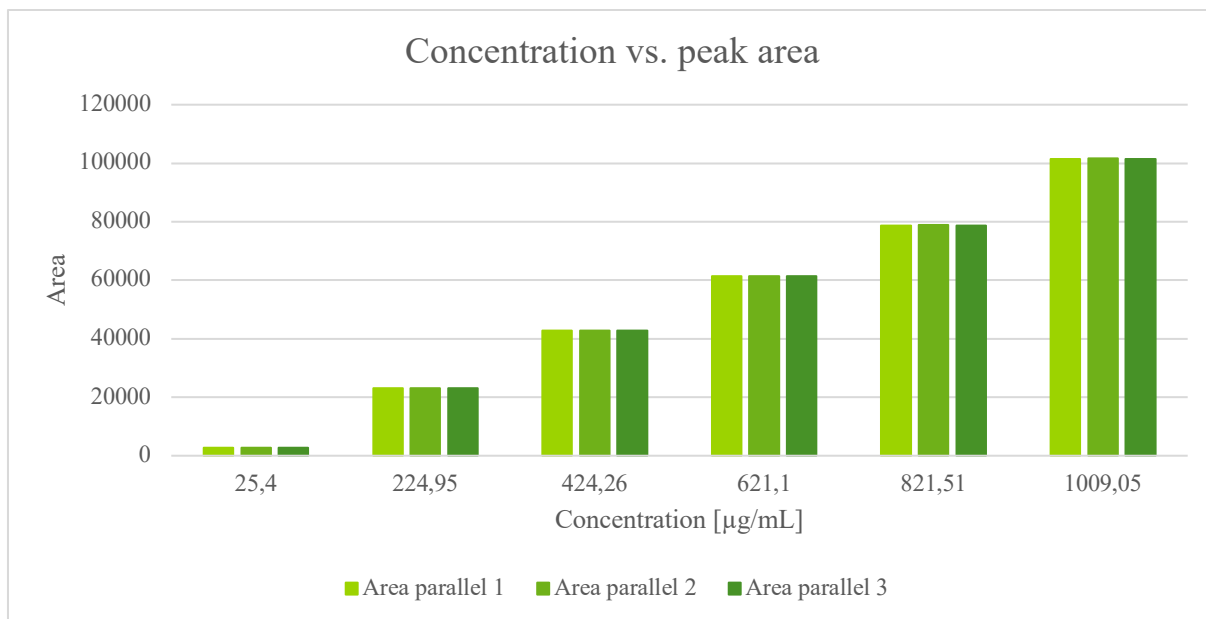


Figure D-1: Concentration of the six standard solutions used to make the calibration curve for HPLC vs measured peak area for the three parallels. As is evident, the peak areas were highly reproducible between parallels.

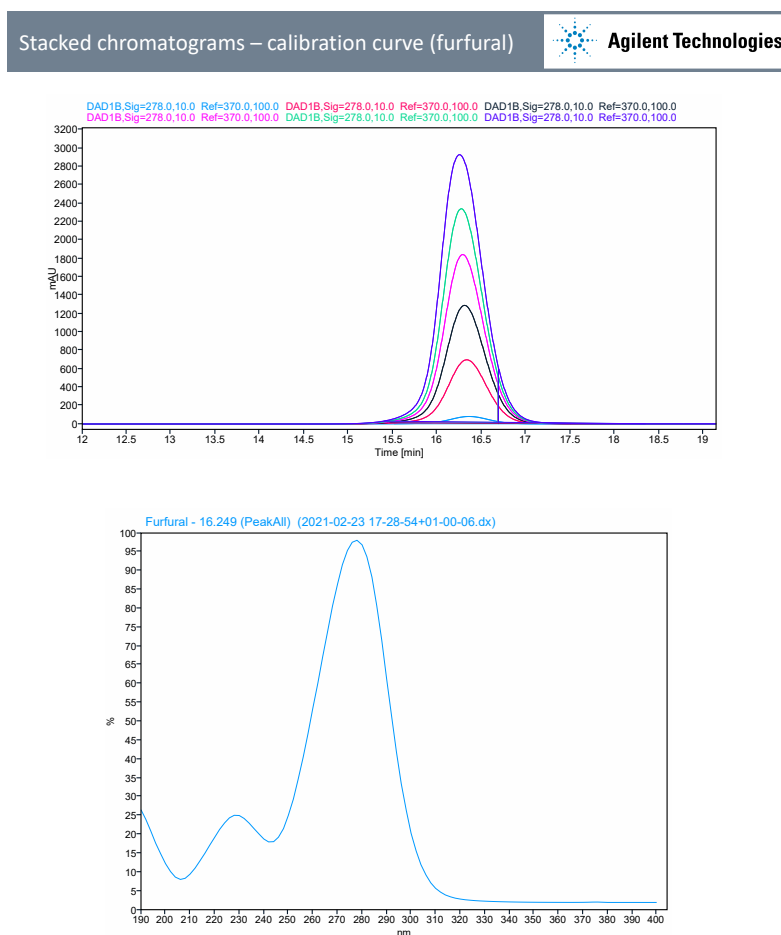


Figure D-2: Stacked chromatograms for the six standard solutions used to make the calibration curve for FUR.

Tabell D-2: Peak areas for FUR, HD and CH used when making the calibration curve for GC-MS.

Sample #	Concentration [$\mu\text{g}/\text{mL}$]	Parallel	Area FUR	Area HD	Area CH
1	9.90	1	4828055	121126071	64995966
		2	3803690	96481297	53969548
2	20.00	1	13674531	115197633	62477969
		2	10388454	95408767	50719419
3	30.80	1	20287942	107149077	62433022
		2	17589817	94178208	56920087
4	37.50	1	27905432	104530050	56471855
		2	23189407	97903071	49860413
5	50.10	1	34737057	100428848	59780264
		2	31139391	91583304	51519227

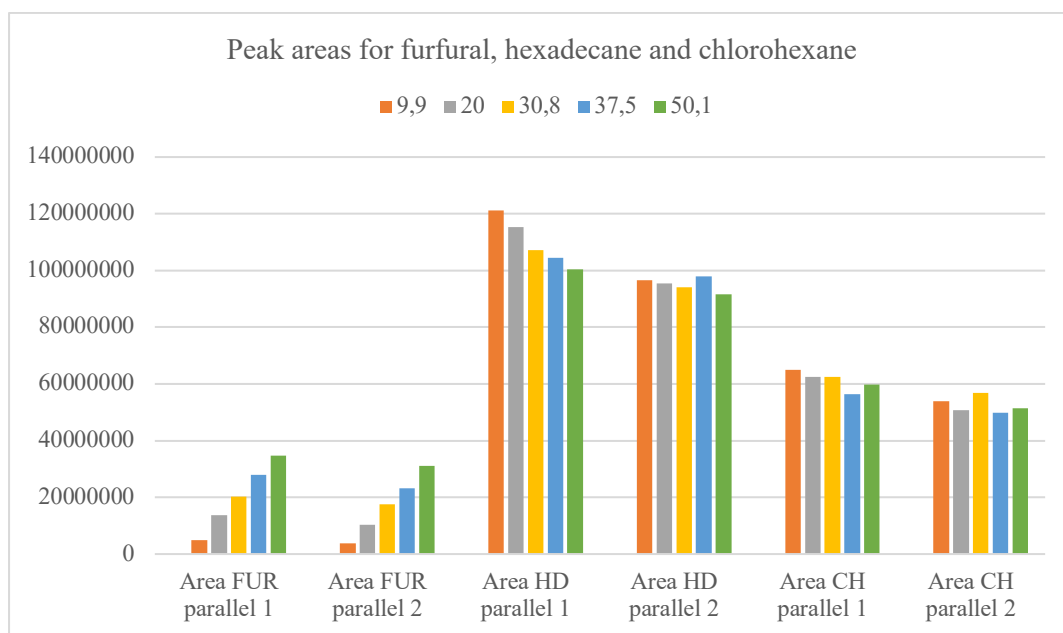


Figure D-3: Measured peak area vs. actual concentration for the five standard solutions containing FUR, hexadecane and chlorohexane used to make the calibration curve for GC-MS.

As is evident from Figure D-3, the peak areas were not reproducible between parallels. However, a pattern of decreasing peak intensity for all three compounds was observed between the two parallels.

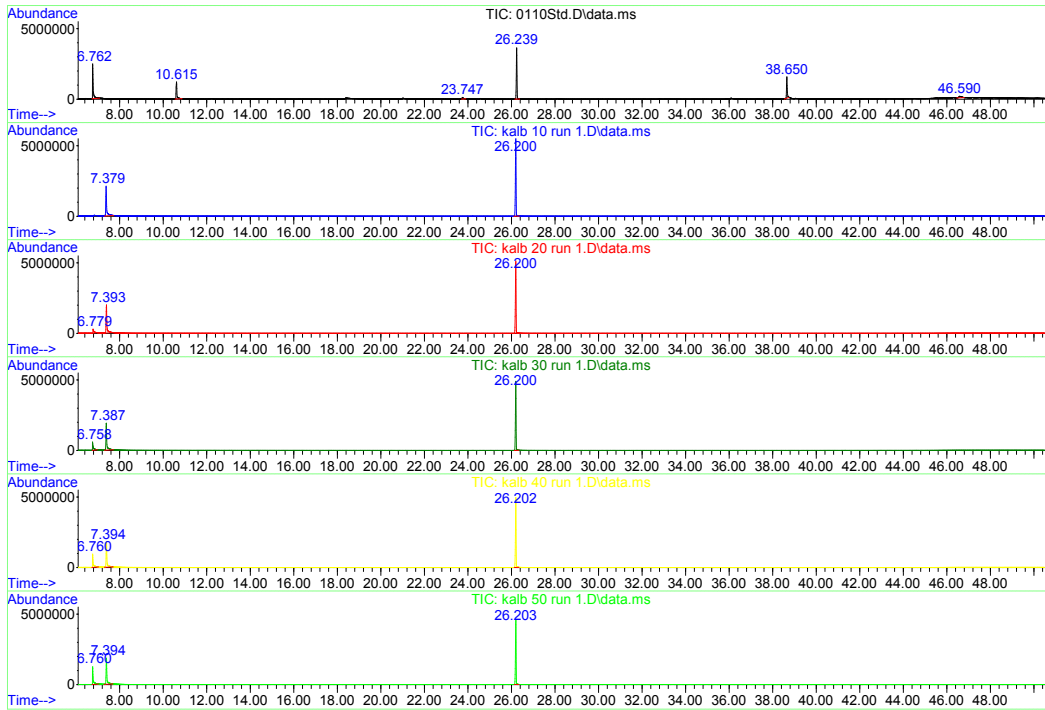


Figure D-4: Chromatograms for the five standard solutions used for construction of the calibration curves (parallel 1). The retention times for FUR, chlorohexane and hexadecane were 6.76, 7.39 and 26.20 min, respectively.

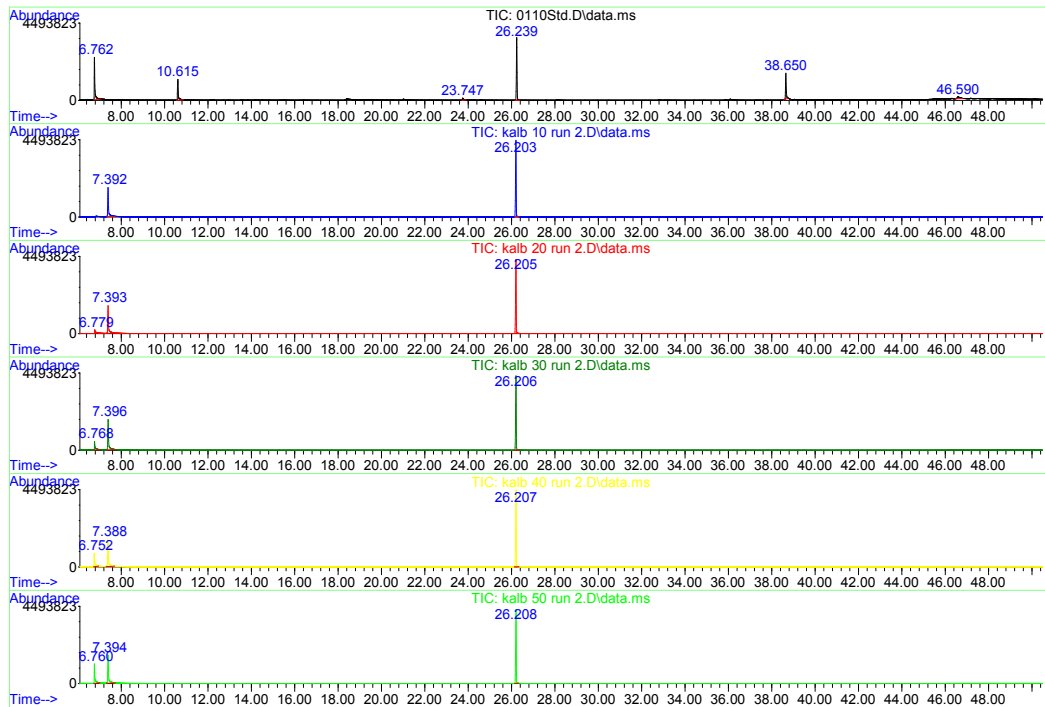


Figure D-5: Chromatograms for the five standard solutions used for constructing the calibration curves (parallel 2).

Table D-3: Temperature program used for GC-MS analysis when MIBK was used as extraction solvent.

	Solvent delay [min]	Rate [°C]	Temperature [°C]	Hold Time [min]	Run time [min]
Initial	6		40	5	5
Ramp 1		6	280	0	45
Ramp 2		40	300	5	50.5

Retention time FUR and HMF were 6.8-7.0 min and 18.4-18.6 min, respectively

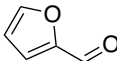
Table D-4: Temperature program used for GC-MS analysis of samples containing GVL.

		Solvent delay [min]	Rate [°C]	Temperature [°C]	Hold Time [min]	Run time [min]
Run 1	Initial	6	-	40	5	5
(pre GVL)	Ramp 1	-	6	64	0	9
Run 2	Initial	12	-	40	5	5
(post GVL)	Ramp 1	-	6	190	0	30

FUR eluted between 6.8-7.0 min in run 1 and HMF eluted between 18.4-18.6 min in run 2.

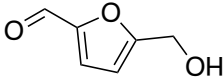
APPENDIX E – PHYSICOCHEMICAL PROPERTIES OF CENTRAL COMPOUNDS

Table E-1: Physical and chemical properties of FUR. Adapted from (Sigma-Aldrich, 2020).

Property	Value
Chemical formula	C ₅ H ₄ O ₂
Structure	
CAS	98-01-1
Appearance ^a	Clear, viscous fluid
Molar mass [g mol ⁻¹]	96.082
Relative density [g mL ⁻¹] ^a	1.16
Refractive index [n ₂₀ /D]	1.53
Melting point [°C]	-36
Flash point [°C]	61.7
Boiling point [°C]	162
Autoignition temperature [°C]	315
Enthalpy of vaporization (ΔH_{vap})[KJ mol ⁻¹]	44.7
Enthalpy of fusion (ΔH_{fus})[KJ mol ⁻¹]	14.4
Solubility in water at 20 °C (g 100 ml ⁻¹ water)	8.3
Dielectric constant (ϵ) ^a	41.799
LD ₅₀ (Rat/Oral) [mg kg ⁻¹]	127
LD ₅₀ (Rabbit/Dermal) [mg kg ⁻¹]	>2000
Vapor pressure	18.0 hPa at 55 °C 2.3 hPa at 20 °C

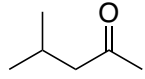
^aMeasured at 25°C

Table E-2: Physical and chemical properties of HMF. Adapted from (Sigma-Aldrich, 2020).

Property	Value
Chemical formula	C ₆ H ₆ O ₃
Structure	
CAS	67-47-0
Appearance ^a	White solid
Molar mass [g mol ⁻¹]	126.11
Relative density [g mL ⁻¹] ^a	1,243 ^a
Refractive index [n ₂₀ /D]	1.562
Melting point [°C]	28-34
Flash point [°C]	79
Boiling point [°C]	114-116
Autoignition temperature [°C]	n/a
Enthalpy of vaporization (ΔH_{vap})[KJ mol ⁻¹]	83,4
Enthalpy of fusion (ΔH_{fus})[KJ mol ⁻¹]	19,8
LD ₅₀ (Rat/Oral) [mg kg ⁻¹]	2500

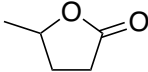
^aMeasured at 25°C

Table E-3: Physical and chemical properties of MIBK. Adapted from (Sigma-Aldrich, 2020).

Property	Value
Chemical formula	C ₆ H ₁₂ O
Structure	
CAS	108-10-1
Appearance ^a	Colorless liquid
Molar mass [g mol ⁻¹]	100.16
Relative density [g mL ⁻¹] ^a	0.801 ^a
Refractive index [n ₂₀ /D]	1.395 ^b
Melting point [°C]	-84.7
Flash point [°C]	14.0
Boiling point [°C]	117-118
Azeotrope boiling point with water [°C]	87.9
MIBK content azeotrope with water [wt%]	75.7
Vapor pressure [kPa]	2.13 ^b
LD ₅₀ (Rat/Oral) [mg kg ⁻¹]	2080

^aMeasured at 25 °C, ^bMeasured at 20 °C

Table E-4: Physical and chemical properties of GVL. Adapted from (Sigma-Aldrich, 2020).

Property	Value
Chemical formula	C ₅ H ₈ O ₂
Structure	
CAS	108-29-2
Appearance ^a	Clear, colorless liquid
Molar mass [g mol ⁻¹]	100.116
Relative density [g mL ⁻¹] ^a	1.0546 ^a
Refractive index [n ₂₀ /D]	1.4333 ^a
Melting point [°C]	-31
Flash point [°C]	96
Boiling point [°C]	207-208
Vapor pressure [kPa]	0.65 (25 °C)
LD ₅₀ (Rat/Oral) [mg kg ⁻¹]	8800

^aMeasured at 20 °C, ^bMeasured at 25 °C

APPENDIX F – SECOND PROCEDURAL BLANK GC-MS

A second procedural blank was prepared for GC-MS in order to control the results obtained from the first procedural blank. Two samples diluted 200 and 400 times were prepared and analyzed in duplicates to see how concentration affected analytical accuracy and precision.

Table F-1: Raw-data from the second procedural blank for GC-MS.

Sample diluted 400 times				
	Area Parallel 1	Area Parallel 2	Deviation parallels [%]	Average
FUR	18702776	16649121	-11.0	17675948
HD	128431806	149522987	16.4	138977397
CH	54478811	56871501	4.4	55675156
FUR/HD ratio	0.1456	0.1113	-23.6	0.128
FUR/CH ratio	0.3433	0.2927	-14.7	0.318
Sample diluted 200 times				
	Area Parallel 1	Area Parallel 2	Deviation parallels [%]	Average
FUR	43197473	44624704	3.3	43911088
HD	150077475	151151858	0.7	150614672
CH	57708543	59398931	2.9	58553737
FUR/HD ratio	0.288	0.306	6.3	0.297
FUR/CH ratio	0.749	0.776	2.3	0.760

FUR = Furfural, HD = Hexadecane, CH = 1-Chlorohexane

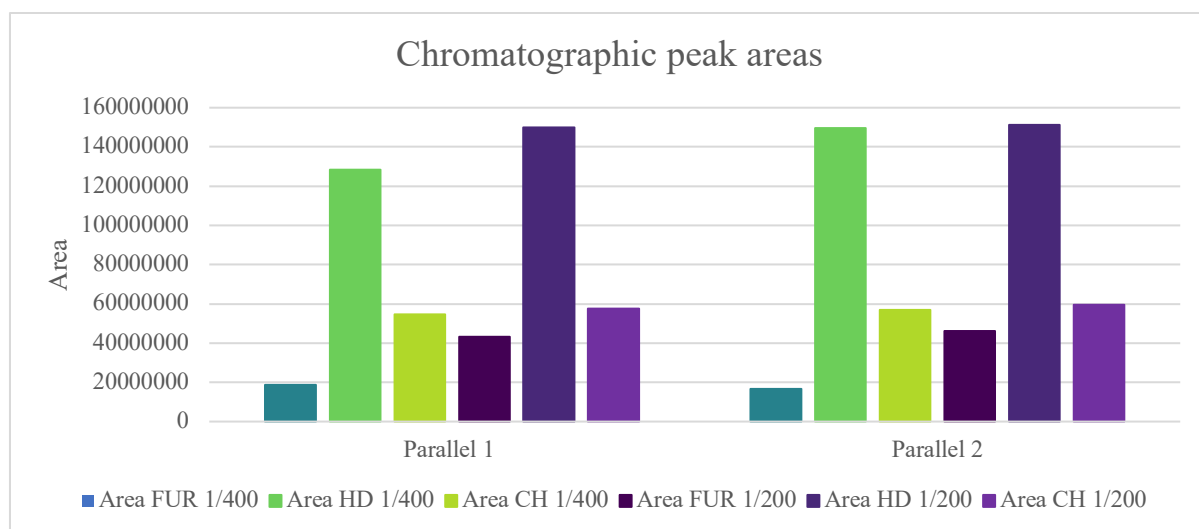


Figure F-1: Chromatographic peak areas for parallel 1 and 2.

In Figure F-1, two samples diluted 1/400 and 1/200 relative to the original concentration were analyzed twice (parallel 1 and 2). A clear systematic trend in terms of relative peak area can be observed between parallel 1 and 2. Hence, the relative peak area between FUR/IS was used when constructing the calibration curves used for the quantification using GC-MS.

Table F-2: Comparison of predicted FUR yields including percentage deviation (actual vs. predicted) using different quantification procedures (relative peak area between FUR and IS and calibration curves). The mass of FUR added to the procedural blank was 0.0490 g.

	m_{FUR} (1/200) [g]	Deviation (1/200) (actual vs. predicted) [%]	m_{FUR} (1/400) [g]	Deviation (1/400) (actual vs. predicted) [%]
$\hat{y}_{(FUR/HD\ ratio)}$	0.0104	-78.8	0.0091	-81.4
$\hat{y}_{(FUR/CH\ ratio)}$	0.0314	-35.9	0.0266	-45.7
$\hat{y}_{(Avg.\ Lin.\ reg.\ FUR/HD)}$	0.0386	-21.2	0.0387	-21.0
$\hat{y}_{(Avg.\ Lin.\ reg.\ FUR/CH)}$	0.0538	9.8	0.0505	3.1

\hat{y} = predicted yield, CH = chlorohexane, HD = hexadecane, FUR = furfural

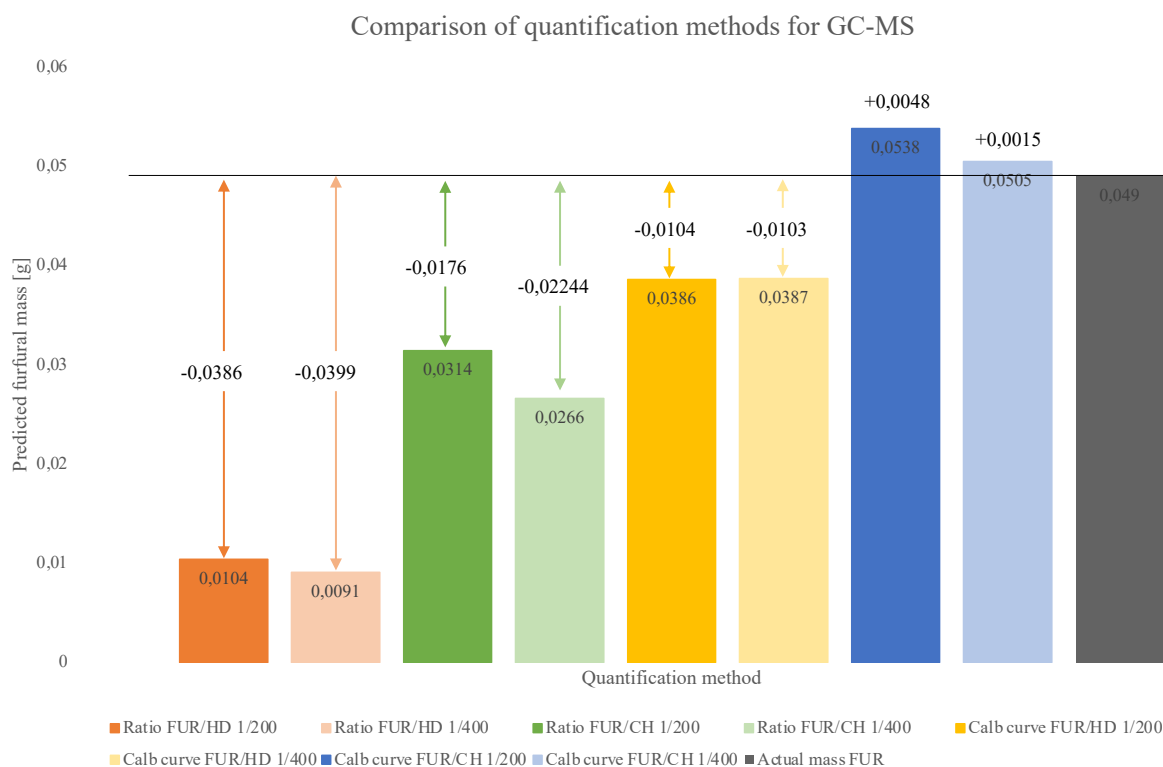


Figure F-2: Actual vs predicted mass of FUR from the procedural blank by comparing relative chromatographic peak areas (ratio FUR/HD/CH) and calibration curves as quantification tools.

When comparing the results obtained from the relative peak areas between FUR and the two internal standards (Table F-2, Figure F-2) with the actual mass of FUR added to the procedural blank (0.0490g) it is evident that both HD (0.0091-0.0104 g) and CH (0.0266-0.0314g) underestimated the amount of FUR present in the sample. In fact, the average deviation for HD and CH were -80.1% and -40.8%, respectively. Each sample was analyzed in duplicates, so no standard deviation was calculated for the predicted yields. However, the results presented above suggests that peak area ratios between FUR and internal standards cannot be used for accurate quantification of FUR. These results coincide with the previously discussed procedural blank and literature findings.

To further examine the possibility of using GC-MS for accurate quantification of FUR, the calibration curves were used to calculate the predicted mass of FUR present in the same procedural blank. When utilizing the calibration curves for hexadecane and chlorohexane in Figure 5-1 to calculate the predicted mass of FUR present in the procedural blank, one can see that CH predicts a higher mass compared to HD, which coincides with the results obtained using area ratios and for the previously discussed procedural blank. The linear regression model

for HD under-estimated the mass of FUR present in the sample by 21.1%, while the model for CH over-estimated the mass of FUR present in the sample by 6.5%.

To further test GC-MS as quantification tool, the response factor for FUR (F_{fur}) using HD and CH as IS were calculated using the following equation:

$$F_a = \frac{A_a}{A_{IS}} \times \frac{m_{IS}}{m_a} \quad (\text{Eq. A1.1})$$

Where a denotes desired compound (FUR), F_a is the response factor for the desired compound, A is the chromatographic peak area, IS is the internal standard and m is mass. When computing the predicted mass of FUR present in the procedural blank, equation F.1a is solved for m_a , which yields the following expression:

$$m_a = \frac{A_a}{A_{IS}} \times \frac{m_{IS}}{F_a} \quad (\text{Eq. A1.2})$$

F_{fur} was calculated for the five calibration solutions using Eq. A1.1 to see whether a reproducible response factor could be generated and used to accurately predict the mass of FUR present in the organic phase. However, the response factors proved to be highly dependent on both type of IS and the concentration of FUR in the sample (Figure F-3). The calculated F_{fur} varied between 3.1 – 5.3 and 6.5 – 11.3 for HD and CH, respectively. These results show that response factors can not be used as a reliable quantification tool to predict the mass of FUR in samples where the concentration of FUR is unknown.

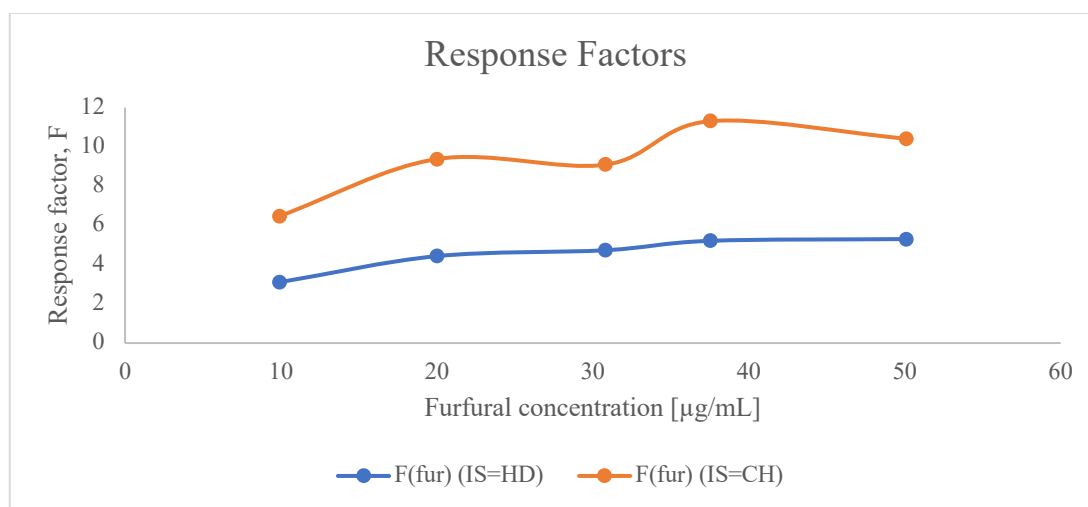


Figure F-3: Calculated response factors for the five calibration solutions.

These results also support the previously discussed findings in chapter 5.1, i.e., that area ratios between FUR/IS, calibration curves, and response factors in combination with GC-MS are inadequate tools for accurate quantification of FUR for the organic phases obtained over the course of this thesis.

APPENDIX G – STACKED NMR SPECTRA OF REPLICATES

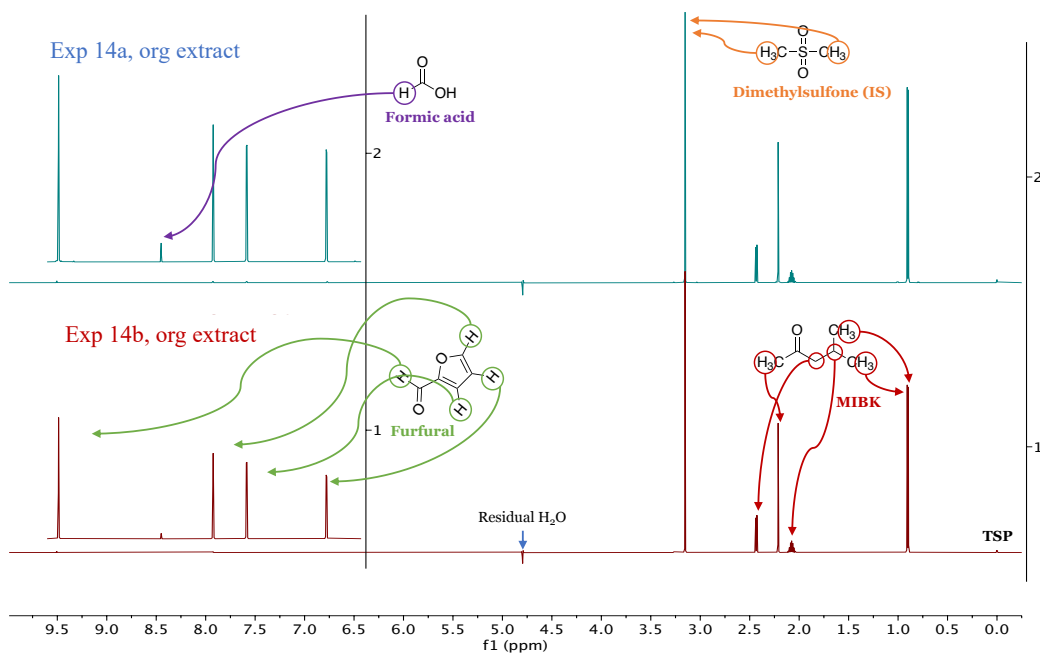


Figure G-1: Stacked $^1\text{H-NMR}$ spectra of the organic phases from experiment 14a and 14b.

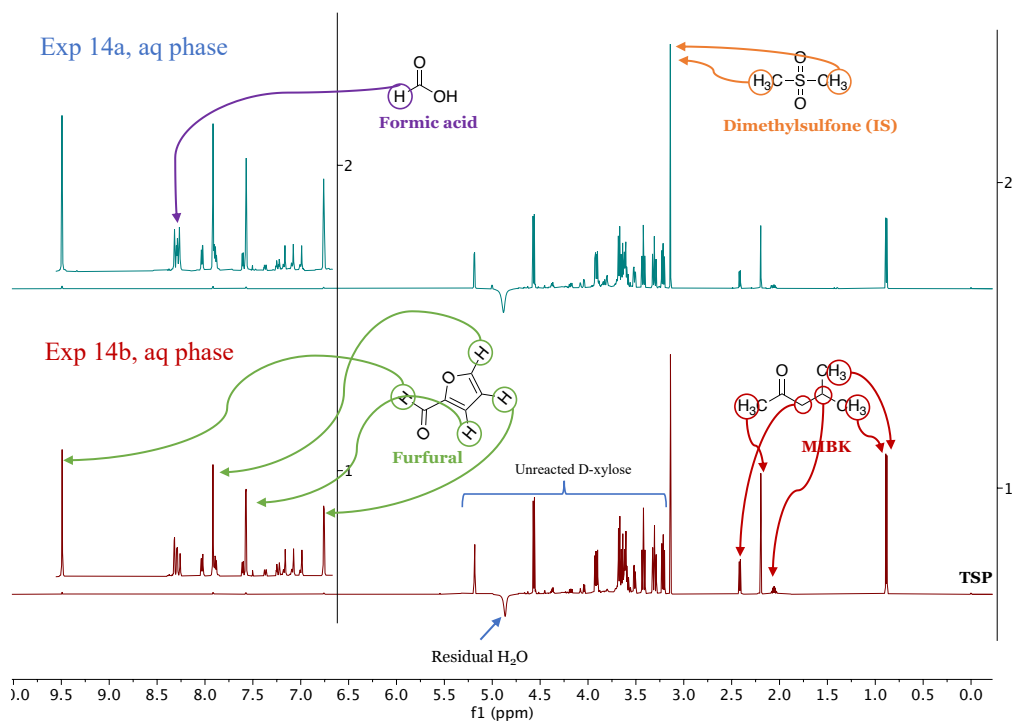


Figure G-2: Stacked $^1\text{H-NMR}$ spectra of the aqueous phases from experiment 14a and 14b.

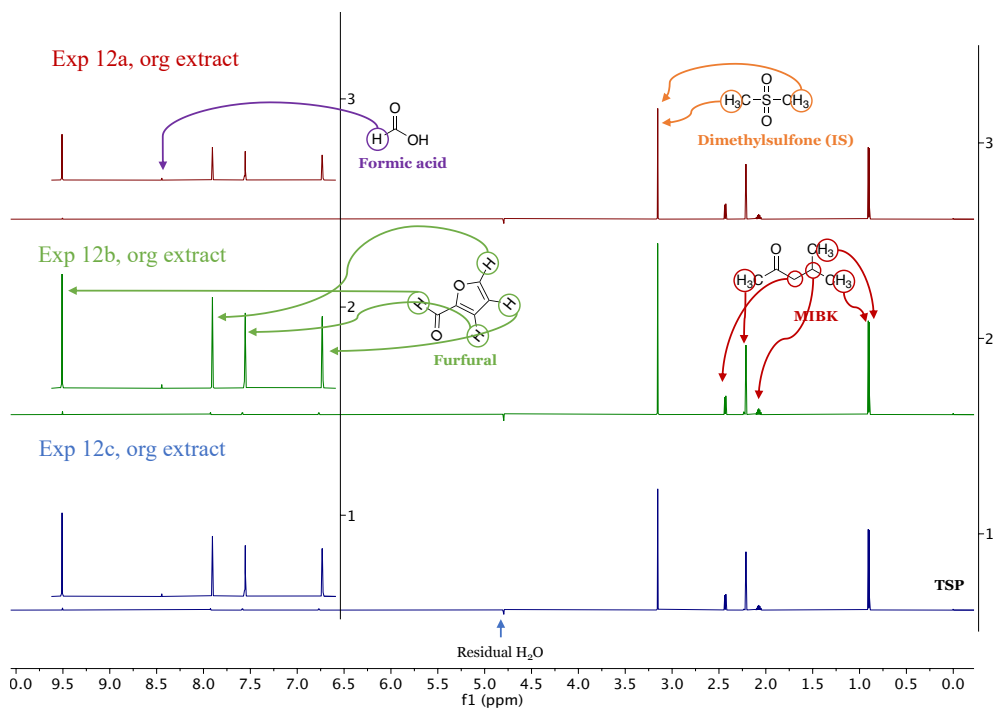


Figure G-3: Stacked ¹H-NMR spectra of the organic phases from experiment 12a and 12b.

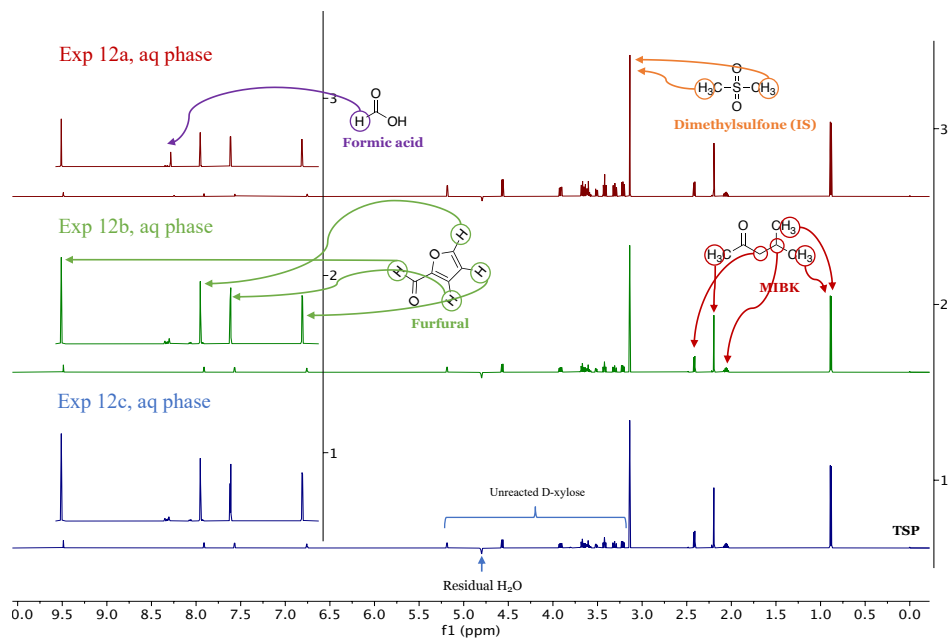


Figure G-4: Stacked ¹H-NMR spectra of the aqueous phases from experiment 12a, 12b, and 12c.

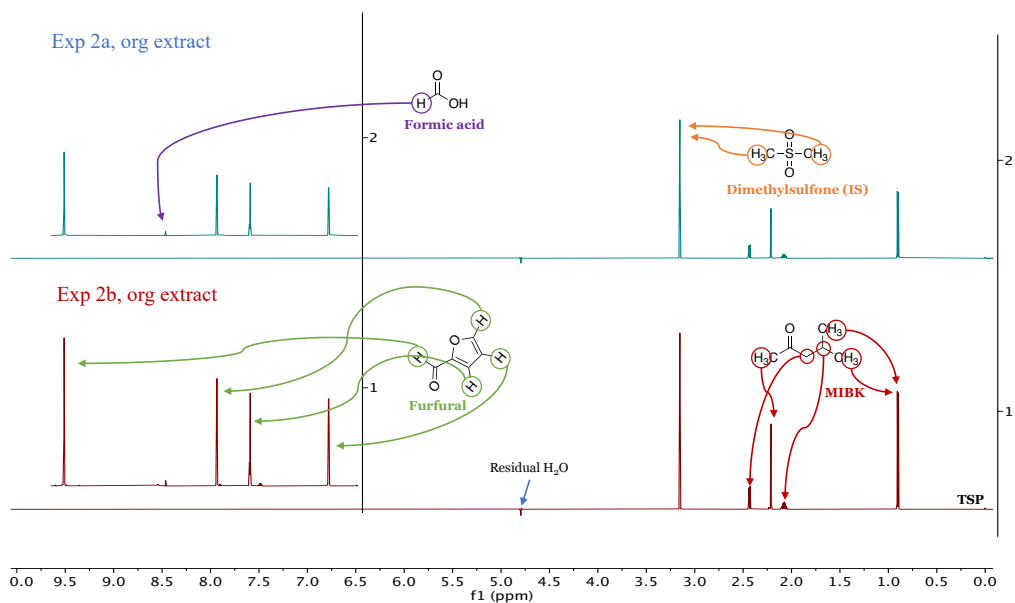


Figure G-5: Stacked ¹H-NMR spectra of the organic phases from experiment 2a and 2b.

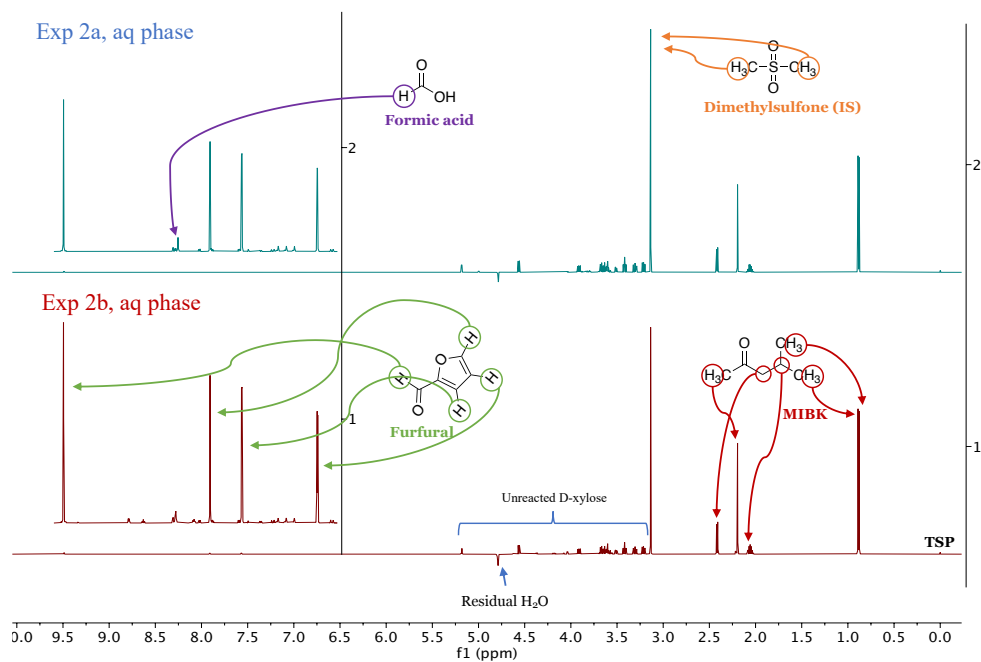


Figure G-6: Stacked ¹H-NMR spectra of the aqueous phases from experiment 2a and 2b.

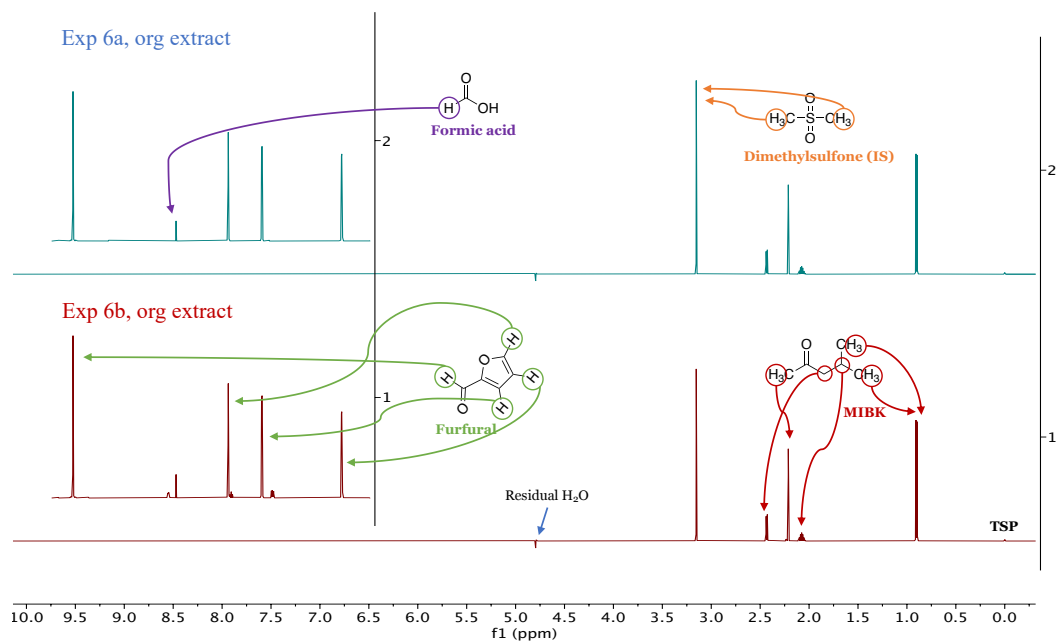


Figure G-7: stacked ¹H-NMR spectra of the organic phases from experiment 6a and 6b.

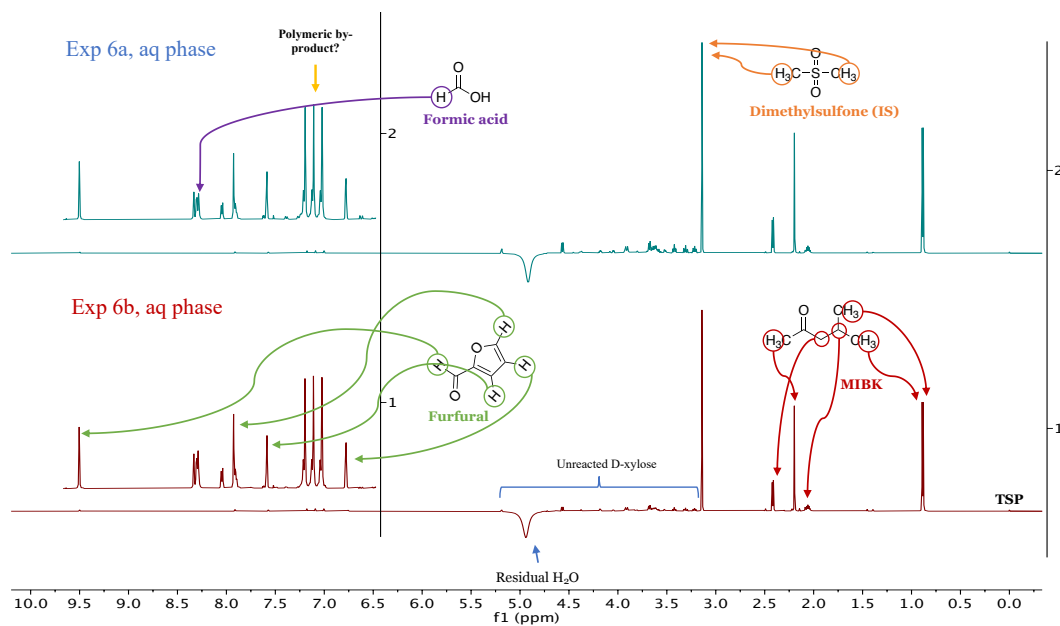


Figure G-8: Stacked ¹H-NMR spectra of the aqueous phases from experiment 6a and 6b.

APPENDIX H – NMR SPECTRA F&B REJECTS

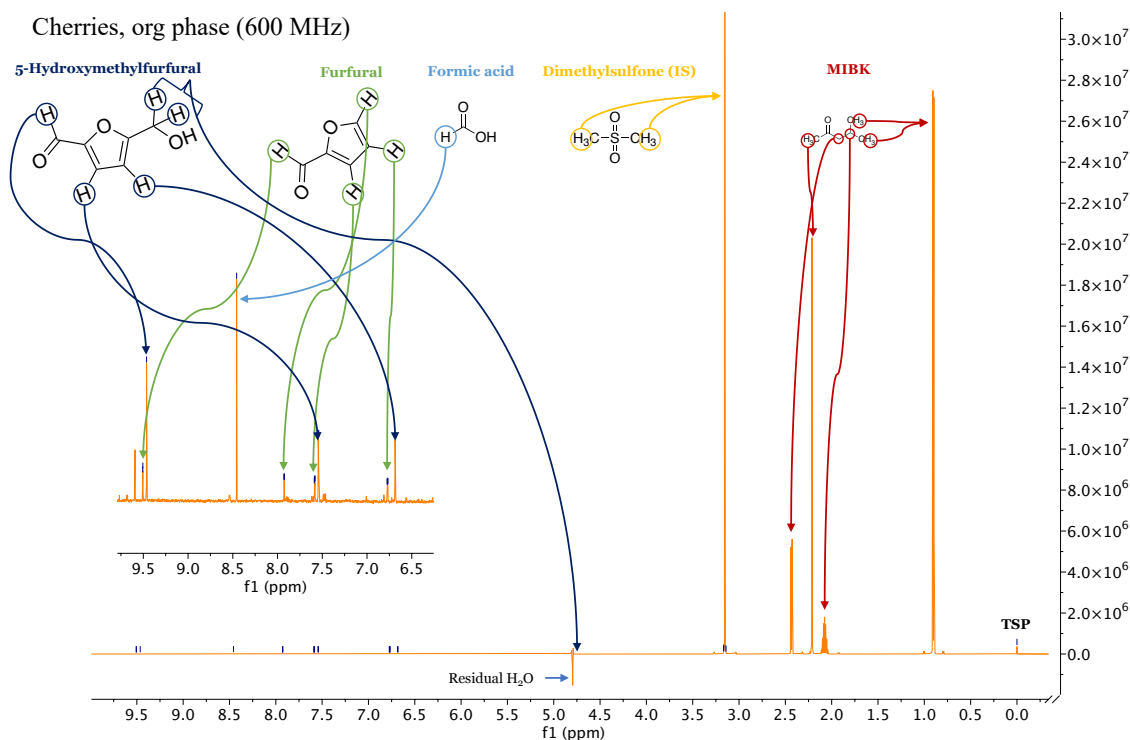


Figure H-1: ¹H-NMR spectra of the organic phase from the experiment where cherries were used as substrate.

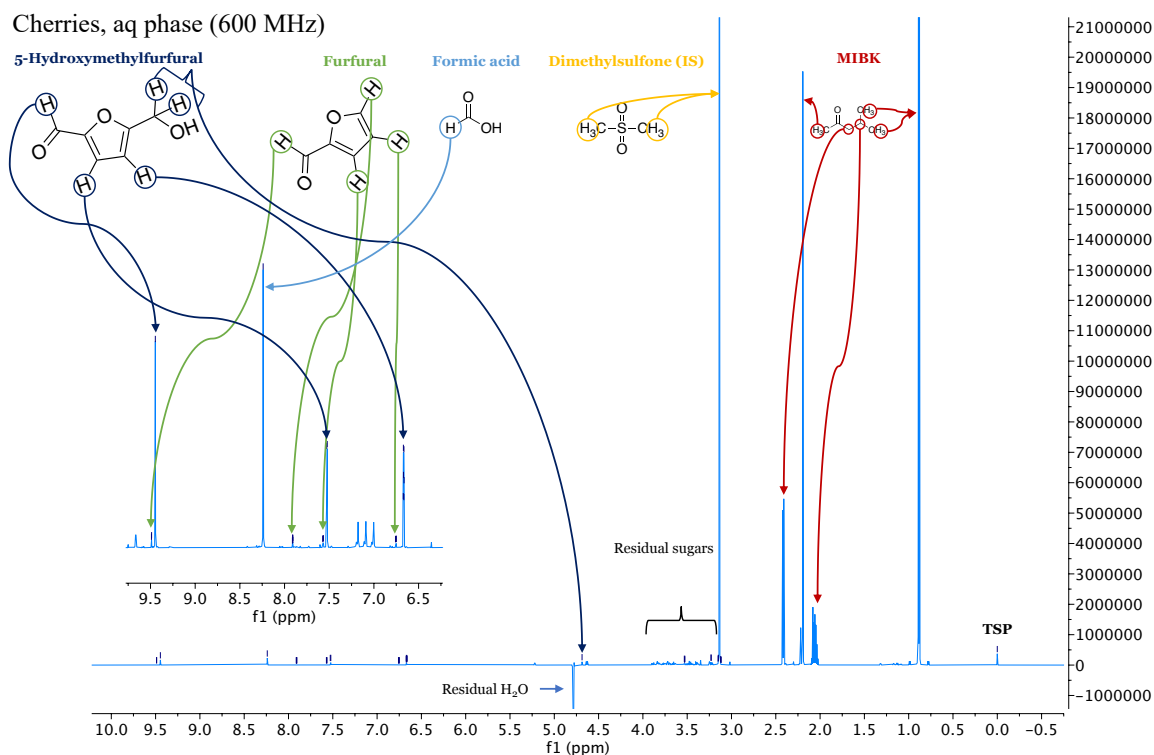


Figure H-2: ¹H-NMR spectra of the aqueous phase from the experiment where cherries were used as substrate.

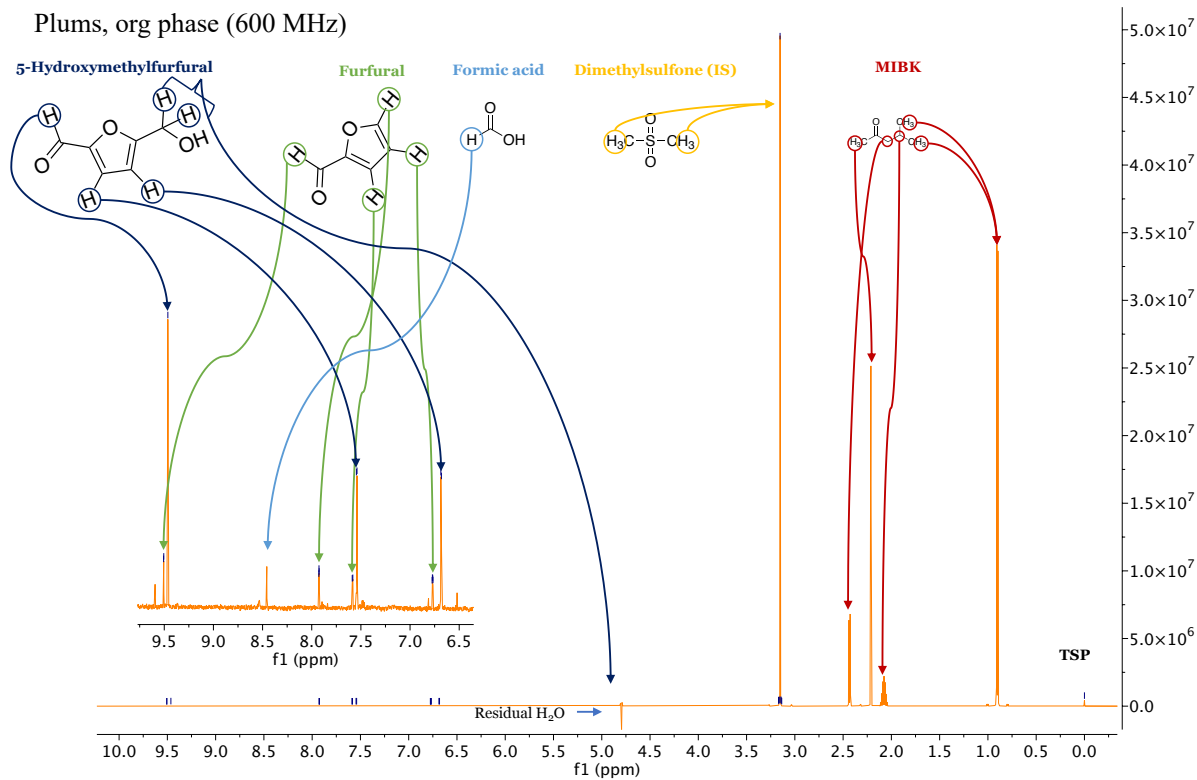


Figure H-3 ¹H-NMR spectra of the organic phase from the experiment where plums were used as substrate.

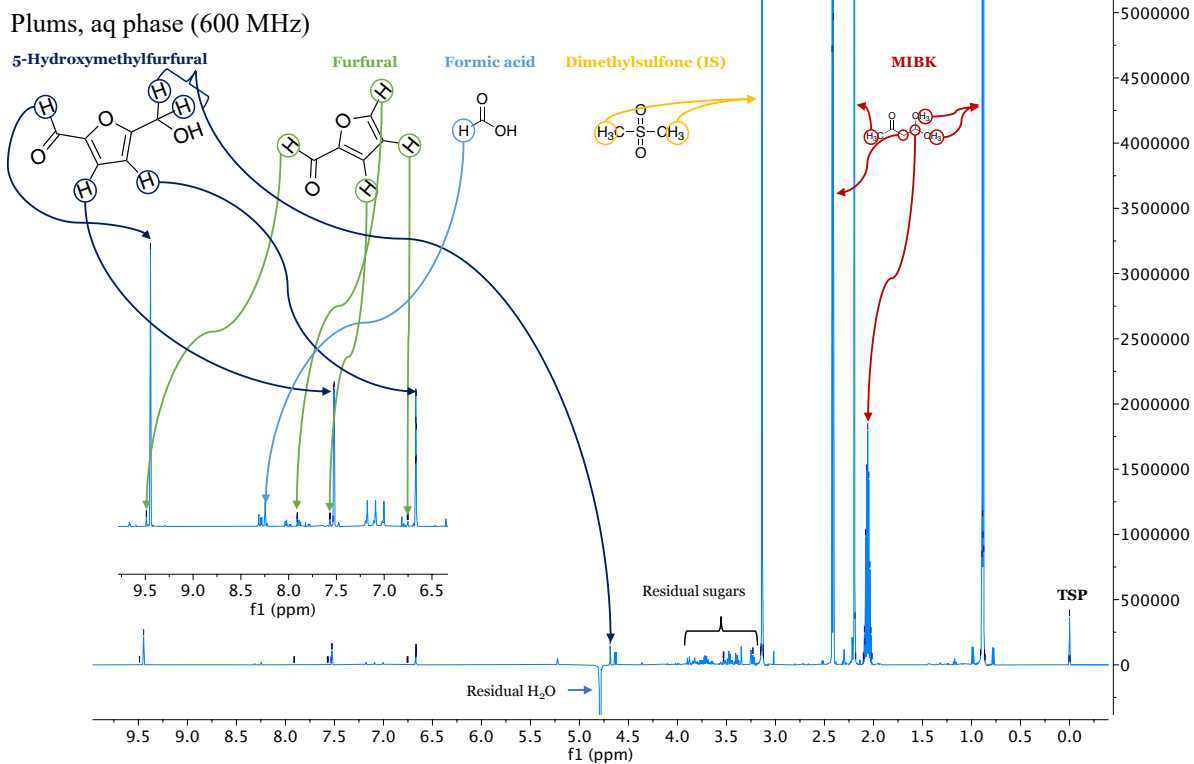


Figure H-4 ¹H-NMR spectra of the aqueous phase from the experiment where plums were used as substrate.

Table H-1: Raw data for calculating yields of FUR and HMF.

		Organic phase					Aqueous phase			
Exp	Compound	Protons	Integral	Concentration [mM]	Factor	Yield [g]	Integral	Concentration [mM]	Factor	Yield [g]
Cherry	Furfural	1	0.0004	0.0362	-	0.00006	0.0016	0.1628	-	0.00007
	HMF	1	0.0017	0.1725	-	0.00035	0.0317	3.2797	-	0.00180
	DMSO₂	6	6.0000	103.5030	0.0097	-	6.0000	103.3528	0.0097	-
	α and β D-Xylose	2	-	-	-	-	0.0197	4.8576	-	0.00317
	Formic acid	1	-	-	-	-	0.0540	5.5811	-	0.00112
Plum	Furfural	1	0.0001	0.0104	-	0.00002	0.0018	0.1810	-	0.00007
	HMF	1	0.0003	0.0313	-	0.00007	0.0416	4.2992	-	0.00231
	DMSO₂	6	6.0000	104.4300	0.0096	-	6.0000	103.4300	0.0097	-
	α and β D-Xylose	2	-	-	-	-	0.0385	3.9821	-	0.00255
	Formic acid	1	-	-	-	-	0.0053	0.5482	-	0.00011

APPENDIX I – CALCULATION OF THEORETICAL YIELD FROM D-XYLOSE AND HEMICELLULOSE

Calculation of the theoretical FUR yield obtainable from D-xylose and hemicellulose can be done by applying some assumptions and simplifications. Starting with Hemicellulose, which is primarily composed of pentose units and no more than 15% hexose units, the molecular weight of one hemicellulose unit can be assumed to be roughly 132g/mol. The molecular weight of FUR is ~96g/mol. This means that from ~132g of hemicellulose, ~96g of FUR can be generated considering 100% conversion and selectivity. This gives a theoretical FUR yield of 72.7mol% from one hemicellulose unit (Luo et al., 2017, Sahu and Dhepe, 2012). The same assumptions can be applied when using D-xylose as a substrate. D-xylose has a molecular weight of ~150g/mol. By applying the same logic as before, a maximum yield of 64.0mol% can be achieved when using D-xylose as starting material.

APPENDIX J – INFLUENCE OF EXTRACTION TIME ON CALCULATED FURFURAL YIELD

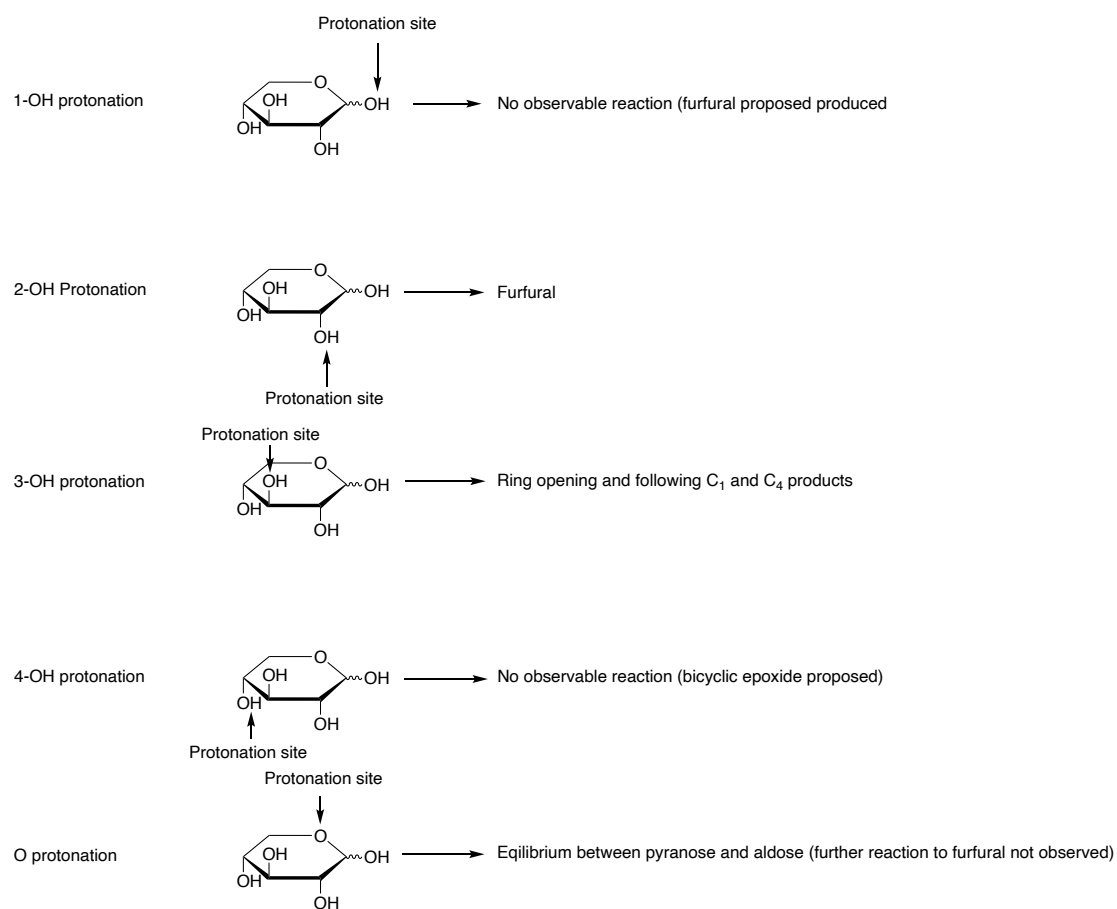
The organic phase was extracted with water and analyzed at different time intervals after extraction to see whether extraction time had a significant effect on the calculated FUR yield. Table J-1 contains the predicted mass of FUR for two experiments that were analyzed using two different extraction times.

Table J-1: Effect of extraction time on the predicted mass of FUR.

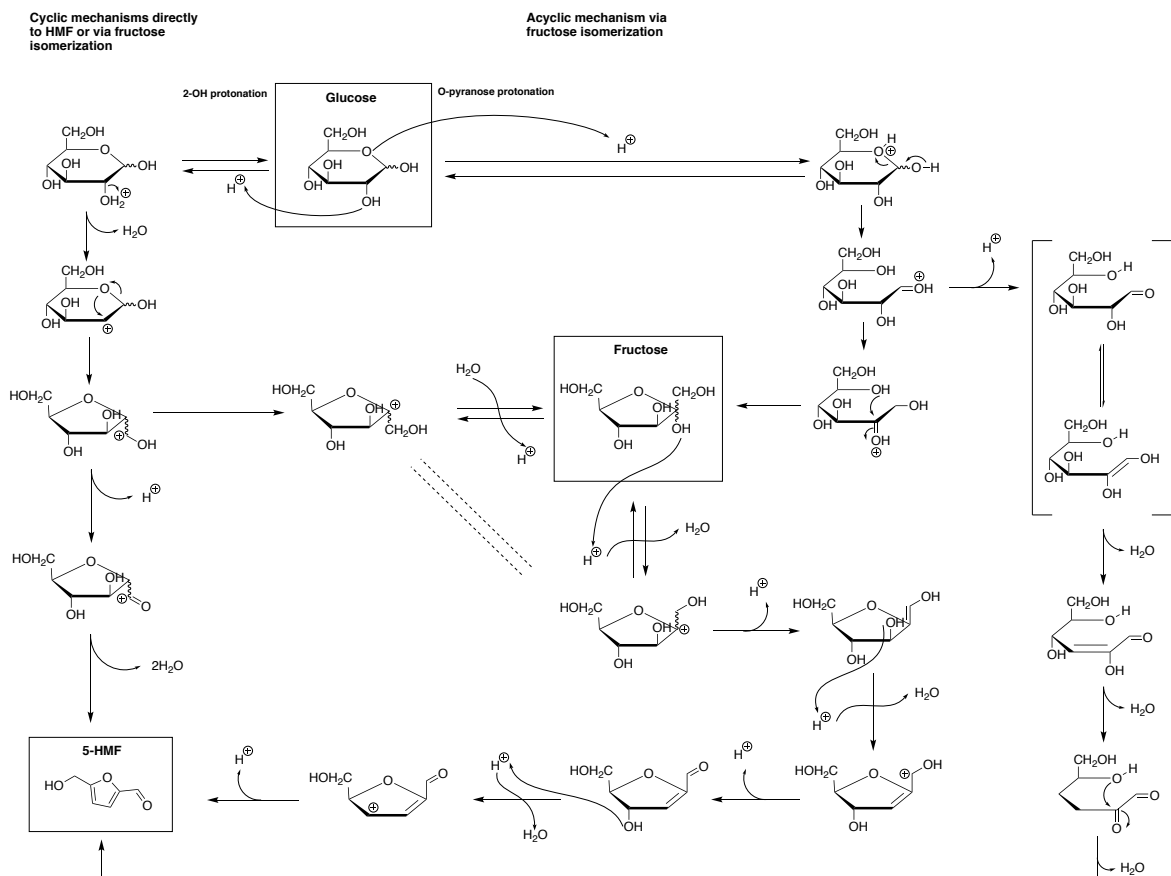
Exp #	Parallel #	Time between extraction and analysis [h]	Predicted mass org. phase	Parallel deviation [%]
14b	1	1	0.0401	3.5
	2	72	0.0421	
16	1	4	0.0975	1.7
	2	28	0.0992	

The organic phase for experiment 14b was analyzed ~1 hour (parallel 1) and ~72 hours (parallel 2) after extraction. The predicted yield for parallel 1 and 2 was 0.0407g and 0.0421g, respectively, which corresponds to a 3.4% deviation. The same procedure was repeated for the organic phase for experiment 16. The extracted organic phase was analyzed ~4h and ~28h after extraction. The calculated yields for the two parallels were 0.0975 g for parallel 1 and 0.0992g for parallel 2 (1.7% deviation). Consequently, it was concluded that the time interval between extraction and analysis did not have a significant effect the overall FUR yield as long as sufficient phase separation was achieved before sample preparation.

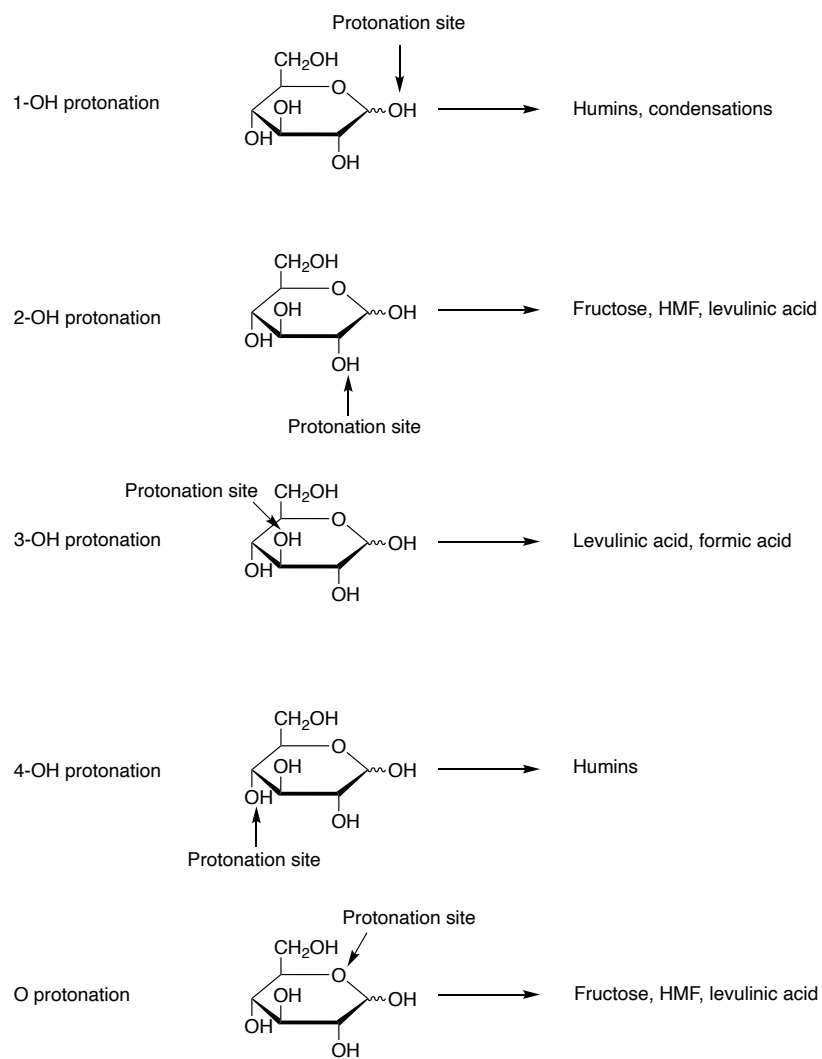
APPENDIX K – ADDITIONAL REACTION SCHEMES AND PICTURES



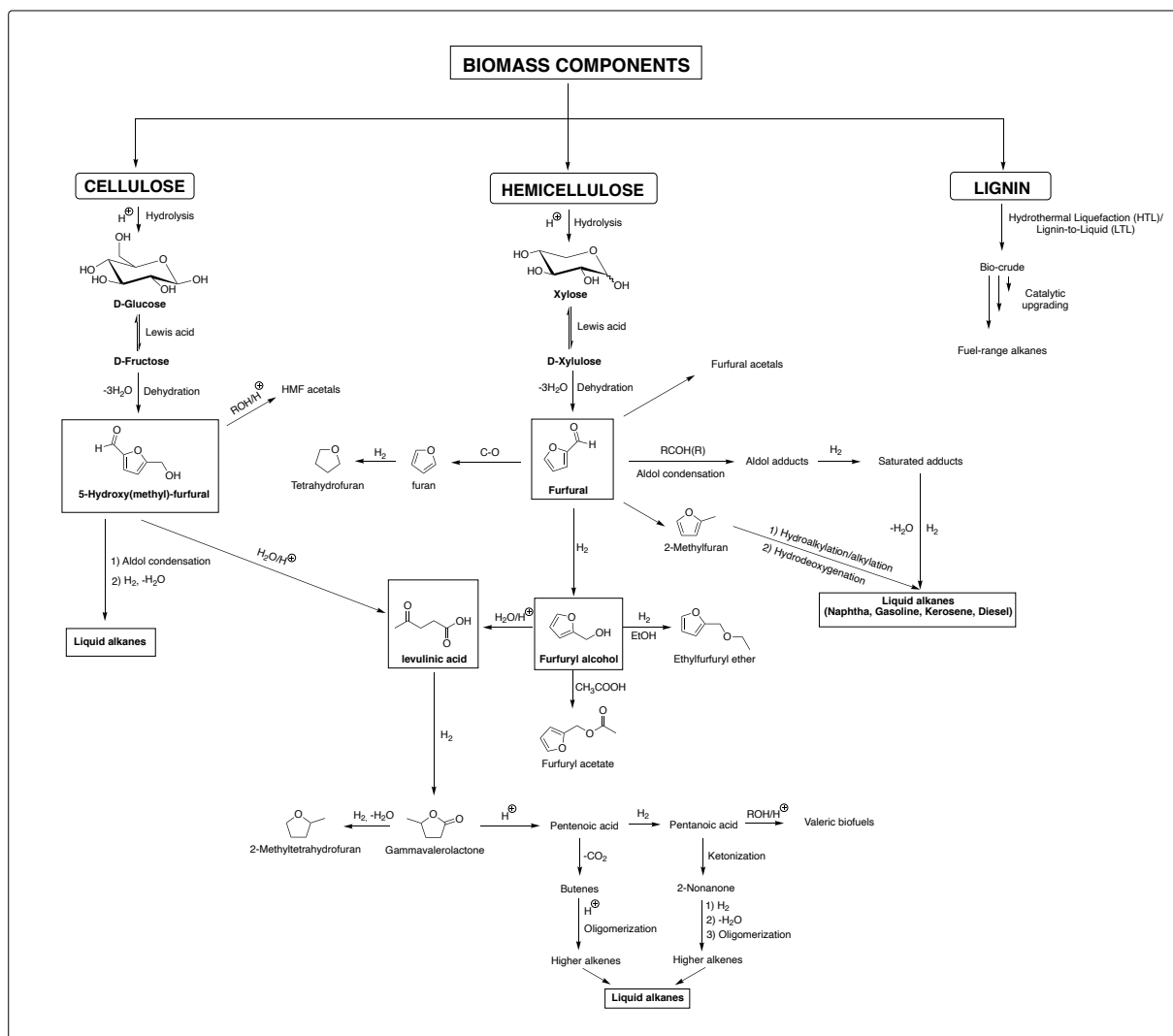
Scheme K-1: Initial site of protonation and subsequent degradation products from D-xylose determined by ab initio molecular dynamics and quantum mechanics modelling. Redrawn from (Rasmussen et al., 2014).



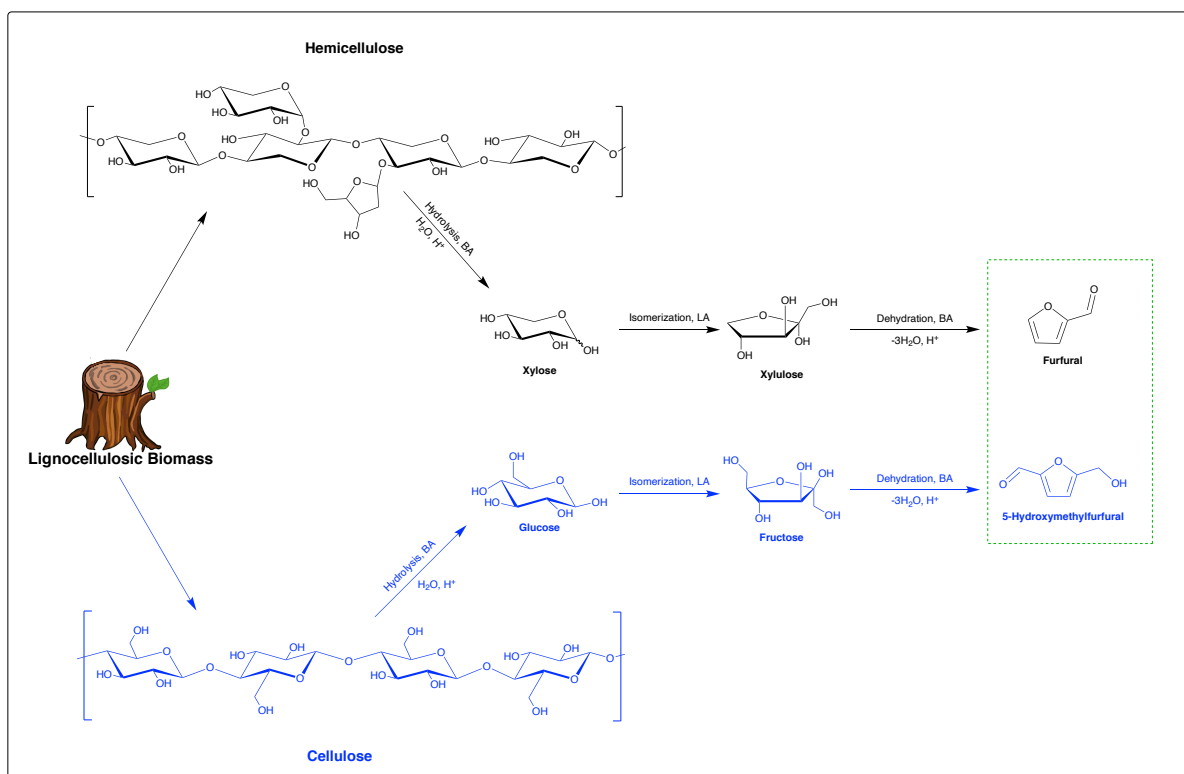
Scheme K-2: Possible synthetic pathways to HMF from glucose via fructose (cyclic and acyclic isomerization) and direct acyclic non-fructose isomerized mechanism. Redrawn from (Rasmussen et al., 2014).



Scheme K-3: Initial site of protonation and subsequent degradation products from glucose determined by ab initio molecular dynamics and quantum mechanics modelling. Redrawn from (Rasmussen et al., 2014).



Scheme K-4: Transformational pathways to fuel-range alkanes and fuel additives from FUR and HMF derived from LCB. Redrawn and adapted from (Climent et al., 2014).



Scheme K-5: Simultaneous production of FUR and HMF from LCB. Redrawn and adapted from (Mittal et al., 2020).



Scheme K-6: Pictures of a Series 4700, 316 Stainless steel batch Parr reactor (22mL) with a polyphenylene lining. The picture to the left shows the different reactor parts when the reactor is disassembled.

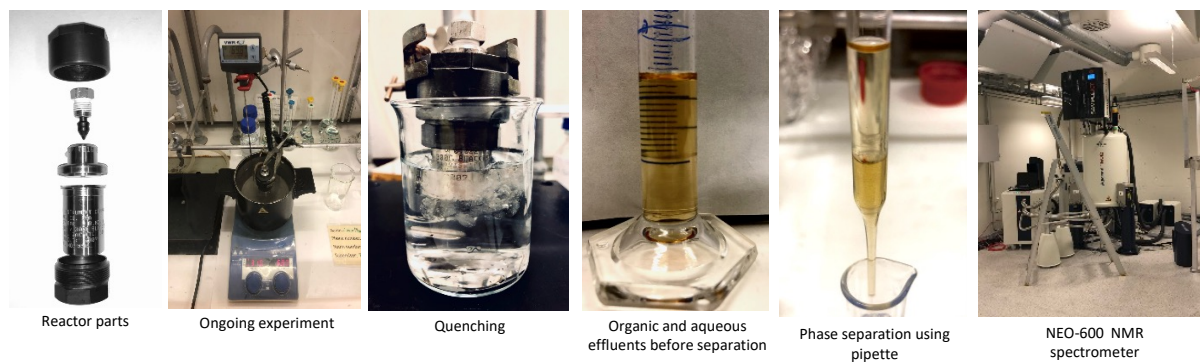


Figure K-7: Pictures of different experimental steps.